UNIVERSITY OF CALIFORNIA

SANTA CRUZ

EXCITON DYNAMICS IN CONJUGATED POLYMER PHOTOVOLTAICS: STEADY-STATE AND TIME-RESOLVED OPTICAL SPECTROSCOPY

A dissertation submitted in partial satisfaction
of the requirements for the degree of

DOCTOR OF PHILOSOPHY

in

PHYSICS

by

Stephanie V. Chasteen

December 2005

The Dissertation of Stephanie V. Chasteen
is approved:

_____
Professor Sue A. Carter, Chair

_____
Professor Frank Bridges

_____
Professor Holger Schmidt

_____
Lisa Sloan
Vice Provost and Dean of Graduate Studies

Table of Contents

List of Figures & Illustrations

Chapter 1. Introduction and Motivation

Chapter 2. Spectroscopy

Chapter 3. Photoexcitations

Chapter 4. Methods

Chapter 5. Characterization of the hole-transporting polymer M3EH-PPV

Chapter 9. Charge separation versus exciton generation: Comparison of blends and layers of M3EH-PPV and CN-ether-PPV

Chapter 10. Summary and Conclusions

Appendices

List of Tables

Abstract

The performance of organic photovoltaics is severely limited by poor exciton dissociation and charge transport due in part to high rates of exciton recombination and low charge mobilities in polymers. This challenge can be partially overcome through the use of blended and layered heterojunctions. Such morphologies offer multiple exciton dissociation sites and separate charge pathways, thus limiting exciton recombination, and allowing for thicker, more absorbing, polymer films.

I have performed photovoltaic device characterization and time-resolved and steady-state photoluminescence on a variety of donor-acceptor heterojunction. I have used these methods to understand excited state dynamics and how they affect device performance.

As hole-transporters I use a derivative of poly-phenylene-vinylene (M3EH-PPV) and poly-3-hexylthiophene (P3HT). As electron-transporters I use the metal oxide titanium dioxide (TiO_2), the electron-transporter CN-PPV, and a fullerene derivative (PCBM). These materials are layered and blended together to form donor-acceptor heterojunctions. All heterojunctions result in enhanced device performance, and 1:4 M3EH-PPV:PCBM resulted in the highest efficiencies.

M3EH-PPV emission is characterized by single-chain excitations, and the decay is dominated by short components of 0.20 and 0.45 ns. CN-ether-PPV is dominated by interchain excited state species -- ie., excimers – with a decay time of 14.0 ns. The broken conjugation imposed by the ether group affect the excited state, resulting in an excited state

species that is particularly vulnerable to quenching. This has important ramifications for material design.

Hole-transporting polymers blended and layered with CN-ether-PPV have high currents (J_{sc} up to 3.3 mA/cm^2) and good quenching relative to CN-ether-PPV (~90%) due to charge separation and generation, respectively. Hole-transporters blended with PCBM result in efficient devices (J_{sc} up to 14 mA/cm^2) due to rapid charge transfer and the existence of charge percolation pathways caused by the presence of aggregates of PCBM. The size of the aggregates affects charge transport, and is highly dependent upon film processing and blend ratio.

The best device performance does not necessarily correlate with the excited state lifetime, however. Morphological differences, such as charge pathways that enable efficient charge transport, often outweigh the effect of charge transfer. Suggestions for improvement of nanoscale morphology are given.

Acknowledgements

I would like to acknowledge the Beyond the Horizons program of DOE-NREL, contract *ACQ-1-306-19-03* and the Graduate Assistance in Areas of National Need (GAANN) for providing financial support for this work.

Thank you to Dr. Sue Carter for years of mentorship and support. Her flexibility in allowing me to decide what I wanted to get out of my degree and unfailing support for my alternative career path has helped me to create a portfolio that has me well on my way to a career in public science communication. She has trained me well as a scientist and has given me the opportunity to make an impact in society at large.

I owe a large debt of gratitude to Dr. Garry Rumbles at NREL, who provided the apparatus for the time-resolved and steady-state photoluminescence measurements and gave cheerfully of his time and expertise. His enthusiasm and interest in the subject sparked my own, and got me through the final year. Another great big thank-you goes to Dr. Marcus Jones for assisting with the analytical software and apparatus for spectroscopic measurements at NREL.

Thanks to Mom, Dad, and Lori, who have supported me over these many years of academia and life experience, never questioning what is undoubtedly a curious career path. Thank you too for being so understanding over the years as I've remained both too poor and too busy to be in contact as much as I should. Now I've no more excuses…

Thanks thanks thanks to…

- Dr. David Belanger for giving me a chance. He supported me in my application to UCSC and helped me to find financial support, making all this possible;
- Dr. Alison Breeze for EQE measurements and mentorship;
- Dr. Melissa Kreger and Dr. Yuko Nakazawa for data and useful discussions;
- Sam Berweger of UCSC for fabrication of some of the devices;
- Charles Dearie for many useful fixes in the lab, like the all-important udders, as well as for help with solar simulator calibrations;
- Jan Haerter who provided the program and performed the simulations of exciton generation and dissociation in M3EH-PPV/CN-ether-PPV layers;
- My friends David Best, Linda Feferman, Carole Gardner, and Jeroen van Duren for proofreading and providing comments on the manuscript;
- Joshua Summit (the man, not the mountain) who got me through the grueling last two weeks of writing with humor, when sane men would (should) have fled;
- Veronica Sholin of UCSC for helping with solar simulation calibration, fabrication of devices, and just generally being really fun to talk to about science. I know I leave the solar cell effort in good hands.

And lastly I want to thank my dear friend Jeff Wilsbacher – housemate, support staff, bad influence, teacher, and big brother – without whose support I wouldn't have been able to change my own oil or finish this degree, or at least I would have been miserable in the process. What will I do without you?

Chapter 1

Introduction and Motivation

1.1 History

Polymer photovoltaics have attracted a great deal of attention in recent years because they offer a way of producing inexpensive electricity from the sun due to the inherent low cost of polymer processing. Still, after a decade of research, the device efficiency of polymer photovoltaics lags significantly behind that of the inorganics. This has hampered the introduction of the technology into the marketplace – the presumed goal of the research efforts.

Bell Laboratories developed the first solar cell in 1965. It was based on silicon, and was about as efficient as the best of today's organic cells – 6% (Chapin, Fuller et al. 1964). Today's triple-junction inorganic cells boast efficiencies of 35.2% in the lab using solar concentrators, and 19.2% in thin film copper indium gallium diselenide. The standard modules found on most rooftops are made of cheaper amorphous silicon with more modest efficiencies -- around 15%.

Since 1980, solar energy production has grown by about 20-25% each year, reaching 427 mega-watt production capacity in 2002 (Scott and Malliaras 1999), accounting for less than 0.1% of the world's energy production. Cost remains the major challenge to more widespread use of photovoltaics. Without subsidies, the cost per kW-hr from photovoltaics is ~ 25 cents, compared to ~10 cents for fossil fuels.

The price of silicon photovoltaics has decreased dramatically since 1976, when amorphous silicon solar cells were developed. The drop in price is due in part to aggressive R&D beginning with the fuel crisis of the 1970's, as well as economies of scale: for each

doubling of production capacity, the price of solar panels drops about twenty percent (see Figure 5.1).

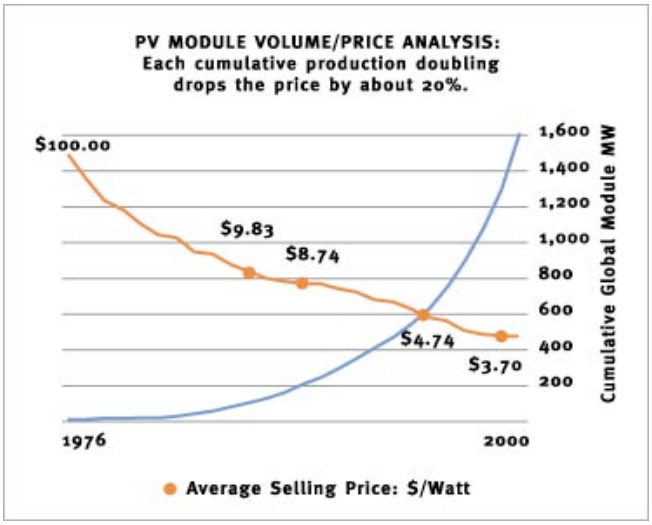

Figure 1.1. The empirical relation of production capacity and price of photovoltaics. Source: http://powerlight.com.

Because of the high material costs of silicon, however, the achievable price reductions from further increases in production volume are reaching a plateau. Silicon and other inorganics require high temperature and vacuum conditions required for their production (such as molecular beam epitaxy and chemical vapor deposition), which form fundamental barriers to lowering costs of photovoltaics. Thus photovoltaics remain too expensive to compete efficiently with fossil fuels on a strict dollar-per-watt basis. When the cost for a typical photovoltaic panel is spread out over its 20-year lifetime, and divided by the approximate amount of power it is expected to produce over that time in a sunny location, it costs about 25 cents per kW-hr -- higher, on average, than current consumer costs of 10-25 cents per kW-hr for utility-generated electricity in California. In fact, it takes an estimated 10 years of use to recoup the energy invested in the manufacture of today's photovoltaics.

> We've reached the limit of economies of scale. The challenge is to figure out the physics to make it cheaper.
>
> ---*Greg Smestad, Ph.D.*

Many modern research efforts focus on reducing material costs: Thin film technologies (silicon, cadmium telluride, etc.) use less material; Amorphous silicon is "dirtier" and thus less expensive to process; Organic photovoltaics, which include electrochemical (Graetzel) cells, polymer cells, and composites of polymers, small molecules, and inorganics, may be processed at room temperature. Inexpensive processing, as well as other benefits, such as mechanical flexibility and semi-transparency, are the main attraction of organic photovoltaics.

Organic molecules have been used in photovoltaics and other semiconductor applications for quite some time. Photoconductivity was observed in anthracene in 1906. Some of the first materials to demonstrate the photovoltaic (PV) effect were dyes, such as methylene blue, and biological molecules, such as chlorophyll and phthalocyanines (Spanggaard and Krebs 2004). Since the late 1980's organic materials have been used as photoconductors in xerography. But most organics are deposited by thermal evaporation, so they remain mechanically inflexible.

In 1977 it was discovered that doped conjugated polymers could act as semiconductors (Chiang, Fincher et al. 1977; Shirakawa, Louis et al. 1977). Alan Heeger, Alan MacDiarmid, and Hideki Shirakawa shared The Nobel Prize in chemistry in 2000 for the discovery and development of conductive polymers. Their work focused on polyacetylene (see Figure 1.2) which was first used in a photovoltaic in 1982 (Weinberger, Akhtar et al. 1982). There is currently broad interest in the charge generation and transport properties of conjugated polymers, due to their potential for flexible electronics with an

incredibly broad range of applications. They have the electronic properties of a semiconductor, but the mechanical flexibility and ease of production of plastics. Because they can be liquid processed at room temperature using simple deposition techniques such as ink-jet printing and screen printing (Shaheen, Radspinner et al. 2001), their materials costs are lower than traditional semiconductors, and they can be deposited over large areas and/or on plastic substrates. In one day a typical sheet-feed printing machine can process the same area of material as a typical Si wafer production plant can process in one year (Brabec 2004). In addition, the band gap of these materials can, to a certain degree, be tuned by tampering with their chemical structure. In practice, however, it remains difficult to design a polymer with the desired spectroscopic, electronic, and charge-transport properties.

Prototypes of flexible transisitors and radio-frequency identification (RFID) tags have already been produced, and polymeric light-emitting diodes (LED's) and flexible displays are on the market through private research and development. Entrepreneurs dream of electronic paper and windows that can double as displays. Such materials are attractive for photovoltaics for the same reasons, and power conversion efficiencies of polymeric hybrid photovoltaic devices have recently approached the 5% believed necessary for cost-efficient commercial production. In the past few months, record power efficiencies for polymer photovoltaics have been reported (4.4 – 5%; J_{sc} = 10.6 mA/cm^2) using P3HT:PCBM blends optimized for film morphology (Li, Shrotriya et al. 2005; Ma, Yang et al. 2005). Higher, but uncertified, efficiencies have been reported for tandem copper phthalocyanine/C_{60} cells which reach 5.7% efficiency (Xue, Uchida et al. 2004). By one recent estimate (Brabec 2004) organic photovoltaics will reach the market in 2007, though more conservative estimates suggest 2010. Futher information about the technological challenges of introducing organic

photovoltaics into the marketplace can be read in a recent review (Brabec 2004). Despite the intense interest in these materials, their fundamental physical properties remain poorly understood. Traditional semiconductor models, notably the free- and independent- electron approximations of the Drude and Sommerfeld models, do an unacceptable job of describing charge motions and interactions in these densely packed, amorphous films, where charges may interact both on the same chain and between chains. The present work investigates the nature and dynamics of the excited state carriers in conjugated polymers, and their relationship to device performance in photovoltaics.

1.2 Photoconduction in conjugated polymers

Conjugated polymers are comprised of alternating single and double carbon-carbon bonds. The simplest is polyacetylene, which consists of a string of carbon atoms joined by alternating single and double bonds (Figure 1.2). The conjugated polymer poly phenylene-vinylene, or PPV (Figure 1.3), contains benzene rings along the polymer chains. Most of the polymers used in the present work (Figure 1.4) are derivatives of PPV, with different side chains off the main polymer structure.

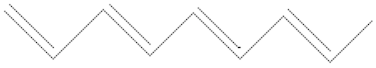

Figure 1.2. Polyacetylene, the canonical conjugated conducting polymer.

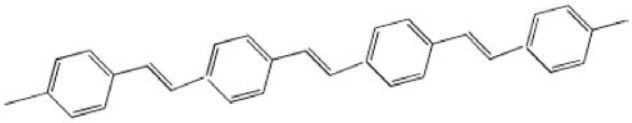

Figure 1.3. PPV – one of the simplest conjugated polymers.

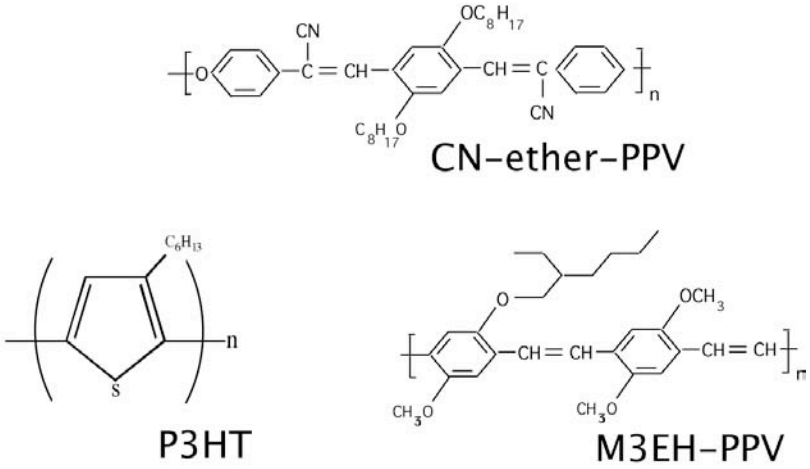

Figure 1.4. The polymers used in the current studies.

How do these materials conduct electricity? The electronic structure of carbon is $1s^2 2s^2 2p^2$. Since the *2s* shell is filled, this would seem to suggest that carbon would form two bonds with its neighbors, with the unpaired $2p^2$ electrons, but we know that it forms four. The answer to the discrepancy lies in hybridization: the s and p orbitals combine to form hybrid orbitals (sp^1, sp^2, and sp^3-- depending upon the number of orbitals that are combined), which give rise to triple, double, or single bonds. In conjugated polymers, the one *s* orbital pairs with two of the *p* orbitals to form 3 sp^2 hybrid orbitals, leaving one *p* orbital

unhybridized. Two of the sp^2 orbitals on each carbon atom form covalent bonds with neighboring carbons, the third generally forms a covalent bond with a hydrogen or side group; This is called a σ *bond,* which is any bond with cylindrical symmetry around the internuclear axis. The unhybridized p_z orbital overlaps with the unhybridized p_z orbital on the neighboring carbon: This is called a π *bond***,** as is any bond which arises from electrons approaching side by side, off the internuclear axis. Thus, these materials are characterized by an alternating single- and double- bond structure (Figure 1.5).

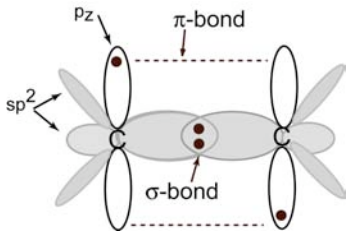

Figure 1.5. Bonding in conducting conjugated polymers.
The sp^2 hybrid orbitals are shown in grey, and the unhybridized p_z orbitals in white. Electrons are represented by black dots. The two thin sp^2 hybrid orbitals on the side extend in and out of the plane of the paper.

The electrons in the π -bonds are loosely bound, and thus this bond is easily broken. These π electrons are the conduction electrons in these materials. In polyacetylene, when we take the unit cell to consist of one carbon atom, this suggests the presence of one electron per unit cell, which should result in a half-filled band and metallic behavior. However, the length of the single and double bonds are not equivalent. The unit cell is thus composed of two carbon atoms and contains two electrons, implying a degenerate ground state because the double- and single- bonds could be exchanged without changing the energy of the system. But the alternating bond length breaks both the periodicity of the lattice and the degeneracy of the ground state, and the broken symmetry opens a gap at the Fermi energy. This phenomenon is not specific to conducting polymers: generally a one-dimensional metal is

unstable with respect to a periodicity that is broken by a modulation equal to twice the lattice constant (Peierls 1955). The distorted phase (ie., alternating bond lengths) is more stable than the undistorted state, resulting in a stable semiconducting state. In non-degenerate ground state polymers (such as the PPV's), a single minimum energy state is obtained by minimization of the Su-Schrieffer-Heeger (SSH) Hamiltonian, which instead takes into account electron correlation effects. The monomer contains 8 carbons, resulting in four filled bands and four unfilled molecular orbitals and semiconducting behavior. Several extensive theoretical reviews by Heeger are very useful in the subject of electronic structure (Heeger, Kivelson et al. 1988; Heeger 2002; Nogueira, Montanari et al. 2003).

The π -cloud is delocalized along the conjugation length of the polymer, bound on either end by an energy barrier, such as defects, kinks, or two double-bonds in a row. Polymer films tend to kink and coil in upon themselves, changing the effective conjugation length dramatically. This changes the effective energy gap of the polymer by changing the width of the potential well confining the excitation, as in a particle in the box, $E = \frac{\left[(n+1)^2 - n^2\right] \cdot \hbar}{2m^* L^2}$. This energy shift affects the absorption and photoluminescence of the polymer; absorption spectra tend to be quite wide due to the broad range of conjugation lengths in the polymer.

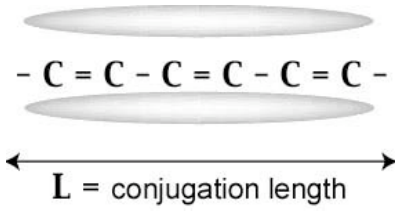

Figure 1.6. The delocalized cloud of π electrons.
The electronic probability density is represented by grey ovals above and below the polymer chain. They are restricted within a conjugation length of the polymer.

1.3 Molecular orbital theory

Now that we understand the mechanism creating the semiconducting properties of these materials, what language do we use to describe the energy states of the electrons within these systems? Due to their amorphous structure, we can no longer use *valence bond theory*, the familiar high school chemistry model in which electrons are associated with particular bonds and atoms, but must instead use *molecular orbital theory*, in which the electrons are seen as spreading throughout the entire molecule.

The motion of electrons in a solid is often described using one of two models: the Drude model (free electron model), or Sommerfeld (nearly free). Both models assume that the atomic cores and their valence electrons act as static scatterers, forming a crystal lattice off which the conduction electrons collide. In the Drude model the conduction electrons are treated as a free electron gas that does not interact with the lattice in between collisions (*free electron approximation*). The interactions between the conduction electrons themselves are neglected (*independent electron approximation*) and the classical Maxwell-Boltzmann distribution is used to describe the electron velocity.

In a solid, the electrons cannot be described by the free electron model, since they interact with the periodic potential of the atomic cores and valence electrons (metallic cations). Forbidden and allowed bands in crystalline solids arise from this periodic potential; if the highest band is filled, the material is an insulator, if it is partially filled then it behaves as a metal. Semiconducting behavior arises from bands that are slightly filled, or slightly empty.

The wave function of a single electron in a periodic potential is given by the Bloch function, $\psi_k = \phi_k(\vec{r}) \cdot e^{i\vec{k}\vec{r}}$, where *r* is the position of the electron, *k* is the wavenumber, and ϕ_k is a function representing the lattice periodicity. In bulk metals, values of *k* are closely spaced, so *E(k)* is an almost continuous function of *k*, and the electrons behave as running waves with momentum $p = k\hbar$.

In a crystal, electrons are weakly perturbed by the periodic potential of the crystal lattice. Electrons travel in crystals via Bloch waves in reciprocal space. Bragg reflections from atoms interfere constructively with reflected waves from neighboring atoms that differ by a phase of 2π, resulting in certain allowed values for *k* that depend upon the periodic lattice structure. At certain places in k-space (the edge of the Brillouin zones), this constructive interference results in standing waves formed by two linear combinations of the traveling waves. These linear combinations have different potential energy values, and this is the origin of the energy gap (Kittel 1976). The energy gap can also be derived from first principles as a boundary value problem of a plane wave in a periodic potential using idealized square wells (Kronig-Penney model) or delta functions to represent the atomic lattice (Kittel 1976).

None of these models take into account a strong interaction between the atoms comprising the crystal structure itself. The tight-binding approximation makes use of the overlap of atomic orbitals from these individual atoms to form *molecular orbitals*. This is also called the Hund-Milliken approach. This approach is more appropriate for disordered organic systems such as polymers, which are semi-crystalline at best, and is the dominant approach in physical chemistry. In the language of molecular orbital theory, the top of the valence band becomes the HOMO (Highest Occupied Molecular Orbital) and the bottom of

the conduction band becomes the LUMO (Lowest Unoccupied Molecular Orbital), as in Figure 1.7.

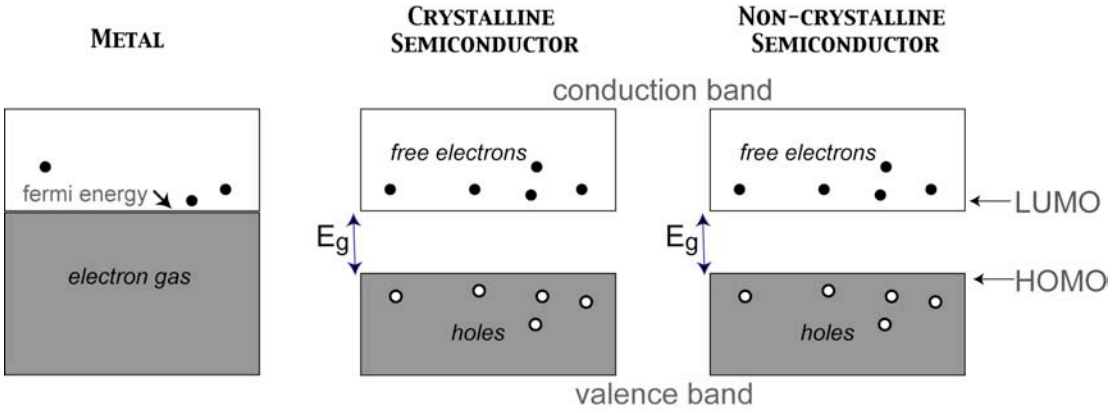

Figure 1.7. Energy bands in metals, crystalline semiconductors, and amorphous semiconductors.

Molecules orbital theory treats molecular solids as follow. Two isolated atoms – of hydrogen or carbon, for example – can each have the same energy level. When they are brought into contact, the degeneracy is split by their interaction, creating two molecular orbitals of different energy. These cannot be solved exactly for most molecules (even an approximation of the molecular orbitals for diatomic hydrogen is quite complicated), and so approximate molecular orbitals are formed by linear combinations of the atomic orbitals, or LCAO. This approach is based on the fact that near each atom the molecular orbital may be approximated by the atomic orbital of that atom. For hydrogen, this would take the form

$$\psi_{\pm} = \psi_{1s}(A) \pm \psi_{1s}(B) \quad \text{where} \quad \psi_{1s}(A) = \sqrt{\frac{1}{\pi a_0^3}} \bullet e^{-r_A / a_0}$$

where A and B represent the constituent atoms and r_A is the distance of the electron from atom A.

The resulting wave functions, $\psi_{\pm}$, are associated with different probability densities, calculated by taking the square of the normalized wavefunction, and different energies. The *bonding orbital* ψ has favorably lower energy *E,* and the electron tends to be spatially localized between the two atoms. The *antibonding orbital* ψ^* has unfavorably higher energy E^*, and an electron in this orbital has a low probability of being found between the two atoms. This is illustrated schematically below in Figure 1.8.

The amplitude of the final wave functions, and their energies, depend upon the overlap integral between the two atomic orbitals: $\alpha = \int [\psi_{1S}(r_A) \cdot \psi_{1S}(r_B)] d\vec{r}$. It can be shown that the energies are given by $E^* = \frac{\beta + \gamma}{1 + \alpha}$ *and* $E = \frac{\beta - \gamma}{1 - \alpha}$, where β is called the *coulombic integral* and represents the energy of an electron on one of the isolated atoms, and γ is the *exchange integral* or *resonance integral*, and is the interaction energy between the electrons on the two atoms. The bandwidth is related to the value of the exchange integral, γ (Simon and Andre 1985).

When several atoms are combined, as in any molecular solid, the individual molecular orbital levels broaden into continuous bands, analogous to the valence and conduction bands which arise from band theory with crystalline semiconductors. The more electrons in the system, and the greater their overlap, the broader the bands and the narrower the band gap. The highest occupied molecular orbital (or HOMO) is the energy level at the top of this continuous band of occupied states, whereas the lowest unoccupied molecular orbital (or LUMO) is the first available energy level in the unoccupied band. See figure 1.9.

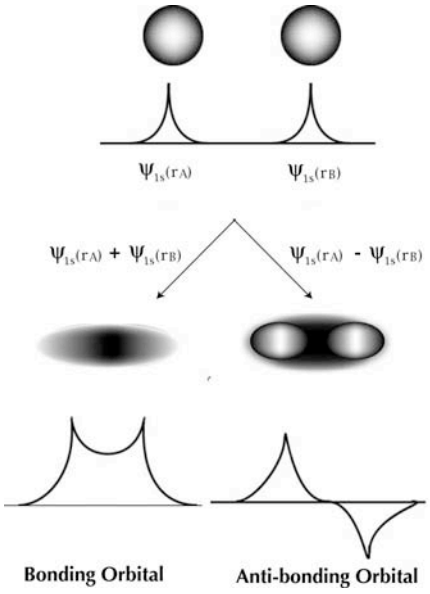

Figure 1.8. A schematic of the amplitude of the atomic orbitals and the resulting bonding and anti-bonding orbitals. Orbitals are shown as a 3D schematic (above) and a plot versus internuclear distance (below). The probability density has a similar shape.

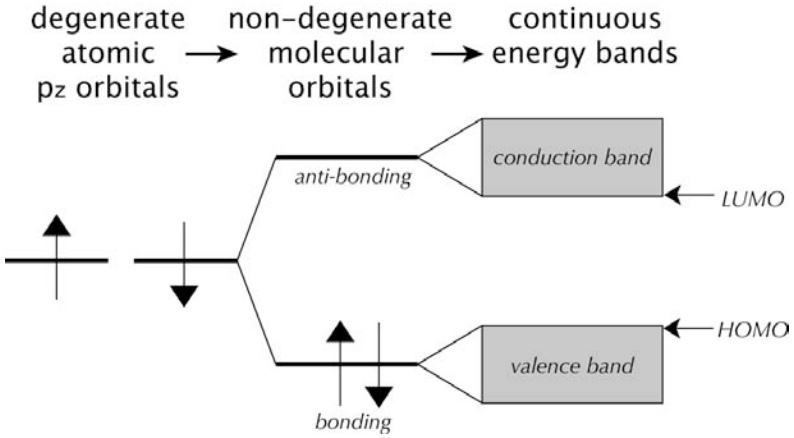

Figure 1.9. Schematic diagram of the formation of molecular orbitals and valence and conduction bands in molecular solids. (Adapted from Halls and Friend 2001).

1.4 Conjugated polymer photovoltaics

Typically, polymer based photovoltaics are fabricated in a planar layered structure with the polymer is sandwiched between two electrodes, one of which is semitransparent. The system is an insulator in the dark – free charges are added via photon absorption (photodoping) as opposed to physical doping. The operating principle is opposite to that of an LED. Light incident upon the polymer film is absorbed, promoting an electron from the HOMO to the LUMO, forming a bound electron/hole pair called an exciton.

The exciton is electrically neutral and is thus restricted to travel via diffusion rather than drift. In order to obtain charge separation – desireable in photovoltaic applications – the exciton must reach an interface where it may be dissociated by two materials of differing electron affinity and ionization potential. This energy difference overcomes the exciton binding energy (generally about 0.2 eV), making the charge-separated state energetically favorable. This can be at the interface between a polymer and a metal or inorganic layer (polymer/TiO_2 or polymer/Au). The light-harvesting capability of the device is therefore limited by the exciton diffusion length of ~10-20 nm (Halls, Pichler et al. 1996; Savenije, Warman et al. 1998), since excitons generated beyond this distance do not contribute to the current. Dissocation may also occur at the interface between donor and acceptor materials (such as two blended polymers, or a polymer blended with small molecules), which enhances the light harvesting capabilities.

The difference in the work functions of electrodes provides an internal electric field (~ open circuit voltage, V_{oc}), which transports the separated electron and hole to their

respective electrodes. The device thus has a polarity and diode-like behavior, which can be characterized by the amount and direction of rectification.

Once the planar layers in the sandwich structure are placed in contact, the Fermi levels equalize, and the energy bands bend (See Figure 1.10). We approximate the bands by straight lines, indicating a constant electric field across the device, since the layers are quite thin. This is an adequate approximation, except in the case where the appropriate materials are used to create a Schottky barrier at one of the metal/polymer interfaces.

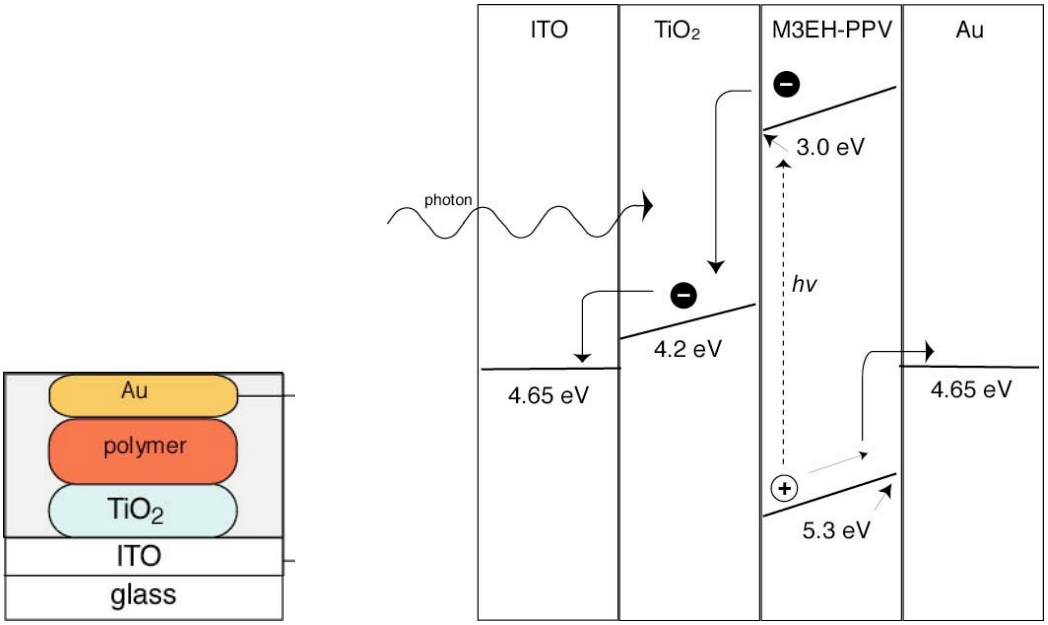

Figure 1.10. Sandwich structure for typical polymer photovoltaics, and energy diagram. Indium tin oxide (ITO) forms the transparent anode, titanium dioxide (TiO_2) acts as an electron-acceptor, the hole-transporting polymer M3EH-PPV is the primary absorbing material, and gold (Au) forms the top contact.

The molecular HOMO and LUMO do not form completely continuous valence and conduction bands due to weak interactions between the molecules. Thus, charge transport

occurs by hopping between localized states, which results in charge mobility that is several orders of magnitude lower than that in inorganics or well-ordered organics (Spanggaard and Krebs 2004). Another important difference between organics and inorganics is the presence of the bound exciton in organic systems. In the inorganics the strong electric field in the depletion zone is sufficient to separate any weakly bound excitonic state and ballistically eject the carriers. In organics the process is much less efficient. One advantage, however, is that the open-circuit voltage, V_{oc} (see Chapter 3) tends to be larger in polymers than in inorganics, where surface defects pin the energy bands to the work function of the metal at the interface, limiting the voltage.

1.5 Summary: Background and principles of device operation

Despite record high efficiencies, the photovoltaic market is hindered by the high price of photovoltaic production. Organics, among other approaches, aim to make cheaper devices by reducing material cost. Organics have other advantages, such as the ability to produce mechanically flexible, semitransparent devices.

Because of the amorphous nature of polymeric materials, they cannot be understood with the typical tools of hard condensed matter – Bloch waves and atomic orbital theory. Instead, a linear combination of hybridized atomic orbitals creates molecular orbitals, resulting in a band gap and semiconducting behavior. In conjugated polymers, the unhybridized p_z electrons are delocalized, providing one electron per unit cell available for conduction. Photoexcitation promotes an electron from the highest occupied molecular orbital (HOMO) to the lowest unoccupied molecular orbital (LUMO). The resulting electron and hole are bound together in a neutral exciton, which diffuses along the polymer chain. If the exciton encounters a location where it is energetically favorable to separate (such as a donor/acceptor interface, or a charge trap), then it does so, and the resulting electron and hole drift in the internal electric field to the electrodes, creating a current.

1.6 Challenges to device performance

In order for organic photovoltaics to break into the marketplace, they must achieve higher efficiencies -- around 5-10% in the lab. Several barriers stand in the way of this goal, due in large part to a poor understanding of many of the fundamental physical processes involved in the operation of these cells, as well as the need to optimize materials and

structure. Several recent reviews are useful for an orientation in the field (Brabec and Sariciftci 2001; Nelson 2002). The basic limitations on device performance are outlined in the following section.

Charge generation

The concentration of photogenerated carriers will depend upon the absorption profile – which may or may not match well with the solar spectrum. In addition, the short exciton diffusion length severely limits the polymer thickness from which useable current may be extracted. The limit on polymer thickness thus limits the amount of light that may be absorbed, and thus the density of photogenerated carriers. The process of generating charge carriers via light absorption is termed photodoping.

Charge dissociation

Once the polymer is photodoped, the electron and its corresponding hole are coulombically bound in an exciton which must be separated at a boundary between a material of high electron affinity and one of low ionization potential. The efficiency of this process, and the available interfacial area, pose limits on device efficiency.

Charge transport

Once separated, the internal electric field across the device drives the charges to their appropriate electrodes. However, electron and hole mobilities are low, compromising device performance in organics. Organic semiconductors typically have charge mobilities several orders of magnitude lower than inorganics. This is because of the weak order present in these

materials. In crystalline semiconductors, the 3D lattice structure spreads the individual atomic energy levels into broad conduction and valence bands. In the weakly ordered organics, however, intermolecular forces are too weak to form well-defined conduction and valence bands. Thus charges must hop between local states in order to exit the device (Spanggaard and Krebs 2004). This severely curtails the charge mobility, as does the presence of charge traps through impurities like kinks in the polymer chain, or oxygen that has diffused into the film. These impurities create energy levels inside the band gap, and additional energy is needed in order to liberate the charge from the trap.

Mobility is also limited by the confinement of the charge to the lattice. Once the exciton is dissociated, it relaxes to form a lattice distortion called a *polaron* (see Chapter 3). In order for the polaron to migrate along the polymer backbone, it must possess enough energy to overcome the energy barrier associated with rearranging that distortion. Polarons have a large effective mass and thus are poorly mobile. Defining an effective mass *m**, mobility is given by $\mu = \frac{e \cdot \tau_c}{m^*}$, where τ_c is the mean time between collisions of electrons with the lattice. The mobility can be extracted explicitly from the photoluminescence decay time since the diffusion length L_n (the distance over which the electron concentration decreases by *1/e*) for electrons is given by $L_n = D_n{}^2 \tau_n{}^2$, and $\mu_n = \frac{eD_n}{kT}$ where D_n is the diffusion constant, τ_n is the average lifetime of the electron, μ_n is the electron mobility, and T is the temperature. Analogous equations hold for hole diffusion. Rearranging shows that $\mu_n \propto \frac{1}{\tau_n}$, as long as the measured exciton lifetime is proportional to the lifetime of a

separated electron. The fill factor (FF; see Chapter 4) provides a qualitative measure of mobility.

The mobility of electrons and holes differ greatly from each other in most polymers. In PPV's field-effect hole mobilities are ~ 10^{-4} cm^2/Vs (Takiguchi, Park et al. 1987; Obrzut, Obrzut et al. 1989) whereas electron mobilities are several orders of magnitude lower, perhaps due to electron traps such as diffused oxygen. Zero-field hole mobility in M3EH-PPV is estimated to be 5 x10^{-7} cm^2/Vs (Breeze, Schlesinger et al. 2004); twice that of MEH-PPV.

Recombination

If an exciton does not dissociate within its diffusion length, or if an electron and hole encounter one another on their path to the opposite electrode, they have a high chance of recombining. Recombination may occur between electron/hole pairs arising from a single exciton (*bimolecular geminate recombination*), or from two different excitons (*non-geminate bimolecular recombination*).

The probability of recombination increases with high light intensities, because this increases the density of charge carriers and thus the chance that charges will cross paths in a random walk. Due to higher recombination at high exciton densities, the photocurrent varies sublinearly with light intensity. This reduces the achievable quantum efficiency, and is not optimal for high intensity illumination under solar conditions.

Upon recombination, the exciton may be dissociated again to contribute to the photocurrent, or decay radiatively or non-radiatively, detracting from the photocurrent.

Other limitations

Polymer films photo-oxidize and must be protected from oxygen and water, as these can degrade the film and create charge traps. In the presence of oxygen the time-decay of photoluminescence becomes more rapid, and the steady-state photoluminescence has been seen to decrease by a factor of two after just 5 minutes in the presence of oxygen and light(Rothberg, Yan et al. 1996), indicating the presence of electron traps. Thus, polymer devices must be encapsulated in order to sustain reasonable lifetimes for commercial use. The organic LED market has made fine progress in encapsulation techniques, and have created devices with lifetimes over 10,000 hours (Halls and Friend 2001), suggesting that this challenge is not insurmountable. UV light can degrade the polymer structure by attacking the bonds along the backbone. Encapsulation with a UV filter helps alleviate this problem.

1.7 Approaches to improvement: Heterojunctions

One approach to circumventing the problem of short exciton diffusion length is to use heterojunction structures – blends or layers of different organic substances with different electron affinities. Heterojunctions of polymers with a variety of electron-transporters (such as PCBM, metal oxides, and other conjugated polymers) have been widely studied as a means to improve the power conversion efficiencies of polymer photovoltaics. By providing multiple exciton dissociation sites, as well as separate charge transport pathways for electrons and holes, both charge generation and collection efficiency may be improved through the use of heterojunctions.

The use of heterojunctions has several advantages:

- Increased charge generation. Materials with absorption in different spectral ranges may be used, increasing the density of photogenerated carriers.
- Increased charge separation. The higher interfacial area, especially in domain-separated blends or nanoparticle blends and layers, increases the available interfaces for exciton separation.
- Reduced recombination. By transporting the hole through one material and electrons through the other, there is a reduced probability of recombination, and more photogenerated excitons contribute to the photocurrent.

The primary advantage of blended (bulk heterojunction) devices over planar layers is their ability to harvest more useful light. Since the exciton must be formed within 10 nm of an interface in order to be dissociated, any material further than 10 nm away from the interface does not contribute to the photocurrent. However, despite high absorption in polymers, the film thickness should be over 100 nm in order to absorb most of the incident light. This can be achieved by using blended structures.

A challenge in blended devices is achieving phase separation on a nanometer scale. The use of highly volatile solvents, which evaporate quickly, help keep the domain size small because energetic equilibrium is not reached in these immiscible blends. One main drawback to blended structures is their often reduced charge transport properties – a serious impediment. In blends, charges must hop from domain to domain, and there is often not a clear path from one electrode to the other. In layered structures, electrons/holes must cross the entire thickness of their respective transport layers.

Polymers tend to be hole-transporters and acceptors. Thus, polymers are often used in heterojunctions with various electron-acceptors. This approach is used in the present work.

The basic classes of electron acceptors are:

- Other polymers (CN-PPV)
- Metal oxides (TiO_2, SnO_2)
- Small molecules (C_{60}, perylene)
- Nanoparticles of inorganic semiconductors (CdSe, PbS)

Polymers

Polymers may be layered or blended (forming phase-separated domains) to form heterojunction cells. To form layered cells, deposition of the second layer must not dissolve or otherwise remove the first. This can be accomplished by first depositing a polymer which is insoluble in the solvent used to deposit the second layer. Tada and colleagues used this approach with poly(p-pyridylvinylene (PPyV) (Tada, Onoda et al. 1999) – soluble in formic acid but not in chloroform – and poly(3-hexylthiophene((P3HT) – soluble in chloroform. Currents produced by these multi-layered cells were about 3 orders of magnitude higher than on the neat polymer films, indicating that the layer interface served as an efficient charge separation region.

When blended, the low entropy of mixing of polymers means that they do not mix well on the molecular scale. Because the solvent evaporates quickly in spin-casting, an equilibrium state of large domains is not reached (Halls and Friend 2001) and they phase separate into domains on the order of 20nm, as in blends of MEH-PPV and CN-PPV (Yu and

Halls 1995; Halls et al 1995, show TEM). Phase-separated polymer blends are particularly prone to problems of charge transport, as the internal field is likely to pull charges into dead-ends in the interpenetrating polymer maze (Halls and Friend 2001). This conjecture is supported by the observation that applied voltages (which could enable tunneling from domain to domain) enhance the photocurrent. Obviously the morphology of polymers blends, which is difficult to control, is crucial to its device performance. Self-assembly techniques have been explored to this end (Durstock, Taylor et al. 2001).

Metal oxides

Metal oxides, such as titanium dioxide, are often used as transparent electron-accepting semiconductors in polymer photovoltaics. They may be deposited in a planar layer or blended in their nanocrystalline form.

Another use of metal oxides is in dye-sensitized electrochemical cells, in which conjugated polymers act as sensitizers for nanocrystalline TiO_2. These cells have power efficiencies of ~ 10% (O'Regan and Gratzel 1991; Gratzel 2001). The limited lifetime of the liquid electrolyte, however, has limited the applicability of this method. This work prompted the use of TiO_2 and other metal oxides as n-type materials in organic photocells. Many photovoltaics are deposited on TiO_2 films (often prepared via a sol-gel method), where the metal oxide/polymer interface acts as a zone for charge separation (Fan, McQuillin et al. 2001) (Arango, Johnson et al. 2000). Enhanced roughness of the metal oxide layer results in better efficiencies due to enhanced interfacial area for charge separation. ZnO has also been used as an electron acceptor in such cells.

Small molecules

Small molecule organics have been used as electron transporters in both blended and layered polymer photovoltaics. C_{60}, or buckminsterfullerene, has a very high electron affinity, resulting in ultrafast (sub- picosecond) charge transfer from polymers to C_{60}, with a quantum yield approaching 100%. However it is poorly soluble, so the soluble derivative PCBM (see Figure 1.11) is often used in polymer applications. The addition of PCBM to polymer films results in quenching of the photoluminescence and reduction of the excited state lifetime. See Chapter 8 for more information on PCBM.

Other small molecules have been successfully used in polymer photovoltaic cells. Perylene, a molecular pigment with a high electron affinity, has been successfully used (Halls and Friend 1997; Dittmer, Petritsch et al. 1999), and is not as sensitive to oxygen as the fullerenes.

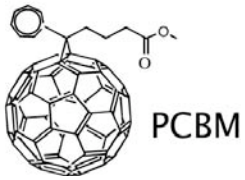

Figure 1.11. Chemical structure of PCBM, a derivative of C_{60} (buckminsterfullerene).

1.8 Decay kinetics and time-resolved spectroscopy

Traditional device characterization (measuring current, voltage, and power efficiencies) gives information about *which* type of device is better than another, but does not provide much insight into *why*. Morphological studies (STM, TEM) can provide valuable information as to the underlying structure, and spectroscopic measurements allow

experimenters to probe underlying energetics. What these methods lack is the ability to probe the dynamics and kinetics within these devices. Ideally, we would have a microscope that allows us to watch the generation, dissociation, recombination, and transport of the excited state species over time. Lacking that, there are a variety of time-resolved techniques that allow a glimpse of these processes. Time-resolved measurements help discern, for example, what processes contribute to quenching – the transfer to an external quencher, or aggregation in the ground state.

One such method, which is used in the current work, is time-resolved photoluminescence (TRPL). What follows is a brief overview of TRPL – more detail is included in Chapter 2. In TRPL a sample is illuminated with a brief flash of monochromatic light, and the time-decay of the resulting light emission is measured. The lifetime of the photoluminesence is used as a proxy to probe the population of the excited state, since at any time *t* the luminescence intensity is directly proportional to the excited state carrier concentration *X*(t)*, as in other decay processes such as radioactive decay:

$$\frac{dX^*}{dt} = -k \cdot X^*, \quad so \quad X^*(t) = X^*(t_0)e^{-kt} \ .$$

Thus, the photoluminescence lifetime does not simply represent the radiative decay of the sample, but the decay due to all de-excitation pathways. The initial population, $X^*(t_0)$, is determined by the steady-state PL intensity at the emission wavelength of interest.

By examining the decay dynamics of the excited states in polymers, we can gain insight into the nature of those excited states and the various routes of energy loss due to recombination, traps, dissociation, etc. Since the current work is concerned with fluorescence decay, observations are of nanosecond-picosecond scale decays from the upper singlet state.

Phosphorescence decays (from the triplet state) are very long-lived, on the order of 1-100 μs, and are not addressed in this work.

There are a variety of mechanisms which deactivate the excited state. The more pathways available for decay of the excited state *X*,* the shorter-lived the state. The lifetime of any of these processes is related to the rate constant (or transition probability), *k*, by:

$$\tau = \frac{1}{k}$$

The observed lifetime, then, is the reciprocal of the sum of all rate constants that may deactivate the excited state, such as radiative recombination (photoluminescence), non-radiative recombination (such as traps) or, in the case of mixtures of materials, transfer to an external quencher, such as in the transfer of an electron from the electron-donating to the electron-accepting material. All such processes act to reduce the number of carriers in the excited state.

Pump-probe, or photoinduced absorption (PIA) experiments are also common ways to explore excited state dynamics. In these experiments the decay of the excited-state absorption, as opposed to the photoluminescence, is explored. The sample is first excited from the ground state (S_0) into the first excited singlet state (S_1) – see Figure 2.1 in the next chapter -- using a pump beam of the appropriate energy (e.g., 390 nm). This populates the S_1 state, which will then begin to decay by all the same mechanism as in TRPL techniques. Simultaneously the sample is hit by a probe beam of a different energy (e.g., 780 nm), which is absorbed by S_1 but not S_0. The transmission of this beam is measured as a function of time, giving a measure of the decay of the excited S_1 state. The time-resolution of PIA measurements is much greater than that of TRPL measurements – on the order of femtoseconds instead of picoseconds. This is a strength of the technique, and also means that

the decay time from TRPL will not necessarily match those of PIA. In TRPL experiments, carriers relax vibrationally into the lowest excited state of S_1 before the measurement is performed; in the ultrafast PIA experiments this is not the case. Thus, depending upon the pump energy used, PIA measurements may probe a different vibrational level, with a different decay time, than a corresponding TRPL experiment.

Time-resolved microwave conductivity (TRMC) is also a common experiment for measuring the lifetime of the charge separated state, but for much longer timescales (tens of nanoseconds). Thus, TRPL provides the best method for measuring time decays, from the lowest vibronic state, in the picosecond to nanosecond range.

1.9 Summary: Motivation

Some of the biggest challenges to improving device performance are low charge dissociation due to the binding energy of the exciton and its short diffusion length of 10 nm; correspondingly low amounts of charge generation due to the necessarily thin layers which are not optimized for light absorption; poor charge transport due to low mobility of the separated charge carriers; and high recombination due to the low diffusion lengths and poor mobilities. Many of these limitations may be overcome by the use of heterojunction films, which increase charge dissociation due to increased interfacial area, increased charge generation through light absorption by allowing for increased film thickness or absorption in different regions of the spectrum, and reduced recombination by separating electron and hole transport in two different materials. The primary electron transporters that have been used in

heterojunctions with hole-transporting polymers are small molecules, metal oxides, nanoparticles, and other polymers. Heterojunctions may be layered or blended.

Time-resolved measurements provide the next best thing to a microscope, allowing one to watch the generation, dissociation, recombination, and transport of charges within these devices. This allows insight into the mechanisms for device improvement in different heterojunction structures.

1.10 References

Brabec, C. (2004). "Organic photovoltaics: technology and market." Sol. Energy Mater. Sol. Cells **83**: 273.

Brabec, C. J. and N. S. Sariciftci (2001). "Recent developments in conjugated polymer based plastic solar cells." Monatsh. Chem. **132**: 421.

Breeze, A. J., Z. Schlesinger, et al. (2004). "Improving power efficiencies in polymer-polymer blend photovoltaics." Sol. Energy Mater. Sol. Cells **83**: 263.

Chapin, D. M., C. S. Fuller, et al. (1964). J. Appl. Phys. **25**: 676.

Chiang, C. K., C. R. Fincher, et al. (1977). "Electrical-conductivity in doped polyacetylene." Phys. Rev. Lett. **39**: 1098.

Dittmer, J. J., K. Petritsch, et al. (1999). "Photovoltaic Properties of MEH-PPV/PPEI blend devices." Synth. Met. **102**: 879.

Durstock, M. F., B. Taylor, et al. (2001). "Electrostatic self-assembly as a means to create organic photovoltaic devices." Synth. Met. **116**(1-3): 373.

Fan, Q., B. McQuillin, et al. (2001). "A solid state solar cell using sol-gel processed material and a polymer." Chem. Phys. Lett. **347**: 325.

Gratzel, M. (2001). "Photoelectrochemical cells." Nature **414**: 338.

Halls, J. J. M. and R. H. Friend (1997). "The photovoltaic effect in a poly(p-phenylenevinylene) / perylene heterojunction." Synth. Met. **85**: 1307.

Halls, J. J. M. and R. H. Friend (2001). Organic Photovoltaic Devices. Clean electricity from photovoltaics: Series on photoconversion of solar energy. M. D. a. H. Archer, R. London, Imperial College Press. **1**.

Halls, J. J. M., K. Pichler, et al. (1996). "Exciton dissociation at a poly(p-phenylenevinylene)/C_{60} heterojunction." Synth. Met. **77**: 277.

Heeger, A. J. (2002). "Semiconducting and metallic polymers: the fourth generation of polymeric materials." Synth. Met. **125**: 23.

Heeger, A. J., S. A. Kivelson, et al. (1988). "Solitons in conducting polymers." Rev. Mod. Phys. **60**: 781.

Kittel, C. (1976). An introduction to solid state physics, 5th edition. New York, John Wiley & Sons.

Li, G., V. Shrotriya, et al. (2005). "High-efficiency solution processable polymer photovoltaic cells by self-organization of polymer blends." Nature **4**(10): Advance Online Publication.

Ma, W., C. Yang, et al. (2005). "Thermally stable, efficient polymer solar cells with nanoscale control of the interpenetrating network morphology." Adv. Func. Mater. **15**(10): Advance Online Publication.

Nelson, J. (2002). "Organic photovoltaic films." Curr. Opin. Solid State Mater. Sci. **6**: 87.

Nogueira, A. F., I. Montanari, et al. (2003). "Charge recombination in conjugated polymer/fullerene blended films studied by transient absorption spectroscopy." J. Phys. Chem. B **107**: 1567.

O'Regan, B. and M. Gratzel (1991). "A low-cost, high-efficiency solar cell based on dye-sensitized colloidal TiO_2 films." Nature **353**: 737.

Obrzut, J., M. J. Obrzut, et al. (1989). "Photoconductivity of poly(p-phenylene vinylene)." Synth. Met. **29**: 103.

Peierls, R. E. (1955). Quantum Theory of Solids. Oxford, Oxford University Press.

Rothberg, L. J., M. Yan, et al. (1996). "Photophysics of pheylenevinylene polymers." Synth. Met. **80**: 41.

Savenije, T. J., J. M. Warman, et al. (1998). "Visible light sensitisation of titanium dioxide using a phenylene vinylene polymer." Chem. Phys. Lett. **287**: 148-153.

Scott, J. C. and G. G. Malliaras (1999). "Charge injection and recombination at the metal-organic interface." Chem. Phys. Lett. **299**: 115.

Shaheen, S. E., R. Radspinner, et al. (2001). "Fabrication of bulk heterojunction plastic solar cells by screen printing." Appl. Phys. Lett. **79**(18): 2996.

Shirakawa, H., E. J. Louis, et al. (1977). "Synthesis of electrically conducting organic polymers - halogen derivatives of polyacetylene, (CH)x." J. Chem. Soc. - Chem. Comm. **16**: 578.

Simon, J. and J.-J. Andre (1985). Molecular Semiconductors: Photoelectrical properties and solar cells. New York, Springer-Verlag.

Spanggaard, H. and F. C. Krebs (2004). "A brief history of the development of organic and polymeric photovoltaics." Sol. Energy Mater. Sol. Cells **83**: 125.

Tada, K., M. Onoda, et al. (1999). "Photocell with heterojunctions of donor / acceptor polymers." Synth. Met. **102**: 982.

Takiguchi, T., D. H. Park, et al. (1987). "Photoconductivity and carrier transport properties in poly(p-phenylene vinylene) film." Synth. Met. **17**: 657.

Weinberger, B. R., M. Akhtar, et al. (1982). "Polyacetylene photovoltaic devices." Synth. Met. **4**: 187.

Xue, J., S. Uchida, et al. (2004). "Assymetric tandem organic photovoltaic cells with hybrid planar-mixed molecular heterojunctions." Appl. Phys. Lett. **85**(23): 5757.

Chapter 2

Spectroscopy

2.1 Steady-state absorption and photoluminescence

Luminescence is the process by which absorbed energy (excitation energy) is transformed into radiant light. The process by which this conversion takes place is complicated, and various processes (optical or non) occur simultaneously.

When light impinges upon a photovoltaic film, an electron is promoted from the ground state (S_0) to one of several singlet excited states (S_1, S_2, S_3…), corresponding to different principle quantum numbers, *n*, as in Figure 2.1 below. Excitation of the triplet state (T_1, T_2, T_3, …) is also possible, usually through *intersystem crossing* from the singlet state, S_1. Relaxation from the triplet state results in a longer-lived phosophorescence, and is not observed for the systems discussed in this work.

In addition to the principle quantum number, each energy level is also described by vibrational and rotational energies. The rotational energy transitions occur in the far infrared (Birks 1970) and are discounted in traditional measurements. The ground state energy levels are then given by

$$E_t = E_e + (m + 1/2)E_{lv},$$

where E_{lv} is the energy of the fundamental vibrational modes in the ground state and *m* is the vibrational quantum number. A similar equation may be written for the excited state:

$$E_t' = E_e' + (n + 1/2)E'_{uv}$$

Absorption then promotes an electron from the ground state (m=0) to a greater electronic and vibrational energy,

$$\begin{aligned}\Delta E_t &= \Delta E_e + \Delta E_v \\ &= (E_e' - E_e) + \tfrac{1}{2}(E'_{uv} - E_{lv}) + nE'_{uv} \\ &\approx (E_e' - E_e) + nE'_{uv}\end{aligned}$$

since E'_{uv} is approximately equal to E_{lv}. The S_0-S_1 transitions correspond to promotion of the electron from the π-π* orbital or the highest occupied to the lowest unoccupied molecular orbital (HOMO-LUMO transition).

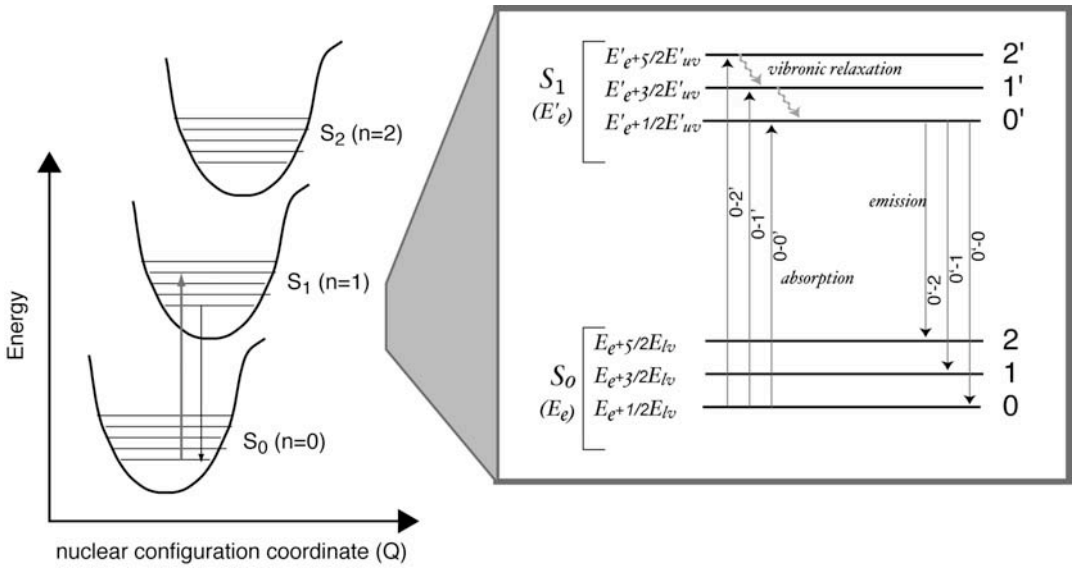

Figure 2.1. Excited states of molecular systems, including emission and absorption processes.

Excitation and emission processes are outlined in Figure 2.1 above. Time-resolved fluorescence experiments excite the molecule into S_1 and measure the time-decay of that fluorescence, whereas photoinduced absorption experiments (PIA) pump the molecule into the excited S_1 state and then probe the decay of the absorption from that state.

The attractive potential of the molecule is shown as a schematic Morse potential, which may be approximated by a parabola near the energy minimum. The Morse potentials,

and the spatial shift of the excited states, are extended from treatment of diatomic molecules. The internuclear distance is replaced by the nuclear configuration coordinate, Q, indicating that the excited electronic state is displaced relative to the mean nuclear configuation of the ground state (Birks 1970). Transitions are shown by vertical arrows after the *Franck-Condon principle*, indicating that such upward transitions occur in a period of time three orders of magnitude faster than the vibrational period of atomic nuclei and core electrons, and thus the atomic cores are essentially stationary during electronic transitions.

Once a molecule is excited into one of the upper vibronic levels, subsequent rapid vibrational relaxation leaves the molecule in the lowest vibrational level of S_1. The emission occurs on the timescale of 10^{-9}-10^{-10} s, whereas the vibrational relaxation occurs several orders of magnitude faster, on the timescale of a molecular vibration, around 10^{-13} s. Thus the molecule fluoresces from the lowest vibrational level of S_1, giving the same emission spectra, independent of excitation wavelength (*Kasha's Rule*). It is clear from this diagram that steady state absorption data allows examination of the first excited state, whereas fluorescence data provides information about the vibronic structure of the ground state. Emission spectra are narrower than absorption spectra. This is because absorption spectra sample a wide range of conjugation lengths, and thus a wide range of energies, resulting in a broad featureless spectrum. After absorption, however, excitons migrate from higher energy to lower energy segments, resulting in a narrower spectrum.

Since the lowest energy absorbed (the 0-0' transition) is greater than the lowest energy emitted in this radiative decay (the 0'-3 transition), emission spectra are red-shifted (lower energy, longer wavelength) relative to absorption spectra. This shift in energy (wavelength) from absorption to emission is termed the *Stokes' shift.* Polymeric materials

show a large Stokes' shift – a variety of chain-segment lengths contribute to the absorption spectrum, resulting in a broad, featureless absorption spectrum because each conjugation length acts as a particle-in-a-box of varying sizes. Upon excitation, however, excitations rapidly relax to the longest chain-segment, and the lowest level of S_1, which emits at a low energy; hence the large Stokes' shift. Time-resolved emission spectra also show a shift towards the red over rapid time scales, due to migration to lower energy states over time.

The time decay of the luminescence at a particular wavelength is related to the steady state fluorescence (in units of photons/nm) with a simple integration over time:

$$I_{steady\ state} = \int_0^\infty I_0 e^{-t/\tau_0} dt = I_0 \tau_0$$

Therefore the intensity of the steady state spectrum, and the value of the quantum yield (see below), are proportional to the lifetime of the excited state.

2.2 Lifetime of the excited state

Radiative lifetime

Spontaneous emission between two states ψ_a and ψ_b is a probabilistic process whose rate is directly proportional to matrix element of the electric dipole moment between the two states. This can be represented as the square of the matrix element $\langle \psi_b | r | \psi_a \rangle$ which can be reduced to $\langle n' l' m' | r | nlm \rangle$ for a spherically symmetric Hamiltonian (Griffiths 1995). This matrix element is nonzero only if $\Delta m = \pm 1$ or 0, due to conservation of the z-component of angular momentum. Thus, some radiative transitions are disallowed by symmetry and/or parity, or occur with low probability due to a low wavefunction overlap. Intersystem

crossing and phosphorescence are additionally forbidden by spin multiplicity, resulting in the long lifetime for that transition.

The actual rate of radiative decay depends upon properties of that material, such as the absorption and emission spectra, the refractive index, and degeneracies of the lower and upper states. This is given by the Strickler-Berg relation (Strickler and Berg 1962):

$$k_r = \frac{8\pi n^2}{c^2}\left\langle \nu^{-3}\right\rangle^{-1}\int \frac{\sigma(\nu)d\nu}{\nu} \text{ where } \left\langle \nu^{-3}\right\rangle^{-1} = \frac{\int L(\nu)d\nu}{\int \nu^{-3}L(\nu)d\nu}$$

where n is the refractive index, $\sigma(\nu)$ is the absorption cross-section per unit frequency ν, and $L(\nu)$ is the photoluminescence spectrum as a function of ν. The radiative decay rate is assumed to be temperature independent.

The radiative lifetime is related to the rate constant (or transition probability), k_r, by

$$\tau_r = \frac{1}{k_r}$$

For a polymer with strong absorption, and a fully allowed radiative transition, k_r is on the order of 10^9 s^{-1}, yielding a natural radiative lifetime of ~1 ns (Samuel, Rumbles et al. 1997). Due to significant non-radiative decay (k_{nr}), the luminescence lifetime in polymers is generally much shorter than 1 ns.

Deactivation of the excited state

Radiative relaxation is not the only means available to deactivate the excited state (see Figure 2.2). Energy loss from this state can occur in the following ways, each characterized by a rate constant k:

1. **Intersystem crossing (k_{ISC}):** Transfer to the triplet state, T_1. The triplet state will relax into the ground singlet state with a long characteristic lifetime, termed

phosphorescence. This does not occur within the timescale of the current experiments.

2. **Internal conversion (k_{nr})**: Non-radiative vibronic relaxation, releasing phonon vibrations. This can be between the upper singlet states (S_2 and S_1, for example) or between vibrational levels in a single state.
3. **Internal quenching (k_{nr})**: Energy transfer to defects or traps (energetically favorable energy levels within the band gap created by impurities, such as oxygen). This is a non-radiative decay channel.
4. **Fluorescence (k_r)**: Radiative decay from the S_1 to a ground state, with the emission of light as fluorescence. The 0'-0, 0'-1, 0'-2, etc., transitions will be represented by distinct peaks in the fluorescence spectrum.
5. **Dissociation / External quenching (k_{ext} or k_D)**: Charge transfer to another material with a different electron affinity, such as an electrode, polymer, C_{60}, or other external quenchers.

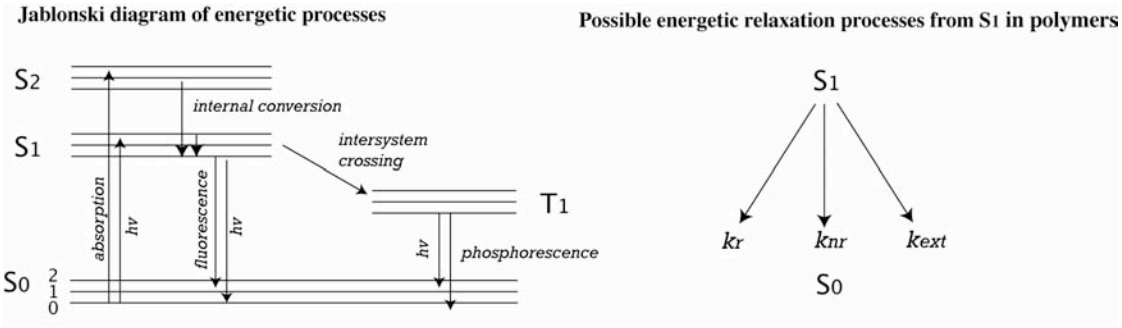

Figure 2.2. Energy transfer processes in molecular systems.
The rate constants *k* represent the rates of radiative (r) decay, non-radiative (nr) decay, and external quenching (ext).

Lifetime of the photoluminescence

Since the luminescence intensity depends upon the number of excited state carriers, the PL intensity can be used as a proxy to probe the population of the excited state. Thus, using time-resolved photoluminescence, I can probe the decay dynamics of the excited state of charge carriers in polymer films. Note that, even though I am measuring the photoluminescence decay, I assume that the observed lifetime is representative of *all* excited state species in the sample, not simply those decaying radiatively, since the luminescence intensity depends upon the concentration of *all* excited state carriers.

The observed decay time of the luminescence, τ, is (Lakowicz 1999):

1. Equal to the time distribution of emitted photons, and as such represents a statistical average;
2. Equal to the average time a fluorophore remains in the excited state (for mono-exponential decay only);
3. Directly proportional to quantum yield;
4. Directly proportional to steady state luminescence intensity; and
5. Directly proportional to *n(t);* concentration of the excited state species.

Physically, the luminescence decay time is a measure of the rate of decay of the excitonic species, *X*:*

$$\frac{\partial X^*}{\partial t} = -[k_0 + k_{ct}(c)] \cdot X^* - \gamma X^{*2}$$

(Maniloff, Klimov et al. 1997), where k_0 is the intrinsic decay of the pristine polymer *($k_0 = k_r + k_{nr}$), k_{ct}* = the rate of charge transfer, which depends upon the concentration *(c)* of the electron acceptor such as C_{60}, and γ is the bimolecular rate constant. While transient PIA

measurements often observe power-law decay indicative of bimolecular recombination, the low laser intensity in TRPL measurements allows us to discount this decay channel. Thus, $X^*(t) = X^*(t_0)e^{-kt}$, just as radioactive decay is a measure of the amount of material present. In PL studies, however, there is more than one method to deactivate the hot state: The rate constant *k* is the sum of all radiative and non-radiative rate constants that deactivate the state *X** (including radiative and non-radiative pathways). The more pathways available for decay of the *X** excited state, the shorter-lived the state.

The time decay of the luminescence is then given by $I(t) = \alpha e^{-t/\tau}$ where *I(t)* is the time-dependent intensity, α is the initial amplitude, τ and is the lifetime. The observed molecular lifetime (including bimolecular processes or an external quenching agent such as a second polymer species or C_{60}), is given by the reciprocal of the sum of all rate constants:

$$\tau = \frac{1}{k_r + k_{nr} + k_D}$$

where k_r = radiative rate constant, k_{nr} = non-radiative rate constant, and k_D = dissociative rate constant. Non-radiative processes include migration to traps and other quenching sites, internal conversion, intersystem crossing to the triplet state, and exciton-exciton annihilation. Few chromophores actually emit at this characteristic lifetime, however; fluorescence is a random process, and the lifetime is a statistical average of the time spend in the excited state.

Multiexponential decay

In practice, decays are often multiexponential, especially in the case of complex systems such as polymers with multiple fluorophores and bimolecular as well as monomolecular processes. For systems with more than 2 energy levels, the luminescence

decay is described by sums of exponents with different characteristic lifetimes:

$I(t) = A_1 e^{-t/\tau_1} + A_2 e^{-t/\tau_2}$. In time-resolved data, however, the true magnitude of the pre-exponential factor is lost because photon counting stops at a pre-determined maximum (such as 20,000), which removes any relative photoluminescence magnitude. A more useful number is the *yield,* which indicates the proportion of the steady state intensity that can be attributed to that fluorophore:

$$yield(\%) = \frac{A_i \tau_i}{\sum_j A_j \tau_j}$$

The average lifetime can be calculated by weighting each lifetime by its yield. The term $\alpha_i\tau_I$ is simply the multiplication of the axis and abscissa of a time-decay plot, and as such represents the area under the curve of the decay and the steady state intensity. This shows that a short decay time generally corresponds to a weak steady state intensity, as long as that intensity is integrated over the entire time of the decay.

2.3 Quantum yield

The *quantum yield* (which has no relation to the % yield defined above for photoluminescence decays) determines how radiative decay competes with other de-excitation processes. In the absence of an external quencher, the quantum yield is called the *natural quantum yield,* φ_0, and is defined by:

$$\phi_0 = \frac{\tau}{\tau_0}$$

where τ is the decay time and τ_0 is the *natural radiative lifetime.*

The more general form of this equation, which allows for a variety of deactivation mechanism such as external quenchers is:

$$\phi = \frac{k_r}{\sum k} = \frac{\tau}{\tau_r}$$

where τ_r is the radiative lifetime.

Because it measures the efficiency of photogeneration of charge carriers, the photoluminescence efficiency sets an upper limit on the external quantum efficiency of the device. If the decay time is shortened by energy transfer to external quenching agents, the total photoluminescence will be quenched. In actual photovoltaic devices, therefore, it is desirable that the luminescence be quenched by external charge and energy transfer, indicating that exciton dissociation competes efficiently with radiative recombination.

The above formula for the quantum yield assumes that every photoexcitation results in creation of a species capable of emission. This is not always the case with conjugated polymers, since some interchain excitations (see Chapter 3) do not emit. Thus, the formula should be modified to include *b*, the fraction of excitation events resulting in formation of emissive species:

$$\phi = \frac{bk_r}{\sum k} = \frac{b\tau}{\tau_r}$$

The quantum efficiency differs in film versus solution, because of the additional mobility of the excited state in films, which is strongly affected by the degree of chain packing and ordering. Because of increased access to non-radiative quenching sites in aggregated and close-packed films, such as P3HT, PL quantum yields are reduced, and the radiative lifetime is increased. Conversely, dilution of the polymer by blending, encapsulation

in a passive matrix, or dissolution in a solvent hampers the interchain transport decreasing the non-radiative recombination, thus increasing the quantum efficiency (Lemmer, Mahrt et al. 1993).

Note that, given the quantum yield and the fluorescence lifetime, the rate constant for any energy transfer process may be computed by

$$k_i = \frac{\phi_i}{\tau_F}$$

where k_i and ϕ_i are the rate constant and quantum yield for the process in question (such as radiation) and τ_F is the fluorescence lifetime. In practice, k_r, and thus τ_r, are often calculated by this method.

The *quenching yield, Q,* in a composite film can be obtained by:

$$Q = 1 - \frac{\tau_{composite}}{\tau_{neat\ film}}$$

This is useful because it allows the calculation of the exciton diffusion length, as well as giving a numerical assessment of the quenching efficiency. Internal quenching mechanisms, such as charge traps, will be included in both the lifetime of the composite and that of the neat film, and won't affect the overall Q value.

2.4 Decay models

Polymers in dilute solutions are often typified by a single relaxation time in the range of several hundreds of picoseconds. The assumption is that this single-exponential decay is from a single excited species, namely intrachain singlet excitons (Hayes, Samuel et al. 1997).

If the system has more than two levels, however, then the decay will be given by the sum of exponents with different values of τ, as described above. In practice, many materials are typified by multi-exponential decays. This is the case in polymer films which allow substantial interaction between chromophores (as opposed to dilute solution where polymer chains are relatively isolated). The multiple exponents may be due to:

a. A variety of photogenerated species with differing characteristic decay times (such as excitons, excimers, or exciplexes, see Chapter 3);
b. More than two levels to the system;
c. A variety of quenching mechanisms (i.e. traps, charge separation at interfaces); or
d. Variable lifetimes for the same species depending upon its environment (e.g., end of chain or middle of chain).

Multiple species

Most commonly, multiple exponents are interpreted as being due to multiple species and their interactions, as outlined below in Figure 2.3. In each model a chromophore, *X*, is excited through absorption of a photon to an initially hot excited state, *X**. That excited state relaxes to form one or two intermediate states, *A** and *B*,* which may decay radiatively or non-radiatively. In our systems, *A** represents the single-chain exciton and *B** the interchain exciton (see Chapter 3), but the model is valid for a variety of species. The measured TRPL decays can give insight into which of the above models is most valid for the system in question, and the relative importance of each decay pathway.

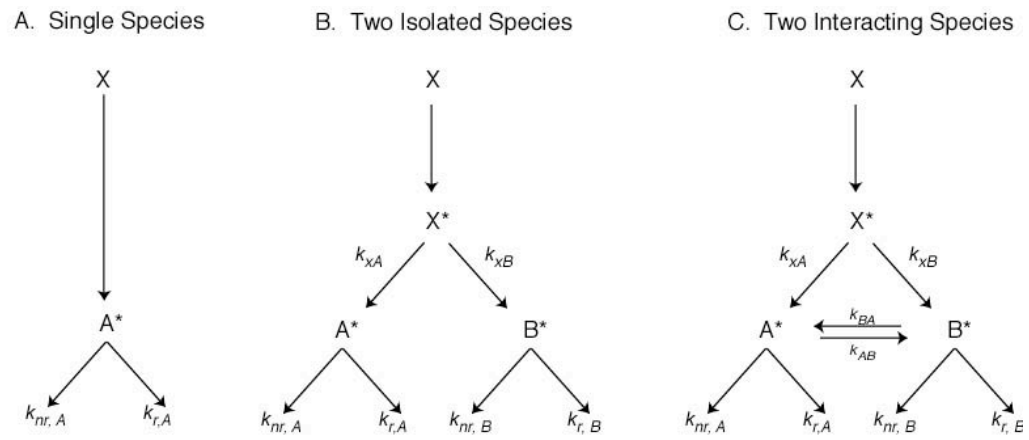

Figure 2.3. Three decay models for polymer systems. Adapted from (Hayes, Samuel et al. 1997).

Model A. Single Species Decay

In this case, the TRPL lifetime measured is equivalent to the excited state lifetime, $\tau = \frac{1}{k_r + k_{nr}}$. This decay should be mono-exponential. The pre-exponential amplitude indicates how much of the species there is at t=0.

Model B. Two Isolated Species

On the other hand, two species may be excited, but they not communicate with each other. The lifetimes of each species can be measured independently, and the decay should be bi-exponential:

$$\tau_A = \frac{1}{k_A} = \frac{1}{k_{r,A} + k_{nr,A}} \quad and \quad \tau_B = \frac{1}{k_B} = \frac{1}{k_{r,B} + k_{nr,B}}$$

$$and\ I(t) = A_1 e^{-t/\tau_A} + A_2 e^{-t/\tau_B}$$

with the pre-exponential factors indicating what fraction of the detected photons are emitted by each species.

Model C. Two Interacting Species

This model is often the most realistic, and of such complexity that data interpretation becomes extremely difficult. The excited state X^* may decay to either A^*or B^*, with characteristic rate constants k_{xA} and k_{xB}, respectively. The states A^* and B^* may decay radiatively or non-radiatively, or interconvert, with characteristic decay rates.

Consider the situation where $k_{ba} = 0$: That is, A^* can convert to B^* but not vice versa. This has been hypothesized to be the case with CN-PPV (Samuel, Rumbles et al. 1997). Thus, A^* may decay by three different routes: radiatively, non-radiatively, or via interconversion to B^*. This, along with the decay of B^*, will again give bi-exponential decay. However, some of the B^* excited state was generated directly via photons, and some indirectly via excitation of A^*. Thus, in addition to direct generation of B^* (k_{xB}), the B^* state will have a slow rise time (grow-in rate) which, if probed, would be the same as the decay of A^*. Once generated, B^* will decay with its characteristic lifetime, $\tau_B = \frac{1}{k_{r,B} + k_{nr,B}}$. Since the indirect and direct processes decay with the same lifetime, it is impossible to separate out the effects of each process by examination of the decay time. It is necessary to investigate the grow-in rate of B^* to try to assess the relative efficiency of the generation of each species (for example, whether k_{AB} dwarfs the effect of k_{XB}).

Now, if we allow that $k_{BA} > 0$, the decay times measured experimentally are no longer *lifetimes* but rather *decay times.* The lifetimes must be extracted from these decay

times, which now represent a mixture of different processes, and are solutions to the quadratic equation (Lakowicz 1999):

$$\tau_A, \tau_B = \frac{2}{(k_A + k_B) \pm \sqrt{(k_B - k_A)^2 + 4k_{AB}k_{BA}}}$$

$$\text{where } k_A = k_{r,A} + k_{nr,A} + k_{AB}$$
$$k_B = k_{r,B} + k_{nr,B} + k_{BA}$$

Where k_{AB} and k_{BA} are the rates of interconversion. Notice that this implies that both species A^* and B^* will have the same double-exponential decay time and will thus be indistinguishable in time-resolved experiments. Again, the pre-exponential factors indicate how much of each species exist at t=0. Thus, the grow-in rate of A^* must also be investigated in order to understand the decays obtained experimentally. Grow-in rates are rarely observable at the resolution of TRPL experiments.

The challenge in data interpretation is to try to understand the relative magnitude of each of the rate constants, which can (in theory) be extracted from the amplitudes of the time constants of each decay, and to find the simplest model which will assign physical species to each decay constant. Average PL lifetimes, calculated by an average of all measured PL decays and weighted by the amplitudes of those decay constants, thus miss many of the subtleties of TRPL data.

Model D. Two Materials

In the case of a mixture of two emitting materials, as in Chapter 9, each material may be represented by Model C. If each polymer is represented by a triple-exponent decay, I will see six decay components in the blend, regardless of whether new species are formed

between the two materials. If new species are formed, such as an exciplex, this will add a new decay component. Thus, it becomes difficult to analyze these decay components quantitatively.

In some systems, only one of the materials shows substantial emission, as in M3EH-PPV:PCBM blends (see Chapter 8). If charge transfer occurs between the two materials (as in the case of rapid charge transfer from M3EH-PPV to C_{60}), then the luminescence decay of M3EH-PPV will be quenched. The same number of excitons are available for decay, but a greater proportion of them are decaying via charge dissociation resulting in a decrease in the overall emission. In the steady state, this will be indicated by a drop in the quantum yield of the emission. In TRPL data, the time constant representing the decay of M3EH-PPV will decrease.

Because of the difficulty of interpreting TRPL results quantitatively, other tools (such as steady-state spectroscopy) are important in order to probe for changes in the emission profile, giving tools for data analysis.

2.5 PPV polymer decay

The steady-state and time-decay parameters for conjugated polymers have been studied by many groups in the past, and key results are summarized below, in Table 2.1. Decay in film is generally faster than decay in solution (with CN-PPV as one notable exception) because of the availability of additional non-radiative channels in film.

Polymer	ϕ_r	τ_r (ns)	τ_{nr} (ns)	τ (ns)	Notes
PPV film	0.27	1.2	0.5	0.32	Dominated by single-chain excitations.
MEH-PPV film	0.10-0.15	5.8 - 12	0.15	0.15 – 0.30	More efficient non-radiative decay than PPV due to low crystallinity leading to conformational defects. Mixture of single-chain and intrachain excitations.
MEH-PPV solution	0.20-0.35	0.9 - 1.1	0.5	0.20 - 0.30	Dominated by single-chain excitations.
CN-PPV film	0.35-0.46	16	8.6	5.6	Highly fluorescent with a long decay time. Dominated by emissive interchain excitations which are poorly coupled to the ground state.
CN-PPV solution	0.52	1.7	1.9	0.9	Dominated by single-chain excitations.
P3HT film	0.02	1.2	0.45	0.32	High crystallinity leads to significant interchain excitations, which are non-emissive.

Table 2.1. Photoluminesence decay parameters for PPV films.
The τ_{nr} for MEH-PPV and P3HT films were calculated from reported values.

References:

PPV film (Yan, Rothberg et al. 1994; Greenham, Samuel et al. 1995)

MEH-PPV film (Smilowitz, Hays et al. 1993; Hayes, Samuel et al. 1997; Samuel, Rumbles et al. 1997)

MEH-PPV solution (Samuel, Crystall et al. 1993; Samuel, Rumbles et al. 1997; de Souza, Rumbles et al. 2001)

CN-PPV film (Samuel, Rumbles et al. 1995; Samuel, Rumbles et al. 1996; Hayes, Samuel et al. 1997)

CN-PPV solution (Samuel, Rumbles et al. 1995; Samuel, Rumbles et al. 1996)

P3HT film (Greenham, Samuel et al. 1995)

2.6 References

Birks, J. B. (1970). Photophysics of aromatic molecules. New York, Wiley-Interscience.

de Souza, M. M., G. Rumbles, et al. (2001). "Cyano-substituted model compounds and conjugated polymers of PPV." Synth. Met. **119**: 635.

Greenham, N. C., I. D. W. Samuel, et al. (1995). "Measurement of absolute photoluminscence quantum efficiencies in conjugated polymers." Chem. Phys. Lett. **241**: 89.

Griffiths, D. J. (1995). Introduction to quantum mechanics. Englewood Cliffs, NJ, Prentice Hall.

Hayes, G. R., I. D. W. Samuel, et al. (1997). "Ultrafast dynamics of photoexcitations in conjugated polymers." Synth. Met. **84**: 889.

Lakowicz, J. R. (1999). Principles of Fluorescence Spectroscopy. New York, Kluwer Academic/Plenum Publishers.

Lemmer, U., R. F. Mahrt, et al. (1993). "Time resolved luminescence study of recombination processes in electroluminescent polymers." Appl. Phys. Lett. **62**(22): 2827.

Maniloff, E. S., V. Klimov, et al. (1997). "Intensity-dependent relaxation dynamics and the nature of the excited-state species in solid-state conducting polymers." Phys. Rev. B **56**: 1876.

Samuel, I. D. W., B. Crystall, et al. (1993). "The efficiency and time-dependence of luminescence from poly(p-phenylene vinylene) and derivatives." Chem. Phys. Lett. **213**(5-6): 472.

Samuel, I. D. W., G. Rumbles, et al. (1995). "Efficient interchain photoluminescence in a high-electron-affinity conjugated polymer." Phys. Rev. B **52**(16): R11573.

Samuel, I. D. W., G. Rumbles, et al. (1996). "Luminescence efficiency and time dependence in a high electron affinity conjugated polymer." Synth. Met. **76**: 15.

Samuel, I. D. W., G. Rumbles, et al. (1997). "Picosecond time-resolved photoluminescence of PPV derivatives." Synth. Met. **84**(1-3): 497.

Samuel, I. D. W., G. Rumbles, et al. (1997). Luminescence efficiency and time-dependence: Insights into the nature of the emitting species in conjugated polymers. Primary photoexcitations in conjugated polymers: Molecular exciton versus semiconductor band model. N. S. Sariciftci. New Jersey, World Scientific Publishing Company.

Smilowitz, L., A. Hays, et al. (1993). "Time-resolved photoluminescence from poly[2-methoxy, 5-(2'-ethylhexyloxy)-p-phenylene-vinylene]: Solutions, gels, films, and blends." J. Chem. Phys. **98**(8): 6504.

Strickler, S. J. and R. A. Berg (1962). "Relationship between absorption intensity and fluorescence lifetime of molecules." J. Chem. Phys. **37**: 814.

Yan, M., L. J. Rothberg, et al. (1994). "Spatially indirect excitons as primary photoexcitations in conjugated polymers." Phys. Rev. Lett. **72**(7): 1104.

Chapter 3

Photoexcitations

3.1 Introduction

The purpose of the present studies are to explore exciton dynamics. Excitons are, in the simplest case, an electron-hole pair energetically separated but physically bound by their coloumb attraction. This binding energy must be overcome to separate the pair and extract useful charge from the device.

There are several variations on the canonical singlet exciton. Excitons may be formed between electrons and holes on the same polymer chain, or on different chains, so the difference between single- and inter-chain excitations must be discussed. The characteristics of excitons and of charge separated states are mediated by phonon vibrations as they move down the lattice. The degree of charge separation may vary from a bound exciton to completely separated charges, with some intermediate states. These issues are the focus of the current chapter.

Energy and charge migration and transfer

Migration is used to indicate transport between chromophores of the same material, as in migration of an exciton along a polymer chain. *Transfer* applies to transport between chromophores of different materials, as in the transfer of excitation from a donor to an acceptor. It is important to distinguish between *energy* migration and transfer, versus *charge* migration and transfer, which have different kinetic behavior. *Energy* migration and transfer refers to the exchange of a neutral excitation (such as a bound electron/hole pair) between chromophores via radiative or non-radiative mechanisms. Energy migration is dominated by diffusion processes, as neutral excitations are not affected by the internal electric field. The

diffusion length is limited by the recombination rate of the excitation. *Charge* migration and transfer, on the other hand, refers to the exchange of a separated electron or hole between chromophores. Charge transfer is prompted by differences in electron affinity between two materials, and transport within a material is dominated by drift due to the influence of the internal electric field. Unlike energy migration, charge migration mobilities are limited by the reorganization of the polymer bond structure around the defect. (see *polarons* in section 3.3).

3.2 Inter- versus single-chain species

As mentioned above, electrons and holes may form complexes on the same chain (intra-chain) or different chains (inter-chain). For clarity, I will refer to intra-chain interactions as "single chain" interactions from this point. Estimates on the amount of interchain excitations in PPV polymers have ranged from 10% (Samuel, Rumbles et al. 1997) to 90% (Rothberg, Yan et al. 1996; Rothberg 1997), though recent studies suggest an estimate of 50% (Jakubiak, Collison et al. 1999). Photoluminescence from interchain species is generally low due to small matrix elements for emission from small wavefunction overlap. Thus, the enhanced interchain interactions in films and concentrated solutions result in lower quantum yield and shorter photoluminescence lifetime as opposed to dilute solution.

Energy transfer due to migration of excited species (i.e. excimers) between chains is more rapid than that of transfer along the polymer chain due to the presence of defects and kinks that hamper transport along the chain (Nguyen, Wu et al. 2000), which aids in transporting excitonic species to a charge-separation interface. The mobility of bound species

(i.e., polaron pairs) that are delocalized over two chromophores and travel as a unit, however, is likely to be low (de Souza, Rumbles et al. 2001), due to a large effective mass. Once the exciton is dissociated at an interface, charge transport, rather than energy transfer, becomes important. The transport of charge-separated species along isolated chains is much more rapid than that of the bulk polymer (Hoofman, de Haas et al. 1998), due to poor interchain mobilities. Despite the low mobilities of charge transport between chains, interchain transport is important for device operation in order to circumnavigate fixed kinks and defects (Schwartz 2003), and because a single chain will not bridge the space from electrode to electrode (McBranch, Campbell et al. 1995).

3.3 Single-chain species

Excitons

In early experiments, it was observed that inorganic semiconductors may absorb light with photon energies smaller than the bandgap, with no resultant increase in conductivity (and thus no increase in free carriers). This is true for materials free of impurities, ruling out the existence of mid-gap impurity bands responsible for absorption of this radiation. This called into question the single-electron model, in which light absorption promotes one electron from the valence to conduction band. Particles called *excitons* – excited molecular complexes of electrons and holes – were postulated to explain the phenomenon. Excitons may recombine (annihilate), releasing their energy in the form of light or lattice vibrations. Excitons are neutral, and thus unaffected by electric fields, and so travel by diffusion rather

than drift. The short diffusion length of excitons is an important consideration in device performance.

Some of the kinetic energy of the exciton (obtained from the absorbed photon) is lost to the binding energy. Thus, the exciton has a lower energy than the combined kinetic energy of the individual charge carriers: $E_{ex} = E_g - G_{ex}$ where E_{ex} is the exciton energy, E_g is the band gap, and G_{ex} is the binding energy, resulting in an exciton level that falls slightly below and above the HOMO and LUMO. In molecular solids, such as conducting polymers, the Frenkel exciton (in which the wavefunction is smaller than the lattice constant) is widely accepted to be the typical excited state species as opposed to the more delocalized Wannier-Mott exciton used in most inorganic semiconductors (Gribkovskii 1998).

Due to a large effective mass of the exciton, the binding energy in polymers is about 0.2 eV, which is higher than that in inorganic semiconductors. The binding energy in GaAs is 4.2 meV, and that in Si is 15 meV (Shionoya 1998), which may be overcome by thermal energy at room temperature (kT = 25 meV). This higher binding energy is a challenge in polymer photovoltaics, and necessitates the use of dissociation interfaces.

Polarons

Once an exciton is dissociated, the resulting electron and hole are not free to move as they would be in a semiconductor – they are bound to the polymer chain and thus cause lattice vibrations as they move along the chain. *Polaron* is a term that encapsulates motions of these charged particles, mediated by the lattice vibrations. This approach approximates the electronic motion as a free electron gas that is bound to the polymer chain via (non-thermal) phonon vibrations.

Once the polymer is photodoped, creating an electron in the π* energy level, the bonds in the benzene rings rearrange to accommodate it. This is called a *polaron.* A single polaron is unstable, and so a second polaron is created to balance it out – this transient state is termed a *neutral polaron*. The polarons define the domain boundaries between the two conformational states of the polymer chain (see Figure 3.1).

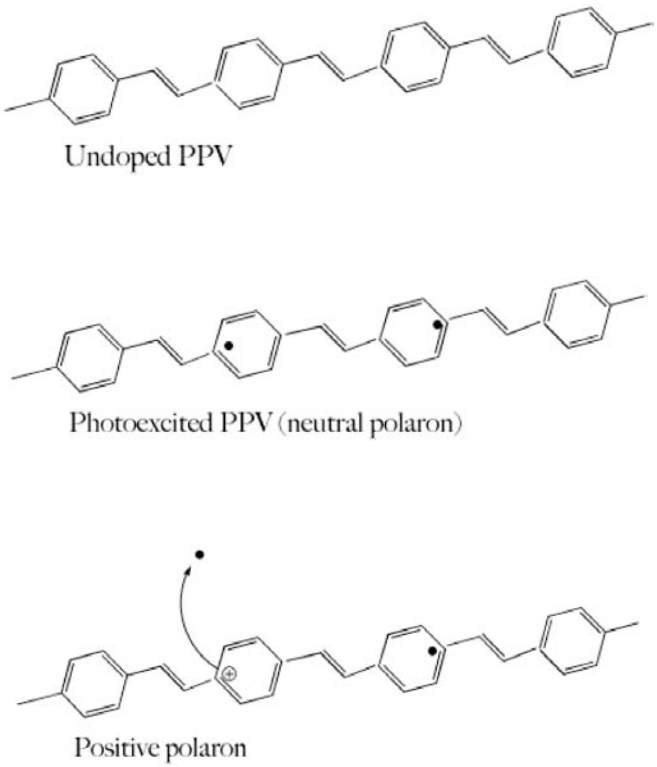

Figure 3.1. Polarons in PPV polymers.
The black dots indicate photoexcited electrons. Note the different bond conformation in the two sections of the polymer, as well as in the undoped versus doped examples.

If the electron is transferred to another species (such as an electron accepting material like PCBM, an electron-accepting polymer, or oxygen), it leaves behind a positive charge. This is then called a *positive polaron.* If both electrons are removed, it is called a positive bipolaron. Note that if the electron is transferred to another polymer, it will create a *negative*

polaron, or negative bipolaron, on that chain. In the language of chemistry, polarons are called radicals: A positive polaron is a *radical cation*, and a negative polaron is a *radical anion.*

Due to the activation energy required for the polaron to hop along the polymer chain (~0.5 eV), the polaron bands occur in the middle of the band gap. These new absorption bands have been observed in photoinduced absorption experiments as a new energetic peak in the absorption (Lane, Liess et al. 1997).

3.4 Inter-chain species

Emission Characteristics

Fluorescence from interchain species is broad and featureless, because these species have access to a wider range of energy segments compared to the more localized single-chain species. Fluorescence is also redshifted compared to exciton fluorescence. The redshift is due to the fact that the delocalized electrons are then bound by a three-dimensional instead of a two-dimensional box, and thus the energy eigenvalue becomes $E = \frac{n\pi\hbar^2}{l^3}$ instead of $E = \frac{n\pi\hbar^2}{l^2}$. Another way of putting this is that the energy eigenvalue of the wavefunction of an interchain excitation, which is comprised of a superposition of the single-chain exciton wave functions on neighboring chains, is minimized relative to that of the individual wavefunctions associated with the charge separated state. Thus the appearance of a new, featureless, low energy peak in the fluorescence spectrum is one sign of formation of an

interchain species. The wavefunction overlap and binding energy of interchain species is less than that of singlet excitons, making them easier to separate.

Emission from interchain excitons can be difficult to detect. Fluorescence from these species tends to be very low, with long radiative lifetimes, because of low overlap of the wavefunctions due to the separation between chains, resulting in a small matrix element for emission (Conwell 1998), as well as a radiative transition that is forbidden by symmetry (Michl and Bonacic-Koutecky 1990) resulting in a metastable state. Since both single-chain and interchain species may exist in the same sample, the emission from the single-chain species can easily overshadow that from the interchain species. The fraction of inter (versus single) chain excitons present in conjugated polymers is a subject of debate, which will be explored later in this chapter.

Ground state aggregates

Most of my discussion will focus on interchain species in the excited state. Multiple chromophores may also share delocalized electrons in the ground state, termed a *photophysical aggregate*. Interchain excited species may be excited directly from such aggregates, or from non-aggregated sections of the polymer.

Note that physical aggregates that do not share electrons are not included in the definition of aggregation -- in photophysical aggregation the electrons are actually delocalized across more than one chromophore, and simple physical proximity of polymer chains (physical aggregation) is insufficient (Schwartz 2003). Aggregates contribute significantly to the excited state in spin-cast films due to the high solution concentrations

used, and the fact that thermal annealing tends to straighten out the polymer chains, allowing them to assume a more ordered, aggregated structure (Schwartz 2003).

Aggregation may be caused by a variety of factors. Some polymers create highly crystalline films, with high degrees of order, which tends to enhance interchain interactions due to close-packing of the chains. Dissolution in a poor solvent causes chains to coil tightly, producing aggregates that survive even through the spin-casting process (Schwartz 2003).

Both aggregates and interchain excitons will result in a shift in the steady-state photoluminescence towards lower energy. Ground-state aggregates, however, will show a similar shift in the absorption spectrum, whereas interchain excitons will not.

Excimers

An *excimer* is a bound state between one chromophore in the ground-state and a separate chromophore in the excited state, which traps the energy of excitation. The excitation is shared equally between the two chains. The term "excimer" is shorthand for "excited state dimer." Excimers may form between adjacent or non-adjacent chromophores, or between chromophores on different polymer chains (George 1989). The charge complex may dissociate, causing emission of a photon. An excimer may also serve as a scavenger for excitons, providing a non-radiative channel for decay (Heeger 2002). Schwartz and colleagues have suggested that the primary interchain species in MEH-PPV are excimer-like, though evidence also suggests that a variety of interchain species with varying degrees of charge-separation exist in these films (Schaller, Lee et al. 2002).

Polaron pairs

When an excimer is created, the shared electron delocalization can lead to charge-transfer from one chromophore to the other, leaving a positive polaron on one chain, and a negative polaron on the other, as described above. The two interacting polarons are termed a *bound polaron pair.* Polaron pairs must be shared between different chains, rather than different conjugation segments of the same chain, in order for the size of the polaron to be small enough for the Coulomb attraction to be greater than kT, creating a stable bond between the pair (Conwell 1997). Polaron pairs are also referred to as *spatially indirect excitons* or *charge-transfer excitons.* They differ from excimers only in that the excitation is no longer shared equally between the two chains, but rather has a degree of charge separation, which will affect its mobility. Excimers and polaron pairs comprise the most extreme cases of what is probably a continuum of charge-separation states (Nguyen, Martini et al. 2000).

Exciplexes

We define an exciplex as a charge-transfer complex similar to an excimer, but between two different species, such as two polymers. It can also been defined more generally as an excitation whose charge transfer character is intermediate between an excimer and a polaron pair (Schwartz 2003). Exciplexes most commonly dissociate non-radiatively, with an extremely long characteristic lifetime due to low wavefunction overlap. Thus, exciplexes may act as external quenching agents in photoluminescence yields, essentially scavenging the excitons before they may recombine radiatively (George 1989). If an exciplex is to form, it must be energetically favorable relative to the exciton. Thus, exciplexes (as with other interchain excitations) will be observed as a new, unstructured emission at low energy. Exciplexes have been reported only a few times previously in π-conjugated polymers

(Osaheni and Jenekhe 1994; Alam and Jenekhe 2004; Morteani, Sreearunothai et al. 2004; Offermans, van Hal et al. 2005).

3.5 Energy transfer

Energy transfer may occur via the excited state of one chromophore to the excited state of another chromophore, as in exciton migration. Energy may also be transferred from the excited state of one species to the ground state of another species, termed *Forster transfer* (George 1989). In other words, if the emission spectrum of polymer A overlaps with the absorption spectrum of polymer B, then radiation emitted from polymer A (through radiative dissociation of excitons, excimers, or exciplexes) may be absorbed by polymer B, causing excitation. This will tend to increase the quantum efficiency of photovoltaic devices, since the energy transferred to radiative recombination in polymer A has some chance of creating useful current. Those complexes in polymer B which dissociate radiatively will necessarily do so at a lower energy (higher wavelength) than the emission of polymer A, tending to shift the emission spectrum to a lower energy than if no Forster transfer occurred.

3.6 Primary photoexcitations in PPVs

Following is a review of the literature on primary photoexcitations in PPV's. The interested reader is directed to two excellent recent reviews for additional detail (Nguyen, Martini et al. 2000; Schwartz 2003). Whether conjugated polymers are dominated by inter-

chain or single-chain excitations is particularly important in device fabrication, as this affects the degree of charge mobility, charge transport, and radiative recombination.

While the photoexcitations in dilute polymer *solution* are widely accepted to be due to singlet excitons residing on a single chain. The excitations in concentrated solution, or films, where there is significant interaction between polymer chains, has been a matter of debate. Hot single chain excitons are probably the primary result of photoexcitations, which diffuse to the longest, low-energy chain segment, and then either relax to form cold single-chain excitons, or undergo some degree of charge separation. This results in interchain excimers or bound polaron pairs (Rothberg, Yan et al. 1996; Rothberg 1997). After cooling, the binding energy of the exciton is high compared to kT, and it can no longer relax to form interchain species.

There is a variety of evidence for the existence of single-chain species in PPV's (except for the cyano-substituted PPV's), such as:

- The photoluminescence spectra of most PPV's is dominated by clear vibronic structure; signature of an intra-molecular species.
- Short lifetimes indicative of an allowed transition
- Small Stokes' shift from solution to film, indicative that the same excited state species is responsible for emission in the two systems.

However, a variety of results suggest that interchain species also play a role in the PPV's, such as:

- A reduction in the intensity and redshift of the photoluminescence in film characteristic of interchain emission (Schwartz 2003).

- Long radiative lifetime in film compared to solution (Samuel, Rumbles et al. 1997).
- One carbonyl group per 400 repeat units is enough to quench the PL, indicating the presence of species which can travel between monomer units (Rothberg, Yan et al. 1996).
- The presence of a nonemissive species (detected in PIA experiments) which is suppressed when aggregation is reduced by embedding MEH-PPV in polystyrene (Rothberg 1997)
- PL efficiency increases under conditions where interchain formations are not favored (ie., decreasing solution concentration, embedding in a polystyrene matrix, or creating samples with short conjugation lengths) (Conwell 1997).
- PL efficiency decreases and redshifts under conditions where interchain formations *are* favored, such as in annealed films or films spun from a favorable solvent such as chlorobenzene (Schwartz 2003).
- Reductions in the PL quantum yield may leave the decay dynamics essentially unchanged, suggesting the excited state lifetime is due to more than one species, one of which is non-emissive (Conwell, Perlstein et al. 1996; Rothberg, Yan et al. 1996).

This evidence suggests that both types of excitations play a role in conjugated polymers, but there is debate over which species dominates, and how they interconvert. The efficiency of these processes has been the subject of much controversy, and Schwartz emphasizes the point that morphology of polymers is highly dependent upon polymer

fabrication and film processing conditions, which could account for the contradictory findings stated in the literature (Nguyen, Martini et al. 2000; Schwartz 2003).

If, indeed, photogeneration creates both emissive and nonemissive species, then the generally accepted relationship between the quantum yield and lifetime:

$$\phi = \frac{k_r}{k_r + k_{nr}} = \frac{\tau}{\tau_r}$$

must be modified, to take into account the fact that the probability of creating an emissive species is not unity:

$$\phi = \frac{bk_r}{k_r + k_{nr}} = \frac{b\tau}{\tau_r}$$

where *b* is the fraction of absorbed photons resulting in creation of an emissive species (Samuel, Rumbles et al. 1997) – ie., k_{xA}. Estimates of *b* range from 0.5 (Jakubiak, Collison et al. 1999) to 0.9 (Samuel, Rumbles et al. 1997). The higher estimates of b, however, depended strongly on the radiative lifetime. Schwartz suggests that these calculations were overestimated due to errors in calculating the radiative lifetime due to large numbers of aggregates in MEH-PPV (Schwartz 2003), and that the disagreement in the field is due to different processing conditions which lead to different interchain species with differing degrees of charge separation characteristics (Nguyen, Martini et al. 2000).

The interpretation of results on MEH-PPV is particularly problematic. The emission profile contains clear vibronic structure, as would be expected of a single-chain species. However, time-resolved measurements show a radiative lifetime that is almost an order of magnitude higher in MEH-PPV film than in solution, which is consistent with emanation from an inter-chain species (Samuel, Rumbles et al. 1997). It is possible that the primary excitation in MEH-PPV is a single-chain singlet exciton, which then converts (with an

unknown efficiency) to an interchain species with a long radiative lifetime. This suggests a shift from Model A to Model C, as outlined in Chapter 2 and Figure 3.2 below, where A* is the single-chain species and B* is the excimer; k_{xA} is much greater than k_{xB}, k_{AB} and $k_{r,A}$ and $k_{nr,B}$ are efficient, whereas $k_{nr,A}$ and $k_{r,B}$ are inefficient and k_{BA} is negligible (Samuel, Rumbles et al. 1997).

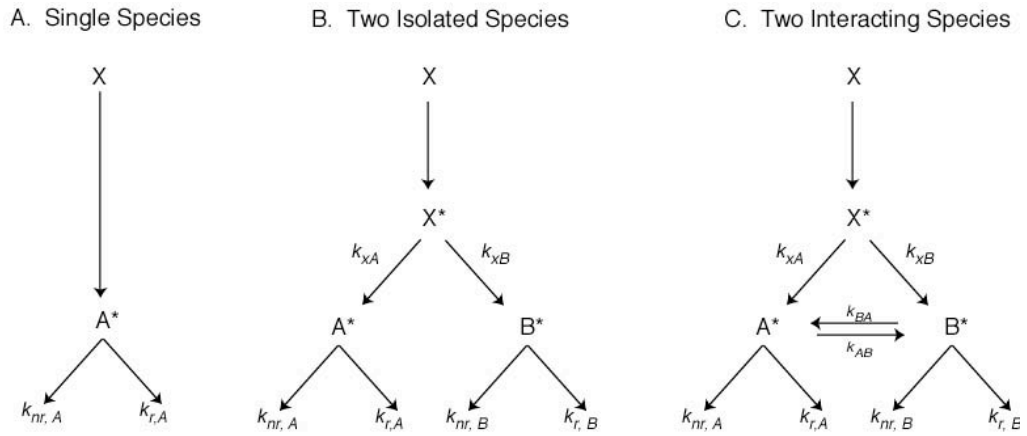

Figure 3.2. Models for decay dynamics of excited state species.

In MEH-PPV, as opposed to other PPVs, the conversion to the inter-chain species (k_{BA}) provides a particularly efficient mechanism for destruction of A*, leading to a short lifetime for A* (τ_A) and a grow-in term for the formation of B* ($-\tau_A$), which is not likely to be observable given the resolution of TCSPC experiments. Thus, the long observed lifetime in MEH-PPV films is due to the long radiative lifetime of this B* state, which overlaps poorly with the ground state. Emission is therefore due to a single-chain species, but greatly reduced in magnitude due to efficient conversion to the inter-chain species. Excimers may also transfer energy to emissive excitons, resulting in single-chain emission despite the presence of interchain species (Jakubiak, Collison et al. 1999).

In CN-PPV, on the other hand, there is clear evidence for interchain species as the dominant photoexcitations. The steady-state PL spectrum is broad and redshifted, whereas the absorption spectrum is not. The photoluminescence is high in this polymer, despite high proportions of excimers, because the interchain distance is small, resulting in a high matrix element for emission. Past work on this polymer is reviewed in detail in Chapter 6.

3.7 Summary

Excitations in conjugated polymers may reside on a single chain, or be shared across multiple chains. Which species dominates is important for device performance due to differing mobilities and separability of the different species. In the steady-state, interchain species show a low, broad, redshifted PL spectrum. Photophysical aggregates (in which electronic delocalization is shared across multiple chromophores in the ground state) are also characterized by redshifted PL, but show redshifts in the absorption spectrum, whereas excited species do not. Decay times of single chain excitons is expected to be short, and that of interchain excitations to be long, due to low rates of radiative recombination in excimers. Single-chain species include excitons and polarons. Interchain species differ in their degree of charge separation, and include excimers, polarons, polaron pairs, and exciplexes.

The primary photoexcitations in conjugated polymer films appear to be a mixture of interchain and single-chain species, with some degree of interconversion between the two. The relative weights of the two species remains unclear, but it is likely that over half of excitations are interchain species with varying degrees of charge-separation. The steady-state

PL spectrum is most likely due to highly emissive single-chain excitons that are generated directly by photoexcitation or by transfer of excimers to emissive excitons.

3.8 References

Alam, M. M. and S. A. Jenekhe (2004). "Efficient solar cells from layered nanostructures of donor and acceptor conjugated polymers." Chem. Mater. **16**: 4647.

Conwell, E. M. (1997). Intramolecular excitons and intermolecular polaron pairs as primary photoexcitations in conjugated polymers. Primary excitations in conjugated polymers: Molecular exciton versus semiconductor band model. N. S. Sariciftci. River Edge, NJ, World Scientific Publishing Company.

Conwell, E. M. (1998). "Mean free time for excimer light emission in conjugated polymers." Phys. Rev. B **57**(22): 14200.

Conwell, E. M., J. Perlstein, et al. (1996). "Interchain photoluminscence in poly(phenylene vinylene) derivatives." Phys. Rev. B **54**(4): R2308.

de Souza, M. M., G. Rumbles, et al. (2001). "Cyano-substituted model compounds and conjugated polymers of PPV." Synth. Met. **119**: 635.

George, G. A. (1989). Luminescence in the solid state: General requirements and mechanisms. Luminescence techniques in solid state polymer research. L. Zlatkevich. New York, Marcel Dekker, Inc.

Gribkovskii, V. P. (1998). Theory of Luminescence. Luminescence of Solids. D. R. Vij. New York, Plenum Press.

Heeger, A. J. (2002). "Semiconducting and metallic polymers: the fourth generation of polymeric materials." Synth. Met. **125**: 23.

Hoofman, R. J. O. M., M. P. de Haas, et al. (1998). "Highly mobile electrons and holes on isolated chains of the semiconducting polymer poly(phenylene vinylene)." Nature **392**: 54.

Jakubiak, R., C. J. Collison, et al. (1999). "Aggregation quenching of luminescence in electroluminescent conjugated polymers." J. Phys. Chem. A **103**: 2394.

Lane, P. A., M. Liess, et al. (1997). "Optical properties of substituted poly(paraphenylene)." Synth. Met. **84**: 641.

McBranch, D. W., I. H. Campbell, et al. (1995). "Optical determination of chain orientation in electroluminescent polymer films." Appl. Phys. Lett. **66**: 1175.

Michl, J. and V. Bonacic-Koutecky (1990). Electronic aspects of organic photochemistry. New York, John Wiley & Sons, Inc.

Morteani, A. C., P. Sreearunothai, et al. (2004). "Exciton regeneration at polymeric semiconductor heterojunctions." Phys. Rev. Lett. **92**: 247402.

Nguyen, T.-Q., I. B. Martini, et al. (2000). "Controlling interchain interactions in conjugated polymers: The effects of chain morphology on exciton-exciton annihilation and aggregation in MEH-PPV films." J. Phys. Chem. **104**: 237.

Nguyen, T.-Q., J. Wu, et al. (2000). "Control of energy transfer in oriented conjugated polymer-mesoporous silica composites." Science **288**: 652.

Offermans, T., P. A. van Hal, et al. (2005). "Exciplex dynamics in a blend of pi-conjugated polymers with electron donating and accepting properties: MDMO-PPV and PCNEPV." Phys. Rev. B **72**: 045213.

Osaheni, J. A. and S. A. Jenekhe (1994). "Efficient blue luminescence of a conjugated polymer exciplex." Macromolecules **27**: 739.

Rothberg, L. J. (1997). Bound polaron pair formation in poly (phenylenevinylenes). Primary photoexcitations in conjugated polymers: Molecular exciton versus semiconductor band model. N. S. Sariciftci. River Edge, NJ, World Scientific Publishing Company.

Rothberg, L. J., M. Yan, et al. (1996). "Photophysics of pheylenevinylene polymers." Synth. Met. **80**: 41.

Samuel, I. D. W., G. Rumbles, et al. (1997). Luminescence efficiency and time-dependence: Insights into the nature of the emitting species in conjugated polymers. Primary photoexcitations in conjugated polymers: Molecular exciton versus semiconductor band model. N. S. Sariciftci. New Jersey, World Scientific Publishing Company.

Schaller, R. D., L. F. Lee, et al. (2002). "The nature of interchain excitations in conjugated polymers: Spatially-varying interfacial solvatochromism of annealed MEH-PPV films studied by near-field scanning optical microscopy (NSOM)." J. Phys. Chem. B **106**: 9496.

Schwartz, B. J. (2003). "Conjugated polymers as molecular materials: How chain conformation and film morphology influence energy transfer and interchain interactions." Annu. Rev. Phys. Chem. **54**: 141.

Shionoya, S. (1998). Photoluminescence. Photoluminescence of Solids. D. R. Vij. New York, Plenum Press.

Chapter 4

Methods

4.1 Device Preparation

Our photovoltaics are built in a sandwich structure on indium tin oxide (ITO) coated glass, as in Figure 4.1 below. ITO is a transparent metal, and thus ideal as a transparent electrode. The ITO is patterned so that 6 devices are fabricated on each substrate.

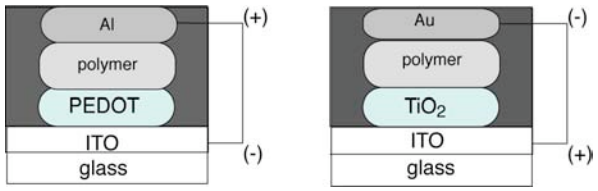

Figure 4.1 Sandwich photovoltaic device structure

Devices are prepared on glass substrates pre-patterned with transparent ITO. Because ITO has a variable workfunction, it is rarely used as the lone bottom electrode. Either PEDOT or TiO_2 is used for the transparent material deposited on top of the ITO substrate, resulting in opposite polarity devices due to differential workfunction steps. A transparent semiconductor, TiO_2 acts as an electron-transporter and hole-blocker due to its extremely low-lying HOMO. When light is incident on TiO_2, it becomes relatively conducting so that the quasi Fermi-level of the photodoped TiO_2 appears to play an important role in determining the open circuit voltage. PEDOT-PSS from Bayer is a metallic polymer polyethelynedioxythiophene (PEDOT) doped with polystyrenesulfonate (PSS) that acts as an oxygen barrier and planarizing layer. It has a substantially larger work function (~5.1 eV) than ITO (~4.8 eV), thus acting as a hole-acceptor. Both TiO_2 and PEDOT-PSS have been

shown to improve device performance over bare ITO (Carter, Angelopoulos et al. 1997; Arias, Granstrom et al. 1999).

PEDOT is deposited by spin-casting at 3000 rpm, and then heating to 100˚C under vacuum to remove water from the film. Titanium dioxide is deposited as a smooth TiO_x solgel (Arango, Johnson et al. 2000) or rough titanium dioxide nanoparticles (~13 nm suspended in water; purchased from Solaronix). In either case, the material is spin-cast at ~1000 rpm to produce a uniform film 50-100 nm thick, then sintered at 450˚C for 30-60 minutes to convert the material to a crystalline anatase phase. The TiO_x film is transparent and smooth relative to the nanoparticle layer, with surface features less than 3 nm.

The TiO_x solgel is prepared using the TiO_2 precursor titanium ethoxide, $Ti(OCH_2CH_3)_4$ (Gelest, Inc.). By volume, 4 parts of Ti ethoxide is added dropwise to a solution of 40 parts ethyl alcohol, which contains 1 part water and has a pH of 1, adjusted with the addition of hydrochloric acid (Aldrich). These reagents hydrolyse the ethoxide, forming –OH bonds, which may then polymerize, leading to gelation (Lianos 2004). The solgel is stored on a stirplate to maintain the suspension and reduce the possibility of precipitation of large particles.

Polymers are dissolved by weight fraction (~0.7 – 1.3%) in a suitable solvent – generally chlorobenzene, toluene, chloroform, or paraxylene – and allowed to form uniform solutions by leaving on a heated stirplate for 2-24 hours. Once dissolved, polymers are spin-cast by pipetting a small amount (approximately 50 μL) onto the PEDOT or TiO_2-coated substrate, and spinning at 1000-4000 rpm. This creates films from 15 nm to 200 nm thick, depending upon spin-speed and solution concentration. The top electrode (generally Ca, Al, or Au) is deposited under vacuum by thermal evaporation.

Upon spin-casting, polymer films are heated to a temperature of 100˚C for 1 hour. When the polymer films are heated past the glass-transition temperature, the polymer chains untangle to form a lower energy configuration, which leads to a semi-crystalline structure and, presumably, better chain packing (Schwartz 2003). Device performance is enhanced upon annealing (Breeze, Schlesinger et al. 2001), and the photoluminescence redshifts and is reduced in intensity, indicating the formation of interchain contacts characteristic of more crystalline films (Schwartz 2003). Mobility, however, has been found to decrease upon annealing due to a more isotropic arrangement of the polymer chains; transport is hampered by the randomization of microscopic domains of ordered structure within the polymer (Jeng, Hsu et al. 2005). Heating also forms a better contact between the polymer and the TiO_2 solgel surface (Fan, McQuillin et al. 2001).

4.2 Device Characterization

Open-circuit voltage and short-circuit current

Current-density vs. voltage curves were measured using a 2400 Keithley source meter. Since all photovoltaics are photodiodes (though not necessarily vice-versa), photovoltaics show rectifying behavior in the dark, with a turn-on voltage roughly equivalent to the band-gap (where the barrier to injection is overcome). In the light the cell still shows a diode-like behavior, but a photocurrent develops. This is shown schematically in Figure 4.2, below. In the short-circuit condition (zero resistance) the voltage is forced to be zero across the whole device, and the resulting measured current is the *short-circuit current (I_{sc})*. Under these conditions, the Fermi levels are aligned with the work functions of the metals. The

resulting slope of the energy bands, as in Figure 4.3 below, indicates a constant built-in electric field across the device, which drives the current. The current is generally divided by the size of the photoactive device to give a short circuit current density (J_{sc}) in units of mA/cm^2, which is independent of device area. Typical J_{sc}'s for polymer and polymer hybrid cells are in the range of 0.3 – 10 mA/cm^2.

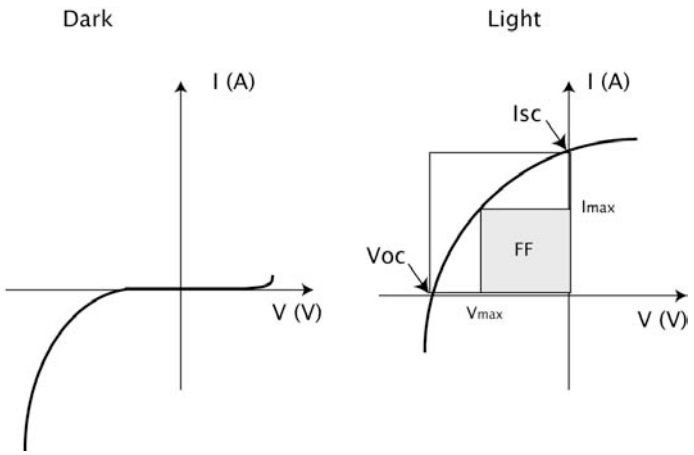

Figure 4.2. I-V curves in the dark and light.

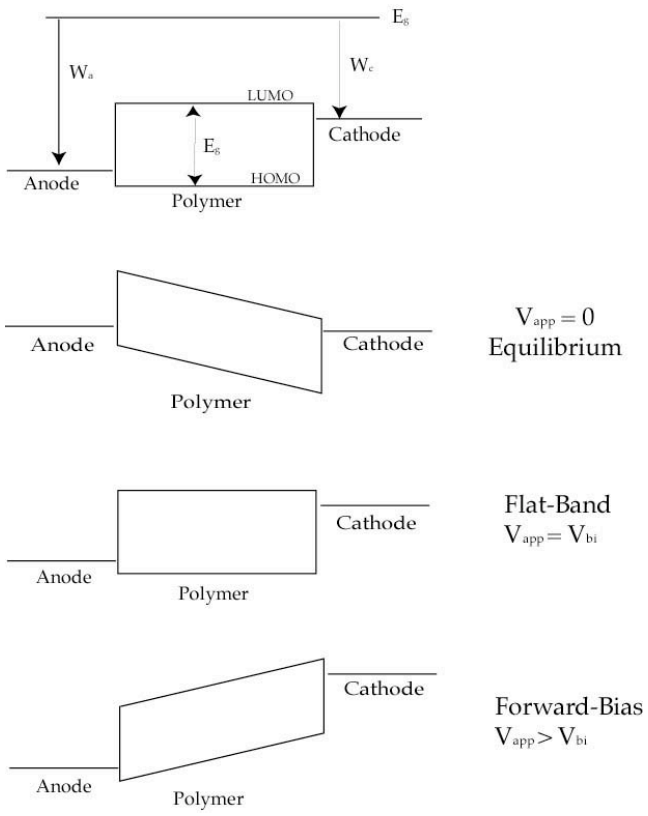

Figure 4.3. Energy band structure under varying bias. $V_{app} = 0$ corresponds to the short-circuit condition (photovoltaic operation), $V_{app} = V_{bi}$ corresponds to the open-circuit condition, and $V_{app} > V_{bi}$ injects charge to drive the device as an LED.

If, instead, the current is forced to be zero (open-circuit condition; infinite resistance), the applied voltage is termed the *open-circuit voltage (V_{oc})*. Electrons and holes flow towards the anode and cathode, and charge buildup continues until the resulting potential overcomes the built-in potential created by the difference in workfunctions. The flat-band energy structure in the middle of Figure 4.4 illustrates this situation; no current flows due to the lack of an overall electric field. Typical V_{oc}'s for organics are in the range of 0.5 – 1.5 V. The sign of V_{oc} depends upon the polarity of the device and the bias of the electrodes.

V_{oc} should, in theory, be equivalent to the work function difference of the electrodes. In practice, open-circuit voltages approach, but do not reach, the workfunction difference due to a variety of losses. For example, In TiO_2/Au cells the difference between the conduction band of TiO2 and the workfunction

of Au is 0.9V, but V_{oc} is generally 0.5-0.7 V. In PEDOT/Al structures, the difference between the workfunction of PEDOT and that of Al is 1.1 V, but V_{oc} is generally 0.9 – 1.0 V.

The origin of V_{oc} in polymers is a complex matter and the subject of debate in the field. Halls and Friend (Halls and Friend 2001) provide a useful review of the topic. The simplest model is that V_{oc} is due to the difference in the HOMO and LUMO of the donor and acceptor, respectively, but moderated by the workfunction difference (Meissner and Rostalski 2001). Fermi-level pinning may further complicate the issue (Heller, Campbell et al. 1997; Brabec, Cravino et al. 2001). V_{oc} in polymer/fullerene cells has been found to depend upon the acceptor strength of the fullerene but not the workfunction of the anode (Brabec, Cravino et al. 2002; Brabec 2004). Even if the same metal is used for the anode and cathode, these cells may have a V_{oc}, indicating that the D/A interface is more important than the electrode workfunction (Gregg 2003). In addition, V_{oc} tends to be limited by energy loss of the electron/hole pair after generation. For example, polarons (delocalized excitons) energetically relax once formed, creating an energy gap smaller than the π- π* gap.

Power Efficiency and Fill Factor

High power efficiencies (or incident power conversion efficiency, IPCE) are the ultimate goal of PV research, as this determines the size of the cell required to produce useable current, and thus the input cost and output power. Power efficiency is given by:

$$\eta = \frac{\text{power out}}{\text{power in}} = \frac{(I \cdot V)_{\max}}{P_{light}}$$

where P_{light} is the power of the illumination source, either in W or W/m^2, depending on the units of the output current. Typical power efficiencies in polymer photovoltaics are <1%. The record efficiency to date is 4.8% (Ma, Yang et al. 2005).

The *fill factor (FF)* is a measure of how much power is extracted from the cell relative to the theoretical maximum. In Figure 4.2 above, this is represented by the maximum power rectangle (small

grey square), normalized by I_{sc} multiplied by V_{oc} (larger square). The closer the I-V curve approaches the large rectangle, and thus the more severe its curvature, the higher the FF. The FF is a reflection of the serial resistance of the devices, which is related to charge mobility. The higher the mobility, the less voltage is required to extract the charge to create current at different points along the curve:

$$FF = \frac{(I \cdot V)_{\max}}{I_{SC} \cdot V_{OC}}$$

Note that the power efficiency may be reformulated in terms of the FF:

$$\eta = \frac{V_{OC} \cdot I_{SC} \cdot FF}{I_{light}}$$

Thus, high power efficiencies are obtained by maximizing the three basic solar cell parameters: I_{sc}, V_{oc}, and FF.

4.3 Solar simulation

Light bulb

Illumination is typically provided by a white light bulb with an output of approximately 80 mW/cm^2. The light intensity is estimated by comparing short-circuit currents on a device under solar simulation versus illumination by the light-bulb. Recent measurements suggest that the intensity may be significantly higher than 80 mW/cm^2, cutting reported device efficiencies by up to half.

This light source has a poor spectral match with the solar spectrum, as shown in Figure 4.4. The increased intensity of the lightbulb in the area from 500 nm – 600 nm will result in a skewing of the photocurrent towards lower energies relative to excitation by a solar simulator. A better spectral match is found using an Oriel solar simulator, as reported below.

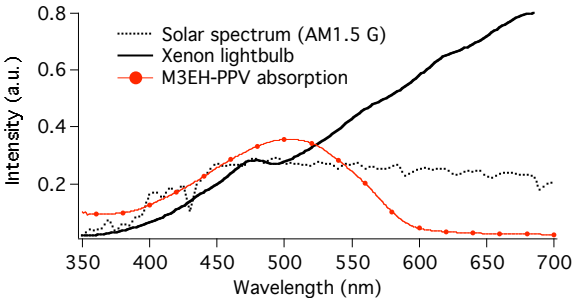

Figure 4.4. Output spectrum of lightbulb as compared to solar spectrum.

Intensities are reported in $W/m^2/nm$ and normalized. Absorption spectrum of M3EH-PPV is shown for comparison. Illumination spectra are recorded with an Ocean Optics spectrometer via an integrating sphere, and corrected for the responsivity of the optics.

While many device characteristics, such as J-V curves and external quantum efficiency (p. 81), are measured using illumination from a standard white light bulb around 800-1000 W/m^2, data obtained in this manner clearly does not match how the cell would perform under natural light conditions, and is difficult to compare between different research groups.

Solar simulations

Standard reporting conditions for solar simulation are AM 1.5 Global, 1000 W/m^2, at 25°C (Sommeling, Rieffe et al. 2000). When the sun is at a zenith angle of 48.2 degrees, the incident radiation passes through 1.5 times as much air mass as at high noon. This radiation is termed AM 1.5. Global radiation includes directly incident radiation, and also includes effects from reflected and scattered light.

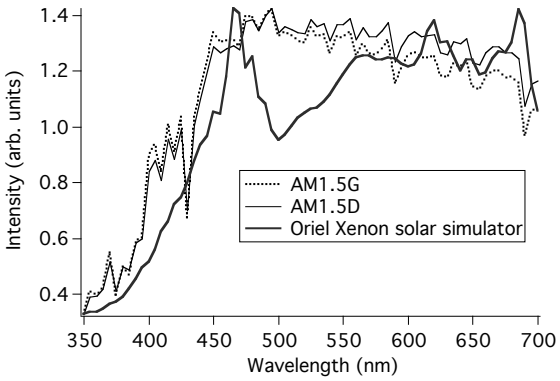

Figure 4.5. The mismatch between our solar simulator and the AM1.5D and AM1.5G spectra. Intensities are reported in $W/m^2/nm$ and normalized. AM1.5 spectra are measured and data provided to the public by the National Renewable Energy Lab.

The solar spectrum is sharply peaked around 400-600 nm, in a shape approximating that of blackbody radiation. Components of the earth's atmosphere (aerosols, ozone, water, carbon dioxide, and oxygen) each absorb characteristic portions of this spectra, so that the solar spectrum that reaches the earth appears as in Figure 4.5. A variety of light sources have been developed to create a spectrum approximating the solar spectrum for use in numerous applications, such as solar cell testing.

Our laboratory uses a 150W Oriel Xenon Arc lamp solar simulator (model 6255). Its output spectra is shown in Figure 4.5. Other available simulation light sources are tungsten, mercury, and metal halide lamps, each of which are a poor match with the actual solar spectrum. The simulator consists of a xenon lamp, whose beam is passed through a spectra correction filter and then collimated and focused on the sample.

We designed a reference cell for calibration of our solar simulator, and calculated the spectral mismatch (*M*) between our simulator, and that of the solar spectrum, as M = 0.987 (AM1.5D) and M = 0.979 (AM1.5G). Thus, under AM1.5D, our power efficiencies are correct to within 2% error, whereas for AM1.5G the error is slightly larger. These are acceptable values. Details on the calibration of our solar simulator and calculation of the spectral mismatch factor are given in Appendix 1. Unfortunately, the calibration was not completed in time to report device performance under solar simulation. Details on calibration are recorded here for documentation purposes.

4.4 Quantum efficiency

Photoaction current spectra, or PACS, measures the spectral dependence of the photocurrent. This gives information about the generation of charge carriers throughout the device, particularly important for heterojunction devices. A device in which charge carriers are primarily produced and dissociated at the first metal/polymer interface will show a PACS curve that roughly matches the absorption spectra of the polymer (*symbatic response*), since maximum absorption corresponds to maximum produced photocurrent. If, on the other hand, charge carriers are primarily produced and dissociated at the second polymer/metal interface, the PACS curve will be a reverse-image of the absorption spectrum (*antibatic response*), such that the maximum absorption corresponds to a minimum in the photocurrent. As the light travels through the polymer layer on its way to the second interface, the wavelengths that reach the second interface are those which are not preferentially absorbed by the polymer. The polymer acts as an optical filter, and the light which is absorbed within a diffusion length of the second interface contributes to the photocurrent.

External quantum efficiency (EQE), or incident photon-to-current efficiency, is necessary for high power efficiency. It is calculated by dividing the device photocurrent by the photocurrent of a silicon photodiode with a known EQE and multiplying by that known EQE. Most polymer photovoltaics have EQE values around 1-7%, whereas inorganics have EQEs approaching 100%. Bulk heterojunctions increase the EQE values to around 25-50% (Brabec 2004). Recently an EQE of 80% was reported in polythiophene:PCBM devices (Schilinsky, Waldauf et al. 2002), though this was under monochromatic illumination. Even with high EQE, however, high power efficiencies have not been obtained because organic solar cells do not absorb strongly in the peak of the spectral power output (around 700 nm).

Our photoaction current spectra are measured with a Keithley 2400 current meter. Illumination is provided by the Oriel Xenon light source used for solar simulation, passed through a monochromator which is stepped in 5 – 10 nm increments. Our photodiode is a silicon photodiode whose absolute EQE

was measured at NREL. It is not appropriate to use the same reference cell for EQE and solar simulation. The gridlines on the solar simulator reference cell will introduce a wavelength dependent aberration due to differential incident angle from the monochromator grating.

4.5 Thickness and morphology

Thickness measurements are made using an atomic force microscope in contact mode. The polymer film is scratched with a razor blade and the resulting step height is measured. AFM is also used for imaging of films. Optical imaging is also performed using a Nikon upright optical microscope with a transmission light source.

4.6 Steady-state spectroscopy

A review of spectroscopic analysis and theory is given in Chapter 2.

Absorption spectra are taken on a Varian optical spectrometer. The instrument baseline is set once every hour using a blank quartz slide. Subsequent measurements are automatically corrected for this baseline. Transmission intensity is collected as the excitation wavelength is increased in 1 nm steps. The absorption is then calculated by $A = -\ln\left[\frac{T}{1-R}\right]$ where R is the reflection and T is the transmission. The absorption coefficient is given by $\alpha = \frac{-1}{d} \cdot \ln\left[\frac{T}{1-R}\right]$ where d is the film thickness. Spectral changes in reflectivity are often small in these materials.

Steady state photoluminescence spectra were recorded using a Fluorolog-3 (JYHoriba) spectrometer that utilized a liquid N_2 cooled CCD detector to minimize thermal noise. Monochromatic excitation light was generated by a Xenon arc lamp with double monochromator. Because it offers the most intensive illumination in the wavelength range of interest (the visible spectrum, 200-800nm), the

xenon arc lamp is the excitation source of choice. The wavelength of interest is selected by an excitation monochromator and the resultant radiation is focused on an emission monochromator. A photomultiplier tube at the exit slit intensifies the signal for measurement. Fluorescence was collected at 22° for film (90° for solutions) relative to the excitation beam, passed through a single monochromator containing a 300 line/mm grating and imaged on the liquid nitrogen-cooled CCD array. Scattered light is a larger problem with thin film analysis, due to the 45 degree angle of incidence/detection. Because the intensity of the xenon lamp and the sensitivity of the detector are not uniform over the spectral range, the resulting emission spectra are corrected for these effects.

Emission spectra are obtained by fixing the excitation wavelength, and sweeping through the range of possible emitted wavelengths at the emission monochromator (as opposed to fixing the detection wavelength and sweeping through possible excitation wavelengths at the excitation monochromator). This is the type of measurement primarily addressed in this work, and provides information about the radiative states in the material.

4.7 Time-resolved fluorescence

Motivation

Measuring fluorescence decays is a challenging problem of instrumentation. The incident light pulse must have a short rise/fall time (ns), so that the luminescence decay can be observed separate from the pulse signal. Such a short-lived pulse must necessarily be of low energy, which leads to a low signal at the detector. However the Fourier composition of a step-function requires a broad range of wavelengths, requiring the incident light pulse to be of high bandwidth, resulting in a high noise factor. Therefore the signal to noise ratio is quite low. Signal-averaging techniques, primarily the Time Correlated Photon Counting Technique (TCSPC) used in this work, are employed to overcome this

problem. Details of this method, as well as schematic breakdowns of the component equipment, are included in Appendix 2.

The TCSPC technique, as its name suggests, measures the probability that a single emitted photon will be detected at a time *t* after the excitation of the sample. This probability is calculated by sampling the emission resulting from a large number of excitation flashes. The probability *p(t)* for detection of a single photon is taken as the intensity distribution *I(t)* of all photons emitted as a result of excitation. In other words, the distribution of arrival times for single photons represents the time-decay of the photoluminescence intensity of the sample. The excitation flash is time-correlated with an electronic pulse by use of the trigger, and the delay between the excitation flash and the first observed photon is back-calculated.

Experimental apparatus

Detailed descriptions of the technique and apparatus are included in Appendix 2. The excitation source was a pulsed, picosecond diode laser (IBH NanoLED-10) with a pulse width of 110 ps, operating at a wavelength of 438 nm and a repetition rate of 1 MHz. Emission was detected at 90° and 22° to excitation for solution and film, respectively, by focusing the emission onto the slits of a 0.25 m monochromator (SPEX minimate), and subsequently detected by a photon counting photomultiplier tube (Hamamatsu H6279*)*. The PMT output was amplified using a 1 GHz amplifier (Philips model 6954) then shaped using a constant fraction discriminator (Ortec, Tennelec model 583). The resulting signal was fed into the start input of a time-to-amplitude converter, (TAC, Ortec, model TC864), which was operated in reverse mode. The stop input to the TAC was supplied by an output directly from the pulsed laser diode controller (IBH NanoLED-C). The TAC output was fed to a multi-channel analyzer (Oxford Instruments PCA3-8K) operating in pulse-height analysis mode.

Data correction

Data will be slightly offset due to background – from both PMT noise and background room light. Both the instrument response functions *P(t)* and the sample data *I(t)* must be corrected for this background noise (B) by a simple subtraction:

$$I_0(t) = I(t) - B$$
$$P_0(t) = P(t) - B$$

Instrument response functions were measured by the same procedures as sample fluorescence, but substituting a dilute non-fluorescent sample for the solution, which acted as a scatterer. The instrument response function (IRF) from this system, when scattering the excitation light from a dilute solution of colloidal silica, was determined to be 220 ps. This represents the shortest time decay measurable by the instrument.

In addition, the decay must be deconvoluted with this instrument response. The true decay of a sample, *I(t),* is a response to a single delta function pulse. In reality, the instrument response function *P(t)* is several picoseconds wide and can be considered to be a series of closely-spaced delta functions of different amplitudes (Lakowicz 1999). The sample data*, I(t),* is thus a sum of exponential decays in response to these different delta function excitations. Therefore the instrument response should be deconvoluted with the sample response in order to obtain the true fluorescence decay, *G(t)*:

$$I_0(t) = \int_0^t P_0(t')G(t-t')dt' = P_0(t) \otimes G(t)$$

Note that t=0 is not defined in TCSPC experiments, since I(t) is a response to a series of delta functions (Lakowicz 1999). Some approximations must be made (O'Connor and Phillips 1984) due to the fact that the data obtained is not a continuous distribution, but rather a histogram.

In the current work, the influence of the instrument response function was removed from the decay curve using a non-linear, least squares iterative reconvolution procedure employing the Marquardt

minimization routine. The true decay kinetics, *G(t),* were reproduced with a temporal resolution of ~ 30 ps.

Least-squares fitting

The least-squares technique (Lakowicz 1999) tries to minimize the difference between a calculated fitting function, Y(t), and the obtained sample decay curve, $I_0(t)$. In particular, the χ^2 (chi-square) function is minimized – the sum of the squares of the difference between the calculated and experimental values as weighted by the photon counts for that particular data point:

$$\chi^2 = \sum_{i=1}^{n} \left[\frac{\left(I_0(t_i) - Y(t_i) \right)^2}{I(t_i)} \right]$$

where *n* is the total number of data points, $Y(t_i)$ is the calculated fitting function, $I(t_i)$ is the corrected photon count, and $I(t_i)$ is the uncorrected photon count which serves as a weighting factor. Details on the least-squares fitting technique is given in Appendix 3, and the reader may find additional details in previous works (O'Connor and Phillips 1984; Lakowicz 1999).

Note that variation of the range of channels used in the fitting can help provide better resolution for particularly short-lived or long-lived decays, by essentially zooming in or panning out on the data. The decay constants themselves shouldn't change, but the goodness of the fit may change. In the case that the decay constant does change significantly, it may be that an additional decay component is being detected upon variation of the range of channels that could not be resolved before.

Goodness of the fit

A variety of parameters are used to judge whether a fitted function is a good approximation of the data (O'Connor and Phillips 1984), as outlined below:

(a) Reduced chi-square, $\chi^2_\nu \approx 1$

The fit can generally be judged to be successful if the χ^2 value is less than the number of data points. A more robust statistic, which is essentially normalized by the size of the data set, is the reduced chi-square value, χ^2_ν:

$$\chi^2_\nu = \frac{\chi^2}{n_2 - n_1 + 1 - p}$$

where n_1 and n_2 are the first and last channels of the decay, and p is the number of variable parameters in the fitting function. χ^2_ν should be close to 1, indicating that χ^2 has approached the number of decay channels used. χ^2_ν values are generally greater than 1 in TCSPC analysis, indicating that the data follows the expected Poisson distribution. If the value is less than one then the signal-to-noise ratio is poor, and the number of data values is insufficient. Values of 1.0-1.2 are "good" values, though even 1.3-1.5 may be considered "good enough" if the data stands up to close examination. See Figure 4.8 for fits with different values of the reduced chi-square.

Even if the χ^2_ν value is good, then additional parameters (such as the residuals and Durbin-Watson, below) should be examined to make sure that the fit is good, since low χ^2_ν values may be obtained in the case of a poor fit.

(b) Plot of the weighted residuals, $r(t_i)$ = random

An heuristic measure of the goodness of a fit may be obtained from the plot of the weighted residuals, $r(t_i)$, a measure which calculates a weighted difference between the calculated fit $Y(t_i)$ and the actual data curve $I_0(t_i)$:

$$r(t_i) = \frac{I_0(t_i) - Y(t_i)}{\sqrt{I(t_i)}}$$

A typical residual curve is shown in Figure 4.8. A good fit will show residuals scattered randomly about the zero line, with no correlation to channel number. A correlation would be indicative of systematic

instrument error. A hump clustered around a certain channel (see Figure 4.6, 2 exponent fit) could indicate a poor fit due to a poor model, and an increase in the number of exponents (or a switch to a different model) may be needed.

(c) Durbin-Watson parameter (DW) ≤ 1.7-1.8

Provides a numerical assessment similar to the graphical representation of the residual plot. A poor fit will have a DW of less than 1.7, 1.75, and 1.8 or lower for single, double, or triple exponential fits, respectively.

$$DW = \frac{\sum_{i=n_1+1}^{n_2}\left[r(t_i) - r(t_{i-1})\right]^2}{\sum_{i=n_1}^{n_2}\left[r(t_i)\right]^2}$$

(d) Standard deviation (SD) of residuals ≈ 1; Root mean square (RMS) of residuals ≈ 1; Skewness (SK) ≈ 0; Kurtosis (K) ≈ 3

Like the DW, these measures indicate how well the residuals are randomly scattered about the channel number. O'Connor indicates that the SD is not a very sensitive measure, and that a definite upper limit cannot be set for the RMS. Positively (or negatively) skewed values occur when positive (or negative) residual values lie far from the mean. It is difficult to set a limit for kurtosis values, because of the small sample size in TCSPC experiments. Values above or below 3 indicate a non-normal distribution of residual values about the mean.

Below, in Figure 4.6, are examples of poor, better, and excellent fits. Examination of the non-random weighted residuals plot (which show a skew at high channels, and a large hump near the start of the pulse), as well as the poor match between the fit function and the sample decay, indicate that the first fit is not a good fit. The high χ^2_ν value confirms this supposition, and we need look no further.

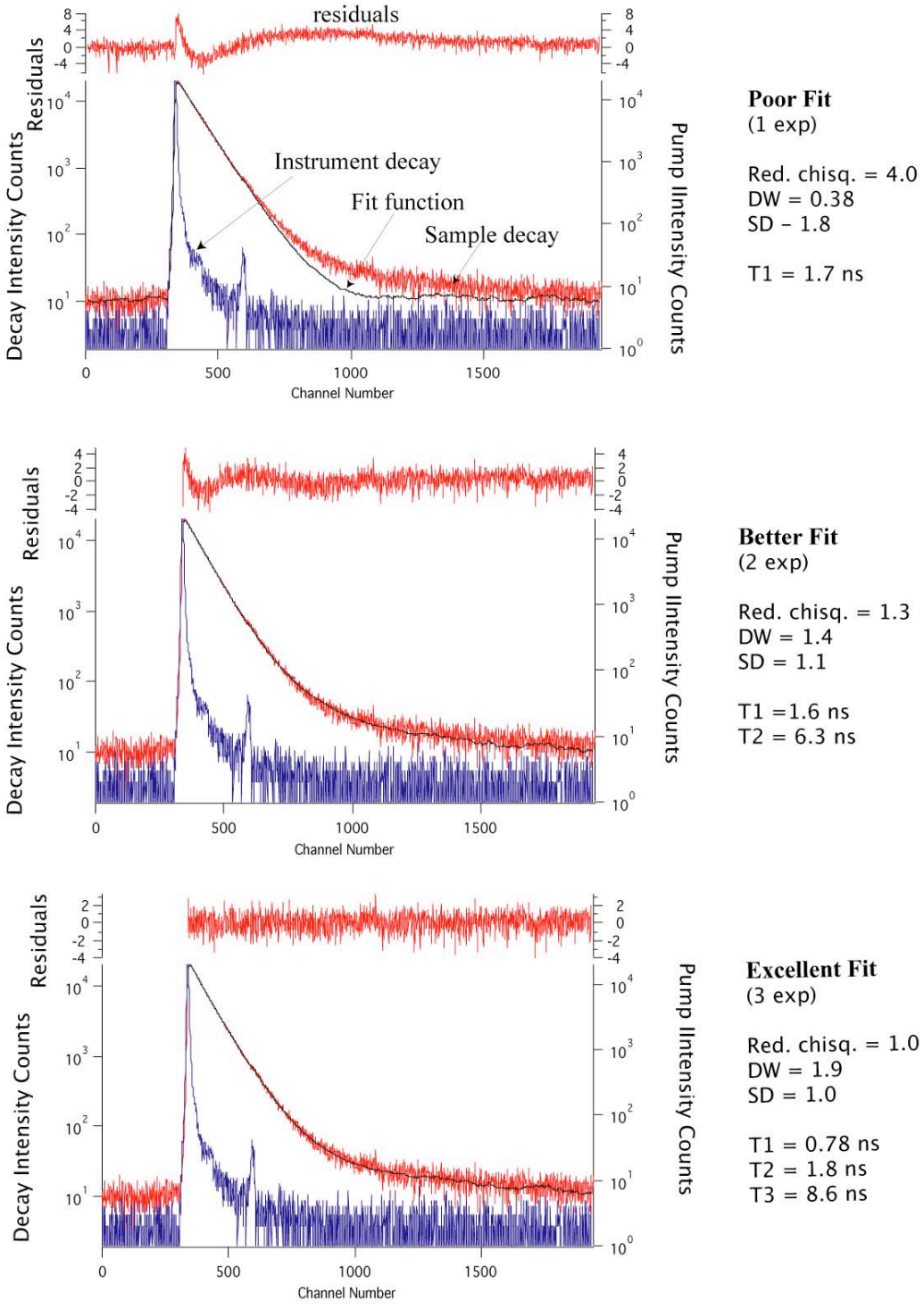

Figure 4.6. Raw fitted data, showing poor, better, and excellent fits, as determined by the fitting parameters and the randomness of the residuals.

The good fit, on the other hand, passes these preliminary tests. The plot of the weighted residuals shows no obvious skew or large humps, though there is a hump near the start of the decay, indicating the presence of an additional decay parameter. I have attempted to minimize the effect of the sharp peak near the start of the decay by beginning the fit at 50% of the rising edge, without success. Still, the χ^2_ν-value is good and this curve could be acceptable.

The excellent fit passes all requirements for the fitting parameters easily. Most of the fits used in this work are of this quality. In the present example, it would be difficult to choose this fit over the 3 exponential fit on the basis of the parameters alone, as both fits are acceptable. For most fits, the difference between 2- and 3- exponential fits was more substantial.

In general, triple and quadruple exponential fits should not be accepted at face value, as it is difficult to achieve true decay kinetics with a large number of parameters. In addition, the multiple kinetic processes in such systems (generally heterojunctions) become complicated due to energy and charge transfer between the different materials. Instead such fitting must be guided, as much as possible, by theoretical models or previous results. The float-fitted results in these studies have been compared with the decay parameters of the constituent materials (for heterojunction structures), or force-fit to those parameters.

Spectral diffusion

Conjugated polymers consist of a range of conjugation lengths, and depending upon the wavelength of the photoexcitation, excitons are created on either long or short conjugation segments. Excitations on short conjugation segments migrate to longer, lower-energy portions of the chain. Thus, the photoluminescence spectrum redshifts and narrows with time. In time-resolved data, the lifetime is shorter at lower emission energies due to the migration of excitons (Ma, Quian et al. 2001). This is termed *spectral diffusion,* and has been observed in many polymer systems. It is clearly present in most of the

samples reported in this work. The high energy luminescence tail generally decays quite rapidly as excitons migrate from high energy, short conjugation segments to longer segments. As they lose energy, there are fewer energetically favorable sites available, and so the migration slows.

Another spectral effect is that the blue edge of the spectrum tends to be more easily quenched in the presence of a quencher, since excitons excited in short conjugation segments are more likely to encounter a quenching site enroute to the longer conjugation segment.

The result of this spectral diffusion is that photoluminescence is due to the low energy, long conjugation segments, while absorption is due to a broader range of conjugation lengths. The absorption is homogenously broadened, and shifted to higher energy, relative to the photoluminescence. Samuel and Rumbles suggest that the Stokes' loss from the peak of the absorption (high energy) to the peak of the photoluminescence (low energy) is due to the migration of excitations, rather than the structural relaxation of the excited state (Samuel, Rumbles et al. 1997). A result of this spectral diffusion is that excitation into the absorption tail results in simpler decay dynamics, since this results in excitation of the longest conjugation segments. Therefore exciton migration along the chain is removed as a decay component.

4.8 References

Arango, A. C., L. R. Johnson, et al. (2000). "Efficient titanium oxide / conjugated polymer photovoltaics for solar energy conversion." Adv. Mater. **12**(22): 1689.

Arias, A. C., M. Granstrom, et al. (1999). "Organic photodiodes using polymeric anodes." Synth. Met. **102**: 953-954.

Brabec, C. (2004). "Organic photovoltaics: technology and market." Sol. Energy Mater. Sol. Cells **83**: 273.

Brabec, C., A. Cravino, et al. (2002). "The influence of materials work function on the open circuit voltage of plastic solar cells." Thin Solid Films **403-404**: 368.

Brabec, C. J., A. Cravino, et al. (2001). "Origin of the Open Circuit Voltage of Plastic Solar Cells." Adv. Func. Mater. **11**(5): 374.

Breeze, A. J., Z. Schlesinger, et al. (2001). "Charge transport in TiO_2/MEH-PPV polymer photovoltaics." Phys. Rev. B **64**(12): 125205.

Carter, S. A., M. Angelopoulos, et al. (1997). "Polymeric anodes for improved polymer light-emitting diode performance." Appl. Phys. Lett. **70**(16): 2067.

Fan, Q., B. McQuillin, et al. (2001). "A solid state solar cell using sol-gel processed material and a polymer." Chem. Phys. Lett. **347**: 325.

Gregg, B. A. (2003). "Excitonic solar cells." J. Phys. Chem. B **107**: 4688.

Halls, J. J. M. and R. H. Friend (2001). Organic Photovoltaic Devices. Clean electricity from photovoltaics: Series on photoconversion of solar energy. M. D. a. H. Archer, R. London, Imperial College Press. **1**.

Heller, C. M., I. H. Campbell, et al. (1997). "Chemical potential pinning due to equilibrium electron transfer at metal/C_{60}-doped polymer interfaces." J. Appl. Phys. **81**(7): 3227.

Jeng, U., C.-H. Hsu, et al. (2005). "Morphology and charge transport in poly(2-methoxy-5-(2'-ethylhexyloxy)-1,4-phenylenevinylene) films." Macromolecules **38**: 6566.

Lakowicz, J. R. (1999). Principles of Fluorescence Spectroscopy. New York, Kluwer Academic/Plenum Publishers.

Lianos, P. (2004). "Use of time-resolved fluorescence analysis to assess molecular mobility and ionic conductivity in nanocomposite organic-inorganic gels." J. Fluor. **14**: 11.

Ma, G.-H., S.-X. Quian, et al. (2001). "Singlet exciton migration in a conjugated polymer by picosecond time-resolved photoluminescence." Chin. Phys. Lett. **18**(7): 944.

Ma, W., C. Yang, et al. (2005). "Thermally stable, efficient polymer solar cells with nanoscale control of the interpenetrating network morphology." Adv. Func. Mater. **15**(10): Advance Online Publication.

Meissner, D. and J. Rostalski (2001). "Photovoltaics of interconnected networks." Synth. Met. **121**: 1551.

O'Connor, D. V. and D. Phillips (1984). Time-Correlated Single Photon Counting. London, Academic Press.

Samuel, I. D. W., G. Rumbles, et al. (1997). Luminescence efficiency and time-dependence: Insights into the nature of the emitting species in conjugated polymers. Primary photoexcitations in conjugated polymers: Molecular exciton versus semiconductor band model. N. S. Sariciftci. New Jersey, World Scientific Publishing Company.

Schilinsky, P., C. Waldauf, et al. (2002). "Recombination and loss analysis in polythiophene based bulk heterojunction photodetectors." Appl. Phys. Lett. **81**(20): 3885.

Schwartz, B. J. (2003). "Conjugated polymers as molecular materials: How chain conformation and film morphology influence energy transfer and interchain interactions." Annu. Rev. Phys. Chem. **54**: 141.

Sommeling, P. M., H. C. Rieffe, et al. (2000). "Spectral response and IV-characterization of dye-sensitized nanocrystalline TiO_2 solar cells." Sol. Energy Mater. Sol. Cells **62**(4): 399.

Chapter 5

Characterization of the hole-transporting polymer M3EH-PPV

5.1 Abstract

We present device and photophysical characterization of the hole-transporting polymer M3EH-PPV, which is used throughout this thesis. Photovoltaic devices on M3EH-PPV show high efficiencies for a single-layer device, up to 1.3% when a rough TiO_2 nanoparticle surface is used for the transparent anode. The device efficiencies are enhanced relative to MEH-PPV due to increased hole moblility and crystallinity, but performance is limited by the poor electron mobility of the polymer.

Steady-state photoluminescence and absorption data are presented, and appear to be dominated by single-chain species.

Dilute solution is dominated by a decay time of 0.35 ns, and thick films are dominated by decays of 0.20 ns (43%) and 0.45 ns (50%). Solution and thin films show spectral diffusion – decay times increase as the emission energy decreases, indicating that excitations fill lower energy sites over time.

The photophysics of thick and thin films are surprisingly different, and I interpret this in terms of increased aggregation in the thick sample due to a low spin-speed (which fails to pull apart weak aggregates in solution), and long evaporation time (which allows the chains to seek energetically favorable conformations).

All environments are characterized by 3-4 exponential fits, indicating complex decays even for isolated chains. The simple model of two possible excited state species (single-chain and interchain) is incomplete.

5.2 Structure and properties

M3EH-PPV is a strictly alternating copolymer of the well-characterized semiconducting polymer poly(2-methoxy-5-(2'-ethylhexyloxy)-1,4-phenylene-vinylene) or MEH-PPV, as shown in Figure 5.1 below. MEH-PPV is a derivative of poly-pheneylene-vinylene (PPV) asymmetrically substituted with alkoxy groups, which confer solubility and create a narrow band gap; thus the emission of MEH-PPV is orange, whereas that of PPV is green. The exciton diffusion length in MEH-PPV is ~ 20 nm (Savenije, Warman et al. 1998).

The principle product of photoexcitation in MEH-PPV is the single-chain exciton, which may decay radiatively or non-radiatively, or migrate to interchain excitons (excimers and polaron pairs). The efficiency of these processes is the subject of debate and are discussed in Chapter 2. The cyano-substituted PPV's (CN-PPV and CN-ether-PPV) are dominated by excimer emission, as will be discussed in Chapter 7.

High degrees of anisotropy have been found in MEH-PPV indicating that chains are oriented within the plane of the film and that the chains behave as rigid rods (Tammer and Monkman 2002), although more recent results show high degrees of coiling in MEH-PPV (Kemerink, van Duren et al. 2005). Annealing has been shown to destroy the anisotropy (Jeng, Hsu et al. 2005), suggesting that crystallinity is low in films used for optoelectronic devices. The asymmetric substitution of the side-chains has been found to inhibit chain stacking, resulting in relatively low degrees of aggregation (Kemerink, van Duren et al. 2005) and lower mobility (Tanase, Wildeman et al. 2005; van Breemen, Herwig et al. 2005). Accordingly, the decay of photoexcitations in MEH-PPV is more rapid than that in PPV because the reduced crystallinity in MEH-PPV increases the non-radiative decay via conformational defects (Hayes, Samuel et al. 1995). Monte Carlo simulations by Conwell

have shown that the lowest energy structure of MEH-PPV consists of a distance of 0.41 nm between chains, with the double bond on one chain overlapping the ring of the nearest neighbor (Conwell 1997). This large intermolecular distance results in a small wavefunction overlap between chains, and thus a small matrix element for emission. Thus, interchain excitations (e.g., excimers) in MEH-PPV are likely to decay non-radiatively.

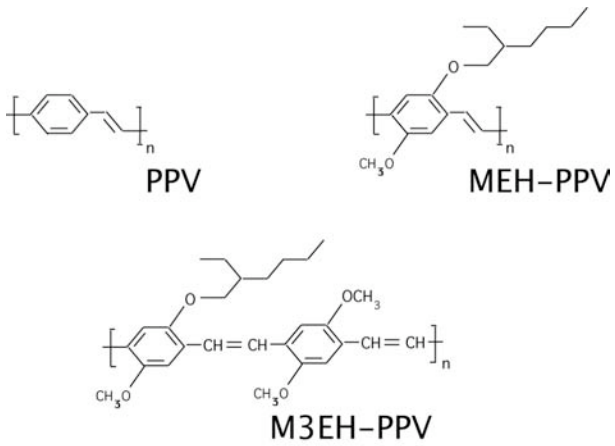

Figure 5.1. Chemical structures of PPV, MEH-PPV, and M3EH-PPV.

M3EH-PPV was synthesized by Horner reaction and has optical properties very similar to MEH-PPV (Pfeiffer and Hoerhold 1999). Both M3EH-PPV and CN-ether-PPV were provided courtesy of H.-H. Hoerhold and H. Tillmann at the University of Jena in Germany. The band gap of M3EH-PPV is taken to be similar to that of MEH-PPV, though it is likely to be slightly shifted, as evidenced by small (~ 5 nm) shifts in the absorption and PL spectra. Compared to MEH-PPV, M3EH-PPV has been found to have twice the zero-field mobility -- 5 x 10^{-7} cm^2/Vs (Breeze, Schlesinger et al. 2004) -- about twice the glass transition temperature (113˚C), and a higher number average molecular weight (44,300) as determined by gel permeation chromatography (GPC) (Pfeiffer and Hoerhold 1999). The high glass

transition temperature indicates a more ordered structure requiring greater energy input in order to initiate a phase transition from an ordered to glassy phase. Its photoluminescence quantum efficiency is similar to that of MEH-PPV (Pfeiffer and Hoerhold 1999).

5.3 Device characterization

Devices prepared from M3EH-PPV are fabricated on a TiO_2//Au or PEDOT//Al structure, as indicated in Figures 5.2A and 5.2B below. See Chapter 4 for details of fabrication and light source (~80 – 100 mW/cm^2).

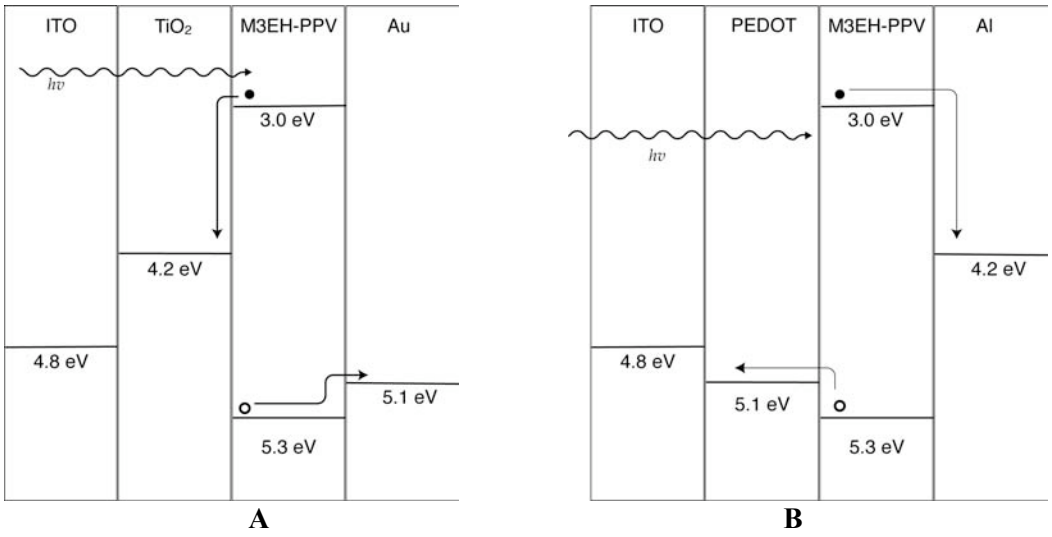

Figure 5.2. Energy band diagrams for M3EH-PPV on two different device architectures: (A) transparent anode and (B) transparent cathode.

M3EH-PPV devices (J_{sc} ~ 1 mA/cm^2) outperform MEH-PPV (J_{sc} ~ 0.14 mA/cm^2) devices by about an order of magnitude, due to enhanced charge mobility and crystallinity in this polymer. Typical J-V curves are showing in Figure 5.3 below. These devices behave as

good diodes, as indicated by good rectification ratios (~10^3 – 10^6). Dark currents are low (10^{-5} – 10^{-9} A/cm^2), and increase as the thickness of the device decreases.

The performance of M3EH-PPV devices on TiO_2//Au is strongly dependent upon device thickness (thinner devices yield higher currents) indicating that device performance is transport-limited rather than absorption-limited. Peak device performance is at about 30 nm and thinner devices are in danger of shorting. Peak power efficiencies are ~0.25% under a light bulb operating at 80-100 mW/cm^2 (see Chapter 4).

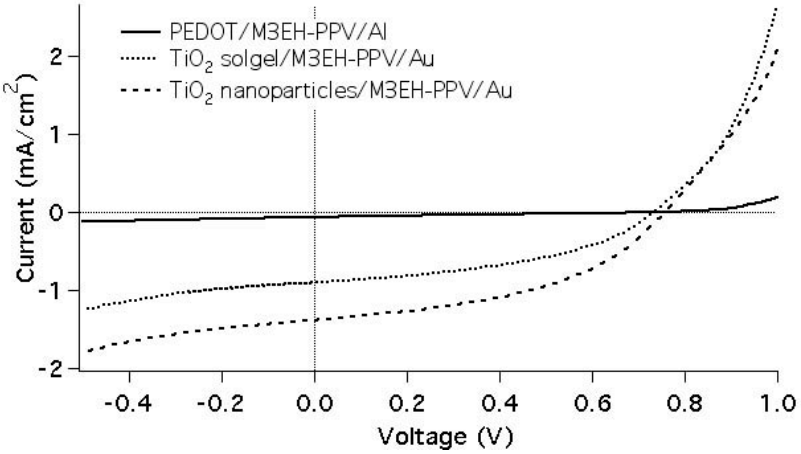

Figure 5.3. M3EH-PPV J-V curves.
All devices are plotted in Quadrant IV for clarity regardless of polarity.
Devices are 30 – 40 nm thick.

Devices on the TiO_2//Au structure (transparent cathode structure; J_{sc} = 0.9 mA/cm^2, V_{oc} = 0.75 V, FF = 42%)) outperform those on the PEDOT//Al structure (transparent anode; J_{sc} = 0.07 mA/cm^2, V_{oc} = 0.96 V, FF = 22%) by an order of magnitude (see Figure 5.3). In TiO_2//Au structures the short-circuit current is correlated with the absorption of the polymer (symbatic response; see Figure 5.4), whereas it is anti-correlated in PEDOT//Al devices (antibatic response) (Arango, Brock et al. 1999; Arango, Johnson et al. 2000), indicating that

the polymer is filtering light before useful charge is generated. The reversed polarity in PEDOT//Al forces the poorly mobile electrons to cross the bulk of the device from the PEDOT/polymer interface. This process is extremely inefficient, and so the bulk of the photocurrent arises from dissociation at the polymer/Al interface; hence, the antibatic response. Only a small portion of the incident light is able to reach this interface, however, resulting in low photocurrents and fill-factors.

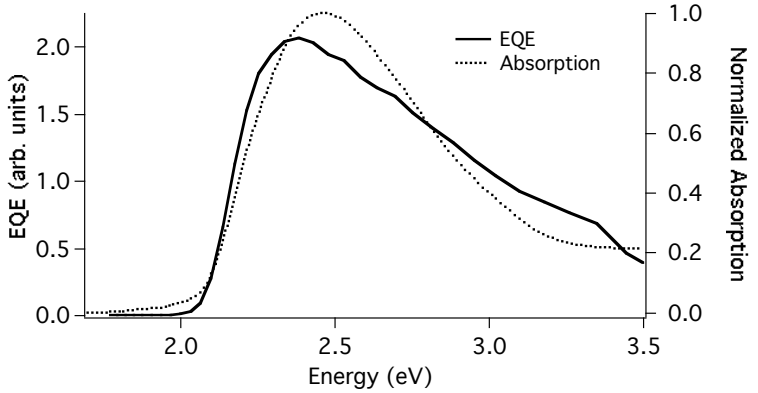

Figure 5.4. Absorption and EQE of a TiO_2/M3EH-PPV/Au device, showing symbatic behavior.

M3EH-PPV devices on TiO_2 nanoparticles, compared to smooth solgel, demonstrate a marked improvement in current, as shown in Figure 5.3. This is due to enhanced surface roughness of the TiO_2, increasing the interfacial area for charge separation, as seen in Figure 5.5. The FF of these devices is also enhanced, from ~ 35% in solgel devices, to up to 56% on nanoparticle devices. This could be due to better charge transport due to the partial penetration of the nanoparticle layer, although a previous study reports FF values of 59% for M3EH-PPV on solgel (Arango, Johnson et al. 2000). Although all M3EH-PPV devices on

TiO_2 show improvement with aging and annealing, this is more pronounced for those devices on TiO_2 nanoparticles. This is attributed to enhanced contact between the TiO_2 and the polymer (Fan, McQuillin et al. 2001) – an effect more pronounced for the rough nanoparticle surface layer.

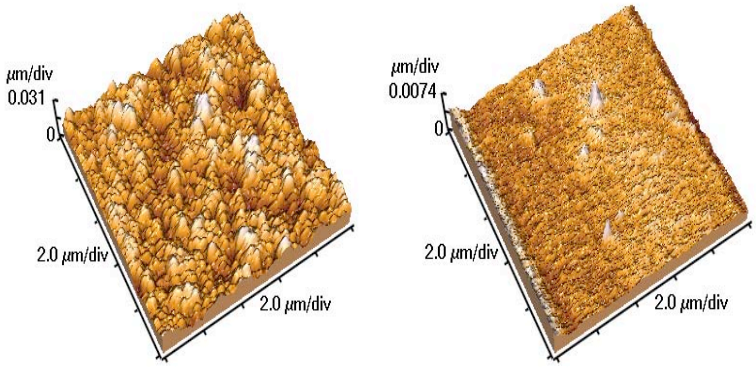

Figure 5.5. AFM images of TiO_2 nanoparticle films (left) and TiO_2 solgel films (right). The solgel film is smooth in comparison to the nanoparticle film; RMS roughness is 2 nm for the solgel film, versus 100 nm for the nanoparticle film (Breeze, Schlesinger et al. 2001).

M3EH-PPV blended with TiO_2 nanoparticles performed poorly. The film quality of these devices was poor due to high amounts of aggregation from addition of the nanoparticles. Charge transfer apparently failed to occur between the polymer and the nanoparticles due to a lack of electrical contact between the two components.

5.4. Steady-state spectroscopy

M3EH-PPV is observed to be slightly less emissive than MEH-PPV, indicating the presence of efficient non-radiative decay in M3EH-PPV as opposed to MEH-PPV. This is in contrast to previous studies (Pfeiffer and Hoerhold 1999), indicative of morphological differences due to film processing conditions. Efficient non-radiative decay could be a result

of more efficient interchain interactions due to more ordered chain stacking, as expected from the high glass transition temperature. Side-chain substitution in M3EH-PPV is more symmetric than that in MEH-PPV, which has been shown to lead to a reduction in coiling of the polymer chains (Kemerink, van Duren et al. 2005), and the side chains of M3EH-PPV are much shorter than those in MEH-PPV, both of which would act to increase the crystallinity of the polymer film. The steady-state PL spectrum of M3EH-PPV resembles that of MEH-PPV, with clear vibronic structure, indicating that the primary emissive species is the same as in MEH-PPV; namely, the singlet single-chain exciton.

Steady-state absorption and photoluminescence profiles for M3EH-PPV in dilute solution in chlorobenzene and thin film are given in Figure 5.6. Absorption peaks at 500 nm indicating a $\pi \rightarrow \pi^*$ transition near 500 nm; the onset of absorption indicates a band gap of about 2.0 eV. These spectra closely resemble those of MEH-PPV, with some insignificant variability that could be due to film quality, indicating that the photophysics in the two polymers is similar.

The photoluminescence spectrum is shifted towards the red relative to absorption; the actual Stokes' shift has been shown to be small (Pauck, Bassler et al. 1996), and the bulk of the apparent shift is due to rapid migration of excitations to longer, low-energy chain segments. The steady-state PL thus represents emission from the lowest-energy chromophores. This shift is more pronounced in film versus solution because lower energy states are more accessible in film due to the high degree of molecular interactions.

The absorption spectra of film is broadened relative to that of solution, indicating that a broad range of conjugation segments are accessible to excitations in film due to kinks, chain packing, and interchain interactions.

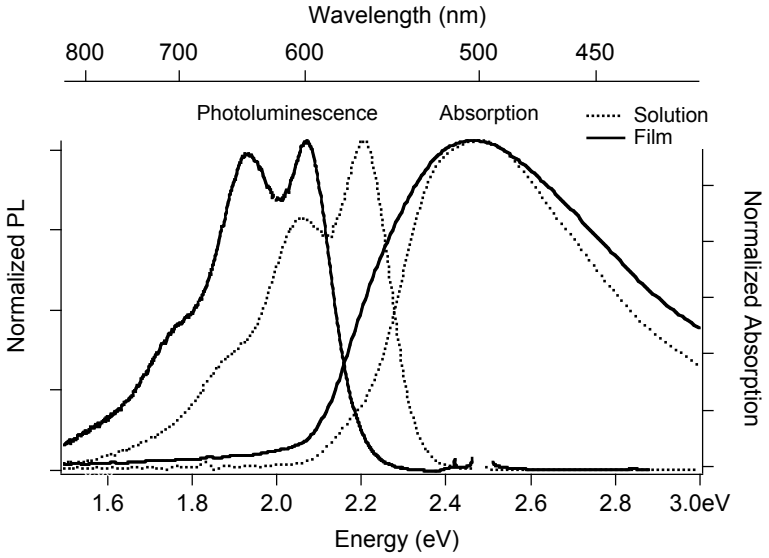

Figure 5.6. Steady-state PL and absorption of M3EH-PPV solution and film. Film is 10 nm thick and solution is extremely dilute (OD < 0.2 at peak absorption). PL is excited at absorption peak of 500 nm; no spectral dependence upon excitation wavelength is observed.

The photoluminescence of both solution and film show clear vibronic structure indicative of single-chain emission. The photoluminescence of film is clearly redshifted relative to solution, such that the 2.2 eV peak in solution corresponds to a peak at 2.07 eV in film; this is expected due to the different environments in solution versus film such that the excited-state species is more broadly delocalized in film (i.e., contained within a 3D- instead of 2D-box). The vibronic structure and intensity in film and solution are similar -- each of the three vibronic peak are spaced by ~0.15 eV – which provides evidence that the emitting species is the same in both environments. The enhancement of the low-energy vibronic relative to the high energy vibronic in film as opposed to solution is due to increased aggregation in film. The data reported in Figure 5.6 are for a 10 nm thick film; however, in thicker films the intensity of the higher-energy vibronic peak is suppressed due to significant self-absorption at that wavelength or increased aggregation.

5.4 Time-resolved fluorescence: Solution

Time-resolved photoluminescence was performed on an extremely dilute (nearly colorless) solution, in order to observe emission from completely isolated, non-interacting polymer chains. Excitation was at 438 nm, which is in the high energy portion of the absorption spectrum. Emission was detected at a variety of wavelengths, from 560 nm (the peak of the solution fluorescence) to 680 nm (the extreme red edge of the fluorescence). The two dominant components were force-fit to global values under the assumption that the same decay mechanisms operate over the entire spectrum, where the third component was allowed to float in order to obtain the best fit.

Results are reported in Table 5.1 and plotted in Figure 5.7. The instrument response function (IRF) is obtained with the sample in place, and detecting at 440 nm, which is slightly off-resonance from the 438 nm emission of the laser. Decay at all wavelengths is dominated by a component of 0.35 ± 0.01 ns, with a percentage yield of 68-84%. This is similar, but slightly longer, than the decay time of 0.27-0.33 ns reported for MEH-PPV in solution by a variety of groups (Samuel, Crystall et al. 1993; Smilowitz, Hays et al. 1993; Samuel, Rumbles et al. 1995; Samuel, Rumbles et al. 1997; de Souza, Rumbles et al. 2001). Since M3EH-PPV is less photoluminescent than MEH-PPV, this suggests the presence of fewer radiative pathways in single chains of M3EH-PPV as compared to MEH-PPV.

The proportion of the steady-state photoluminescence attributable to a particular decay component is represented by the percent yield. Since the % yield is related to the

lifetime, it provides a poor estimate of the relative population of carriers contributing to each of these decay times: $yield(\%) = \frac{A_n \tau_n}{\sum_m A_m \tau_m}$.

The normalized amplitude provides a better measure of the relative population of that state: $A_{n,normalized} = \frac{A_n}{\sum_m A_m}$, where $X^*(t) = \sum_m A_m e^{-t/\tau_m}$.

For comparison, both the % yield and the amplitude are reported in Table 5.1, 5.3, and 5.4. For most samples, amplitudes will only be reported where they are of interest. The dominant component (as determined by the % yield) is in bold for clarity, and this will be the method of reporting for the rest of this work. It is easy to see that the excited state population for components with short decay times (such as the primary component of thin films) is much higher than one would expect from an inspection of the % yield.

Emis.	τ_1 (ns) ± 0.02	A_1	τ_2 (ns) ± 0.01	A_2	τ_3 (ns) ± 0.04	A_3	τ_{ave}	χ^2_ν	DW
560	0.12 (13%)	0.31	**0.35 (84%)**	0.68	0.89 (2%)	0.01	0.33	1.1	1.7
600	0.12 (11%)	0.29	**0.35 (72%)**	0.64	0.73 (16%)	0.07	0.39	1.2	1.9
640	0.12 (10%)	0.27	**0.35 (70%)**	0.64	0.75 (20%)	0.05	0.40	1.0	1.8
680	0.12 (10%)	0.27	**0.35 (68%)**	0.63	0.75 (22%)	0.10	0.41	1.1	1.9

Table 5.1. Decay Times for M3EH-PPV in dilute solution. 'Emis' = Emission (nm). Percent of steady-state photoluminescence yield (__%) is reported in parentheses below each decay component. A_i's represent normalized pre-exponential factors, which are uncorrelated with decay time.

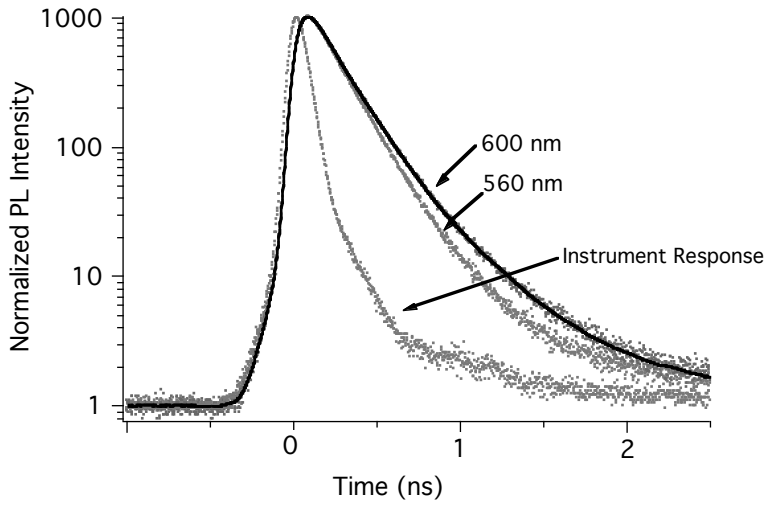

Figure 5.7. The time-decay of M3EH-PPV solution. The fitting function is plotted as a black line on this graph for comparison to the raw data. The goodness of fit for this sample is similar to other samples in this work; only the raw data will be plotted in future figures.

Two other decays are present with roughly equal weight; 0.12 ± 0.01 ns and ~ 0.80 ± 0.04 ns. The failure to adequately fit to less than 3 exponentials is interesting because it indicates the presence of a variety of excited state species even in non-interacting chains. This data refutes the simple model that excitation of a single chain results in a single excited state species – namely, the canonical single-chain exciton. The additional decay times could, for example, represent (a) single-chain excitons at different portions in the chain, such as end versus middle (Charas, Morgado et al. 2003) which have differing degrees of access to decay channels; or (b) single-chain excitons which are partially trapped at defects, and thus decay with longer lifetimes; or (c) self-aggregation caused by coiling of the polymer chains. Due to relatively poor solubility, such self-aggregation may occur, as observed in MEH-PPV in poor solvents (Nguyen, Doan et al. 1999) and MEH-PPV films (Kemerink, van Duren et al. 2005). It is also important to note that these decay times may be non-physical, and assignment of decay times to specific excitonic species should be done with caution.

The decay at 560 nm emission (near the peak emission) is somewhat anomalous. The dominant 0.35 ns component is present in both increased yield (84%) and population density (0.68). The increase in the 0.35 ns component occurs at the expense of the long 0.83 ns component, whose percentage yield drops to 3%, resulting in a reduction in the overall decay rate (Figure 5.7). Decays detected in the high-energy tail of the emission in film also show some anomalous behavior, indicating that excitation of short conjugation lengths results in complex decays due to the presence of lower-energy sites.

5.6 Time-resolved fluorescence: Film

Table 5.2 provides a comparison of decays at 600 nm emission, and Tables 5.3 and 5.4 report decay components for aggregated M3EH-PPV film on quartz. All decays are fit to 3 exponentials, except for 550 nm which is fit to 4 exponentials due to the presence of an additional, fast 0.07 ns component (16%), which I attribute to rapid relaxation from high energy chain segments.

Sample	τ_1 (ns)	A_1	τ_2 (ns)	A_2	τ_3 (ns)	A_3	τ_{ave}
Solution	0.12 ± 0.02 (11%)	0.29	**0.35** ± 0.01 **(72%)**	**0.64**	0.73 ± 0.04 (16%)	0.07	0.39
Thin Film	**0.10** ± 0.03 **(59%)**	**0.83**	0.30 ± 0.1 (34%)	0.15	1.0 ± 0.07 (6%)	<0.01	0.27
Thick Film	**0.20** ± 0.04 **(43%)**	**0.64**	**0.45** ± 0.09 **(53%)**	**0.35**	1.7 ± 1.3 (3%)	<0.01	0.38

Table 5.2. Dominant decay components at 600 nm emission. Percent yield is reported in parentheses below each decay component. A_i's represent normalized pre-exponential factors.

Emis. (nm)	τ_1 (ns)	Error/ A_1	τ_2 (ns)	Error/ A_2	τ_3 (ns)	Error/ A_3	τ_{ave}	χ^2_ν	DW
550	**0.08 (54%)**	± 0.03 0.85	0.30 (31%)	± 0.1 0.13	1.0 (12%)	± 0.3 0.02	0.33	1.2	1.7
600	**0.10 (59%)**	± 0.03 0.83	0.30 (34%)	± 0.1 0.15	1.0 (6%)	± 0.07 0.01	0.27	1.2	1.8
650	**0.10 (57%)**	± 0.02 0.83	0.30 (35%)	± 0.07 0.16	1.0 (7%)	± 0.35 0.01	0.30	1.3	1.6
700	**0.10 (48%)**	± 0.04 0.77	0.30 (39%)	± 0.1 0.20	1.0 (11%)	± 0.5 0.02	0.35	1.1	2.0
750	**0.10 (42%)**	± 0.04 0.73	0.30 (40%)	± 0.2 0.24	1.0 (15%)	± 0.5 0.03	0.41	1.2	1.8

Table 5.3. Decay components for thin (10 nm) M3EH-PPV film. Percent yield is reported in parentheses below each decay component. A_i's represent normalized pre-exponential factors. Decay is fit to 4 exponentials; 4th component (~4.5 ns ± 2.3, 1%) not reported.

Emis. (nm)	τ_1 (ns)	Error/ A_1	τ_2 (ns)	Error/ A_2	τ_3 (ns)	Error/ A_3	τ_4 (ns)	Error/ A_4	τ_{ave}	χ^2_ν	DW
550	0.07 (16%)	± 0.09 0.49	**0.28 (55%)**	± 0.1 0.42	0.63 (28%)	± 0.3 0.09	3.1 (2%)	± 1.8 <0.01	0.40	1.1	1.9
600			0.20 (43%)	± 0.04 0.64	**0.45 (53%)**	± 0.09 0.35	1.7 (3%)	± 1.4 <0.01	0.38	1.2	1.6
650			0.20 (46%)	± 0.01 0.67	**0.45 (50%)**	± 0.01 0.33	1.6 (4%)	± 0.1 <0.01	0.38	1.2	1.8
700			0.20 (41%)	± 0.01 0.64	**0.45 (52%)**	± 0.02 0.36	1.5 (6%)	± 0.1 <0.01	0.41	1.2	1.9
750			0.20 (40%)	± 0.02 0.64	**0.45 (51%)**	± 0.06 0.36	1.3 (9%)	± 0.2 <0.01	0.43	1.1	2.0

Table 5.4. Decay components for thick (100 nm) M3EH-PPV film. Percent yield is reported in parentheses below each decay component. A_i's represent normalized pre-exponential factors.

The presence of multiple decay components, as with solution, is indicative that a simple model (excitation of a singlet interchain exciton which decays to give carriers) is insufficient to understand the dynamics of these conjugated polymers; multiple excitonic species are present in both film and solution. In film, chains may be either coiled or stretched (Kemerink, van Duren et al. 2005) adding additional decay parameters.

I tested the data for robustness of decay components. The reported data were taken with a TAC ramp of 200. The data was retaken at a TAC ramp of 100 for the thicker film, which provides twice the resolution. The decay components matched well for both TAC ramps, suggesting that these decay times are robust. The experiment was repeated on a second sample of M3EH-PPV (100 nm thick), with similar results, though the decay was slightly longer at higher emission wavelengths. Such small variations are inevitable with the different film qualities across samples.

Spectral diffusion

Except for emission at 550 nm (which is anomalous), decays become slightly longer as the emission energy decreases; this is termed *spectral diffusion*. Our laser excitation energy (438 nm) falls in the high energy portion of the absorption spectrum of M3EH-PPV, and so will preferentially excite shorter chain segments. Excitons will migrate from the shorter to longer conjugation segments over time, and this energy transfer is often observed as a short component that disappears at longer emission wavelengths or a gradual lengthening of the decay as the emission enegy is lowered. Spectral diffusion is more pronounced in film than solution because (a) kinks and defects result in multiple chromophore lengths on the same chain, (b) interchain interactions allow excitons to explore lower energy levels via interchain transfer. Thus, at long wavelengths, decay tends to be more homogenous because all excitations have relaxed to the longer chain segments.

Lifetimes

Film decays more rapidly than solution, which is expected due to increased access to quenching sites in film (Samuel, Rumbles et al. 1995). Previous results comparing solution and film have showed that the relationship varies by excitation density (Samuel, Rumbles et al. 1997) and excitation wavelength (Samuel, Crystall et al. 1993), suggesting that it is difficult to explicitly compare decay times across the two environments.

The decay of thicker (100 nm) films is dominated by two main components of 0.20 ns (~43%) and 0.45 ns (~50%). These decay times are similar to those previously reported for MEH-PPV (Samuel, Crystall et al. 1993) and steady-state luminescence was measured to be less than half that of MEH-PPV. This indicates the presence of highly efficient non-radiative recombination paths in M3EH-PPV. I estimate the quantum yield and natural lifetime of M3EH-PPV by integrating the relative steady-state photoluminescence of M3EH-PPV and MEH-PPV and using the relative magnitudes as a correction factor for the quantum yield of MEH-PPV films (0.12) (Greenham, Samuel et al. 1995). Taking into account the experimental error in relative steady-state photoluminescence measurements, I estimate a quantum yield of 0.03 - 0.07 and a natural radiative lifetime of 5.4 – 12.7 ns.

We attribute both decays to single-chain exciton decay, since excimer emission would be lower efficiency and characterized by a longer decay. The long τ_3 component may be due to excimer emission; a previous study has attributed a similar 1.5 – 3.0 ns decay to excimer emission in MEH-PPV (Whitelegg, Buckley et al. 2001). Inspection of the amplitudes indicates that the 0.20 ns species has a higher population, even though both species contribute about equally to the photoluminescence. The 0.45 ns component is

particularly stubborn – it is poorly quenched in most heterojunctions, including those with PCBM.

The decay of very thin (10 nm) films is faster than that of thick films and is dominated by a fast 0.10 ns component (~55%), and a longer 0.30 ns decay (~35%). Both are attributed to single-chain species. The short 0.10 ns component is present with increased yield at low emission energy (probing energetically relaxed excitons in long conjugation segments), whereas the yield of the 0.30 ns component decreases at these energies; thus, the 0.10 ns is associated with short chain segments and the 0.30 ns component is associated with longer chain segments. Differences between thick and thin films are discussed in detail in section 5.7.

5.7 Morphological effects

There are some significant differences in the spectroscopic features of M3EH-PPV of varying thicknesses, presumably due to different film morphologies in the two samples. The relationship to film thickness may be spurious as film thickness correlates to different spin-casting speeds and viscosities. Thin films are spin-cast at ~4000 rpm from ~0.5% solution concentration by weight, whereas thick films are spin-cast at ~2000 rpm from ~1% solution concentration by weight. The polymer chains are loosely aggregated at the solution concentrations used for spin-casting (0.7 – 1% polymer by weight) and so high spin-speeds may result in extended chain conformation (Shi, Liu et al. 2000), and high evaporation rates associated with high spin speeds may result in less ordered films (Li, Shrotriya et al. 2005).

Schwartz recently published a detailed review of spectroscopic evidence for interchain species and aggregation in MEH-PPV (Schwartz 2003) for the interested reader.

I compare the time decay of three environments (solution, thin and thick films) in Table 5.2, which reports the dominant decays at 600 nm. Figure 5.8 shows the same decays plotted on a time scale. Thin, quickly-spun films decay much more rapidly than thick, slowly spun films, as would be expected from enhanced access to quenching sites via increased interchain interactions due to enhanced aggregation. The amplitude of the 0.10 ns component in thin films is quite high (0.83), indicating the presence of particularly efficient deactivation pathways in this sample, as would be expected if the thin, quickly spun film were highly aggregated. Thin, quickly spun M3EH-PPV films also show stronger spectral diffusion than thick film, which could indicate enhanced access to a variety of conjugated segments in the thinner sample, as would be expected from a highly aggregated film.

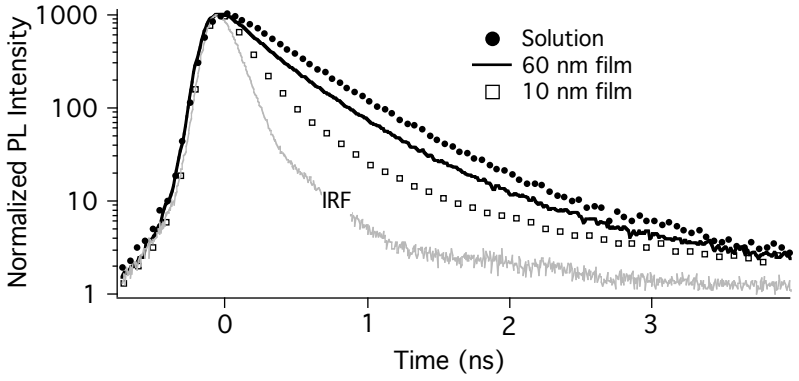

Figure 5.8. Time-decay of M3EH-PPV solution and film of varying thickness, obtained by varying the spin speed (1000 vs 4000 rpm) and solution concentration (1% vs 0.5% by weight). Emission is detected at 650 nm.

The hypothesis that thin, quickly spun films are more aggregated is not borne out, however, by inspection of the steady-state spectroscopic data. (Figure 5.9, below). There is

indeed a slight redshift in the absorption spectra for thinner films, as would be expected by an aggregated sample with greater electronic delocalization, but this effect disappears when the non-normalized spectra are compared. The *photoluminescence* of the thin, quickly spun film, however, is clearly *blueshifted* relative to the thick films, suggesting reduced aggregation and the presence of a more localized excited state species, such as a polaron. Furthermore, the enhanced 1.9 eV (650 nm) vibronic peak in thicker, slowly spun films has been associated with excimer emission (Shi, Liu et al. 2000), and the enhancement of the low-energy vibronic has been observed with greater aggregated films (Nguyen, Doan et al. 1999; Schwartz 2003; Kemerink, van Duren et al. 2005). That said, the spectral shift could be due in part to self-absorption effects, and the bulk of the photoluminescence appears to be due to single-chain excitons for both films (because it is marked by clear vibronic structure), though it could be shifted due to as much as 20% emission from aggregates (Nguyen, Martini et al. 2000). The vibronic structure in the PL spectrum is not consistent across samples, indicating variable coupling between the ground and excited states (Huang-Rhys parameter). It is thus difficult to base firm conclusions upon differential vibronic heights.

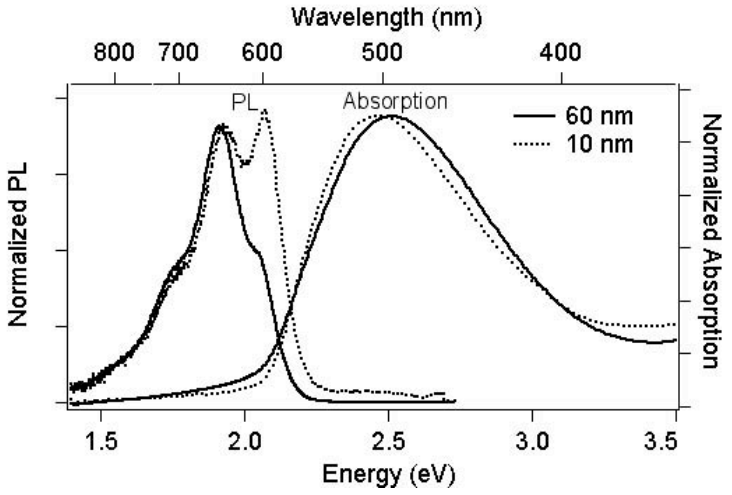

Figure 5.9. PL and absorption spectra of thick (60 nm) films and thin (10 nm) films.

It is possible that the faster decay of thin, quickly spun films, therefore, is related to *decreased* aggregation in those films, as I will now explain. Previous work has suggested that faster spin-speeds resulted in *decreased* aggregation in MEH-PPV (Shi, Liu et al. 2000) – at higher speeds the centrifugal force pulls apart loosely aggregated chains, and the faster evaporation rate for thinner films does not allow the chains to relax into more favorable closely-packed configurations. The authors of this study also observe a slight redshift of the absorption spectra in thin, quickly spun films (in contrast to a blueshift of the PL), which they interpret as due to an increased chain extension in those films due to the faster spin speed.

If this is the case in the present study, the short 0.10 ns time-decay of thin, quickly spun films could represent fast decay of single-chain excitons. In thicker films with enhanced aggregation, interchain interactions could result in long-lived excimer states (which cause a redshift of the steady state PL). Those long-lived excimer states could either decay with a time constant of 0.45ns, which is short for an interchain species. More likely, long-lived excimers could thermally reactivate the single-chain excitons (back-transfer), as in the work of Collison and Rothberg (Jakubiak, Collison et al. 1999; Collison, Rothberg et al. 2001; Collison, Treemaneekarn et al. 2001) who found longer lifetimes with increased aggregation due to poor solvent quality in MEH-PPV. This delayed luminescence could increase the lifetime and yield for single-chain excitons to 0.45 ns (50%) in aggregated (thicker) films.

Further support for this hypothesis comes from results on CN-ether-PPV (see Chapter 7 for structure and properties), which is dominated by interchain excitation and emission. In CN-ether-PPV films I have the advantage of knowing which components are due to single-chain excitations (short decay) versus interchain excitations (long decay). The same behavior

was observed in CN-ether-PPV as in M3EH-PPV: decay times were shorter for thinner versus thicker films due to a shortening of all decay components as shown in Figure 5.10.

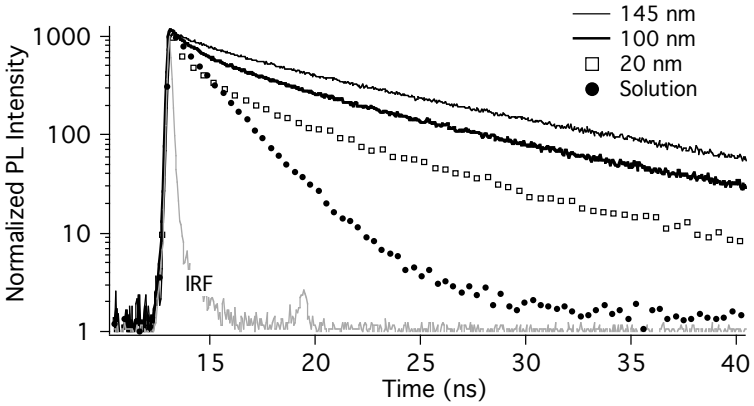

Figure 5.10. Time-decay of CN-ether-PPV film of varying thicknesses, obtained by varying the spin-speed (1000 vs 4000 rpm). Emission is detected at 600 nm.

Analysis of the weights (A) of each component in CN-ether-PPV reveals that the long *interchain* component is present at increased weight in *thick* films (A = 0.34) versus thin films (A = 0.13), whereas the short *single-chain* component is present at increased weight in *thin* films (A = 0.58) versus thick films (A = 0.30). This seems to suggest that the thicker films are more aggregated, resulting in greater interchain interactions, supporting my hypothesis.

This hypothesis that thicker films are more aggregated is further supported by the fact that spectroscopy of the thin films is similar to that in blends of M3EH-PPV:TiO_2, which I believe to be poorly aggregated. My reasoning is as follows. There was no evidence of charge transfer between M3EH-PPV and TiO_2 in these blends, as device performance was not enhanced by addition of nanoparticles. Relative steady-state photoluminescence measurements revealed a 30X photoluminescence enhancement in 1:4 M3EH-PPV:TiO_2 blends – well outside the 20% margin of error of these measurements. This suggests that

interchain interactions are disrupted by the addition of the nanoparticles, reducing a pathway for non-radiative decay and enhancing the photoluminescence. Similar behavior is observed in P3HT on TiO_2 nanoparticle layers in Chapter 7. The steady-state spectrum of TiO_2 blends (~ 100 nm thick) show no spectral shifts, and the vibronic peak heights are similar to 10 nm thin films of M3EH-PPV. As the proportion of TiO_2 in the blend is increased from 0% to 80%, both the primary and secondary decay components decrease, until the decay is dominated by a short component (~0.10 ns) and a medium component (~0.30 ns), as in the thinnest M3EH-PPV film. The yield for the short component is drastically higher in the TiO_2 blends (79%) than the M3EH-PPV films (59%), however, making it difficult to draw firm conclusions from this data.

A kinetic scheme illustrating the hypothesis that aggregated films result in a lengthening of the time-decay is presented in Figure 5.11 below. A* is the single chain species and B* represents the interchain species and heavy lines indicate efficient pathways. Enhanced interchain interactions in film result in a shorter lifetime compared to solution due to the addition of k_{xB} and k_{AB} as de-excitation pathways. Using measurements of the quantum yield from MEH-PPV solution (Collison 1996), we estimate k_r for A* to be 9.4 $10^8 s^{-1}$ and k_{nr} to be 19.2 $10^8 s^{-1}$, both slightly lower than those in MEH-PPV due to the slightly longer lifetime. In film, the non-radiative decay of B* results in re-activation of A* resulting in a delayed luminescence of A*, and thus a longer lifetime in more strongly aggregated films. The strong intermixing of excited state species, and inability to resolve different time components for single-chain and interchain species in films, has made it impossible to make reasonabley accurate calculations for B*, even with detailed temperature-dependent spectroscopic results (Collison 1996).

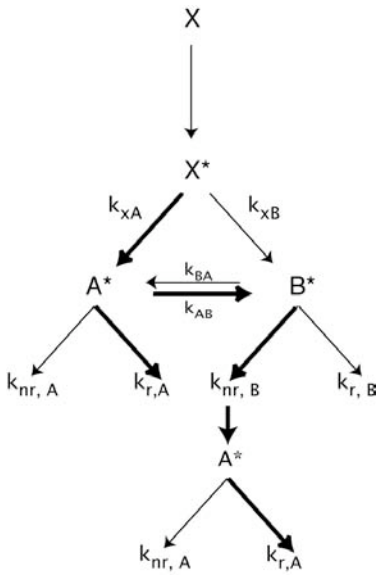

Figure 5.11. Decay kinetics for M3EH-PPV films. A* represents the single-chain species and B* the interchain species. Efficient pathways are indicated by heavy lines.

5.8 TiO_2 nanoparticles and solgel

Device efficiencies are improved when M3EH-PPV is deposited on TiO_2 nanoparticle films, due to enhanced surface roughness, suggesting increased charge transfer from M3EH-PPV to TiO_2 nanoparticles relative to solgel. Measuring changes in the photoluminescence (steady-state or time-resolved) poses a particular challenge with these films, however, since the signal from the polymer film (10 – 20 nm) is likely to overwhelm the signal from the small interfacial area (~ 5 nm). In addition, the different reflectivity of the solgel versus nanoparticle film will introduce interference effects which will affect steady-state measurements.

To reduce the signal from the bulk film, very thin (10 nm) polymer films were used. Films were all spin-cast at the same speed from the same solution to minimize sample-to-sample variations. However, the relative PL is unquenched within the 20% error of the

measurements, as in Figure 5.12, although there are some vibronic shifts. The signal of TiO_2 alone is several orders of magnitude lower than M3EH-PPV and is unlikely to affect these measurements.

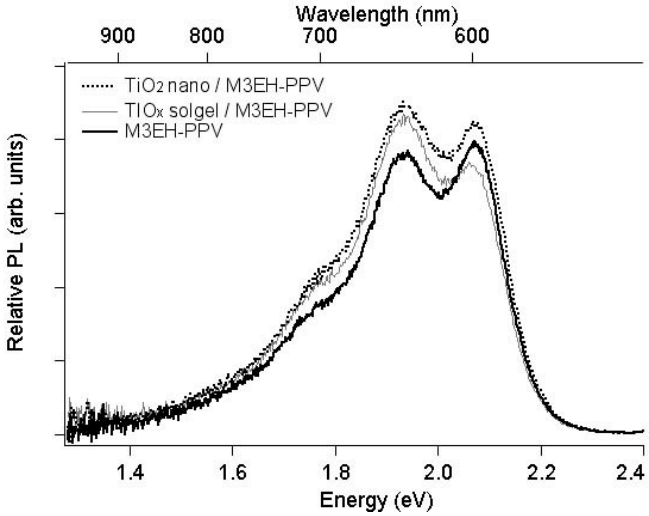

Figure 5.12. Relative SSPL of TiO_2/M3EH-PPV films. All films are ~10 nm thick, and spin-cast from the same solution at the same speed. Excitation is at 500 nm.

Results of time-resolved analyses are reported below in Figure 5.13 and Table 5.5. Decays do not appear to be quenched by inspection of the time decay (Figure 5.13), although when decays were probed on working photovoltaic devices, those which had higher photovoltaic currents showed slightly faster decays for M3EH-PPV deposited on the TiO_2 nanoparticle portions of the substrate than for that part of the film deposited on glass only (Figure 5.13, inset). Thus, quenching is not observable except in the very best quenched cases, due to strong emission from the bulk.

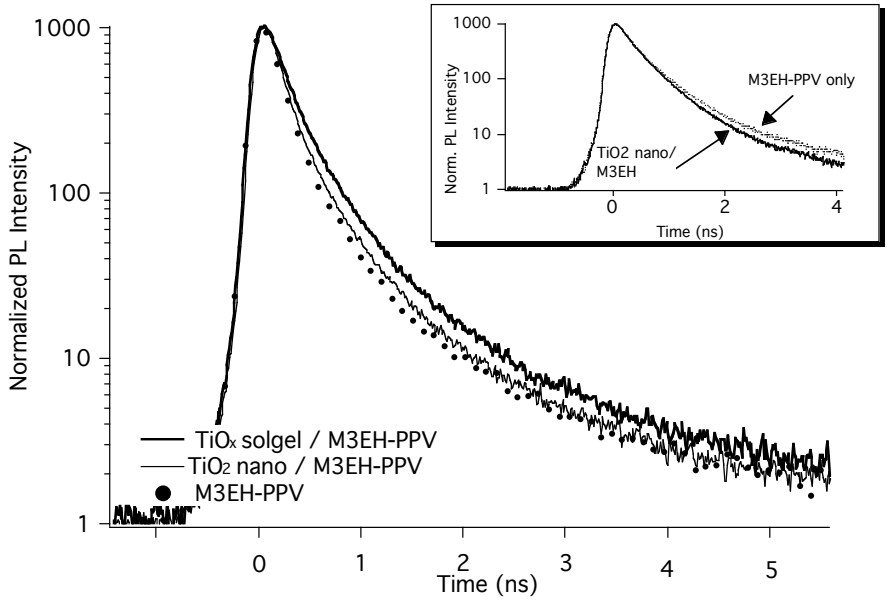

Figure 5.13. Time-decay of M3EH-PPV on TiO_2 solgel and nanoparticles. Emission is detected at 600 nm. Intensity is normalized to 1000 counts. Inset shows time-decay of a working photovoltaic device measured (a) over glass to probe the decay of M3EH-PPV alone, and (b) over TiO_2 nanoparticles to probe the charge-transferred state.

Sample	τ_1 (ns)	τ_2 (ns)	τ_3 (ns)	τ_{ave}
M3EH-PPV (10nm)	**0.10** ± 0.03 **(59%)**	0.30 ± 0.01 (34%)	1.0 ± 0.4 (6%)	0.27
TiOx solgel alone	0.14 ± 0.06 (17%)	**0.65** ± 0.15 **(41%)**	**3.3** ± 0.54 **(42%)**	1.7
TiOx solgel/M3EH	**0.12** ± 0.03 **(42%)**	**0.32** ± 0.10 **(44%)**	0.93 ± 1.2 (9%)	0.35
TiO2 nano/M3EH	**0.10** ± 0.02 **(71%)**	0.36 ± 0.10 (26%)	1.8 ± 0.93 (3%)	0.22

Table 5.5. Decay parameters of M3EH-PPV on TiO_2 solgel and nanoparticles. Emission is detected at 600 nm, except for TiO_x solgel, which is detected at 560 nm.

The decay components for M3EH-PPV on TiO_2 nanoparticles (Table 5.5) do appear slightly faster than those on M3EH-PPV, due to a large percentage of the fast 0.10 ns component (71%). This decay is strikingly similar to that of blends of M3EH-PPV with TiO_2 nanoparticles in which there was no charge transfer, however, suggesting that differences in decay are due to morphological changes related to the rough nanoparticle surface, such as disruption of the pi-pi stacking.

5.9 Conclusions

In conclusion, I performed steady-state and time-resolved photoluminescence, as well as device characterization, using the conjugated polymer M3EH-PPV. Devices on TiO_2//Au structure have short circuit currents of about 0.9 mA/cm^2, whereas those on the PEDOT//Al structure have currents of about 0.07 mA/cm^2 – this electron-dominated device suffers from the poor electron mobility of the polymer. Devices on rough TiO_2 nanoparticle surfaces show improvement over those on smooth solgel, due to enhanced surface roughness.

Devices using M3EH-PPV outperform those on MEH-PPV by an order of magnitude due to enhanced mobility and increased crystalline order. The enhanced crystallinity reduces the luminescence efficiency slightly with respect to MEH-PPV, resulting in a long radiative lifetime. The absorption spectrum in film is broad, indicating a range of conjugation lengths, and the apparent Stokes shift is due to migration of excitons to the lower-energy long conjugation segments.

The steady-state photoluminescence shows clear evidence of emission from a single-chain species; the vibronic structure is clear, and the emission from film is only moderately shifted from that of the solution. I observe similar steady-state photophysics, despite enhanced device performance, in M3EH-PPV in comparison to MEH-PPV. Thus, the primary emissive species (the single-chain exciton) may not play a major role in photoconduction. The enhanced crystallinity in M3EH-PPV appears to promote formation of non-emissive inter-chain species, which may enhance device performance without significantly altering the photophysics.

The time-resolved data supports the conclusion that the primary observed species is single-chain, as all time decay components are short and on the same order of magnitude.

There is no decay or emission peak characteristic of an interchain species, although there is evidence that interchain species affect the decay by providing additional non-radiative pathways and thermally exciting the single-chain exciton. At 600 nm emission, solution response is dominated by a time component of 0.35 ns (the isolated single-chain exciton). Thin films are dominated by a component of 0.10 ns, and thick films by 0.20 ns and 0.45 ns.

Investigations of thick versus thin films, however, indicate some morphological differences that are difficult to resolve with the current data.. Thick films could be more aggregated due to slow evaporation processes and slower spin-casting speeds, which allow chains to seek energetically relaxed configurations, or they could be less aggregated due to increased distance from the glass substrate, which may have an ordering effect. If thick films are more aggregated, then the long decay in these films could be explained by formation of long-lived excimers, which may decay, or thermally re-excite single-chain excitons resulting in delayed luminescence. This is not a common interpretation, but it is supported by the decay of CN-ether-PPV, in which the interchain decay component is present in increased weight in thick films vs. thin films, suggesting that thick films are more aggregated. It is also supported by the similarity of the time-decay of thin films and that of (probably) poorly aggregated M3EH-PPV:TiO_2 blends. Although I am not able to come to a firm conclusion about the reason for the difference in the time-decay of thin and thick films of M3EH-PPV, I can conclude that morphology can have a significant effect upon the excited state lifetime, as much or more so than the effect of charge-transfer.

I did not observe significant quenching in the steady-state or time-resolved data for M3EH-PPV on TiO_2 nanoparticles and solgel, despite known charge transfer to these

materials. This is because the luminescence from the bulk overshadows the quenching at the narrow interface in these layered films.

Decay dynamics in all environments were complex, represented by 3-4 exponentials. This represents a variety of single-chain excitations, such as those at the middle or end of a chain or trapped at a defect, as well as delayed luminescence from re-excitation of the single-chain exciton by interchain species.

5.10 References

Arango, A. C., P. J. Brock, et al. (1999). "Charge transfer in photovoltaics consisting of interpenetrating networks of conjugated polymer and TiO_2 nanoparticles." Appl. Phys. Lett. **74**(12): 1698.

Arango, A. C., L. R. Johnson, et al. (2000). "Efficient titanium oxide / conjugated polymer photovoltaics for solar energy conversion." Adv. Mater. **12**(22): 1689.

Breeze, A. J., Z. Schlesinger, et al. (2001). "Charge transport in TiO_2/MEH-PPV polymer photovoltaics." Phys. Rev. B **64**(12): 125205.

Breeze, A. J., Z. Schlesinger, et al. (2004). "Improving power efficiencies in polymer-polymer blend photovoltaics." Sol. Energy Mater. Sol. Cells **83**: 263.

Charas, A., J. Morgado, et al. (2003). "Steady-state and time-resolved photoluminescence properties of alternating polyfluorene copolymers." Synth. Met. **135-136**: 387.

Collison, C. J. (1996). Photoluminescence studies of excited states in poly(para-phenylene-vinylene) derivatives. Ph.D. Thesis, Imperial College of Science Technology and Medicine, University of London.

Collison, C. J., L. J. Rothberg, et al. (2001). "Conformational effects on the photophysics of conjugated polymers: A two-species model for MEH-PPV spectroscopy and dynamics." Macromolecules **34**: 2346.

Collison, C. J., V. Treemaneekarn, et al. (2001). "Aggregation effects on the structure and optical properties of a model PPV oligomer." Synth. Met. **119**: 515.

Conwell, E. M. (1997). Intramolecular excitons and intermolecular polaron pairs as primary photoexcitations in conjugated polymers. Primary excitations in conjugated

polymers: Molecular exciton versus semiconductor band model. N. S. Sariciftci. River Edge, NJ, World Scientific Publishing Company.

de Souza, M. M., G. Rumbles, et al. (2001). "Cyano-substituted model compounds and conjugated polymers of PPV." Synth. Met. **119**: 635.

Fan, Q., B. McQuillin, et al. (2001). "A solid state solar cell using sol-gel processed material and a polymer." Chem. Phys. Lett. **347**: 325.

Greenham, N. C., I. D. W. Samuel, et al. (1995). "Measurement of absolute photoluminscence quantum efficiencies in conjugated polymers." Chem. Phys. Lett. **241**: 89.

Hayes, G. R., I. D. W. Samuel, et al. (1995). "Exciton dynamics in electroluminescent polymers studied by femtosecond time-resolved photoluminescence spectroscopy." Phys. Rev. B **52**(16): R11569.

Jakubiak, R., C. J. Collison, et al. (1999). "Aggregation quenching of luminescence in electroluminescent conjugated polymers." J. Phys. Chem. A **103**: 2394.

Jeng, U., C.-H. Hsu, et al. (2005). "Morphology and charge transport in poly(2-methoxy-5-(2'-ethylhexyloxy)-1,4-phenylenevinylene) films." Macromolecules **38**: 6566.

Kemerink, M., J. K. J. van Duren, et al. (2005). "Substitution and preparation effects on the molecular-scale morphology of PPV films." Macromolecules **38**: 7784.

Li, G., V. Shrotriya, et al. (2005). "High-efficiency solution processable polymer photovoltaic cells by self-organization of polymer blends." Nature **4**(10): Advance Online Publication.

Nguyen, M., V. Doan, et al. (1999). "Conjugated polymer aggregates in solution: Control of interchain interactions." J. Chem. Phys. **110**(8): 4068.

Nguyen, T.-Q., I. B. Martini, et al. (2000). "Controlling interchain interactions in conjugated polymers: The effects of chain morphology on exciton-exciton annihilation and aggregation in MEH-PPV films." J. Phys. Chem. **104**: 237.

Pauck, T., H. Bassler, et al. (1996). "A comparative site-selective fluorescence study of ladder-type para-phenylene oligomers and oligo-phenylenevinylenes." Chem. Phys. **210**: 219.

Pfeiffer, S. and H.-H. Hoerhold (1999). "Investigation of poly(arylene viylene)s, 41. Synthesis of soluble dialkoxy-substituted poly(phenylene alkenylidene)s by applying the Horner-reaction for condensation polymerization." Macromol. Chem. Phys. **200**: 1870.

Samuel, I. D. W., B. Crystall, et al. (1993). "The efficiency and time-dependence of luminescence from poly(p-phenylene vinylene) and derivatives." Chem. Phys. Lett. **213**(5-6): 472.

Samuel, I. D. W., G. Rumbles, et al. (1995). "Efficient interchain photoluminescence in a high-electron-affinity conjugated polymer." Phys. Rev. B **52**(16): R11573.

Samuel, I. D. W., G. Rumbles, et al. (1997). "Picosecond time-resolved photoluminescence of PPV derivatives." Synth. Met. **84**(1-3): 497.

Savenije, T. J., J. M. Warman, et al. (1998). "Visible light sensitisation of titanium dioxide using a phenylene vinylene polymer." Chem. Phys. Lett. **287**: 148-153.

Schwartz, B. J. (2003). "Conjugated polymers as molecular materials: How chain conformation and film morphology influence energy transfer and interchain interactions." Annu. Rev. Phys. Chem. **54**: 141.

Shi, Y., J. Liu, et al. (2000). "Device performance and polymer morphology in polymer light emitting diodes: The control of thin film morphology and device quantum efficiency." J. Appl. Phys. **87**(9): 4254.

Smilowitz, L., A. Hays, et al. (1993). "Time-resolved photoluminescence from poly[2-methoxy, 5-(2'-ethylhexyloxy)-p-phenylene-vinylene]: Solutions, gels, films, and blends." J. Chem. Phys. **98**(8): 6504.

Tammer, M. and A. P. Monkman (2002). "Measurement of the Anisotropic Refractive Indices of Spin Cast Thin Poly(2-methoxy-5-(2-ethyl-hexyloxy)-p-phenylenevinylene) (MEH-PPV) Films." Adv. Mater. **14**(3): 210.

Tanase, C., J. Wildeman, et al. (2005). "Optimization of the charge transport in poly(phenylene vinylene) derivatives by processing and chemical modification." J. Appl. Phys. **97**: 123703.

van Breemen, A. J. J. M., P. T. Herwig, et al. (2005). "High-performance solution-processable poly(p-phenylene vinylene)s for air-stable organic field-effect transistors." Adv. Func. Mater. **15**: 872.

Whitelegg, S. A., A. Buckley, et al. (2001). "Time-resolved PL studies of partially conjugated MEH-PPV: Control of excimer emission." Synth. Met. **119**: 575.

Chapter 6

The effects of broken conjugation upon an interchain excited state: CN-ether-PPV versus CN-PPV

6.1 Abstract

I investigate the effect of broken conjugation on the excited state dynamics of excimers in cyano-substituted PPV polymers. I compare previous studies on the well-characterized CN-PPV with CN-ether-PPV, in which the conjugation is disrupted by the insertion of oxygen within the polymer backbone. Despite the broken conjugation, there is a good deal of correspondence between the spectroscopic behavior of the two materials. The single-chain exciton created by photoexcitation in solution is found to be similar in CN-PPV and CN-ether-PPV, despite the break in conjugation. The decay time is twice as long in the ether-substituted version (1.8 ns), indicating that the broken conjugation restricts the exciton within a conjugation segment, reducing its access to internal quenching sites.

Emission in CN-ether-PPV film is due to an interchain excimer, as previously reported for CN-PPV. The excimer absorption and emission in thin film are blueshifted by about 0.2 eV relative to CN-PPV, indicating that the excimer in CN-ether-PPV is less stable than that in CN-PPV. The decay time in CN-ether-PPV is twice as long (14 ns) as that in CN-PPV. The long lifetime indicates a large exciton diffusion length, making these species particularly vulnerable to quenching by other materials. This work has implications for design of conjugated polymers for efficient optoelectronic devices.

6.2 Structure and properties

The future of molecular and polymer electronics rests in some part upon the ability to tune materials for color, band-gap, efficiency, and other characteristics necessary to optimize

their use for a particular application (photovoltaics, transistors, light-emitting diodes, etc.). As such, considerable time has been spent investigating the relationship between molecular structure and the nature of the excited state species in the PPV derivatives which are popularly used in optoelectronics (Samuel, Rumbles et al. 1995; Hayes, Samuel et al. 1997; Rumbles, Samuel et al. 1999; de Souza, Rumbles et al. 2001). Because of the strong inter-molecular interactions in these thin films, inter-chain interactions (such as dimers, excimers, and exciplexes), in addition to the intra-chain exciton, may play an important role in the electronic properties of these materials. Polymers with a high electron-affinity are relatively rare, and a thorough understanding of the excited state carriers in these materials is of particular importance in light-emitting diodes and photovoltaics, which often rely upon D/A blends to achieve high efficiencies. I use time-resolved photoluminescence to investigate the effects of side groups upon the nature of these species in two electron-transporting PPV derivatives.

The conjugated polymer poly(2,5,2',5'-tetrahexyloxy-8,7'-dicyano-di-p-phenylenevinylene), or CN-PPV (see Figure 6.1) has been studied extensively. CN-PPV is a highly luminescent cyano-substituted derivative of PPV which serves as an electron-acceptor and electron transporter, though recent work suggests that bipolar charge transport may occur in this material (Correia and Ramos 2003). The cyano group confers a higher electron-affinity while the oxyalkyl group confers solubility. CN-PPV produces efficient photovoltaic devices when blended with the hole-transporting polymer MEH-PPV (Halls, Walsh et al. 1995; Yu, Gao et al. 1995) or P3HT (Onoda, Tada et al. 1998; Roman, Arias et al. 2003) due to its higher electron affinity.

The addition of CN groups has also been found to increase the quantum yield and the decay lifetime in polymers (de Souza, Rumbles et al. 2001), and the photoexcitations in CN-PPV have been found to consist quite clearly of inter-chain species (ie., excimers, or polaron pairs). The cyano substitution results in a broad, featureless redshifted emission spectrum with a large Stokes' loss (Samuel, Rumbles et al. 1997; Rumbles, Samuel et al. 1999; de Souza, Rumbles et al. 2001), and a long-lived photoexcitation in film of ~5.6 ns which is much longer than that in solution (Samuel, Rumbles et al. 1995; Samuel, Rumbles et al. 1996; de Souza, Rumbles et al. 2001). The long radiative lifetime of 16 ns (Rumbles, Samuel et al. 1999) suggests that the radiative transition in CN-PPV film is not fully allowed, as would be expected of an interchain excitation with low wavefunction overlap and a transition that is disallowed by symmetry. This is in contrast to other conjugated polymers such as MEH-PPV or PPV which show clear vibronic structure in their emission spectrum and slight shifts in the emission spectrum. They are also characterized by short lifetimes (0.3 – 0.5 ns) in both solution and film, suggesting a short radiative lifetime of about 1 ns(Samuel, Crystall et al. 1993; Smilowitz, Hays et al. 1993; Hayes, Samuel et al. 1997; Samuel, Rumbles et al. 1997). It is likely that the primary photoexcitation in both cases (MEH-PPV and CN-PPV) is the hot intra-chain exciton, which can vibrationally relax and then decay directly or migrate to form interchain species (Samuel, Rumbles et al. 1995; Rumbles, Samuel et al. 1999).

The preferential formation of interchain species in CN-PPV is likely due to the relatively short interchain distance of 0.34 nm (Conwell, Perlstein et al. 1996; Conwell 1997), as well as a slipped-chain cofacial/lamellar stacking of the molecules (ie., the cyano group from one chain overlapping the edge of an aromatic ring in a neighboring chain) (Conwell 1997; Chen, Su et al. 2004), resulting in more crystal-like order (Samuel, Rumbles et al.

1997) than in other PPV's. The increased chain coupling in CN-PPV is due to the high electron affinity of this polymer (Conwell, Perlstein et al. 1996) as well as more extended chain conformations as observed in symmetrically substituted PPVs (Kemerink, van Duren et al. 2005). This reduced interchain distance results in a matrix element for emission that is 16-20 times larger for excimers in CN-PPV as opposed to MEH-PPV (Conwell, Perlstein et al. 1996).

Although the mobility of charged carriers (electrons, holes) along a single chains is greater than that between chains (Hoofman, de Haas et al. 1998), the mobility of these interchain *excitonic* species is likely to be high compared to single-chain species (Nguyen, Wu et al. 2000), due to their ability to circumnavigate kinks and defects. This results in an increased exciton diffusion length, as well as a long lifetime due to poor coupling to the ground state. The formation of inter-chain excitations, with a long radiative lifetime (Conwell 1998), may be advantageous to photovoltaic device performance since it increases the chances for decaying via non-radiative means, such as charge transfer at a suitably provided interface. Thus, an understanding of the effects of polymer structure upon these excitations is of interest to the field.

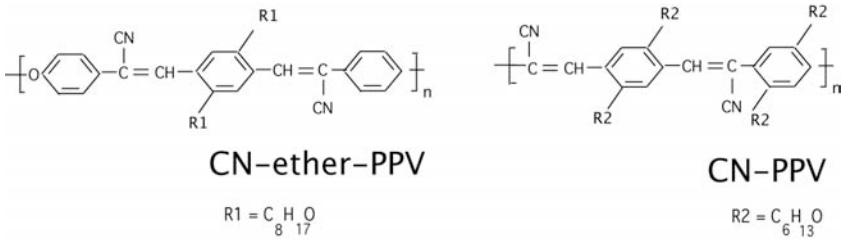

Figure 6.1. Chemical structures of CN-PPV and CN-ether-PPV.

Poly[oxa-1,4-phenylene-1,2-(1-cyano)-ethenylene-2,5-dioctyloxy-1,4-phenylene-1,2-(2-cyano)-ethenylene-1,4-phenylene] or CN-ether-PPV (see Figure 6.1) is a derivative of CN-PPV and is designed to increase solubility and electron affinity relative to CN-PPV. CN-ether-PPV was obtained courtesy of the University of Jena in Germany and synthesized as described elsewhere (Tillmann and Hoerhold 1999). It has HOMO and LUMO levels of 3.5 and 5.9 eV, respectively, a number-average molecular weight (MW) of 28,100 as determined by gel permeation chromatography (GPC) analysis, and a glass transition temperature of 61°C (Tillmann and Hoerhold 1999). When blended or layered with M3EH-PPV (an alternating copolymer of MEH-PPV) it results in photovoltaic devices with short-circuit currents of 3 mA/cm^2 and power conversion efficiencies of ~1.0% under 0.80 mA/cm^2 illumination (Breeze, Schlesinger et al. 2004; Chasteen, Haerter et al. in review). It is similar in structure to PCNEPV, which has been the subject of recent studies (Veenstra, Verhees et al. 2004; Loos, Yang et al. 2005; Offermans, van Hal et al. 2005; Quist, Savenije et al. 2005). The addition of an ether linkage along the backbone in CN-ether-PPV is likely to disrupt the conjugation and affect the chain packing morphology due to increased flexibility in the chain at the sites of conjugation breaks. Broken conjugation has been found to disrupt energy and charge migration in conjugated polymers (Gelinck, Staring et al. 1997; Candeias, Padmanaban et al. 2001; Candeias, Grozema et al. 2003). I have investigated the photophysics of CN-ether-PPV and compared it to past work on CN-PPV in order to explore these effects on the excited state.

I have been unable to fabricate working photovoltaic devices from CN-ether-PPV, presumably due to high leakage current, or dewetting of the polymer from the substrate (Veenstra, Verhees et al. 2004).

6.3 CN-ether-PPV in solution

Steady-state photoluminescence

CN-PPV has been well characterized in previous studies. In solution, the absorption of CN-PPV peaks at 450 nm and the photoluminescence peaks at 555 nm; in film, absorption peaks at 490 nm and photoluminescence at 690 nm (Samuel, Rumbles et al. 1995; Samuel, Rumbles et al. 1996). CN-PPV is highly photoluminescent and is characterized by a long decay time; it has a luminescence quantum yield of 0.35 in film (τ = 5.6 ns) and 0.52 in solution (τ = 0.9 ns) (Samuel, Rumbles et al. 1995; Samuel, Rumbles et al. 1996). See Table 6.1 for a comparison of several PPV's.

CN-ether-PPV is similar to CN-PPV except for the addition of an ether group (a single oxygen) along the conjugation length, which is expected to disrupt the conjugation and affect chain packing. Steady-state absorption and photoluminescence for films and solution of CN-ether-PPV are shown in Figure 6.2.

As in CN-PPV, photoluminescence in solution is narrow with clear vibronic peaks, Despite the broken conjugation, the spectral positions of CN-ether-PPV solution are almost completely consistent with previously reported results on CN-PPV (Samuel, Rumbles et al. 1995) (Figure 6.2 *unfilled arrows*).

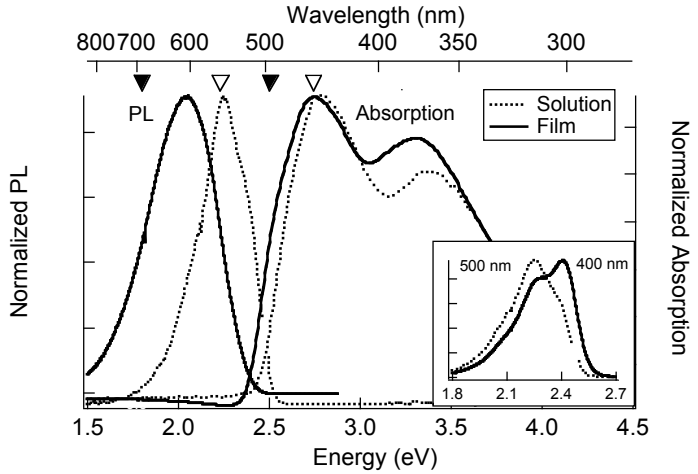

Figure 6.2. Steady-state photoluminescence and absorption for CN-ether-PPV film and solution at 500 nm excitation. Position of spectral peaks in CN-PPV (Samuel, Rumbles et al. 1995) are indicated by filled (film) and unfilled (solution) arrows. For solution, excitation at 500 nm results in a redshifted PL and the first vibronic peak is increased in strength relative to 400 nm (inset).

I note that the PL for solution shows a dependence on excitation wavelength, in violation of Kasha's Rule. When excited at 400 nm it no longer resembles the steady-state spectrum for CN-PPV, due to the enhancement of the vibronic peak at 2.4 eV (Figure 6.2, inset). Excitation at 400 nm will preferentially create intra-chain excitons on short conjugation segments, which may not be able to migrate to longer conjugation segments due to the break in the conjugation. Thus, the 400 nm excitation results in a short effective conjugation length (analogous to an increase in temperature leading to conformational disorder); this leads to an increase in the high-energy vibronic peak due to a corresponding shift in the Huang-Rhys parameter (Yu, Hayashi et al. 1996; Yu and Lin 1997), indicative of a change in the coupling strength between the ground and excited states.

Time-resolved photoluminescence

The time-decay of CN-ether-PPV is plotted in Figure 6.3, and results of multiexponential fits are reported in Tables 6.1 – 6.4. All fits were characterized by reduced chisquare ≤ 1.2 and Durbin-Watson ≥ 1.8.

In Table 6.1, below, I report the decay parameters of CN-ether-PPV at the red edge of the PL emission, which I take to represent the characteristic decay time of the excited state species following energetic relaxation and migration to longer, low energy, conjugation segments. CN-ether-PPV solution was dominated by a decay time of 1.8 ns (87%), which I take to be the characteristic decay time of the isolated intrachain singlet exciton. This is twice as long as the previously measured lifetime for CN-PPV in solution (Samuel, Rumbles et al. 1995), and indicates that single-chain excitons are confined by the break in conjugation, reducing their ability to visit quenching sites. There was evidence for additional decay components, including an 11 ns component (5%) at low emission energy, which I assign to excimer emission due to self-coiling of the polymer chain (Hsu, Fann et al. 2001).

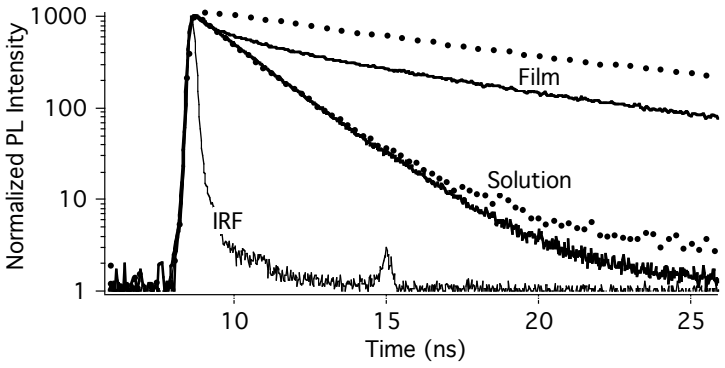

Figure 6.3. Time decay of CN-ether-PPV film and dilute solution. Circles correspond to detection at the low-energy edge (650 nm in solution; 700 nm in film), and thick lines correspond to detection at the high-energy edge (550 nm for both film and solution).

	ϕ	τ_1 (ns)	τ_2 (ns)	τ_3 (ns)	τ_{ave} (ns)	τ_r (ns)	k_r ($10^8 s^{-1}$)	τ_{nr} (ns)	k_{nr} ($10^8 s^{-1}$)
CN-PPV solution[a]	0.52 ±0.05	0.9 ±0.1				1.7 ±0.2	5.8 ±0.05	1.9 ±0.2	5.3 ±0.05
CN-PPV film[a]	0.35 ±0.03	5.6 ±0.2				16 ±2	0.6 ±0.06	8.6 ±0.8	1.2 ±0.1
CN-ether-PPV solution	0.55[b]	1.8 ± 0.02 (87%)	0.7 ± 0.08 (8%)	11.3 ± 0.48 (5%)	1.8	3.2	3.1	4.0	2.5
CN-ether-PPV film	0.45[b]	14 ± 0.12 (69%)	6.2 ± 0.14 (31%)		11.6	23-31	0.3-0.4	18-23	0.4-0.5
PPV film[c]	0.27	0.32				1.2		0.5	
MEH-PPV film[d]	0.26	0.15-0.20				1.1			

Table 6.1. Decay parameters for a variety of PPV's, both measured and extracted from literature values. CN-ether-PPV decays are detected at the low energy edge (650 nm for solution, 700 nm for film). CN-ether-PPV film is 150 nm thick. Values for CN-ether-PPV film are calculated using both the average lifetime and that of the 14 ns component.

References:

[a]CN-PPV solution and film (Samuel, Rumbles et al. 1995; Samuel, Rumbles et al. 1996)
[b]CN-ether-PPV ϕ (Tillmann and Horhold 1999)
[c]PPV film (Greenham, Samuel et al. 1995)
[d]MEH-PPV film (Samuel, Crystall et al. 1993; Hayes, Samuel et al. 1997)

6.4 CN-ether-PPV films

The behavior of CN-PPV in film is qualitatively different from that in solution. The photoluminescence spectra is narrow with clear vibronic peaks in solution, but redshifted, broad and featureless for film. There is no corresponding shift in the absorption spectra, indicating that the spectral shift is due to an excited state species; i.e., an excimer. CN-PPV film has a luminescence quantum yield of 0.35 and a long decay time of 5.6 ns (Samuel,

Rumbles et al. 1995; Samuel, Rumbles et al. 1996). This makes CN-PPV one of the most luminescent conjugated polymers with a lifetime about twenty times longer than that observed in related PPV's, indicating a very small rate of non-radiative decay.

In CN-ether-PPV film, unlike solution, both absorption and photoluminescence curves are substantially blueshifted (to higher energy) by about 0.2 eV relative to CN-PPV film (Figure 6.2 *filled arrows*). This reduced Stokes' loss from solution to film in CN-ether-PPV could be explained by the presence of excimers in CN-ether-PPV that are less stable relative to CN-PPV. Broken conjugation has been found to reduce excimer emission in MEH-PPV (Whitelegg, Buckley et al. 2001), supporting this possibility. The spectral shift may also be due to preferential weighting towards shorter, high energy chain segments due to the disruption of the conjugation. Both mechanisms would result in greater confinement of the excited state species and thus a shift to higher energy.

At 700 nm the decay of CN-ether-PPV film was dominated by a long component of 14.0 ns (69%), which I take to be the interchain exciton, or excimer. I also see a secondary 6.2 ns component (31%), suggesting that, as with CN-PPV, at least two species are present in the excited state (Collison 1996). Our measured PL lifetimes are similar to those measured for a derivative of CN-ether-PPV termed PCNEPV (Offermans, van Hal et al. 2005).

I base the assignment of the 14.0 ns component to an excimer upon arguments from previous studies of temperature-dependence and photoluminescence in film and solution of CN-PPV (Samuel, Rumbles et al. 1995; Samuel, Rumbles et al. 1997; Rumbles, Samuel et al. 1999), the broad featureless redshifted steady-state spectrum, the longer lifetime of film compared to solution, and the fact that the 14 ns component is easily quenched in heterojunctions with both electron- and hole-transporters.

Emission (nm)	τ_1 (ns)	τ_2 (ns)	τ_3 (ns)	τ_{ave}	χ^2_ν	DW
520	0.7 ± 0.23 (4%)	**1.7** ± 0.05 **(93%)**	3.4 ± 0.72 (3%)	1.8	1	1.9
550	0.81 ± 0.14 (7%)	**1.7** ± 0.03 **(92%)**	5.8 ± 0.71 (1%)	1.7	1.1	1.8
600	0.8 ± 0.11 (8%)	**1.8** ± 0.02 **(90%)**	8.6 ± 0.55 (2%)	1.8	1	1.9
650	0.7 ± 0.08 (8%)	**1.8** ± 0.02 **(87%)**	11.3 ± 0.48 (5%)	2.1	1.1	2.0

Table 6.2. Decay components of CN-ether-PPV solution.

Emission (nm)	τ_1 (ns)	τ_2 (ns)	τ_3 (ns)	τ_{ave}	χ^2_ν	DW
550	0.33 ± 0.02 (4%)	3.5 ± 0.10 (27%)	**11.2** ± 0.08 **(69%)**	8.7	1.2	1.8
600	0.30 ± 0.03 (2%)	4.3 ± 0.12 (26%)	**12.2** ± 0.09 **(73%)**	10	1.2	1.8
650		5.0 ± 0.11 (25%)	**12.9** ± 0.11 **(75%)**	10.9	1.1	1.8
700		6.2 ± 0.14 (31%)	**13.9** ± 0.12 **(69%)**	11.6	1.1	1.9

Table 6.3. Decay components of CN-ether-PPV film (150 nm).

As discussed in Chapter 5, decay times decrease for thinner samples of CN-ether-PPV, due to a decreased amplitude of the long interchain component and an increased amplitude of the short single-chain component. I interpret this to mean that thicker samples are more aggregated due to slower evaporation rate and spin-speed.

The percent yield of the long inter-chain component increases with decreasing emission energy, similar to results from Rumbles et al. (Rumbles, Samuel et al. 1999) on CN-PPV, so that the decay at 700 nm is taken to be representative of the stable emission from the inter-chain component (14.0 ns at 69% yield). Unlike CN-PPV, there is still a sizeable intra-

chain component at low energies (4 ns at 20% yield), suggesting that the restriction of the exciton between the ether-groups in CN-ether-PPV reduces the efficiency of inter-chain interactions in favor of intra-chain interactions

Decay times for CN-ether-PPV increased as emission energy decreased, consistent with diffusion from shorter to longer conjugation segments and the relaxation of hot singlet excitons to form lower energy excimers, and diffusion from longer to shorter chain segments over time. The spectral diffusion is more pronounced than in other polymers I have studied, which could indicate a wide range of conjugation lengths present in CN-ether-PPV, which would be inconsistent with our conclusion that the ether linkage disrupts the conjugation length, resulting in comparatively short conjugation segments. It is more likely that this spectral diffusion indicates relaxation to a variety of low-energy interchain excimer states.

The effect of broken conjugation

The 14.0 ns excimer decay is more than double the 5.6 ns lifetime of CN-PPV (Samuel, Rumbles et al. 1995)**,** and the secondary lifetime is similarly twice as long as that measured in CN-PPV (Collison 1996), suggesting that the breakage in the conjugation along the backbone imposed by the ether linkage significantly affects the nature and dynamics of the excited state. As in films of CN-PPV, I measure high photoluminescence in the steady state and a long excited state lifetime. Based on previous studies (Tillmann and Hoerhold 1999), the quantum yield of CN-ether-PPV in solution nearly matches that of CN-PPV (0.55), but in film CN-ether-PPV is slightly more photoluminescent (0.45 vs 0.35 in CN-PPV) (Samuel, Rumbles et al. 1995). Using $\phi = \frac{\tau}{\tau_r}$ this gives τ_r = 26 ns for CN-ether-PPV using the average lifetime and assuming that the emitting species is formed with unit quantum

efficiency. For the species which decays with a time constant of 14 ns, τ_r = 31 ns – about twice that measured for CN-PPV.

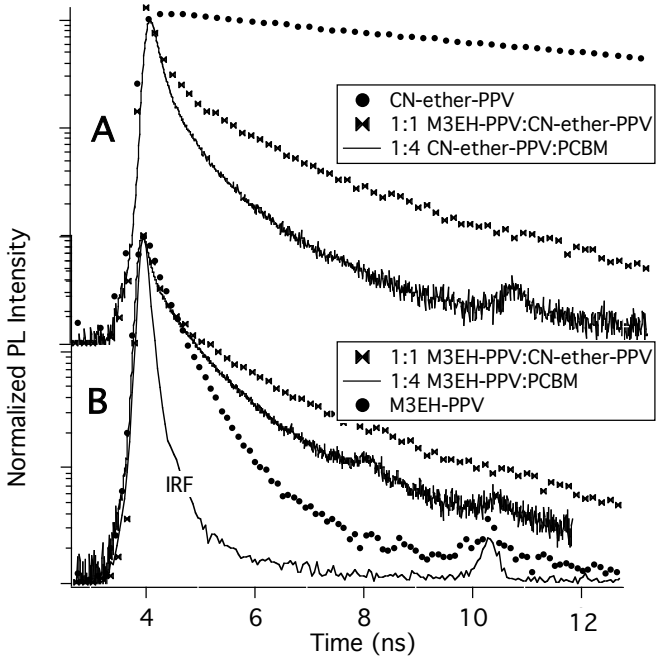

Figure 6.4. Time-decay of heterojunctions of (A) CN-ether-PPV and (B) M3EH-PPV. Emission is detected at 650 nm. CN-ether-PPV is more easily quenched by PCBM and other PPV's than is M3EH-PPV.

Longer time-decay and higher photoluminescence has been previously reported for poorly conjugated PPV (Samuel, Crystall et al. 1993). It is interesting that the same behavior is found in a cyano-substituted PPV, which is dominated by interchain excitonic species. Broken conjugation will not restrict an interchain species within a single conjugation length, as it would for a single-chain species. The radiative lifetime of CN-ether-PPV is one of the longest natural radiative lifetimes ever measured in a photoluminescent polymer and, because it is significantly longer than that of other PPV's, indicates that this radiative transition is not fully allowed, consistent with the presence of an excimer. Thus the photoluminescence from

excitons formed in CN-ether-PPV should be much easier to quench than those in most PPV's. I find this to be true – the steady-state photoluminescence, and the 14.0 ns component, are easily quenched by a variety of external quenchers, including another soluble PPV, P3HT, PCBM, and TiO_2 (SSPL only), whereas the decay components of a copolymer of MEH-PPV (i.e., M3EH-PPV (Pfeiffer and Hoerhold 1999; Breeze, Schlesinger et al. 2004)) are far more robust, as shown in Figure 6.4. Charge transfer from CN-ether-PPV to PCBM is extremely efficient, despite a published HOMO/LUMO offset of only 0.2 eV, that the photoluminescence of CN-ether-PPV is quenched by three orders of magnitude, and emission from PCBM itself is observed (see Section 6.5). Thus, CN-ether-PPV may serve as an efficient provider of photogenerated charges for photovoltaic devices.

Kinetic models

The long radiative lifetime and large quantum yield suggest that both radiative and non-radiative processes are less efficient in CN-ether-PPV than in CN-PPV. Calculation of the radiative rate constants (Table 6.1, and Figure 6.5, below) indicates that this seems to be true. Note that the values in Figure 6.5 assume that the emitting species (the interchain exciton in film) is generated with unit quantum efficiency; if this is not the case, then these rate constants could be up to twice the reported values. Values for CN-ether-PPV are based upon previous measurements of the photoluminescence quantum efficiency (Tillmann and Hoerhold 1999), of unknown accuracy.

Despite differences in detail, the general kinetic scheme developed by Rumbles, Collison, and Samuel (Collison 1996; Rumbles, Samuel et al. 1999) is still valid. In solution, only single-chain (*A**) species are excited. In film, excitation leads to formation of single-

chain and interchain species, with crossing to the interchain species competing efficiently with the radiative and nonradiative decay of the single chain species.

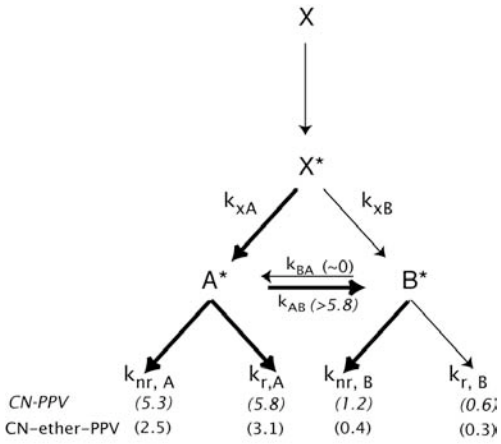

Figure 6.5. Decay kinetic scheme for CN-PPV and CN-ether-PPV. CN-PPV results are from previous authors (Collison 1996; Rumbles, Samuel et al. 1999). *A** represents the single-chain excitation and *B** the interchain excitation. Bold arrows represent efficient deactivation pathways.

In CN-ether-PPV, however, $k_{nr,B}$ is about half that for CN-PPV due to the break in the conjugation, judging from the doubling of the excited state lifetime. A rise-time was observed in the decay of CN-ether-PPV films at short time scales (not shown), indicating that the primary decay component arises from an intermediate state – ie., the single-chain exciton, in agreement with this proposed kinetic scheme.

6.5 CN-ether-PPV:PCBM blends

CN-ether-PPV blended with PCBM did not result in working photovoltaics. The presence of large aggregated structures (see Figure 6.6) resulted in a poor film quality.

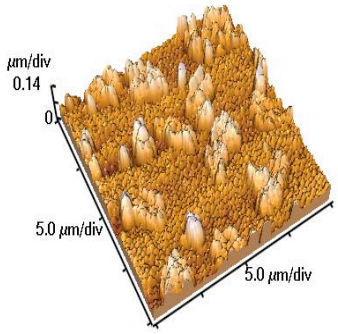

Figure 6.6. AFM image of aggregated structures in CN-ether-PPV:PCBM blends. In addition to tall structures, the lower portions of the film show regular features.

Figure 6.7 shows the relative quenching of the CN-ether-PPV photoluminescence by addition of PCBM. The peak PL is quenched by nearly three orders of magnitude, indicating efficient charge transfer. The published HOMO and LUMO levels of PCBM are only 0.2 eV higher than those estimated for CN-ether-PPV, providing a very low driving force for charge separation in the face of the binding energy of the exciton, estimated to be 0.2 eV in conjugated polymers. This could indicate that either (a) the HOMO/LUMO values for either material are shifted from their published values, and/or (b) the binding energy of the interchain exciton in CN-ether-PPV is very small, which would account for the facile quenching of this species.

Inspection of Figure 6.7, below, shows there is a spectral shift for the quenched PL. This shift is more apparent in Figure 6.8. The PL of this 1:4 blend is severely shifted to lower energy relative to the PL of dilute solution. Since I would not expect emission from CN-ether-PPV in this region (which is far below the bandgap of CN-ether-PPV), I attribute it to weak emission from PCBM aggregates. The shape and position of this spectra matches previous measurements on other fullerenes (Capozzi, Casamassima et al. 1996; Dmitruk,

Dmitruk et al. 2004), including PCBM (van Duren, Yang et al. 2004-a). The presence of this peak is not observed in M3EH-PPV:PCBM or P3HT:PCBM.

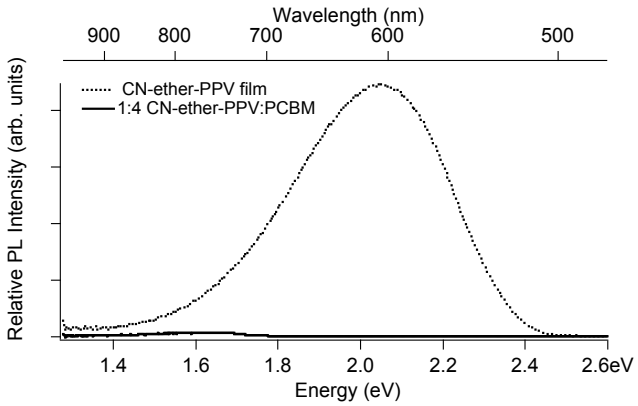

Figure 6.7. PL quenching by addition of PCBM in a 1:4 CN-ether-PPV:PCBM blend. Film is excited at 450 nm (the absorption maximum). The peak PL is quenched by nearly three orders of magnitude at 2.0 eV.

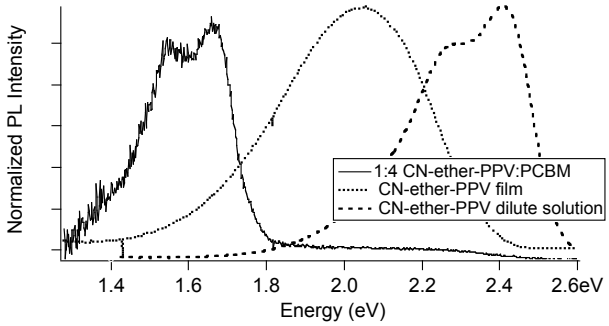

Figure 6.8. Normalized photoluminescence of CN-ether-PPV film, solution, and 1:4 blend with PCBM. Excitation is at 450 nm,

The time decay of CN-ether-PPV:PCBM blends changes dramatically across the spectrum in tandem with the steady-state spectral shift (see Table 6.4). At high energies (550 nm) the decay is dominated by a fast component of 0.01 ns (74%), which may be attributed to ultrafast charge transfer to PCBM that efficiently deactivates the excited state in this region, as indicated by the absence of residual emission in the steady-state. At the onset of the low-

energy SSPL feature at 700 nm, however, the dominant decay switches to an almost monoexponential decay with a time constant of 1.3 ns (97%).

Emission (nm)	τ_1 (ns)	τ_2 (ns)	τ_3 (ns)	τ_{ave}	χ^2_ν	DW
550	**0.01** ± 0.003 **(74%)**	0.11 ± 0.01 (22%)	0.43 ± 0.05 (4%)	0.05	1.4	2
600	**0.02** ± 0.003 **(52%)**	0.15 ± 0.007 (33%)	0.60 ± 0.03 (15%)	0.15	1.3	1.8
650	**0.05** ± 0.004 **(44%)**	0.25 ± 0.01 (35%)	0.97 ± 0.02 (20%)	0.3	1.3	1.8
700	0.02 ± 0.01 (9%)	0.24 ± 0.02 (12%)	**1.3** ± 0.01 **(80%)**	1.1	1.3	1.7
750		0.14 ± 0.03 (3%)	**1.3** ± 0.003 **(97%)**	1.2	2	1.2

Table 6.4. Decay components of 1:4 CN-ether-PPV:PCBM.

6.6 Conclusions

I have investigated the effects of ether linkage on the photophysics and excited state dynamics of a well-characterized conjugated polymer, CN-PPV. CN-PPV in solution is dominated by intrachain singlet excitons, whereas film is dominated by interchain species, such as excimers. The ether substituted version, CN-ether-PPV, shows similar behavior to CN-PPV: Emission in thin film is broad, featureless, and redshifted compared to solution, and decay in film is longer than solution. A very long decay component of 14 ns dominated the decay in film, suggesting a radiative lifetime of 31 ns for that component, one of the longest measured in a photoluminescent polymer. Measured decay components in solution and thin film were at least twice as long as those previously measured for CN-PPV. These results suggest that the broken conjugation in this polymer confines the exciton or excimer,

reducing its ability to visit quenching sites and resulting in a long lifetime and efficient photoluminescence.

Steady-state emission and the dominant 14 ns decay component in CN-ether-PPV are easily and (generally) completely quenched by blending with a variety of electron- and hole-accepting materials. CN-ether-PPV emission is quenched so effectively when blending with PCBM that the weak PCBM emission is visible, allowing us to time-resolve decay of PCBM with a time constant of 1.3 ns. The facile quenching of CN-ether-PPV suggests that the interchain excimers have a low binding energy and are vulnerable to quenching by external agents. Such long-lived states that are easily quenched by charge transfer may be advantageous to devices, such as photovoltaics.

6.7 References

Breeze, A. J., Z. Schlesinger, et al. (2004). "Improving power efficiencies in polymer-polymer blend photovoltaics." Sol. Energy Mater. Sol. Cells **83**: 263.

Candeias, L. P., F. C. Grozema, et al. (2003). "Positive charge carriers on isolated chains of MEH-PPV with broken conjugation: Optical absorption and mobility." J. Phys. Chem. B **107**: 1554.

Candeias, L. P., G. Padmanaban, et al. (2001). "The effect of broken conjugation on the optical absorption spectra of the triplet states of isolated chains of poly(phenylene vinylene)s." Chem. Phys. Lett. **349**: 394.

Capozzi, V., G. Casamassima, et al. (1996). "Optical characterization of fullerite C_{60} thin films." Synth. Met. **77**: 3.

Chasteen, S. V., J. O. Haerter, et al. (in review). "Comparison of blended versus layered structures for PPV-based polymer photovoltaics." J. Appl. Phys.

Chen, S. H., C. H. Su, et al. (2004). "Molecular aggregation and luminescence behavior of bulk poly (2,5,2',5'-tetrahexyloxy-8,7-dicyano-di-p-phenylynevinylene)." J. Phys. Chem. B **108**: 8855.

Collison, C. J. (1996). Photoluminescence studies of excited states in poly(para-phenylene-vinylene) derivatives. Ph.D. Thesis, Imperial College of Science Technology and Medicine, University of London.

Collison, C. J. (1996). Photoluminescence Studies of Excited States in Poly(para-Phenylene-Vinylene) Derivatives. Chemistry. London, England, Imperial College of Science Technology and Medicine, University of London.

Conwell, E. M. (1997). Intramolecular excitons and intermolecular polaron pairs as primary photoexcitations in conjugated polymers. Primary excitations in conjugated polymers: Molecular exciton versus semiconductor band model. N. S. Sariciftci. River Edge, NJ, World Scientific Publishing Company.

Conwell, E. M. (1998). "Mean free time for excimer light emission in conjugated polymers." Phys. Rev. B **57**(22): 14200.

Conwell, E. M., J. Perlstein, et al. (1996). "Interchain photoluminscence in poly(phenylene vinylene) derivatives." Phys. Rev. B **54**(4): R2308.

Correia, H. M. G. and M. M. D. Ramos (2003). "Modeling charge transport properties of cyano-substituted PPV." Materials Science and Engineering C **23**: 773.

de Souza, M. M., G. Rumbles, et al. (2001). "Cyano-substituted model compounds and conjugated polymers of PPV." Synth. Met. **119**: 635.

Dmitruk, I. M., N. L. Dmitruk, et al. (2004). "Optical characterization of fullerene films on flat and patterned semiconductor substrates." Carbon **42**: 1089.

Gelinck, G. H., E. G. J. Staring, et al. (1997). "The effect of broken conjugation and aggregation on photo-induced charge separation on polyphenylenevinylene chains." Synth. Met. **84**: 595.

Greenham, N. C., I. D. W. Samuel, et al. (1995). "Measurement of absolute photoluminscence quantum efficiencies in conjugated polymers." Chem. Phys. Lett. **241**: 89.

Halls, J. J. M., C. A. Walsh, et al. (1995). "Efficient photodiodes from interpenetrating polymer networks." Nature **376**: 498.

Hayes, G. R., I. D. W. Samuel, et al. (1997). "Ultrafast dynamics of photoexcitations in conjugated polymers." Synth. Met. **84**: 889.

Hoofman, R. J. O., M. P. de Haas, et al. (1998). "Highly mobile electrons and holes on isolated chains of the semiconducting polymer poly(phenelyne vinylene)." Nature **392**: 54.

Hsu, J.-H., W. S. Fann, et al. (2001). "Decay dynamics of interchain excited states in luminescent conjugated polymer CN-PPV." Chem. Phys. **269**: 367.

Kemerink, M., J. K. J. van Duren, et al. (2005). "Substitution and preparation effects on the molecular-scale morphology of PPV films." Macromolecules **38**: 7784.

Loos, J., X. Yang, et al. (2005). "Morphology determination of functional poly[2-methoxy-5-(3,7-dimethyloctyloxy)-1,4-phenylenevinylene]/Poly[oxa-1,4-phenylene-1,2-(1-cyanovinylene)-2-methoxy,5-(3,7-dimethyloctyloxy)-1,4-phenylene-1,2-(2-cyanovinylene)-1,4-phenylene] blends as used for all-polymer solar cells." J. Appl. Polym. Sci. **97**: 1001.

Nguyen, T.-Q., J. Wu, et al. (2000). "Control of energy transfer in oriented conjugated polymer-mesoporous silica composites." Science **288**: 652.

Offermans, T., P. A. van Hal, et al. (2005). "Exciplex dynamics in a blend of pi-conjugated polymers with electron donating and accepting properties: MDMO-PPV and PCNEPV." Phys. Rev. B **72**: 045213.

Onoda, M., K. Tada, et al. (1998). "Photoinduced charge transfer of conducting polymer composites." IEICE Trans. Electron **E81-C**(7): 1051.

Pfeiffer, S. and H.-H. Hoerhold (1999). "Investigation of poly(arylene viylene)s, 41. Synthesis of soluble dialkoxy-substituted poly(phenylene alkenylidene)s by applying the Horner-reaction for condensation polymerization." Macromol. Chem. Phys. **200**: 1870.

Quist, P. A. C., T. J. Savenije, et al. (2005). "The effect of annealing on the charge-carrier dynamics in a polymer/polymer bulk heterojunction for photovoltaic applications." Adv. Func. Mater. **15**(3): 469.

Roman, L. S., A. C. Arias, et al. (2003). "Photovoltaic devices based on photo induced charge transfer in polythiophene:CN-PPV blends." Brazilian J. Phys. **33**(2): 376.

Rumbles, G., I. D. W. Samuel, et al. (1999). "Temperature dependent photoluminescence from a cyano-substituted phenylene vinylene polymer." Synth. Met. **101**: 158.

Samuel, I. D. W., B. Crystall, et al. (1993). "The efficiency and time-dependence of luminescence from poly(p-phenylene vinylene) and derivatives." Chem. Phys. Lett. **213**(5-6): 472.

Samuel, I. D. W., B. Crystall, et al. (1993). "Time-resolved luminescence measurements in poly(p-phenylenevinylene)." Synth. Met. **54**(1-3): 281.

Samuel, I. D. W., G. Rumbles, et al. (1995). "Efficient interchain photoluminescence in a high-electron-affinity conjugated polymer." Physical Review B-Condensed Matter **52**(16): R11573-6.

Samuel, I. D. W., G. Rumbles, et al. (1995). "Efficient interchain photoluminescence in a high-electron-affinity conjugated polymer." Phys. Rev. B **52**(16): R11573.

Samuel, I. D. W., G. Rumbles, et al. (1996). "Luminescence efficiency and time dependence in a high electron affinity conjugated polymer." Synth. Met. **76**: 15.

Samuel, I. D. W., G. Rumbles, et al. (1997). "Picosecond time-resolved photoluminescence of PPV derivatives." Synth. Met. **84**(1-3): 497.

Samuel, I. D. W., G. Rumbles, et al. (1997). Luminescence efficiency and time-dependence: Insights into the nature of the emitting species in conjugated polymers. Primary photoexcitations in conjugated polymers: Molecular exciton versus semiconductor band model. N. S. Sariciftci. New Jersey, World Scientific Publishing Company.

Smilowitz, L., A. Hays, et al. (1993). "Time-resolved photoluminescence from poly[2-methoxy, 5-(2'-ethylhexyloxy)-p-phenylene-vinylene]: Solutions, gels, films, and blends." J. Chem. Phys. **98**(8): 6504.

Tillmann, H. and H.-H. Hoerhold (1999). "Synthesis, Optical and Redox Properties of Novel Segmented Cyano-PPV Derivatives." Synth. Met. **101**: 138.

Tillmann, H. and H.-H. Horhold (1999). "Synthesis, Optical and Redox Properties of Novel Segmented Cyano-PPV Derivatives." Synth. Met. **101**: 138-139.

van Duren, J. K. J., X. Yang, et al. (2004-a). "Relating the morphology of poly(p-phenylene vinylene)/Methanofullerene blends to solar-cell performance." Adv. Func. Mater. **14**: 425.

Veenstra, S. C., W. J. H. Verhees, et al. (2004). "Photovoltaic properties of a conjugated polymer blend of MDMO-PPV and PCNEPV." Chem Mater. **16**: 2503.

Whitelegg, S. A., A. Buckley, et al. (2001). "Time-resolved PL studies of partially conjugated MEH-PPV: Control of excimer emission." Synth. Met. **119**: 575.

Yu, G., J. Gao, et al. (1995). "Polymer photovoltaic cells: enhanced efficiencies via a network of internal donor-acceptor heterojunctions." Science **270**: 1789.

Yu, J., M. Hayashi, et al. (1996). "Temperature effect on the electronic spectra of poly(p-phenylenevinylene)." Synth. Met. **82**: 159.

Yu, J. and S. H. Lin (1997). "Theoretical modeling of the electronic spectra of poly(p-phenylene vinylene)." Synth. Met. **85**: 1115.

Chapter 7

Characterization of heterojunctions of a hole-transporting polythiophene: P3HT

7.1 Abstract

We present time-resolved photoluminescence studies in conjunction with device characterization of a variety of heterojunctions with poly-(3-hexylthiophene), or P3HT, as a means to understand how exciton dynamics affect device performance. I find that blends of P3HT with the electron-transporting polymer CN-ether-PPV and with the fullerene derivative PCBM result in ~4-fold and ~15-fold improvements in short-circuit currents, respectively, over neat-film P3HT on TiO_2 solgel. Despite efficient charge-transfer in P3HT:PCBM films, as evidenced by enhanced device performance and quenched steady-state luminescence, I observe only moderate reduction of the excited state lifetime, due to the already efficient non-radiative pathways in P3HT. I observe spectral evidence for a new state that I tentatively assign to an exciplex in blends of P3HT with the electron-transporting polymer CN-ether-PPV. The exciplex state, which confirms the existence of charge-transfer between the two polymers, may account for the enhanced device performance of these blends by acting as a scavenger for excitons that would otherwise decay rapidly via non-radiative pathways. The long-range order of P3HT is disrupted when spin-cast on rough TiO_2 nanoparticles, and this results in a blueshift of the PL spectrum and a new long-lived decay component that I attribute to long-lived single-chain polarons. P3HT on smooth TiO_2 solgel films shows little or no quenching of the excited state, despite known charge transfer from P3HT to TiO_2.

7.2 Structure and properties

Poly-3-hexylthiophene, or P3HT, has been considered a promising candidate for high-efficiency photovoltaics because of its semi-crystalline nature and tendency to form lamellar structures. This ordered morphology enhances charge transport and mobility, especially in regio-random versions of the polymer (Jiang, Osterbacka et al. 2003; Song, Kim et al. 2003), and P3HT has field effect hole mobilities up to 0.1 cm^2/Vs, the highest yet observed (Sirringhaus, Tessler et al. 1998). Due to the efficient stacking, it is expected that the primary photoexcitations in P3HT are bound polaron pairs (Conwell 1997), and the nonemissive nature of the interchain interactions in P3HT result in a low quantum yield for fluorescence (Xu and Holdcroft 1993; Rumbles, Samuel et al. 1996). The drawback of P3HT is high variability of the polymer purity and molecular weight, depending upon synthesis and purification techniques.

P3HT on mesoporous TiO_2 films has yielded power efficiencies of ~0.45% under AM1.5 (Coakley and McGehee 2003). P3HT has been successfully combined with CN-PPV, resulting in enhanced photocurrents and quenching of the photoluminescence of CN-PPV, indicating charge transfer between the two species (Onada, Tada et al. 1998). Blends of P3HT:CdSe nanorod blends have achieved power efficiencies of 1.7% under AM1.5 (Huynh, Dittmer et al. 2002). Polythiophene:PCBM devices have been well characterized (Gebeyehu, Padinger et al. 1999; Schilinsky, Waldauf et al. 2002; Gamaioni, Ridolfi et al. 2003) and are known to have high photoluminescence quenching, and good device performance. In the past few months, record power efficiencies for polymer photovoltaics have been reported (4.4 –

5%; J_{sc} = 10.6 mA/cm^2) using P3HT:PCBM blends optimized for film morphology (Li, Shrotriya et al. 2005; Ma, Yang et al. 2005).

Regio-regular poly-(3-hexylthiophene), was purchased from Aldrich and purified using the Soxhlet procedure (first in hexane and then in chloroform) to obtain pure samples with a number-average MW ~20,000 as determined by gel permeation chromatography (GPC) analysis.

7.3 Device characterization

J-V curves for the various device types are shown below in Figure 7.1. Neat film P3HT devices (on a TiO_2//Au structure) exhibit short circuit currents around 0.36 mA/cm^2 with a V_{oc} of 0.60 V and 42% FF, comparable to currents obtained in other studies (Coakley and McGehee 2003). Analogous structures on TiO_2 nanoparticles are expected to produce currents about twice as high, based on experiments on similar devices. P3HT devices on a PEDOT//Al architecture performed poorly (J_{sc} < 0.001 mA/cm^2, V_{oc} = 1.3 V) presumably because the transparent PEDOT cathode forces the poorly mobile electrons to cross the bulk from the P3HT/Al interface. Blends of P3HT with the electron-transporting polymer CN-ether-PPV had short-circuit currents up to 1.7 mA/cm^2 (V_{oc} = 0.94 V; FF = 24%). The fourfold improvement in current over neat film P3HT indicates efficient charge transfer from P3HT to CN-ether-PPV (and vice versa), as does the increase in V_{oc} due to the separation of electrons and holes to the HOMO of P3HT (~5.0 eV) and the LUMO of CN-ether-PPV (3.5 eV). The concomitant drop in FF suggests that charge transport is compromised in the blend. This may be due to space-charge limited current due to an inequality in charge mobility for

the two polymers, as suggested by the long tail in the J-V curve near V_{oc}. This is not observed in M3EH-PPV:CN-ether-PPV blends (Chapter 9). Unlike blends of M3EH-PPV:CN-ether-PPV, P3HT:CN-ether-PPV blends did not perform well on PEDOT//Al architecture, indicating that charge transport is not bipolar in the P3HT blends and performance is still severely limited by poor electron transport. This suggests that the mobilities of CN-ether-PPV and P3HT are poorly matched relative to those of CN-ether-PPV with M3EH-PPV. Thus, the zero-field mobility of CN-ether-PPV may be ~ $5x10^{-7}$ cm/Vs, whereas that of P3HT is much higher or much lower. Poorer miscibility of the two polymers may also affect the transport in these blends.

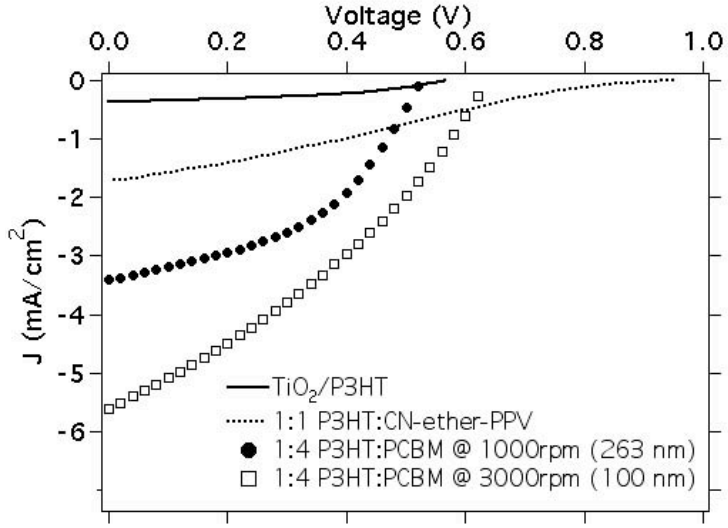

Figure 7.1. J-V curves for P3HT heterojunctions.
Device thicknesses are 50-100 nm, except for the PCBM blend spun at 1000 rpm, which is 260 nm. All devices are on TiO_2 solgel//Au structure, except P3HT:PCBM devices, which are on PEDOT//Al structure and sourced negative so that all J-V curves appear in the same quadrant for ease of comparison.

Not surprisingly, 1:4 blends of P3HT:PCBM outperformed all other structures, with currents as high as 5.6 mA/cm^2 (V_{oc} = 0.63 V; FF = 34%). Power efficiencies range from ~ 0.1% (TiO_2/P3HT) to 1.5% (P3HT:PCBM).

The currents of P3HT devices are, on average, half as large as those for M3EH-PPV heterojunctions. This is contrary to expectations due to the reported high mobilities in P3HT. The similarity in the FF for pristine polymer devices on TiO_2//Au (FF=42%) indicates that both materials have good charge transport.

P3HT and P3HT:CN-ether-PPV device performance is thickness-dependent, as expected for charge-transport limited devices. The performance is correlated with thickness and not simply with spin-speed. At first inspection, it appears that P3HT:PCBM devices are also thickness-dependent, contrary to expectations (Riedel and Dyakonov 2004). Devices spun at 3000 rpm performed better than those spun at 1000 rpm by a factor of 1.6, as can be seen in Figure 7.1 above. Though the devices differ in thickness (100 nm versus 260 nm), microscopic inspection of these films show morphological differences which may covary with thickness.

As can be seen in Figure 7.2, below, aggregated features appear in P3HT:PCBM devices at all spin speeds, but they comprise a larger portion of the film at slower spin speeds (e.g., 1000 rpm; Figure 7.2[A] and 7.2[B]) than at faster spin speeds (e.g., 3000 rpm; Figure 7.2[C]). In addition, for two films of equal film thickness (260 nm) but different morphologies (see Figure 7.2[A] and 7.2[B]), the device with fewer aggregated islands exhibits better performance. Thus, charge transport is most certainly hampered by the poor quality of films with more aggregated structures. I assume that these features are due to equilibrium processes that tend to be suppressed at higher spin speeds.

A. 1000 rpm
(260 nm; 3.4 mA/cm^2; 46% FF)

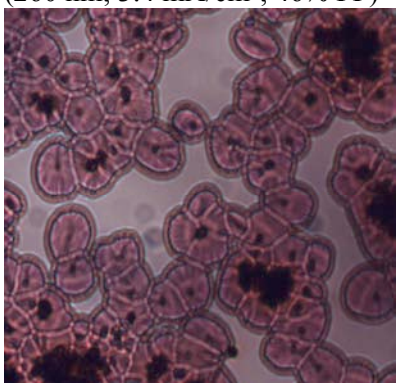

B. 1000 rpm
(260 nm; 4.0 mA/cm^2; 31% FF)

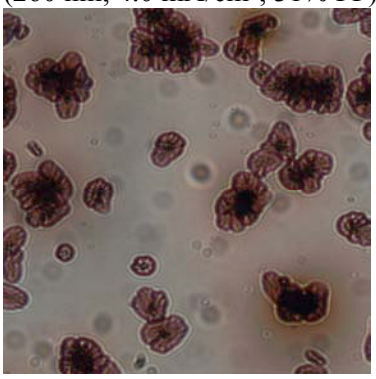

C. 3000 rpm
(100 nm; 5.6 mA/cm^2; 34% FF)

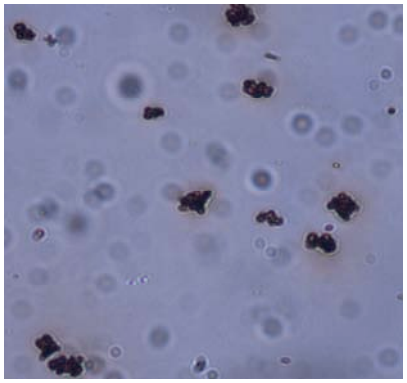

D. AFM image of feature

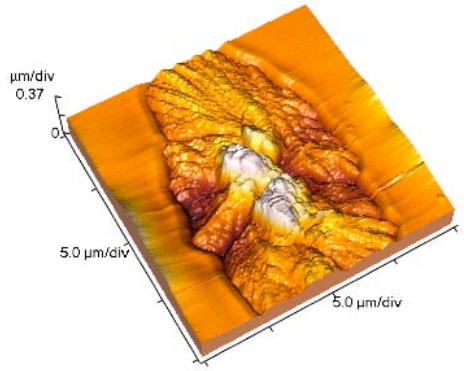

Figure 7.2. Optical images of 1:4 P3HT:PCBM mixtures spin-cast at [A] and [B] 1000 rpm (260 nm thick) and [C] 3000 rpm (100 nm thick). Images are 200 µm across. Surface features indicate increased aggregation with slower spin speed. Part [D] shows an AFM image of one of the smaller surface features, about 10 µm wide (5 µm/div horizontal; 0.37 µm/div vertical).

An AFM image of one of the small features from the 4000 rpm film is shown in Figure 7.2[D]; it is about 20 um wide and 0.5 um tall. Similar star-like structures have been observed in 1:4 blends of P3HT with PCBM, becoming smaller at 1:1 blend ratios, suggesting that they can be attributed to crystallization of PCBM (Chirvase, Parisi et al.

2004). In MDMO-PPV:PCBM blends, phase separation is observed starting at 1:1 blend ratios, with domains of pure PCBM formed in a polymer matrix at higher blend ratios, resulting in improved current densities for 1:4 blend ratios due to enhanced electron transport through the PCBM (Martens, D'Haen et al. 2003; van Duren, Yang et al. 2004). The same mechanism would appear to be at work in the present devices, with phase separation modulated by spin-speed rather than blend ratio. Some recent studies suggest that 1:1 ratios are thus more optimal for device performance (Riedel and Dyakonov 2004; Kim, Choulis et al. 2005). Only 1:4 blend ratios were studied in the present work, which may explain the lower efficiencies.

7.4 Pristine P3HT and CN-ether-PPV

Steady-state photoluminescence and absorption spectra of P3HT (solution, 30 nm film, and 100 nm film) are shown below in Figure 7.3, below. P3HT films exhibit poor photoluminescence efficiency due to the high crystallinity in which radiative transitions are suppressed by strong non-luminescent interchain interactions (Jiang, Osterbacka et al. 2003). All spectra, except for solution absorption, show clear vibronic structure. The broad absorption spectra of solution and film are characteristic of a distribution of conjugation lengths in the sample, in addition to a homogeneous broadening mechanism that arises from coupling between these segments (Scholes, Larsen et al. 2000; Yang, Dykstra et al. 2005). Excited species in solution are contained within a 1D environment on isolated single chains, as opposed to a 3D environment within the strongly crystalline film structure, as evidenced by the strong redshift of both the absorption and PL spectra from solution to film. The 0-3'

vibronic peak at 2.4 eV is less prominent in the absorption of thin (30 nm) films, which could be due to microcavity effects, a suppression of that transition in thin film, or an increase in the effective conjugation length due to high film crystallinity resulting in extended chains. The large Stokes' loss from absorption to PL indicates that the excited state has a different conformation than the ground state.

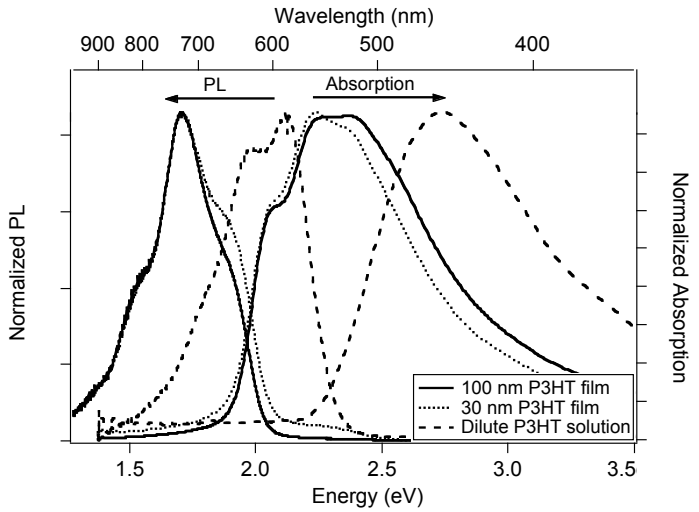

Figure 7.3. Absorption and PL spectra of P3HT film and dilute solution. PL spectra are excited at 2.82 eV, and neither absorption nor PL show a dependence upon excitation wavelength.

Time-resolved fluorescence

Decay components of P3HT and CN-ether-PPV are reported in Table 7.1, below. P3HT solutions decay with a characteristic lifetime of 0.54 ns, similar to previously published observations (Rumbles, Samuel et al. 1996; Magnani, Rumbles et al. 1997). As stated previously, P3HT films and solution create drastically different environments for the excited state carriers, as evidenced by the difference in emission spectra; it is thus difficult to compare the decay times in film and solution; I consider the similarity of τ_3 in solution and

film to be coincidental. Due to the strong vibronic structure and narrow emission spectrum in the steady-state, as well as the relatively short decay lifetimes, I take the excited state carriers to be single-chain excitons. The presence of multiple decay channels for single-chain excitons suggests that the simple model (light absorption results in creation of singlet excitons which decay via radiative and non-radiative channels) is incomplete. Excitons in different environments (for example, in the middle of a chain, the end of a chain, or a defect) may decay with different characteristic lifetimes.

Thick (100 nm) and thin (30 nm) films vary dramatically in their time decay. Both share a 27% yield of a medium length component, τ_3 (0.51 – 0.60 ns), but the dominant component of thick P3HT is 0.11 ns (68%) whereas that of thin P3HT is 0.26 ns (55%). It is possible that long-range order is more easily developed in the thick films, enabling faster decay of the 0.26 ns component due to enhanced pi-stacking.

	τ_1 (ns)	τ_2 (ns)	τ_3 (ns)	Ave τ
P3HT solution			**0.54** ± 0.0001 **(100%)**	0.54
100 nm P3HT	**0.11** ± 0.002 **(68%)**		0.51 ± 0.01 (27%)	0.41
30 nm P3HT	0.05 ± 0.003 (17%)	**0.26** ± 0.005 **(55%)**	0.60 ± 0.009 (27%)	0.32
CN-ether-PPV	6.2 ± 0.14 (31%)	**13.9** ± 0.12 **(69%)**		11.6

Table 7.1. Decay components for P3HT and CN-ether-PPV.
All films are fit to 3 exponentials; decay components with less than 15% weight are not reported for clarity. All emissions were detected at the PL peak of 700 nm, except for dilute solution, which was detected at 650 nm (the PL peak of solution).

It is interesting to compare P3HT and CN-ether-PPV decays, as both are known to be strongly affected by interchain interactions. Those in P3HT are primarily non-emissive, however, resulting in fast decay due to a large non-radiative rate constant. Those in CN-

ether-PPV, however, have a larger matrix element for emission. It is unclear why this is the case, as the wavefunction overlap in P3HT should be higher than that in CN-ether-PPV.

7.5 P3HT:CN-ether-PPV blends

Steady-state spectroscopy

Absorption spectra of P3HT:CN-ether-PPV blends are well approximated by linear combinations of the neat polymers. The absorption and PL of CN-ether-PPV are shown, in comparison to P3HT film spectra, in Figure 7.4. The two polymers are spectrally distinct.

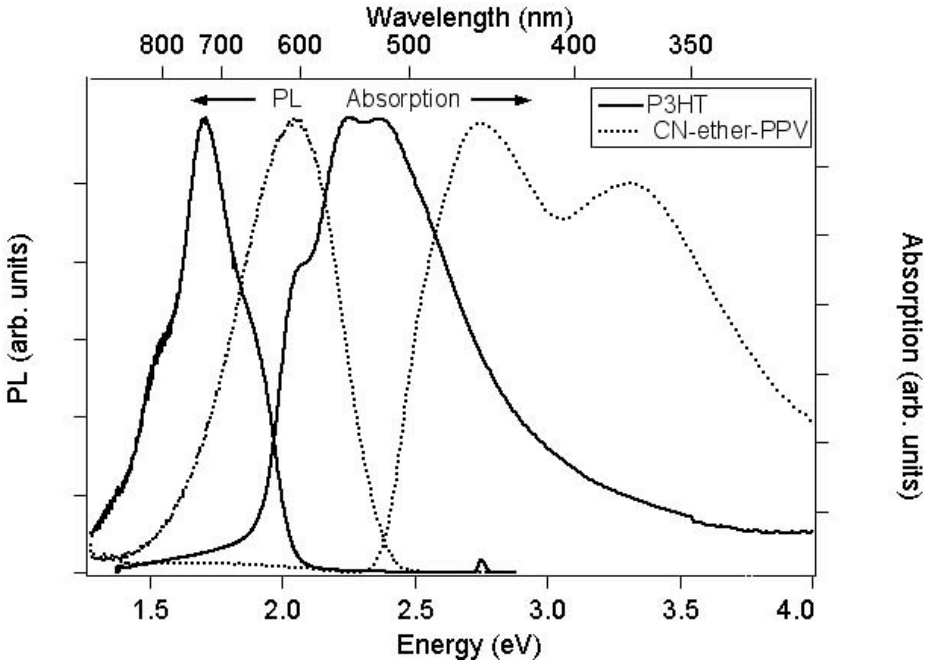

Figure 7.4. Normalized steady-state absorption and photoluminescence spectra for P3HT and CN-ether-PPV film. PL spectra are excited at 400 nm (3.1 eV) – on the blue edge of the absorption. The excitation energy had no observable effects upon the shape of the PL spectra.

The magnitude of the photoluminescence P3HT:CN-ether-PPV blends are well-quenched with respect to neat films. The relative photoluminescence measurements were obtained by comparing the intensity of the photoluminescence peaks for the films, corrected by the optical density at that excitaton wavelength. The error in these relative measurements is large, ± 20%, and all quenching proportions are well outside this margin of error. Quenching percentage is calculated by the difference in intensity between the neat film and the blend, normalized by the intensity of the neat film. At 2.0 eV emission, P3HT:CN-ether-PPV blends are quenched 96% relative to neat CN-ether-PPV.

The spectra of P3HT:CN-ether-PPV blends shifts from that of pristine P3HT, as seen below in Figure 7.5, where a new PL feature at 1.85 eV is present. The spectrum of the blend contains spectral features at positions that are very similar to the neat P3HT films, where they are attributed to vibronic structure. It is difficult to understand how the blending of the two polymers can have such a dramatic impact on the profile, with an apparent reduction in the Huang-Rhys parameter, although an intensity distortion by re-absorption effects might suggest such an effect. A slight reduction in the high energy vibronic of P3HT is observed in thicker (100 nm) versus thinner (20 nm) films, which would support this hypothesis. However, the similarity between the energy of this new peak and the HOMO/LUMO offset of P3HT and CN-ether-PPV (1.5 eV) suggests the presence of a new species formed by a complex between a hole (positive polaron) on P3HT and an electron (negative polaron) on CN-ether-PPV; i.e., an exciplex. The persistence of vibronic structure, however, casts some doubt upon this assignment. The exciplex peak is present upon excitation of both P3HT and CN-ether-PPV (2.5 eV), and also upon excitation of CN-ether-PPV (3.1 eV). Thus, excitation of CN-ether-PPV alone results in charge transfer to P3HT and formation of the

exciplex, as would be expected because the exciplex is minimized in energy relative to CN-ether-PPV though not with respect to P3HT. I cannot make a definitive statement regarding whether excitation of P3HT alone results in charge transfer to CN-ether-PPV, though it is likely that it does not, since the exciplex is not minimized in energy relative to excitations on P3HT. Note that there is significant overlap between the PL of CN-ether-PPV and the absorption of P3HT, suggesting that Förster energy transfer may occur from CN-ether-PPV to P3HT.

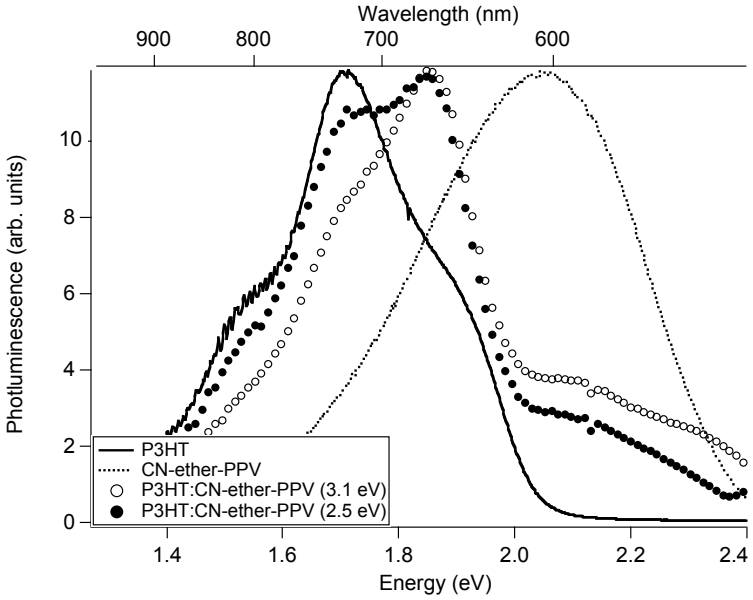

Figure 7.5. Steady-state photoluminescence spectra for P3HT, CN-ether-PPV, and a blend of the two. A new peak is present at 1.85 eV, which I attribute to an exciplex. The exciplex peak is present both at 2.5 eV excitation (P3HT and CN-ether-PPV) and 3.1 eV excitation (primarily CN-ether-PPV), and cannot be attributed to a linear combination of the pristine polymers

Time-resolved photoluminescence

The photoluminescence decay profile of P3HT:CN-ether-PPV blends is well-quenched with respect to the long decay of CN-ether-PPV: The dominant 13.9 ns component

of the CN-ether-PPV (which I assign to an interchain species due to the broad excimer-like PL spectrum of CN-ether-PPV) is completely absent in blends of P3HT:CN-ether-PPV. The absence of this emissive component can account, in part, for the efficient quenching of the CN-ether-PPV PL in the steady-state. Decay profiles and components are reported in Figure 7.6 and Table 7.2, below.

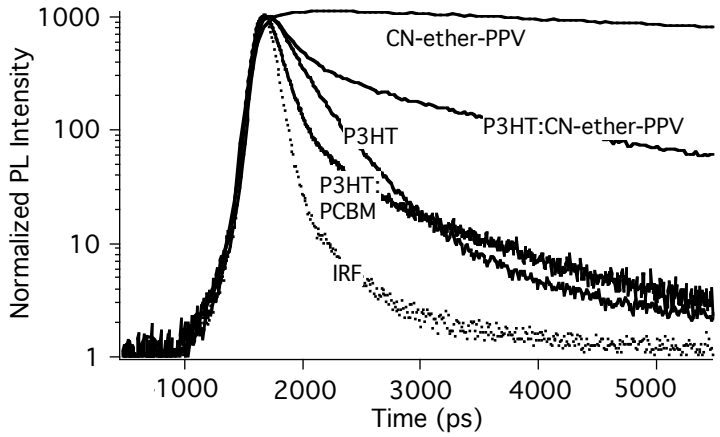

Figure 7.6. Time decays of P3HT blended with different electron transporters. Films are thick (100-250 nm) w.r.t. the exciton diffusion length.

	Film	τ_1 (ns)	τ_2 (ns)	τ_3 (ns)	Ave τ
Pristine Polymers					
	100 nm P3HT	**0.11** ± 0.002 **(68%)**	0.51 ± 0.01 (27%)		0.41
	CN-ether-PPV	6.2 ± 0.14 (31%)	**13.9** ± 0.12 **(69%)**		11.6
Blend					
	1:1 P3HT:CN-ether-PPV	0.44 ± 0.03 (18%)	**2.1** ± 0.25 **(42%)**	6.4 ± 0.63 (24%)	2.5

Table 7.2. Decay components for P3HT, CN-ether-PPV, and blends of the two at 700 nm emission. Film thicknesses are 100 – 150 nm. Pristine films are fit to 3 exponents and the blend to 4 exponents – parameters under 15% weight are not reported for clarity.

As can be seen in Figure 7.7, below, the average lifetime of the P3HT:CN-ether-PPV blends reaches a peak at 1.9 eV. This is due to an increase in the length (in ns) and the % yield of the 2.1 ns component and concomitant decrease in the shorter 0.44 ns component around 1.9 eV, as illustrated in Figure 7.7, inset. Recalling the new peak in the steady-state emission at 1.85 eV, attributed to the exciplex, I assign the 2.3 ns, 46% yield component to decay of the exciplex. The 0.44 ns component is assigned to a delocalized excitonic species in P3HT neat film which transfers charge to the exciplex state. The slightly longer lifetime indicates that the exciplex state acts as a charge-trap state, perhaps resulting in a delayed luminescence.

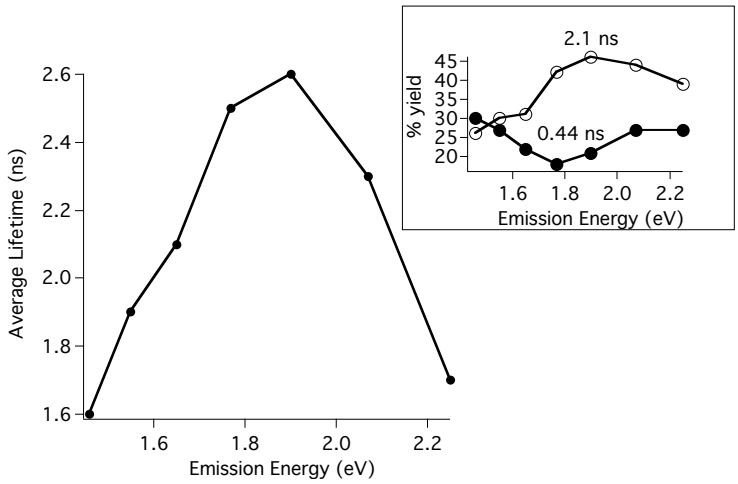

Figure 7.7. Average lifetime and % yields by emission energy for P3HT:CN-ether-PPV blends. The increase in lifetime at 1.9 eV, which is caused by an increase in the lifetime and yield of the long T_3 component, is attributed to exciplex emission at that energy.

7.6 P3HT:PCBM blends

Steady-state spectroscopy

Unlike that of P3HT:CN-ether-PPV blends, the profile of the steady-state spectrum of P3HT:PCBM blends is not significantly different from that of neat P3HT. At 1.7 eV emission, P3HT:PCBM films are quenched 99% relative to neat P3HT.

Time-resolved photoluminescence

The P3HT:PCBM blend appears only mildly quenched relative to P3HT. There is an increase in yield, and thus a greatly increased amplitude, for the short T_1 component, as well as a slight decrease in the longer T_3 component. This indicates that there is efficient charge transfer from P3HT to PCBM. This can be seen in the decay profile in Figure 7.6, above and the reported decay components in Table 7.3, below. The sample used was spun at 2000 rpm and shows aggregated features as in Figure 7.2[B]. The long tail in the PL is due to a relatively high percentage yield (15%) of a medium-length component (1.2 ns), which may be due to emission from PCBM aggregates, as observed in M3EH-PPV:PCBM blends and CN-ether-PPV:PCBM blends.

Film	**τ_1 (ns)**	**τ_2 (ns)**	**τ_3 (ns)**	**Ave τ**
100 nm P3HT	**0.11** ± 0.002 **(68%)**	0.51 ± 0.01 (27%)		0.41
1:4 P3HT:PCBM	0.09 ± 0.002 (73%)	**0.45** ± 0.03 **(15%)**	1.2 ± 0.07 (15%)	0.30

Table 7.3. Decay components for P3HT and 1:4 P3HT:PCBM blends at 700 nm emission. Pristine films are fit to 3 exponents and the blend to 4 exponents – parameters under 15% weight are not reported for clarity.

7.7 TiO_2/P3HT

Steady-state spectroscopy

Comparison of the photoluminescence intensity of films on nanoparticle and solgel layers poses a particular challenge, since the photoluminescence from the bulk film is likely to outweigh quenching effects at the interface, which may span only 5-10 nm. In an attempt to overcome this problem, thin, 30 nm films were deposited. All three films were deposited from the same solution at the same concentration and spin speed, resulting in similar film thicknesses. Results are shown below in Figure 7.8.

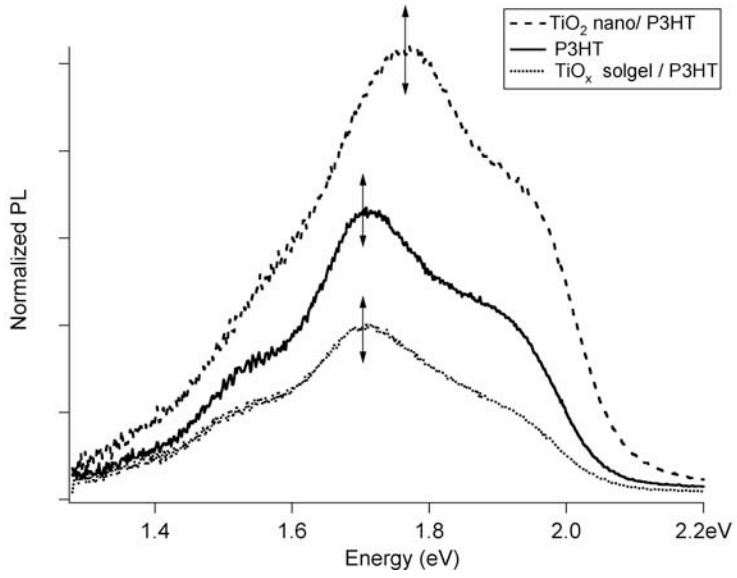

Figure 7.8. Relative steady-state photoluminescence at 3.1 eV excitation for 30 nm films of P3HT – neat film and deposited on TiO_2. P3HT on smooth solgel shows moderate quenching, whereas P3HT on rough nanoparticles shows some enhancement of the PL. Error bars represent 20% error in reproducibility of results.

The photoluminescence intensity is partially quenched by the solgel, but enhanced by the nanoparticle surface. Partial quenching by solgel is expected due to charge transfer to the solgel. The PL enhancement on the nanoparticles, as well as the shift of the photoluminescence peak towards the blue, is due to disruption of the crystalline order by the rough nanoparticle surface, suppressing interchain interactions and allowing additional radiative recombination. Such a blueshift has been previously observed in studies of P3HT infiltrated into mesoporous titania, which exhibit poor hole transport due to the disruption of pi-stacking in the polymer (Coakley and McGehee 2003).

Time-resolved fluorescence

TiO_2/P3HT heterojunction films are ~ 30 nm thick and should be compared to 30 nm P3HT neat films, as in Figure 7.9 and Table 7.4 below. Both types of TiO_2/P3HT heterojunctions (smooth TiO_2 solgel and rough TiO_2 nanoparticles) appear surprisingly unquenched with respect to the decay of neat-film P3HT of similar thickness (~35 nm). The lack of quenching and absence of a new fast component due to charge transfer from P3HT to TiO_2 may be due to the dominance of the bulk emission over the quenching from the small interfacial area. A long decay component can be seen in the decay plots, and a new 0.91 ns component (21%) is present in TiO_2 nanoparticle/P3HT films. I attribute these long decay components to long-lived single-chain polaron states in P3HT which are enhanced in films on nanoparticle layers, which disrupt the crystalline pi-stacking. I note the striking similarity of TiO_2 solgel/P3HT decay components to those of 100 nm P3HT, which may be due to a poorly understood effect of the solgel upon P3HT morphology.

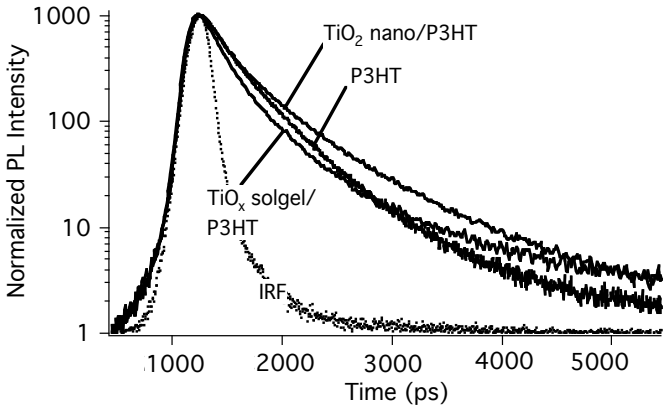

Figure 7.9. Time decays of P3HT layered with TiO_2. Films are ~ 30 nm thick.

	τ_1 (ns)	τ_2 (ns)	τ_3 (ns)	Ave τ
30 nm P3HT	0.05 (17%)	**0.26 (55%)**	0.60 (27%)	0.32
TiO_2 nano/P3HT	0.10 (36%)	**0.36 (43%)**	0.91 (21%)	0.38
TiO_x solgel/P3HT		**0.22 (68%)**	0.51 (27%)	0.34

Table 7.4. Decay components for TiO2/P3HT layered films. Thickness of P3HT is ~ 30 nm in all films.

7.8 Conclusions

In conclusion, I performed device characterization, steady-state, and time-resolved spectroscopy measurements on a variety of heterojunctions of P3HT with electron transporting materials. I find that P3HT:CN-ether-PPV and P3HT:PCBM blends show enhanced currents over P3HT on TiO_2 solgel alone.

P3HT:PCBM devices show difference in aggregation depending upon spin-speed, such that lower spin-speeds result in increased aggregation at the expense of device performance. Aggregation of PCBM in the polymer matrix may provide the best charge-

transport structure at the cost of efficient charge separation. The decay times of P3HT:PCBM films are not drastically reduced compared to neat film P3HT. The lack of clear quenching is due to the pre-existing efficient non-radiative pathways in P3HT as well as the presence of a long decay component that may be due to emission from PCBM aggregates. Thus, despite efficient charge-transfer from P3HT to PCBM, as evidenced by the quenching of the steady-state emission and enhanced device performance, the present study does not provide sufficient resolution in order to observe marked differences in the kinetics, unlike previous time-resolved infrared absorption studies (Meskers, van Hal et al. 2000).

We find evidence for an exciplex state between a positive polaron in P3HT (hole) and a negative polaron (electron) in CN-ether-PPV in P3HT:CN-ether-PPV blends. The exciplex is marked by a new photoluminescence peak at 1.9 eV in the steady-state, and a new 2.3 ns component which reaches a maximum yield, also at 1.9 eV. The exciplex is evidence of charge-transfer between the two polymers, which accounts for the quenching of the steady-state photoluminescence of CN-ether-PPV and enhanced device performance. The exciplex may also aid device performance by acting as a scavenger for excitons, which would otherwise decay via efficient non-radiative transfer.

Despite known charge transfer from P3HT to TiO_2 (due to the ability to create working photovoltaics on this structure), charge-transfer in the form of a short decay component is not observed in TiO_2 solgel/P3HT films. The time-decay appears longer-lived, which I attribute to long-lived polaron states in TiO_2. Thus, charge-transfer may correspond to longer, instead of shorter, decay times in time-resolved photoluminescence. TiO_2 nanoparticle layers disrupt the long-range order of P3HT, as evidenced by (a) a blueshift of the PL spectrum, indicating the shift from a 3D to 2D environment for excited carriers and (b)

an enhancement of the steady-state PL, due to a decrease in non-radiative interchain carriers. Long-lived single-chain polaron states in this disordered film are evidenced in a new 0.91 ns decay component.

7.9 References

Chirvase, D., J. Parisi, et al. (2004). "Influence of nanomorphology on the photovoltaic action of polymer-fullerene composites." Nanotechnology **15**: 1317.

Coakley, K. M. and M. D. McGehee (2003). "Photovoltaic cells made from conjugated polymers infiltrated into mesoporous titania." Appl. Phys. Lett. **83**(16): 3380.

Conwell, E. M. (1997). Intramolecular excitons and intermolecular polaron pairs as primary photoexcitations in conjugated polymers. Primary excitations in conjugated polymers: Molecular exciton versus semiconductor band model. N. S. Sariciftci. River Edge, NJ, World Scientific Publishing Company.

Gamaioni, N., G. Ridolfi, et al. (2003). "A stabilization effect of [60]fullerene in donor-acceptor organic solar cells." Sol. Energy Mater. Sol. Cells **76**: 107.

Gebeyehu, D., F. Padinger, et al. (1999). "Characterization of large area flexible plastic solar cells based on conjugated polymer/fullerene composites." Int. J. Photoenergy **1**: 95.

Huynh, W. U., J. J. Dittmer, et al. (2002). "Hybrid nanorod-polymer solar cells." Science **295**: 2425.

Jiang, X. M., R. Osterbacka, et al. (2003). "Photoexcitations in regio-regular and regio-random polythiophene films." Synth. Met. **137**: 1465.

Kim, Y., S. A. Choulis, et al. (2005). "Composition and annealing effects in polythiophene/fullerene solar cells." J. Mat. Sci. **40**: 1371.

Li, G., V. Shrotriya, et al. (2005). "High-efficiency solution processable polymer photovoltaic cells by self-organization of polymer blends." Nature **4**(10): Advance Online Publication.

Ma, W., C. Yang, et al. (2005). "Thermally stable, efficient polymer solar cells with nanoscale control of the interpenetrating network morphology." Adv. Func. Mater. **15**(10): Advance Online Publication.

Magnani, L., G. Rumbles, et al. (1997). "Photoluminescence studies of chain interactions in electroluminescent polymers." Synthetic Metals **84**(1-3): 899-900.

Martens, T., J. D'Haen, et al. (2003). "Disclosure of the nanostructure of MDMO-PPV:PCBM bulk hetero-junction organic solar cells by a combination of SPM and TEM." Synth. Met. **138**: 243.

Meskers, S. C. J., P. A. van Hal, et al. (2000). "Time-resolved infrared-absorption study of photoinduced charge transfer in a polythiophene-methanofullerene composite film." Phys. Rev. B **61**(15): 9917.

Onada, M., K. Tada, et al. (1998). "Photoinduced charge transfer of conducting polymer composites." IEICE Trans. Electron **E81-C**(7): 1051.

Riedel, I. and V. Dyakonov (2004). "Influence of electronic transport properties of polymer-fullerene blends on the performance of bulk heterojunction photovoltaic devices." Phys. Status Solidi A **201**(6): 1332.

Rumbles, G., I. D. W. Samuel, et al. (1996). "Chromism and luminescence in regioregular poly(3-dodecylthiophene)." Synth. Met. **76**(1-3): 47.

Schilinsky, P., C. Waldauf, et al. (2002). "Recombination and loss analysis in polythiophene based bulk heterojunction photodetectors." Appl. Phys. Lett. **81**: 3885.

Scholes, G. D., D. S. Larsen, et al. (2000). "Origin of line broadening in the electronic absorption spectra of conjugated polymers: Three-pulse-echo studies of MEH-PPV in toluene." Physical Review B **61**(20): 13670-13678.

Sirringhaus, H., N. Tessler, et al. (1998). "Integrated optoelectronic devices based on conjugated polymers." Science **280**: 1741.

Song, M. Y., J. K. Kim, et al. (2003). "Temperature effect on photocurrent generation of TiO_2/conjugated polymer photovoltaic devices." Synth. Met. **137**: 1389.

van Duren, J. K. J., X. Yang, et al. (2004). "Relating the morphology of poly(p-phenylene vinylene)/Methanofullerene blends to solar-cell performance." Adv. Func. Mater. **14**: 425.

Xu, B. and S. Holdcroft (1993). "Molecular control of luminescence from poly(3-hexylthiophenes)." Macromolecules **26**: 4457.

Yang, X. J., T. E. Dykstra, et al. (2005). "Photon-echo studies of collective absorption and dynamic localization of excitation in conjugated polymers and oligomers." Physical Review B **71**(4).

Chapter 8

Efficient charge-transfer and charge-transport in bulk heterojunctions: M3EH-PPV:PCBM blends

8.1 Abstract

I have investigated the relationship between excited state dynamics and device performance in polymer-fullerene blends. I have blended the hole-transporting polymer M3EH-PPV with the electron-accepting fullerene derivative, PCBM. Photovoltaic devices are characterized and time-resolved photoluminescence measurements reveal information about the underlying morphology. Devices with 80 wt% of PCBM in the blend are found to have higher currents and fill-factor (J_{sc} = 13 mA/cm^2, FF = 37%) than blends with 20 wt% PCBM (J_{sc} = 4.8 mA/cm^2, FF = 29%) under white light illumination. Despite poorer device performance, the time-decay of 20 wt% blends is more rapid than that of 80 wt% blends due to (a) better dispersion of the fullerene, and (b) the absence of a long PCBM decay component. This is due to the presence of large domains of PCBM in 80 wt% blends, which presumably provide a continuous percolation pathway for the transportation of mobile electrons, resulting in high currents and fill-factor. The ideal blend ratio for charge separation does not coincide with the ideal ratio for charge transport, due to blend morphology. Morphological changes in the blended film relative to the pristine polymer are also evidenced by a strong blueshift in the steady-state fluorescence. A new spectral peak of unknown origin is observed at 2.5 eV when the films are excited at low energy.

8.2 Structure and properties

Buckminsterfullerene (C_{60}), or derivatives thereof, is one of the most common electron acceptors used in polymer heterojunction photovoltaics, resulting in the highest recorded power efficiencies to date. C_{60} is fairly transparent and is a good electron acceptor and transporter. It shows negligible luminescence because of highly efficient intersystem crossing to the triplet state. Electron transfer from MEH-PPV to C_{60} is rapid and the charge-separated state is long-lived; the steady-state photoluminescence is quenched by nearly three order of magnitude and the photoluminescence lifetime is reduced to the instrument response, <60 ps, implying a charge transfer efficiency of almost 100% (Sariciftci, Smilowitz et al. 1992; Sariciftci, Smilowitz et al. 1993). In 1993 the first C_{60}/polymer cell was created by thermally evaporating C_{60} to form a bilayer cell (Sariciftci, Braun et al. 1993). Halls and colleagues thoroughly studied PPV/ C_{60} layered photovoltaics, finding a maximum EQE of 9% (Halls, Pichler et al. 1996; Halls, Pichler et al. 1996). These devices are characterized by high FF (~48%); optimization of the layer thicknesses has given peak current densities of 1.4 mA/cm^2, with a V_{oc} of about 0.5 V (Durstock, Spry et al. 2003).

These layered C_{60} devices, however, are limited by the interfacial area available in a planar layered device, prompting a search for methods to disperse the C_{60} within the polymer matrix. Low solubility of C_{60} was an obstacle until the development of soluble C_{60} derivatives by Hummelen in 1995, including phenyl-C61-butyric acid methyl ester (PCBM) (Hummelen, Knight et al. 1995), which has a HOMO and LUMO of 6.1 and 3.7 eV, respectively. The transport properties of such derivatives will suffer due to the increased distance between the fullerene moieties in the blend. Devices using PCBM were first

fabricated shortly thereafter by Yu, Hummelen et al., in a 1:4 blend by weight resulting in a cell that was 80 wt% fullerene with an EQE of 29% under monochromatic illumination (Yu, Gao et al. 1995) – a highly efficient cell for the time. Under monochromatic illumination, Shaheen et al. reported QE values of 85%, and an efficiency of 2.5%, for a 1:4 MDMO-PPV:PCBM cell (Shaheen, Brabec et al. 2001). MEH-PPV:PCBM blends have current densities of ~ 3.0 mA/cm^2, FF of 45%, and efficiencies of about 1.2% (Zhang, Johansson et al. 2003), and MDMO-PPV:PCBM cells have currents of 5-6 mA/cm^2 at 100 mW/cm^2 illumination (Riedel and Dyakonov 2004). Recent optimization of the morphology of P3HT:PCBM cells, however, has resulted in currents of 10-13 mA/cm^2 and power efficiencies approaching 5% (Li, Shrotriya et al. 2005; Ma, Yang et al. 2005).

Charge transfer is rapid and efficient. The addition of just a few percent by weight of PCBM results in luminescence quenching of three orders of magnitude, because charge transfer to PCBM occurs within ~50 fs -- three orders of magnitude faster than the radiative recombination which competes even with the vibrational relaxation of the polymer chains (Brabec, Zerza et al. 2001; Zerza, Brabec et al. 2001).

Photoexcitation of the polymer is the dominant process of charge generation; even at 80 wt% PCBM, about 2/3 of the absorbed photons at 500 nm will result in photoexcitation of PPV (Savenije, Kroeze et al. 2004). The high electron mobility of PCBM -- at least 3 orders of magnitude higher than those in PPV's (Mihailetchi, van Duren et al. 2003) -- is advantageous to device performance, but the mismatch in carrier mobility leads to space-charge limited current (Mihailetchi, Wildeman et al. 2005). The percolation threshold of PCBM is 17 vol% (Aharony and Stauffer 1993), corresponding to about 25 wt%, with best performance around 60 – 80 wt% due to a compromise between absorption, charge

separation, and material mobilities (Mihailetchi, Koster et al. 2005). Past 60 wt% the combination of charge separation and mobility reaches an optimum value (Savenije, Kroeze et al. 2004) due to the formation of large PCBM domains which enable the transport of electrons across the device. Surprisingly, the hole-transport properties in the polymer are also enhanced, by up to two orders of magnitude, by the addition of PCBM (Choulis, Nelson et al. 2003; Pacios, Nelson et al. 2003; Melzer, Koop et al. 2004; Mihailetchi, Koster et al. 2005), perhaps by the enhancement of interchain interactions. The closer match between electron and hole mobilities results in enhanced device performance due to reduced charge buildup (Li, Shrotriya et al. 2005; Mihailetchi, Koster et al. 2005).

The energy diagram for M3EH-PPV:PCBM devices is given in Figure 8.1, and the polymer structures in Figure 8.1, inset.

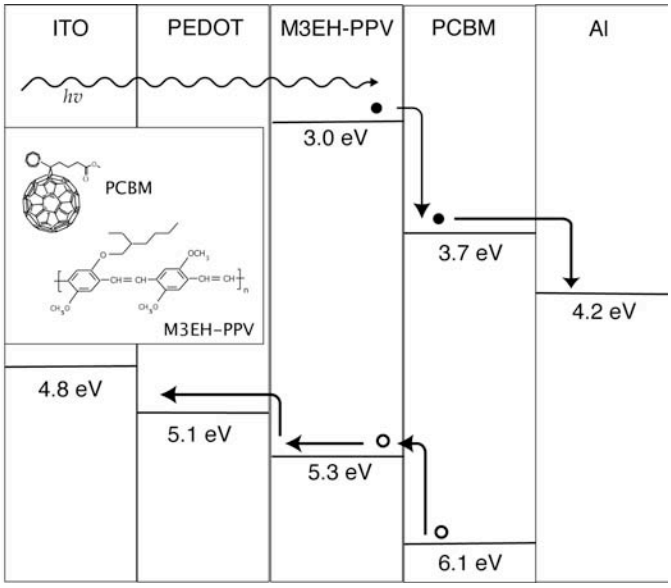

Figure 8.1. Energy diagram for M3EH-PPV:PCBM solar cells. Material structures are given in inset.

8.3 Device characterization

As reported previously for other PPV polymers, 1:4 blends (80 wt% PCBM) outperformed devices with lower wt% of PCBM (Figure 8.2*). Phase separation begins at 67 wt% in MDMO-PPV:PCBM blends; at higher wt%, large PCBM domains form within a polymer:PCBM matrix. This leads to enhanced performance at 80 wt% due to enhanced electron transport through the interconnected PCBM network (Martens, D'Haen et al. 2003; Savenije, Kroeze et al. 2004; van Duren, Yang et al. 2004-a).

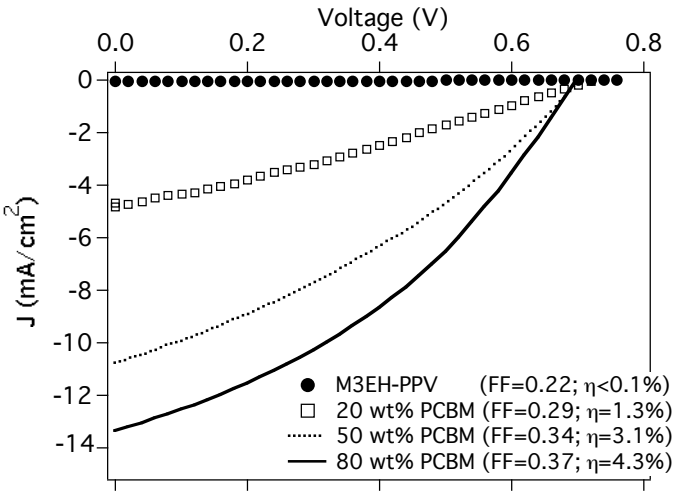

Figure 8.2. J-V curves of M3EH-PPV:PCBM blends. All devices are on PEDOT//Al architecture.

The same mechanism appears to control the performance of M3EH-PPV:PCBM devices. The short-circuit currents of 50 wt% and 80 wt% blends are similar, but the enhanced FF in 80 wt% blends results in a higher efficiency for these devices, presumably due to the

* The majority of photovoltaic devices reported in this section were fabricated and characterized by colleague Veronica Sholin.

presence of large PCBM domains which enhance electron transport. This is similar to observations on P3HT:PCBM (see Chapter 7). The presence of good electron transport is indicated by the destruction of the diode behavior of the devices in the dark; rectification ratios drop dramatically on M3EH-PPV:PCBM blends ($10^0 – 10^1$) from M3EH-PPV devices ($\sim 10^3 – 10^6$).

Fill factor (FF)

Fill-factor increased as the wt% of PCBM in the blend was increased (Figure 8.3), with a slope neatly mirroring the increase in current. This suggests that the same mechanism is responsible for the increase in each parameter; namely, the increased size of the PCBM domains which enhance electron-transport across the device. At 80 wt% PCBM the ~40% FF of pristine M3EH-PPV devices on TiO_2//Au (in which transport is dominated by mobile holes) is regained. It is surprising that the peak FF is not higher due to the enhanced mobility of both electrons and holes upon the addition of PCBM. The FF has been found to exceed 60% in MDMO-PPV:PCBM cells; a similar enhancement in FF in our devices would result in significant improvements in efficiency . It appears that charge transport is not as efficient in M3EH-PPV:PCBM cells due to poorer electron percolation or low hole mobility. The zero-field hole mobility has been estimated at 5×10^{-7} cm^2/Vs for both MDMO-PPV and M3EH-PPV (Breeze, Schlesinger et al. 2004; Kemerink, van Duren et al. 2005), although the charge mobility of MDMO-PPV has been shown to increase by two orders of magnitude upon addition of PCBM (Melzer, Koop et al. 2004). The same may not be true for M3EH-PPV. If indeed the hole mobility is lower in M3EH-PPV:PCBM blends, then the poor match

between electron and hole mobility would restrict current flow and reduce the FF due to build-up of holes in the device (Li, Shrotriya et al. 2005).

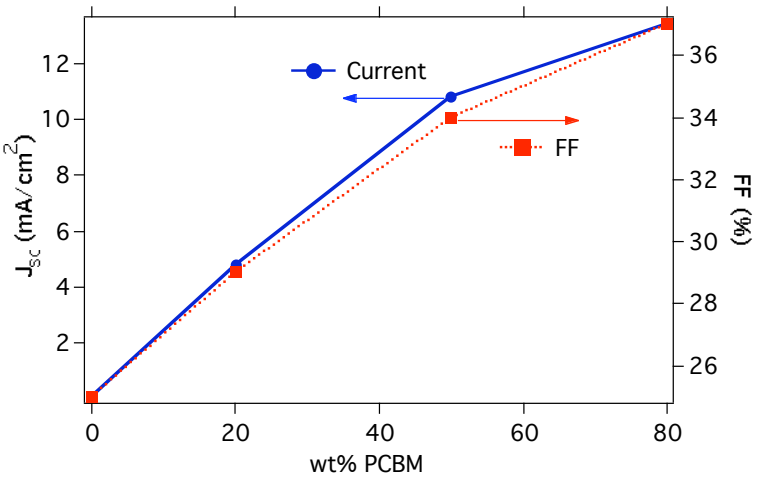

Figure 8.3. Short-circuit current and fill-factor by PCBM wt%.

Thickness dependence

Unlike P3HT:PCBM, PPV-based PCBM blends are expected to be transport limited (Riedel and Dyakonov 2004). Accordingly, thinner devices have higher currents, though this effect is mitigated by both the solution concentration and the spin-speed, suggesting that morphology is co-varying with thickness and affecting device performance. Based upon previous observations on P3HT in this thesis, and thickness dependent and depth-profile imaging studies of PCBM blended with MDMO-PPV (van Duren, Yang et al. 2004-a), it is likely that more rapid evaporation (i.e., faster spin-speed and low solution concentration) results in smaller PCBM domains. Past a critical wt% of PCBM where continuous percolation pathways have already formed, these smaller PCBM domains are advantageous to device performance.

Devices with low wt% of PCBM had better performance for thinner device structures (~ 40 nm) than those for high wt% of PCBM (~ 70 nm), suggesting that better charge transport due to larger PCBM domains in high wt% blends pose fewer restrictions upon device thickness. These results are confounded, however, with the fact that low wt% blends naturally result in thinner devices than high wt% blends.

8.4 Steady-state spectroscopy

Absorption

Absorption of M3EH-PPV:PCBM films is shown in Figure 8.4. The absorption peak is shifted slightly to the red for increasing wt% of PCBM, indicating the presence of ground-state aggregates, increased chain extension, or reduced access to high energy excited states relative to pristine M3EH-PPV. The spectral peaks at high energies are of unknown origin; they are far from the absorption maximum of PCBM.

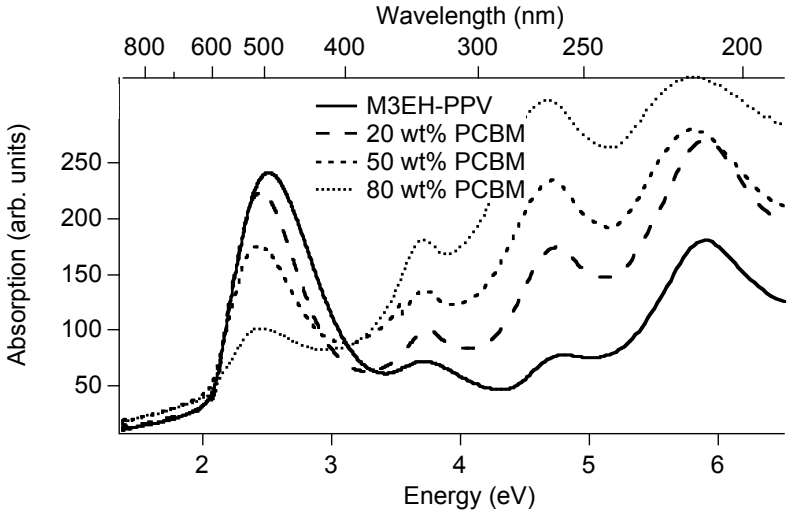

Figure 8.4. Relative absorption of M3EH-PPV and M3EH-PPV:PCBM blends. Films are 70 – 100 nm thick.

Photoluminescence

Relative steady-state photoluminescence (not shown), corrected for optical density, is quenched by two orders of magnitude relative to M3EH-PPV for 80 wt% PCBM, and three orders of magnitude for 20 and 50wt% PCBM, indicating efficient charge transfer. The lack of complete quenching at 80wt% PCBM as opposed to MDMO-PPV (Brabec, Zerza et al. 2001) and MEH-PPV (Sariciftci, Smilowitz et al. 1993) suggests slightly different blend morphology in our materials. Relative PL measurements on thin films without use of an integrating sphere, however, are prone to error and difficult to reproduce due to local variations in film quality, differences in optical density, and interference effects. The error in reproducibility of the current data is ±20%.

Steady-state spectra were integrated over a longer time period to increase the signal, and subsequently normalized (Figure 8.5). The characteristic 1.7 eV emission of PCBM was not observed (Byrne, Maser et al. 1995). The lack of clear residual PCBM emission in M3EH-PPV:PCBM blends, as opposed to CN-ether-PPV:PCBM blends (see Chapter 6), is indicative of more efficient hole transfer from PCBM to M3EH-PPV than CN-ether-PPV, as would be expected due to the energetic favorability of hole transfer to M3EH-PPV.

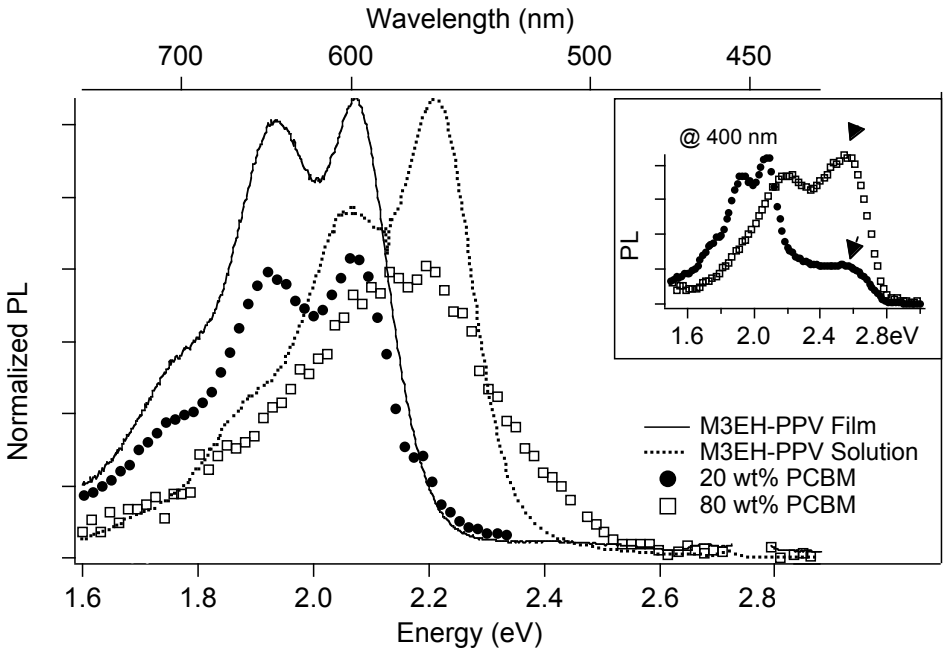

Figure 8.5. Steady-state normalized PL for M3EH-PPV and blends with PCBM, showing spectral features. M3EH-PPV spectra do not depend upon excitation wavelength. PCBM blends are excited at 450 nm. Inset shows new PL band at 2.5 eV for excitation at 400 nm.

The photoluminescence is strongly blueshifted as the wt% of PCBM is increased, to a new peak emission at 2.2 eV in 80 wt% blends, as seen in Figure 8.5, above. This corresponds roughly with the emission from M3EH-PPV solution, though there is a lack of vibronic structure. This vibronic structure was regained in 20 wt% and 50 wt% blends, indicative of stronger residual M3EH-PPV emission; an observation which conflicts with the apparently lower photoluminescence quantum yield observed in these low-weight PCBM blends. The blueshift in PL has been observed previously in MEH-PPV:PCBM (Sariciftci, Smilowitz et al. 1992) and P3HT:PCBM blends (Wang, Grigorova et al. 1997; Theander, Yartsev et al. 2000; Hoppe 2004). The blueshift has been attributed to conformational changes such as coiling of the polymer chains within tightly packed polymer domains, or

residual emission from high-energy states which have not equilibrated since charge-transfer to PCBM occurs on a timescale faster than that of spectral diffusion to lower energy segments. The latter is unlikely because time-resolved measurements (see Section 8.5) indicate that excitons in 20 wt% blends are better quenched than in 80 wt% blends; residual emission would thus blueshift 20 wt% relative to 80 wt% blends instead of vice-versa.

When excitation is shifted to 400 nm, which lies within the high-energy tail of the absorption, a distinct spectral peak at 2.5 eV is observed – a much larger shift than observed in any previous studies known to us. This peak is related to the presence of PCBM; it is stronger relative to the residual M3EH-PPV peak height for 80 wt% blends than for 50 wt% blends (Figure 8.5, inset). These peaks do not seem to be due to Raman effects, and scattering peaks have been removed. I am uncertain how to interpret this spectral peak, and unfortunately time-resolved data were not collected at this emission wavelength because this was not the primary region of interest.

8.5 Time-resolved photoluminescence

Quenching of the excited state lifetime

Unlike similar systems such as MDMO-PPV, in which the addition of 2% PCBM reduces the lifetime to the time resolution of the instrument (van Duren, Yang et al. 2004-b), the decay times of 1:4 M3EH-PPV:PCBM are only moderately quenched relative to M3EH-PPV, as seen in Table 8.1 and 8.2, below. At 650 nm the average decay is increased from 0.38 ns in M3EH-PPV to 0.7 ns in 1:4 M3EH-PPV:PCBM. The dominant component of M3EH-PPV (0.45 ns) appears particularly stubborn, and is still present at large yields in 80

wt% blends. Since the steady-state photoluminescence is quenched by two orders of magnitude, this suggests that both (a) the majority of exciton decay occurs on a timescale faster than our instrument resolution, (b) the underlying morphology of M3EH-PPV:PCBM devices may differ from that of PCBM blended with MEH-PPV and MDMO-PPV and (c) the efficient charge transfer leaves behind a small population N_{ex}, which decays via its intrinsic channels with a moderately long lifetime of 0.45 ns. This particular excitonic species is only efficiently quenched when PCBM is well-dispersed within the blend, as in 20 wt% blends. It is unlikely that the observed lengthening of the lifetime is due to the decay of the charge-transferred polaron state (electrons in C_{60} and holes in the polymer); the polaron decay occurs on the nanosecond – millisecond scale (due to the energetically unfavorable back transfer) and is unlikely to be observed in the time-window of my measurements (Meskers, van Hal et al. 2000; Nogueira, Montanari et al. 2003).

Emis. (nm)	τ_1 (ns)	Error/ A_1	τ_2 (ns)	Error/ A_2	τ_3 (ns)	Error/ A_3	τ_{ave}	χ^2_v	DW
600	0.20 (43%)	± 0.04 0.64	**0.45 (53%)**	± 0.09 0.35	1.7 (3%)	± 1.4 <0.01	0.38	1.2	1.6
650	0.20 (46%)	± 0.01 0.67	**0.45 (50%)**	± 0.01 0.33	1.6 (4%)	± 0.1 <0.01	0.38	1.2	1.8
700	0.20 (41%)	± 0.01 0.64	**0.45 (52%)**	± 0.02 0.36	1.5 (6%)	± 0.1 <0.01	0.41	1.2	1.9
750	0.20 (40%)	± 0.02 0.64	**0.45 (51%)**	± 0.06 0.36	1.3 (9%)	± 0.2 <0.01	0.43	1.1	2.0

Table 8.1. Decay components of M3EH-PPV, 60 nm thick. Percent of steady-state photoluminescence yield (__%) is reported in parentheses below each decay component. A_i's represent normalized pre-exponential factors, which are uncorrelated with decay time.

Emission (nm)	τ_1 (ns)	Error/A_1	τ_2 (ns)	Error/A_2	τ_3 (ns)	Error/A_3	τ_{ave}	χ^2_ν	DW
600	0.05 (36%)	± 0.01 0.86	**0.50 (49%)**	± 0.04 0.13	1.9 (16%)	± 0.26 0.01	0.6	1.2	1.6
650	0.05 (30%)	± 0.01 0.86	**0.52 (47%)**	± 0.04 0.12	2.0 (22%)	± 0.21 0.02	0.7	1.3	1.5
700	0.05 (21%)	± 0.01 0.80	**0.58 (50%)**	± 0.06 0.17	1.9 (27%)	± 0.25 0.03	0.9	1.2	1.8
750	0.05 (18%)	± 0.02 0.80	**0.60 (50%)**	± 0.07 0.18	1.9 (32%)	± 0.31 0.03	0.9	1.2	1.8

Table 8.2. Decay components of 80 wt% (1:4) M3EH-PPV:PCBM blend, 62 nm thick. Percent of steady-state photoluminescence yield (__%) is reported in parentheses below each decay component. A_i's represent normalized pre-exponential factors, which are uncorrelated with decay time.

Emission (nm)	τ_1 (ns)	Error/A_1	τ_2 (ns)	Error/A_2	τ_3 (ns)	Error/A_3	τ_{ave}	χ^2_ν	DW
600	**0.02 (73%)**	± 0.01 0.98	0.36 (14%)	± 0.15 0.01	1.3 (13%)	± 0.05 0.003	0.24	1.2	1.8
650	**0.02 (77%)**	± 0.01 0.99	0.32 (11%)	± 0.10 <0.001	1.3 (12%)	± 0.27 <0.001	0.21	1.1	1.9
700	**0.02 (65%)**	± 0.03 0.99	0.36 (15%)	± 0.23 0.01	1.4 (19%)	± 0.63 <0.001	0.33	1.1	1.9

Table 8.3. Decay components of 50% (1:1) M3EH-PPV:PCBM blend, 45 nm thick. Percent of steady-state photoluminescence yield (__%) is reported in parentheses below each decay component. A_i's represent normalized pre-exponential factors, which are uncorrelated with decay time.

Emission (nm)	τ_1 (ns)	Error/A_1	τ_2 (ns)	Error/A_2	τ_3 (ns)	Error/ A_3	τ_{ave}	χ^2_ν	DW
600	Unable to resolve								
650	**0.02 (95%)**	±0.001 1.0			1.0 (5%)	±0.022 <0.001	0.07	2	1
700	**0.02 (89%)**	±0.001 1.0			1.0 (11%)	±0.014 <0.001	0.13	1.4	1.5
750	**0.02 (85%)**	±0.01 1.0			1.0 (15%)	±0.12 <0.001	0.16	1.2	1.8

Table 8.4. Decay components of 20 wt% (4:1) M3EH-PPV:PCBM blend, 77 nm thick. Percent of steady-state photoluminescence yield (__%) is reported in parentheses below each decay component. A_i's represent normalized pre-exponential factors, which are uncorrelated with decay time.

Ratio dependence

Contrary to the naïve assumption that more PCBM should result in increased charge transfer, which should shorten the lifetime, the rate of decay *increases* as the wt% of PCBM in the blend is *decreased* (Figures 8.6 and 8.7 below and Tables 8.2 - 8.4 above). The difference is not likely to be due to exciton/exciton annihilation as in previous studies (Vacar, Maniloff et al. 1997), due to the lower power of our laser. In the vast majority of reports, decay time decreases as the wt% of PCBM increases (Haugeneder, Neges et al. 1999), though many of these measurements are performed at shorter timescales than the current study and so might not detect decays > 1 ns. A less pronounced, but similar effect has been seen in TCSPC on MDMO-PPV:PCBM blends (van Duren, Yang et al. 2004-a; van Duren, Yang et al. 2004-b), attributable to emission from the PCBM phase.

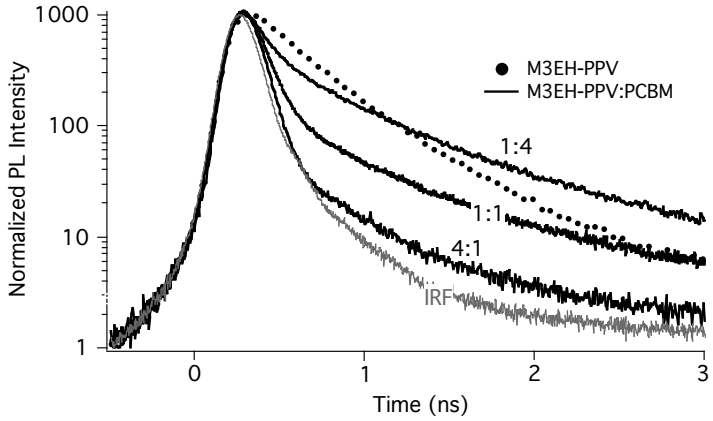

Figure 8.6. Time-decays of varying ratios of M3EH-PPV:PCBM blends. Emission is detected at 600 nm. Film thicknesses are 45-75 nm.

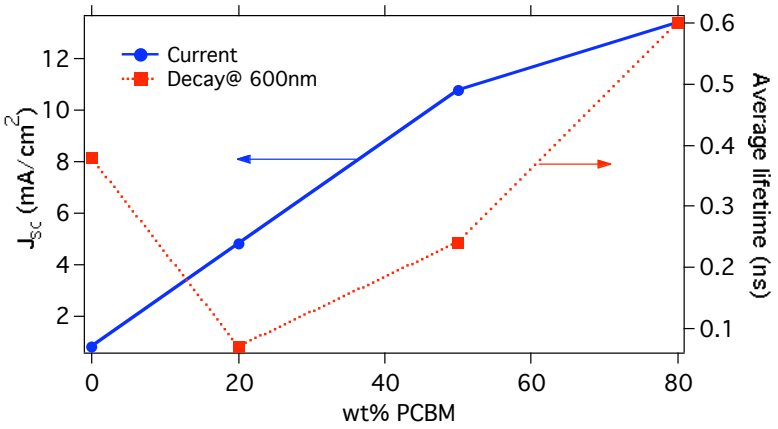

Figure 8.7. Photoluminescence decay and short-circuit current by PCBM wt%.

At lower wt% of PCBM in MDMO-PPV:PCBM blends, the size of PCBM domains decreases, reaching a minimum at the onset of phase separation at 67 wt% (Martens, D'Haen et al. 2003; van Duren, Yang et al. 2004-a). Thus, the faster decay for low wt% of PCBM in my studies is due to better dispersion of these smaller domains, resulting in increased charge transfer. This is counter to prior suggestions that the dissociation efficiency of MDMO-PPV:PCBM blends decreases as the wt% of PCBM is decreased (from 80 wt% to 50 wt%), due to decreased hole mobility and lower dielectric constant (Mihailetchi, Koster et al. 2005). It appears that the more symmetric substitution of M3EH-PPV sidechains affects both the size of PCBM domains in the blend and the hole mobility relative to MDMO-PPV:PCBM.

Inspection of the decay components reveals that as the wt% of PCBM is decreased the fast 0.05 ns decay component (attributable to the quenched M3EH-PPV exciton) becomes faster and its yield increases (Figure 8.8A, below). At 50 wt% the majority of M3EH-PPV excitons are quenched within the time-response of the system, but this does not correspond to the best device performance due to less efficient percolation pathways for electron transport.

A.
M3EH-PPV exciton @ 600 nm

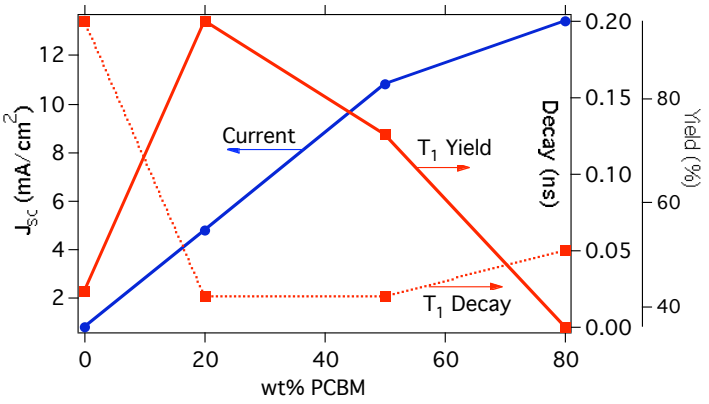

B.
PCBM exciton @ 700 nm

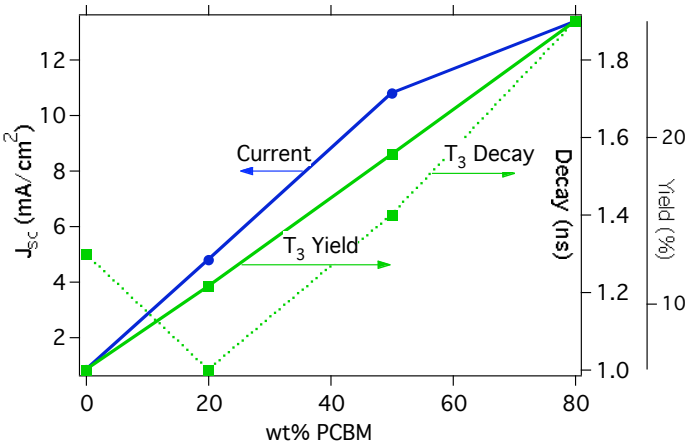

Figure 8.8. Time-decay and % yield of time-components in M3EH-PPV:PCBM blends. (A) Short T1 component detected at 600 nm characteristic of M3EH-PPV emission and (B) Long T3 component detected at 700 nm characteristic of PCBM emission.

At 700 nm the emission from PCBM can be monitored, corresponding to the long 1.2 – 1.9 ns decay time (Figure 8.8B, below). The decay rate of this PCBM component slows and the % yield grows linearly with the wt% of PCBM in the blend, as would be expected for the decay of excitons created within the PCBM aggregates. The PCBM decay is longer for the larger domains present in high wt% blends since the polymer/PCBM interface is less accessible to excitons created within PCBM. The ~1.9 ns PCBM decay is still present in 50 wt% blends, indicating that the domains formed even at this low wt% are larger than the

exciton diffusion length in PCBM, unlike in MDMO-PPV (van Duren, Yang et al. 2004-a). PCBM appears to form larger domains in M3EH-PPV than in other PPV polymers.

These results are presented schematically in Figure 8.10 (see Conclusions).

TRPL on photovoltaic devices

In order to directly probe the relationship between device performance and time-decay of the photoluminescence, the TRPL of working photovoltaic devices was examined. This is a somewhat unusual technique, although some recent work has examined PIA of working photovoltaics under operating conditions (Offermans 2005). The results of three such devices are reported below in Figure 8.9 and their decay components in Table 8.5.

The most striking result is that of Device 1, my best device with a short circuit current of 13 mA/cm^2 and a power efficiency of ~3%. It shows the longest decay of the three, due to a large percentage of a long, 3.5 ns decay component. I attribute this decay component to emission from extremely aggregated sections of PCBM due to its similarity to PCBM's characteristic decay (1.3 – 1.9 ns) at low emission energies. Device 2 was similar to Device 1 in all respects (same thickness, same spin processing speed), but without efficient quenching at short time scales, and its short-circuit current was almost half that of Device 1. Thus, Device 1 may exemplify a near-ideal mix between charge transport (interconnected PCBM aggregates, identified by a long time decay) and charge separation (fast decay at short time scales).

Device 3 was spin-cast at a slower speed (2000 rpm) than the other two devices. This device was dominated by an ultrafast component of 0.03 ns (the limit of the time resolution of our instrument), an order of magnitude faster than Device 1 and two orders of magnitude

faster than Device 2. This may indicate better dispersion of the PCBM within the polymer matrix, although this is in conflict with my previous argument that slow spin-speeds and thicker devices result in large PCBM domains. The current of this device was similar to that of Device 2, indicating that improved dispersion of PCBM is detrimental to charge transport through the PCBM matrix.

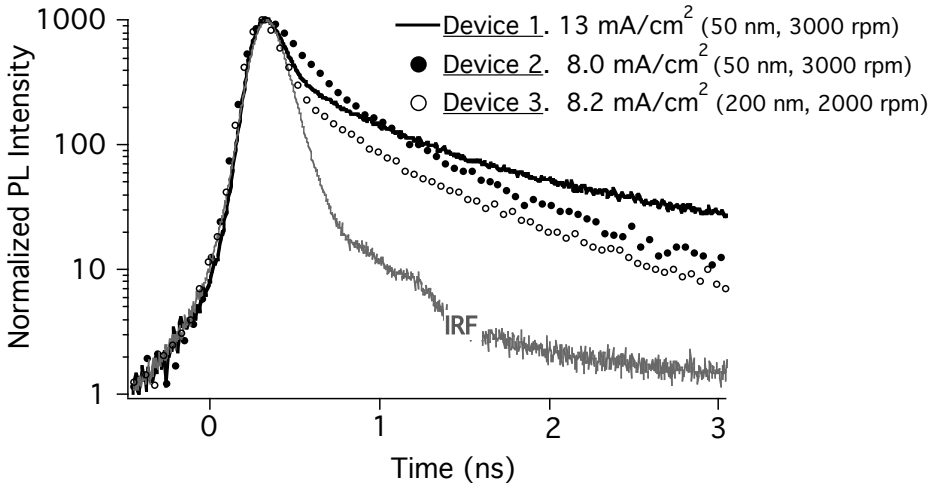

Figure 8.9. Time-decays of three different 1:4 M3EH-PPV:PCBM devices with differing performance. Emission is detected at 600 nm.

Device	J (mA/ cm^2)	Thick - ness (nm)	τ_1 (ns)	Error/ A_1	τ_2 (ns)	Error/ A_2	τ_2 (ns)	Error/ A_3	τ_{ave}
1	13	50	0.03 (32%)	±0.008 0.77	0.58 (32%)	±0.05 0.22	3.5 (31%)	±0.35 0.01	1.3
2	8	50	0.11 (40%)	±0.03 0.96	**0.48 (48%)**	±0.07 0.04	1.9 (11%)	±0.21 < 0.001	0.49
3	8.2	200	**0.03 (52%)**	±0.006 1.0	0.48 (38%)	±0.007 < 0.001	2.4 (10%)	±0.76 < 0.001	0.45

Table 8.5. Time decays of 3 working photovoltaic devices. Emission was detected at 600 nm. Percent of steady-state photoluminescence yield (__%) is reported in parentheses below each decay component. A_i's represent normalized pre-exponential factors, which are uncorrelated with decay time.

8.6 Summary and Conclusions

The perfect morphology for charge generation does not correspond to that for ideal charge-transport in M3EH-PPV:PCBM devices. Charge-transfer from M3EH-PPV to PCBM is most efficient for 20 wt% PCBM blends, as evidenced by efficient quenching of the M3EH-PPV exciton lifetime. At 20 wt% the PCBM is well-dispersed and phase separation is incomplete, resulting in high surface-area ratio between the polymer and PCBM, but a device that is severely transport-limited due to the lack of efficient percolation pathways via well-connected PCBM domains through the device. At 80 wt%, however, large PCBM domains have formed, which decrease the optical density of the film as well as the surface area ratio available for charge dissociation. The resulting percolation pathways through PCBM reduces charge recombination and allows the highly-mobile electrons to dominate the transport, increasing the FF. This boosts the current almost 3X above 20 wt% blends and more than an order of magnitude above pristine M3EH-PPV (see Figure 8.10).

The PCBM domains in M3EH-PPV:PCBM blends appear to be slightly larger than those in MDMO-PPV:PCBM blends, judging by the spectroscopic evidence for emission from aggregated PCBM clusters and the relatively high device performance at 50 wt% PCBM. This could be due to decreased miscibility of M3EH-PPV with PCBM because of incompatible side-chains, or an artifact of the long annealing time (1 hour at 100°C) (Yang, van Duren et al. 2004). This may improve our device performance by creating continuous charge pathways for electrons at lower wt% of PCBM than in MDMO-PPV. Devices remain severely transport-limited, however, as indicated by low FF and a dependence of short-circuit

current upon device thickness. The relatively low FF indicates that the hole and electron mobilities are not well matched in M3EH-PPV:PCBM devices, unlike MDMO-PPV:PCBM. This failure to enhance the hole mobility would account for the low TRPL quenching efficiency in high wt% blends, since holes are less able to reach the interfaces. An understanding of why the hole mobility is enhanced in MDMO-PPV, but not M3EH-PPV, is of interest for material selection for polymer:fullerene solar cells.

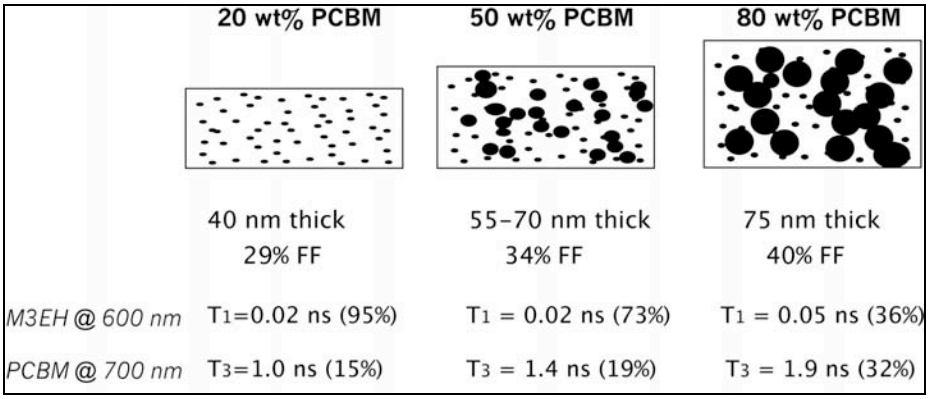

Figure 8.10. Schematic representation of PCBM domain size and dispersion in M3EH-PPV:PCBM blends, with effect on device parameters and time-resolved decay.

Further nanoscale morphological improvements – such as better chain-stacking in the polymer achievable by careful film growth, and smaller, well-dispersed PCBM domains -- should result in enhanced device performance. The photoluminescence is blueshifted as the wt% of PCBM in the blend is increased, suggesting conformational effects such as chain coiling as PCBM is added to the blend. Extended (ie., stretched) chain conformations should lead to a more ordered structure for the polymer matrix and thus better hole transport. The formation of percolation pathways for lower wt% PCBM would also improve device performance through an increase in the optical density of the film and enhanced exciton dissociation.

8.7 References

Aharony, A. and D. Stauffer (1993). Introduction to percolation theory. London, Taylor and Francis.

Brabec, C. J., G. Zerza, et al. (2001). "Tracing photoinduced electron transfer process in conjugated polymer/fullerene bulk heterojunctions in real time." Chem. Phys. Lett. **340**(3-4): 232.

Breeze, A. J., Z. Schlesinger, et al. (2004). "Improving power efficiencies in polymer-polymer blend photovoltaics." Sol. Energy Mater. Sol. Cells **83**: 263.

Byrne, H. J., W. K. Maser, et al. (1995). "Photophysical and photochemical processes in fullerenes under high-intensity illumination." J. Mat. Proc. Tech. **54**: 149.

Choulis, S. A., J. Nelson, et al. (2003). "Investigation of transport properties in polymer/fullerene blends using time-of-flight photocurrent measurements." Appl. Phys. Lett. **83**(18): 3812.

Durstock, M. F., R. J. Spry, et al. (2003). "Investigation of electrostatic self-assembly as a means to fabricate and interfacially modify polymer-based photovoltaic devices." J. Appl. Phys. **94**: 3253.

Halls, J. J. M., K. Pichler, et al. (1996). "Exciton diffusion and dissociation in a poly(p-phenylenevinylene)/C_{60} heterojunction photovoltaic cell." Appl. Phys. Lett. **68**(22): 3120.

Halls, J. J. M., K. Pichler, et al. (1996). "Exciton dissociation at a poly(p-phenylenevinylene)/C_{60} heterojunction." Synth. Met. **77**: 277.

Haugeneder, A., M. Neges, et al. (1999). "Exciton diffusion and dissociation in conjugated polymer/fullerene blends and heterostructures." Phys. Rev. B **59**(23): 15346.

Hoppe, H. (2004). Nanomorphology-efficiency relationship in organic bulk heterojunction plastic solar cells. Ph.D Thesis, Johannes Kepler University Linz.

Hummelen, J. C., B. W. Knight, et al. (1995). "Preparation and characterization of fulleroid and methanofullerene derivatives." J. Org. Chem. **60**: 532.

Kemerink, M., J. K. J. van Duren, et al. (2005). "Substitution and preparation effects on the molecular-scale morphology of PPV films." Macromolecules **38**: 7784.

Li, G., V. Shrotriya, et al. (2005). "High-efficiency solution processable polymer photovoltaic cells by self-organization of polymer blends." Nature **4**(10): Advance Online Publication.

Ma, W., C. Yang, et al. (2005). "Thermally stable, efficient polymer solar cells with nanoscale control of the interpenetrating network morphology." Adv. Func. Mater. **15**(10): Advance Online Publication.

Martens, T., J. D'Haen, et al. (2003). "Disclosure of the nanostructure of MDMO-PPV:PCBM bulk hetero-junction organic solar cells by a combination of SPM and TEM." Synth. Met. **138**: 243.

Melzer, C., E. Koop, et al. (2004). "Hole transport in poly(phenylene vinylene)/methanofullerene bulk heterojunction solar cells." Adv. Func. Mater. **14**: 865.

Meskers, S. C. J., P. A. van Hal, et al. (2000). "Time-resolved infrared-absorption study of photoinduced charge transfer in a polythiophene-methanofullerene composite film." Phys. Rev. B **61**(15): 9917.

Mihailetchi, V. D., L. J. A. Koster, et al. (2005). "Compositional dependence of the performance of poly(p-phenylene vinylene):methanofullerene bulk-heterojunction solar cells." Adv. Func. Mater. **15**: 795.

Mihailetchi, V. D., J. K. J. van Duren, et al. (2003). "Electron transport in a methanofullerene." Adv. Func. Mater. **13**: 43.

Mihailetchi, V. D., J. Wildeman, et al. (2005). "Space-charge limited photocurrent." Phys. Rev. Lett. **94**: 126602.

Nogueira, A. F., I. Montanari, et al. (2003). "Charge recombination in conjugated polymer/fullerene blended films studied by transient absorption spectroscopy." J. Phys. Chem. B **107**: 1567.

Offermans, T. (2005). "Charge carrier dynamics in polymer solar cells: An opto-electronic study." PhD Thesis(University of Eindhoven).

Pacios, R., J. Nelson, et al. (2003). "Composition dependence of electron and hole transport in polyfluorene:[6,6]-phenyl C_{61}-butyric acid methyl ester blend films." Appl. Phys. Lett. **83**(23): 4764.

Riedel, I. and V. Dyakonov (2004). "Influence of electronic transport properties of polymer-fullerene blends on the performance of bulk heterojunction photovoltaic devices." Phys. Status Solidi A **201**(6): 1332.

Sariciftci, N. S., D. Braun, et al. (1993). "Semiconducting polymer-buckminsterfullerence heterojunctions: Diodes, photodiodes, and photovoltaic cells." Appl. Phys. Lett. **62**(6): 585.

Sariciftci, N. S., L. Smilowitz, et al. (1992). "Photoinduced electron transfer from a conducting polymer to buckminsterfullerene." Science **258**: 1474.

Sariciftci, N. S., L. Smilowitz, et al. (1993). "Semiconducting polymers (as donors) and buckminsterfullerene (as acceptor): photinduced electron transfer and heterojunction devices." Synth. Met. **59**: 333.

Savenije, T. J., J. E. Kroeze, et al. (2004). "Mobility and decay kinetics of charge carriers in photoexited PCBM/PPV blends." Phys. Rev. B **69**: 155205.

Shaheen, S. E., C. J. Brabec, et al. (2001). "2.5% efficient organic plastic solar cells." Appl. Phys. Lett. **78**(6): 841.

Theander, M., A. Yartsev, et al. (2000). "Photoluminescence quenching at a polythiophene/C60 heterojunction." Phys. Rev. B **61**(19): 12957.

Vacar, D., E. S. Maniloff, et al. (1997). "Charge-transfer range for photoexcitations in conjugated polymer/fullerene bilayers and blends." Phys. Rev. B **56**(8): 4573.

van Duren, J. K. J., X. Yang, et al. (2004-b). "Relating the morphology of a poly(p-phenylene vinylene)/methanofullerene blend to bulk heterojunction solar cell performance." Proc. SPIE **5215**: 99.

van Duren, J. K. J., X. Yang, et al. (2004-a). "Relating the morphology of poly(p-phenylene vinylene)/Methanofullerene blends to solar-cell performance." Adv. Func. Mater. **14**: 425.

Wang, H. L., M. Grigorova, et al. (1997). "Variations in the optical properties of poly(3-hexylthiophene)/C_{60} blends and poly(3-hexylthiophene)/sol-gel composites." Synth. Met. **84**: 781.

Yang, X., J. K. J. van Duren, et al. (2004). "Morphology and thermal stability of the active layer in poly(p-phenylenevinylene)/methanofullerene plastic photovoltaic devices." Macromolecules **37**: 2151.

Yu, G., J. Gao, et al. (1995). "Polymer photovoltaic cells: enhanced efficiencies via a network of internal donor-acceptor heterojunctions." Science **270**: 1789.

Zerza, G., C. J. Brabec, et al. (2001). "Ultrafast charge transfer in conjugated polymer-fullerene composites." Synth. Met. **119**: 637.

Zhang, F. L., M. Johansson, et al. (2003). "Polymer solar cells based on MEH-PPV and PCBM." Synth. Met. **137**(1-3): 1401.

Chapter 9

Charge separation versus exciton generation: Comparison of blends and layers of M3EH-PPV and CN-ether-PPV

9.1 Abstract

I characterize and compare blended and bilayered heterojunctions of polymer photovoltaic devices using CN-Ether-PPV and M3EH-PPV as electron- and hole-transporting polymers, respectively. I find that both blended and bilayered structures have substantially improved current densities (> 3 mA/cm^2) and power efficiencies (~1% under solar conditions) over neat films. Improved exciton dissociation at multiple interfaces and reduced recombination due to energy and charge transfer increases the charge carrier collection in both types of heterojunction devices, but low electron mobilities in the polymers lead to low fill factors that limit the power efficiency**.** Time-resolved photoluminescence reveals that both the hole and electron-transporting polymers undergo efficient quenching in blended structures. The exciton decay is dominated by the existence of two new fast decay channels of 0.05 ns and 2.0 ns that are assigned to interspecies charge transfer and account for the increased short-circuit current observed. For layers, these new components are not as prevalent. This result indicates that greater exciton generation at the dissociating interface and more efficient charge collection in the thin layers is primarily responsible for the improved short-circuit current, a conclusion that is further supported by numerical simulations. I also report evidence for an intermediate exciplex state in both types of structures with the greatest yield for 1:1 blends. Overall, the improved performance is due to different processes in the two structures; efficient bulk exciton quenching and charge transfer in blends, and enhanced exciton generation and charge collection in layers. The optimization of each photovoltaic heterostructured device relies on this understanding of the mechanisms by which each material architecture achieves high power efficiency.

9.2 Background

Blends of electron-acceptor and -donor materials result in dramatically enhanced device performances and high degrees of photoluminescence quenching relative to their neat film counterparts (Halls, Walsh et al. 1995; Yu, Gao et al. 1995; Yu and Heeger 1995; Arango, Brock et al. 1999; Dittmer, Petritsch et al. 1999; Offermans, van Hal et al. 2005), due in part to multiple, closely spaced, dissociation interfaces and separate charge pathways for the electrons and holes; however, control over domain size and morphology in such films is difficult. Less attention has been afforded to bilayered polymer devices where the large interfacial area between the donor and acceptor provides an additional interface for exciton dissociation, with charge transport expected to be improved over blends due to the potential for more ordered, shorter charge-transport pathways and less probability for bimolecular recombination. In addition, layer thickness is easier to control than domain size although material choice is more limited since the first layer cannot be dissolved in the process of spin-coating the second. Polymer/polymer bilayers such as PPV/BBL(Jenekhe and Yi 2000), MEH-CN-PPV/POPT (Granstrom, Petritsch et al. 1998), and PPyV/PAT6 (Tada, Onoda et al. 1999), polymer/C_{60} (Halls, Pichler et al. 1996; Zhang, Johansson et al. 2003), and polymer/small molecule (Osaheni, Jenekhe et al. 1994; Breeze, Salomon et al. 2002) have shown improved device performance over comparable single-layer films.

A recent study of MEH-PPV/BBL and PPV/BBL bilayers, under proper annealing temperatures and low light intensities, found device efficiencies that reached 1.1% under 80 mW/cm^2 (Alam and Jenekhe 2004). A comparison of blended and layered MEH-PPV:C_{60} devices found higher currents in the blended device (Zhang, Johansson et al. 2003), but

PPV:C_{60} blended cells were found to have poorer charge transport than similar layered devices (Feldrapp, Brutting et al. 1999). Due to the inability to tune the absorption of C_{60} and difficulties in controlling the blend morphology and C_{60} solubility in different polymer films, some effort has been taken to replace the C_{60} with either another nanoparticle or with an electron-transporting polymer. For these systems, no direct comparison between blends and layers of electron- and hole-transporting materials has been undertaken. In this paper, I compare electron- and hole-transporting polymers in blended and layered film morphologies in order to better understand charge generation and transport in these materials. My results suggest a pathway for optimizing the polymer film morphology to achieve greater power efficiency for polymer-based photovoltaics.

MEH-PPV and CN-PPV phase separate on the order of the exciton diffusion length of 20 nm (Halls, Walsh et al. 1995), and MDMO-PPV and PCNEPV phase separate on the order of 30 – 50 nm (Veenstra, Verhees et al. 2004; Loos, Yang et al. 2005) and have been used in blended devices with good results. I expect the phase-separation in M3EH-PPV and CN-ether-PPV to be similar. The selective solubility of M3EH-PPV, which dissolves well in chlorobenzene but poorly in both toluene and p-xylene, allows us to spin-cast layered devices. Thus, CN-ether-PPV in p-xylene spin-cast on top of M3EH-PPV in chlorobenzene should result in layers with relatively low blending of the polymers at the interface. Thus, the choice of these two polymers provides a good opportunity for comparing blended and layered structures.

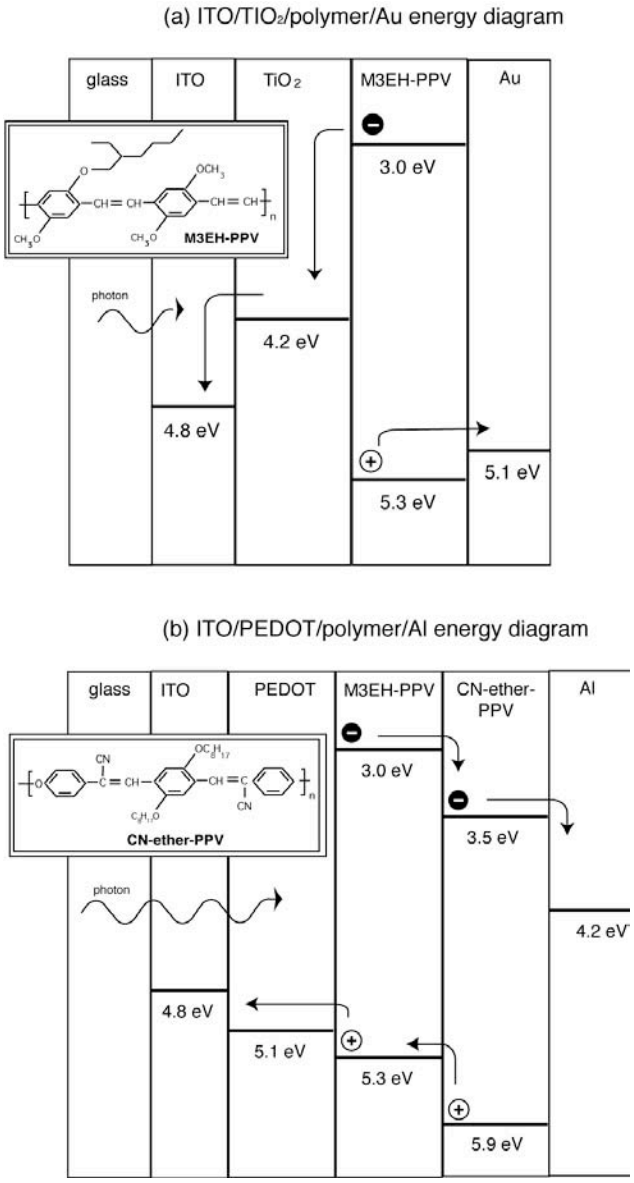

Figure 9.1. Energy level diagrams for different device structures, plus chemical structure of polymers (inset). The PEDOT//Al structure forces holes to cross the bulk from the first incident electrode, whereas the TiO_2//Au structure forces the electrons to cross the bulk.

The heterojunction photovoltaic devices were prepared using two different electrode structures with opposite charge transport polarity. Due to the electric field reversal across device architectures, ITO was sourced negative in TiO_2//Au devices and positive in

PEDOT//Al devices, resulting in J-V curves located in Quadrant IV. The transparent electron-accepting structure ITO/TiO_2/polymer/Au (Figure 9.1a) forces the holes to travel the bulk of the polymer layer, and the transparent hole-accepting structure ITO/PEDOT-PSS/polymer/Al (Figure 9.1b) forces the electrons to travel across the bulk. Neat M3EH-PPV devices and blends of M3EH-PPV:CN-ether-PPV may be fabricated on either structure; however, layered devices are restricted to the PEDOT/M3EH-PPV/CN-ether-PPV/Al structure because of the high solubility of CN-ether-PPV. We were unsuccessful in making photovoltaics with appreciable open circuit voltage from neat CN-ether-PPV films, presumably due to high leakage current, poor mobility in the polymer, or dewetting of CN-ether-PPV from the substrate (Loos, Yang et al. 2005; Quist, Savenije et al. 2005).

9.3 Device characterization

In Figure 9.2 we show typical current-voltage (J-V curves) for optimized devices. Blended and layered devices that are optimized for performance show similar short circuit current densities, up to 3.3 mA/cm^2 at 80 mW/cm^2 white light intensity, more than a threefold improvement over neat M3EH-PPV films on TiO_2 and thirteen fold over M3EH-PPV on PEDOT. We observed more variations in device performance for layered structures, and current densities were higher on average for blends than for layers. Film thicknesses for optimized devices were normally 30 ± 5 nm for each polymer layer, except for layers in which the best device had thicknesses of 20 nm M3EH-PPV/50 nm CN-ether-PPV. Peak power conversion efficiency was 0.35% for plain M3EH-PPV on TiO_2 and ranged from 0.66 to 1% for blended and layered devices, the variability being due to changes in V_{oc} across

device structures. In blends, V_{oc} was adversely affected by an increase in the percent of CN-ether-PPV in the blend, suggesting large leakage in that polymer. Transport in CN-ether-PPV is likely to be disrupted by the presence of ether groups, which disrupt the conjugation and thus intrachain transport. V_{oc} was higher in layers than in blends, indicating that V_{oc} is created by the HOMO/LUMO difference in layers, but by V_{bi} due to the electrodes in blends, a conclusion supported by simulations not reported here (Haerter, Chasteen et al. 2005).

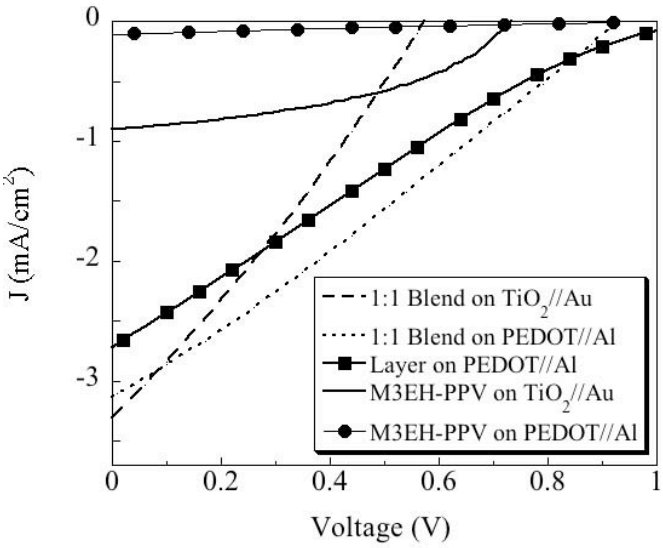

Figure 9.2. J-V Curves for optimized devices showing how the open-circuit voltage, current, and fill factor varies with device architecture. ITO is sourced negative in TiO_2//Au devices, for ease of comparison across architectures. Device thicknesses are 40 ± 10 nm thick, except for the layered device, which is 25 nm M3EH-PPV / 50 nm CN-ether-PPV

The dramatic improvement of device performance of blended and layered devices (J ~3.3 mA/cm^2) over neat M3EH-PPV (J = 0.07 mA/cm^2) films on PEDOT//Al is a strong indication of more efficient exciton dissociation and charge collection. Neat M3EH-PPV devices on TiO_2//Au have current densities (J = 0.9 mA/cm^2) more than 13 times higher than those for M3EH-PPV on PEDOT//Al (J = 0.07 mA/cm^2), due to the poor electron mobility of

M3EH-PPV and the use of a transparent electron-accepting structure that forces the poorly mobile electrons to travel the bulk (Arango, Johnson et al. 2000). Unlike these single-layer M3EH-PPV devices, blended devices performed equally well on both the TiO_2//Au or PEDOT//Al structures. Thus device polarity is no longer a limiting factor in these bulk heterojunction devices and both charge carriers are able to exit the device. When device polarity of layered devices was reversed by deposition of the CN-ether-PPV layer prior to the M3EH-PPV layer (resulting in a partially but not totally blended device), V_{oc} and I_{sc} reversed direction, because the internal electric field is created by the HOMO/LUMO offset of the polymers. This is consistent with the assumption that holes exit the device through M3EH-PPV and electrons through the CN-ether-PPV, following separate charge pathways thus minimizing recombination.

Blend ratios

I tested a variety of blend ratios from 20:1 to 1:10 M3EH-PPV:CN-ether-PPV (see Figure 9.3A). Blend ratios of 1:1 by weight exhibited the highest currents and power efficiencies. Other groups examining related MEH-PPV:CN-PPV blends have used a variety of blend ratios from 1:10 to 1:14, and found the most efficient quenching with 5:2 to 5:1 blends, indicative of a difference in the relative charge carrier mobilities in the two systems. The fill factor plummeted as I increased the percent of CN-ether-PPV in the blend, with typical values above 40% for TiO_2/M3EH-PPV/Au and 30% for blends on TiO_2//Au (25% on PEDOT//Al). Layered devices were also compromised by these low fill factors, around 25%. The decrease in fill factor is consistent with relatively poor electron transport in the CN-ether-PPV, and with previous studies on MDMO-PPV:CN-ether-PPV blends (Veenstra,

Verhees et al. 2004; Quist, Savenije et al. 2005). The plot of current and FF versus wt% of CN-ether-PPV (Figure 9.3B) is in stark contrast to that for wt% of PCBM in Chapter 8. The mechanism responsible for the increase in current in these blends (namely, enhanced interfacial area) is not also responsible for increased charge transport.

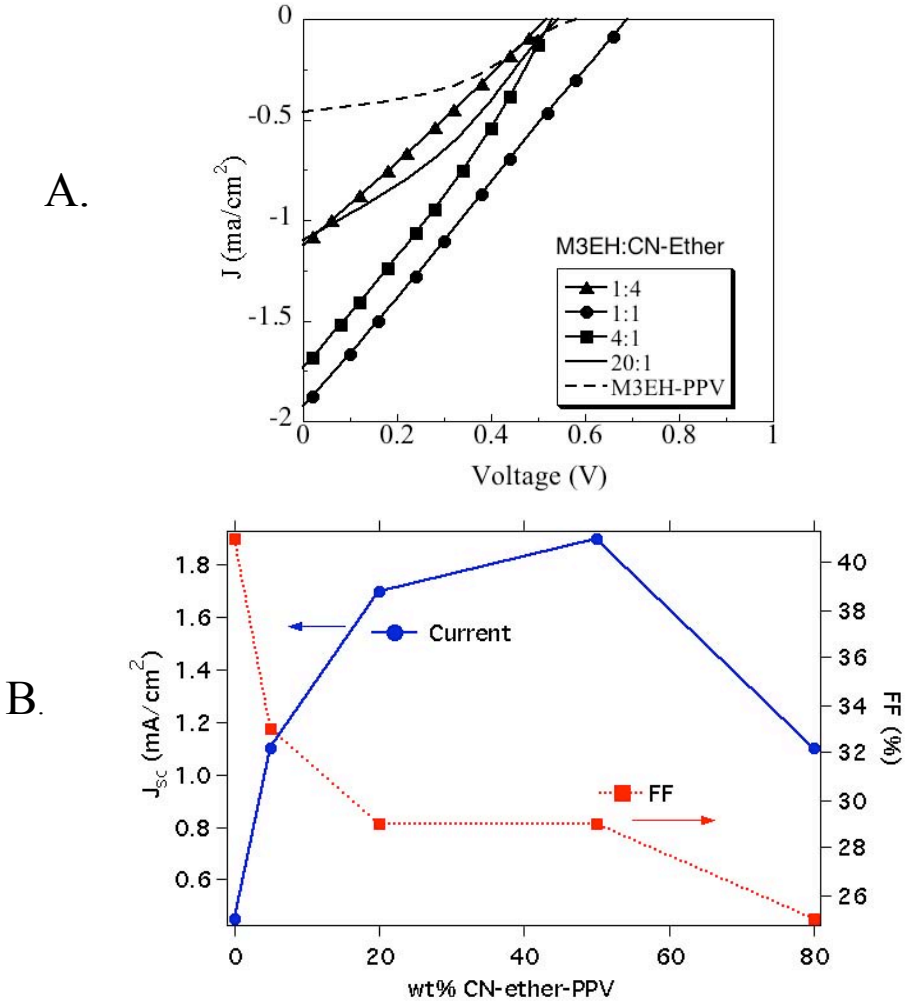

Figure 9.3. (A) J-V Curves for various blend ratios showing the increase in short-circuit current for blends over neat films, and (B) FF and current versus wt% of CN-ether-PPV. Optimal current occurs for 1:1 blends. The fill factor is reduced as CN-ether-PPV concentration increases. All devices are on TiO_2//Au structure and are 55 ± 15 nm thick. Reported ratios are M3EH-PPV:CN-ether-PPV.

External quantum efficiency

External quantum efficiency was measured for a variety of blend ratios (see Figure 9.4). Maximum external quantum efficiency was 24% for blends, 15% for layers, and 7% for neat M3EH-PPV films. Both polymers contribute significantly to the photocurrent; the high contribution of CN-ether-PPV is surprising given its low absorption relative to M3EH-PPV. The long lifetime for charge carriers in CN-ether-PPV allows them to diffuse further to quenching sites, making CN-ether-PPV a particularly efficient source of charge carriers. Peak EQE was about 24% for the best 1:1 blended device; a significant improvement over M3EH-PPV (7%).

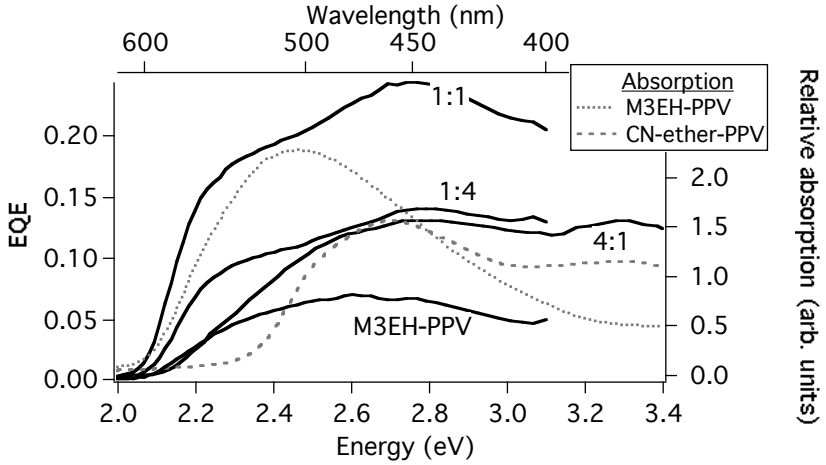

Figure 9.4. EQE and absorption curves for varying ratios of M3EH-PPV:CN-ether-PPV blends.

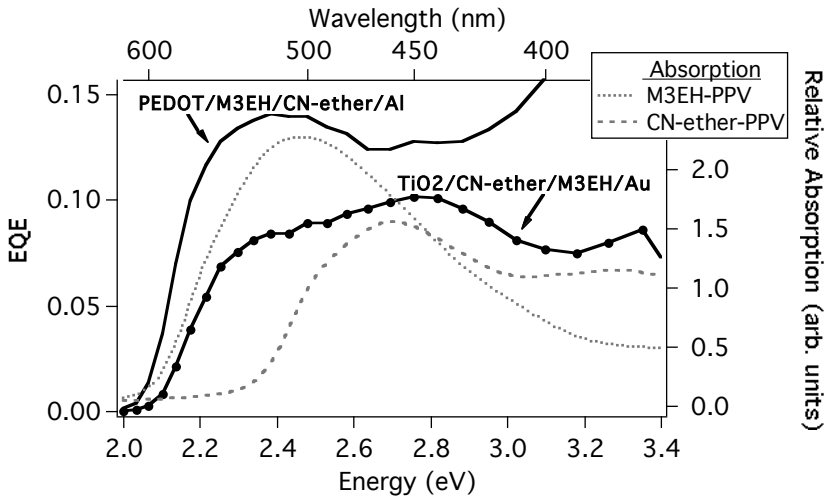

Figure 9.5. EQE and absorption curves for layers of M3EH-PPV and CN-ether-PPV. Illumination is through PEDOT or TiO_2. TiO_2/CN-ether-PPV/M3EH-PPV/Au devices will be slightly blended due to the use of a common solvent.

The external quantum efficiency of blended and layered devices was mostly symbatic with the absorption curves of the neat films, indicating efficient charge separation throughout the bulk. Layer EQE was slightly antibatic with CN-ether-PPV (see Figure 9.5) perhaps due to reflection from the aluminum electrode; a conclusion supported by simulations (see Section 9.5). This behavior disappeared when the layer order was switched, such that light was first incident upon M3EH-PPV. This evidence points towards the electrode/M3EH-PPV and the M3EH-PPV/CN-ether-PPV interfaces as being the important areas for exciton dissociation, rather than the CN-ether-PPV/electrode interface, though there is some variability in quantum efficiency curves indicating variability in film morphology across devices.

Surface morphology

No surface features could be seen via AFM in these blends, unlike blends with CN-PPV (see Figure 9.6 below). Thus, CN-ether-PPV and M3EH-PPV intermix well, without forming aggregated features. Phase separation is most likely on the ~ 20 nm scale, as I do not observe it in AFM measurements.

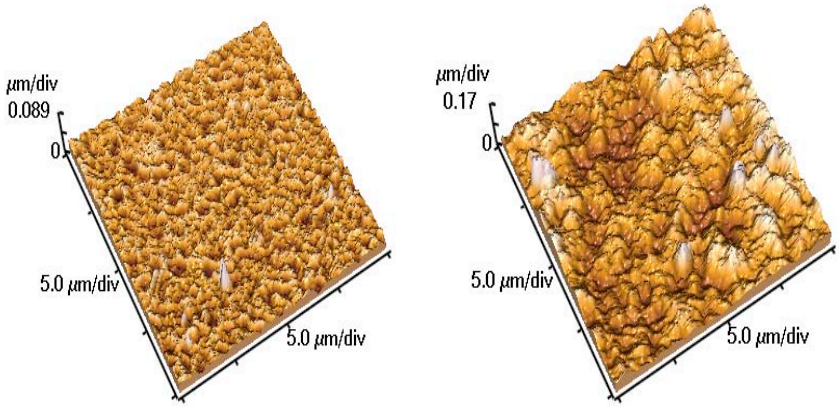

Figure 9.6. AFM images showing increase in aggregated structures in M3EH-PPV:CN-PPV blends as the wt% of CN-PPV is increased from 20% (left) to 80% (right). M3EH-PPV:CN-ether-PPV films, on the other hand, are featureless for all blend ratios.

All blended devices were transport-limited, not absorption-limited. Current density decreased as the thickness of the device was increased, for neat M3EH-PPV devices and 1:1 blends of M3EH-PPV:CN-ether-PPV. The current of blended devices fell by nearly a factor of 2 from a 30 nm to a 90 nm thick film. This is similar to findings in neat-film devices where the drop is more appreciable (Arango, Johnson et al. 2000; Breeze, Schlesinger et al. 2001). Poor charge transport is due in part to the poor electron transport in CN-ether-PPV, charge hopping from domain to domain in phase-separated blends and domain sizes that may be larger than the exciton diffusion length in M3EH-PPV (<10 nm).

Layered devices

For layered devices, the relationship between device performance and layer thickness was less clear (see Figure 9.7). The best device was comprised of 25 nm M3EH-PPV / 50 nm CN-ether-PPV layers, slightly thicker than equal layer thicknesses of 30 nm which also gave good results. In general, device performance decreased with M3EH-PPV thickness. Similar data was observed for PPV/BBL bilayer devices, where layers of 50 nm each gave the best device performance (Jenekhe and Yi 2000). To understand the changes that occur in my layered devices with thickness, I had to consider how optical interference and absorption affected the exciton generation rate. These simulations are discussed in Section 9.7.

The increased current density for layered heterojunction devices is caused in part by greater exciton dissocation due to increased interfacial area. However, since the layer structure can only account for at most a doubling or tripling of the interfacial area available for charge dissociation, the enhanced interfacial area cannot account for the thirteen-fold current increase of a layered device over neat M3EH-PPV film as shown in Figure 9.2. The exact surface roughness is unknown, although there appears to be about 10 nm of interpenetration of the layers (see next paragraph). Thus, the current increase is attributable to increased charge collection in thinner polymer layers and reduced charge recombination due to separate charge pathways and subsequent greater efficiency of charge collection.

An unexpected result of my device measurements was the similarity in the performance of optimized blended and layered devices (although on average, blends outperformed layers) despite drastically different morphology. Nonetheless, time-resolved measurements and device simulations suggest that different mechanisms are responsible for device performance enhancement. The similarity could suggest some interpenetration of the

layers at the polymer/polymer interface in layered devices, resulting in a somewhat blended device. The total device thickness was consistently ~10 nm thinner compared to the combined thicknesses of each polymer layer spun alone, suggesting about 10 nm of commingling at the interface. Spectroscopy data, discussed in Section 9.4 below, suggest that the recombination pathways in the 30 nm M3EH-PPV / 30 nm CN-ether-PPV layered device are very different than 1:1 M3EH-PPV:CN-ether-PPV devices, and similar to a 1:6 M3EH-PPV:CN-ether-PPV device. Thus, if there is blending at the interface, it is incomplete.

9.4 Steady-state spectroscopy

Relative absorption and photoluminescence spectra for blended films are shown in Figure 9.7, and for layered films in Figure 9.8. In both blended and layered films, the absorption curve closely matched a linear combination of the composite polymers, with roughly equal weight. This result implies (a) that the polymers are not interacting in the ground state (e.g., to form additional aggregate species), and (b) that equal weight fractions correspond roughly to equal volume fractions in film. Because I observe a factor of two greater absorption coefficient in M3EH-PPV compared to CN-ether-PPV, appreciably greater exciton generation is expected to occur in M3EH-PPV for similar film thickness.

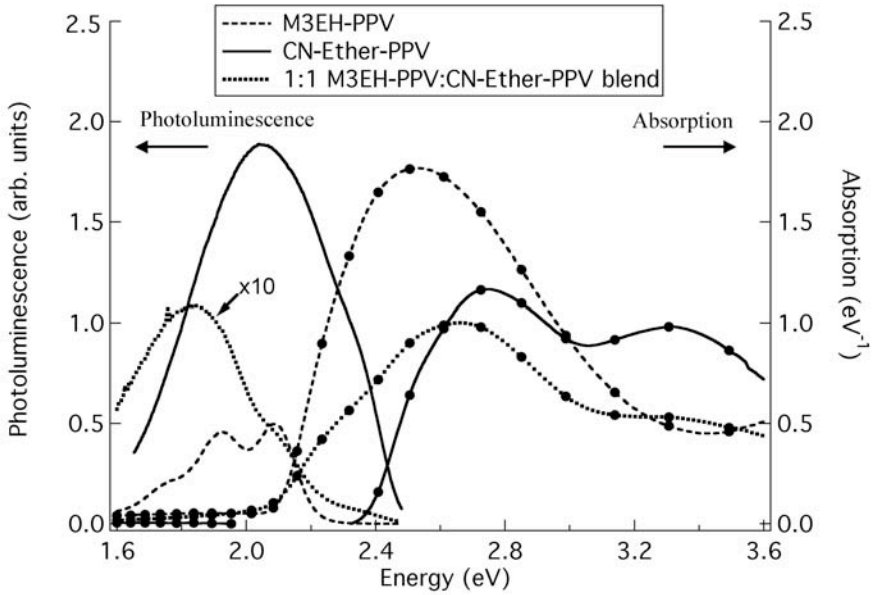

Figure 9.7. Relative photoluminescence and absorption for M3EH-PPV, CN-ether-PPV, and blended films on quartz substrates. Absorption spectra are marked with circles. All films are 100±15nm thick. Relative photoluminescence data was excited at 600 nm and was corrected for optical density of the film. Relative PL data has a 20% margin of error in reproducibility.

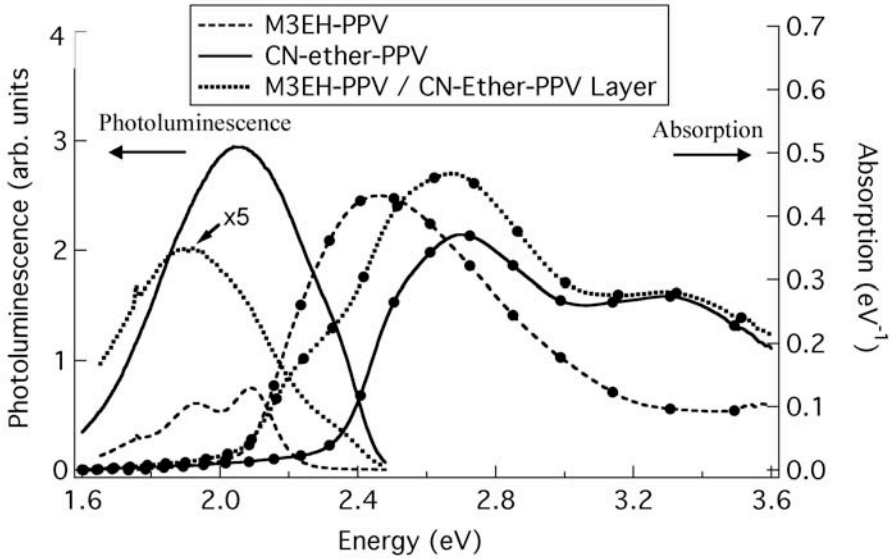

Figure 9.8. Relative photoluminescence and absorption for M3EH-PPV, CN-ether-PPV, and layered films on quartz substrates, showing quenching in the layered film. Absorption spectra are marked with circles. Layered sample consists of 20±5nm thick layers. Layered device absorption is a 1+1 linear combination of M3EH-PPV and CN-ether-PPV absorption. Other parameters are as in Figure 9.7.

Relative photoluminescence measurements revealed that both blends and layers were strongly quenched relative to the neat films. The 20 nm /20 nm layers were quenched by 87% relative to 20nm CN-ether-PPV, and a 100 nm 1:1 blend was quenched by 94% relative to 100 nm CN-ether-PPV, indicating more efficient exciton dissociation and reduced recombination in heterojunctions as expected. The photoluminescence peak of highly luminescent CN-ether-PPV is strongly quenched in the steady state. Some of this quenching in the 2.1 – 2.4 eV range could be due to Foerster energy transfer from CN-ether-PPV to M3EH-PPV since considerable overlap occurs between the photoluminescence spectrum of CN-ether-PPV and the absorption spectrum of M3EH-PPV in that region.

The photoluminescence of heterojunction films peaks at about 1.9 eV in layers and 1.8 eV in blends. The spectra for blends or for layers differs significantly from a linear combination of neat films, even considering a higher weight of M3EH-PPV emission than expected due to Foerster transfer. I take the new 1.8 eV peak in blends and the PL shift in layers to be indicative of a charge-transfer state between an electron on CN-ether-PPV and a hole on M3EH-PPV (an energy gap of 1.8 eV), i.e., an exciplex. Exciplexes have been reported only a few times previously in π-conjugated polymers (Osaheni and Jenekhe 1994; Alam and Jenekhe 2004; Morteani, Sreearunothai et al. 2004), including a recent study using a blend of MDMO-PPV and an ether-substituted CN-PPV similar to what we term CN-ether-PPV which reported an exciplex peak at 1.85 eV (Offermans, van Hal et al. 2005).

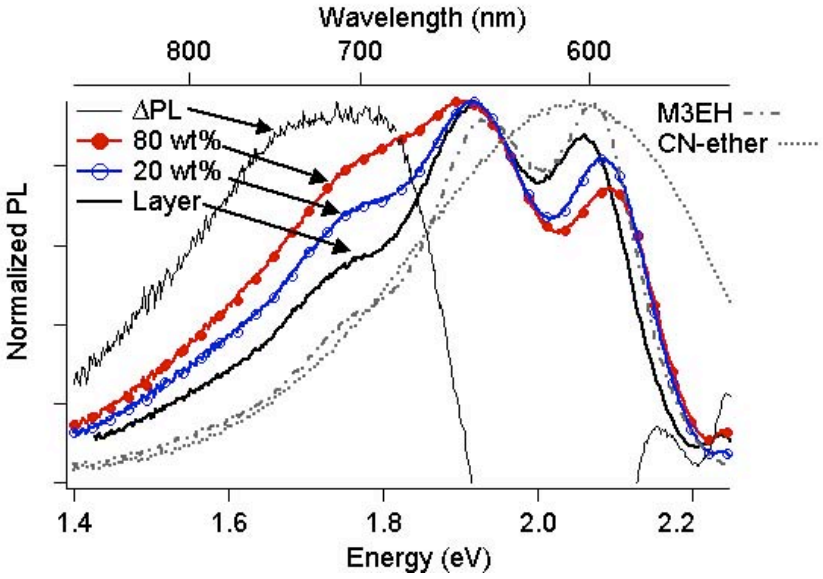

Figure 9.9. Normalized photoluminescence from blended and layered films excited at 540 nm (M3EH-PPV absorption). Wt% refers to the wt% of CN-ether-PPV in the blend; the spectrum of 50wt% was similar to that of 80wt%. The ΔPL is a subtraction of the M3EH-PPV spectrum from that of the 80wt% blend. Vibronic peak heights in the M3EH-PPV spectrum are consistent with peak shifts with varying thickness of the M3EH-PPV layer and are not important in the current analysis.

The existence of an exciplex or similar charge-transfer state in both types of heterostructures is supported by the fact that neither layers nor 1:1 blends exhibit the characteristic photoluminescence of M3EH-PPV when excitation is shifted to 540 nm, where only M3EH-PPV absorbs. Instead, the peak at 1.8 eV remains or shifts, while the characteristic emission of M3EH-PPV becomes more apparent, as shown in Figure 9.9 above, suggesting that charge transfer occurs from M3EH-PPV to CN-ether-PPV. The exciplex peak intensity increases slightly with increased wt% of CN-ether-PPV, suggesting that charge transfer also occurs from CN-ether-PPV to M3EH-PPV. Offermans, van Hal, et al. were able to determine that photogeneration of either polymer component resulted in the formation of an exciplex within 100 ps after excitation; this is likely to be the case in my system as well. The presence of neat-film photoluminescence indicates that radiative recombination also

takes place within each polymer as well as within the exciplex. CN-ether-PPV emission is notably absent.

9.5 Time-resolved fluorescence

Results for 600 nm emission (PL peak of both polymers) are given in Table 9.1. Decays were force-fit to triple and quadruple exponentials for neat films and heterojunctions, respectively. Attempts to fit to fewer parameters resulted in poor fits, as demonstrated by the fact that the reduced chisquare at least doubled; all reported fits have reduced chisquares of 1.0 or 1.1. While previous groups have found equally good fits for stretched exponentials in MEH-PPV (Smilowitz, Hays et al. 1993), representing diffusion of carriers after separation and prior to recombination, the repeatability of decay components across samples and heterojunctions is convincing evidence that the measured decays are intrinsic features of these films. This number of exponentials indicates the presence of multiple exciton decay mechanisms as could be expected from thin polymer films where interchain and intrachain dynamics, as well as charge transfer, can all lead to distinct decay species. Interconversion between these species means that these decay times may not represent the lifetimes of the constituent species. Energy transfer between the ground and excited states should not play a significant role at 600 nm due to the low absorption of M3EH-PPV at that energy.

The decay of CN-ether-PPV was dominated by a long component of 12.2 ns (66%), which I take to be the interchain exciton, or excimer, and a secondary component of 4.3 ns (26%), which I take to be the intrachain exciton, as argued in Chapter 6. The decay of 60 nm thick M3EH-PPV was dominated by components of 0.20 ns (43%) and 0.45 ns (53%), and

the decay of 10 nm thick M3EH-PPV was dominated by components of 0.10 ns (59%) and 0.30 ns (34%). Hypotheses for these differences in M3EH-PPV decay are given in Chapter 5.

A. 600 nm emission (M3EH-PPV peak)

Film	τ_1 (ns)	τ_2 (ns)	τ_3 (ns)	τ_4 (ns)	Average τ (ns)
M3EH-PPV (60 nm)	0.20 ± 0.04 (43%)	**0.45** ± 0.09 **(53%)**			0.38
M3EH-PPV (10 nm)	**0.10** ± 0.03 **(59%)**	0.30 ± 0.1 (34%)			0.27
20 wt% CN-ether	**0.05** ± 0.006 **(52%)**	0.46 ± 0.05 (27%)	2.0 ± 0.21 (18%)		0.86
50 wt% CN-ether	**0.05** ± 0.002 **(51%)**	0.46 ± 0.02 (20%)	2.0 ± 0.08 (22%)		1.0
80 wt% CN-ether	**0.05** ± 0.007 **(30%)**	0.46 ± 0.05 (25%)	2.0 ± 0.2 (25%)	7.8 ± 0.45 (19%)	5.7
50nm/50nm Layer	**0.05** ± 0.006 **(39%)**	0.46 ± 0.05 (17%)	2.0 ± 0.2 (27%)	6.9 ± 1.4 (17%)	1.8
100 wt% CN-ether-PPV			4.3 ± 0.12 (26%)	**12.2** ± 0.09 **(73%)**	10.0

B. 700 nm emission (exciplex peak)

Film	τ_1 (ns)	τ_2 (ns)	τ_3 (ns)	τ_4 (ns)	Average τ (ns)
M3EH-PPV (60 nm)	0.20 ± 0.01 (41%)	**0.45** ± 0.02 **(52%)**			0.41
M3EH-PPV (10 nm)	**0.10** ± 0.04 **(48%)**	0.30 ± 0.1 (39%)			0.35
20 wt% CN-ether	0.06 (22%)	0.48 (22%)	**2.1 (47%)**	9.2 (10%)	2.0
50 wt% CN-ether	0.06 ± 0.002 (9%)	0.48 ± 0.03 (13%)	**1.9** ± 0.06 **(50%)**	4.9 ± 0.17 (28%)	2.5
80 wt% CN-ether	0.06 ± 0.01 (4%)	0.71 ± 0.08 (16%)	**3.1** ± 0.17 **(55%)**	9.7 ± 0. 5 (24%)	4.2
50nm/50nm Layer	0.06 ± 0.01 (6%)	0.85 ± 0.05 (18%)	**3.1** ± 0.15 **(59%)**	9.6 ± 0.59 (16%)	3.6
100 wt% CN-ether-PPV			6.2 ± 0.14 (31%)	**13.9** ± 0.12 **(69%)**	11.6

Table 9.1. Decay parameters at (A) 600 nm and (B) 700nm, by wt% of CN-ether-PPV. Reduced χ^2 is 1.0-1.2 and DW is 1.7-1.9 for all samples except for layer, which is a slightly poorer fit. First three decay components are forced to global values for blended samples.

A. CN-ether-PPV heterojunctions

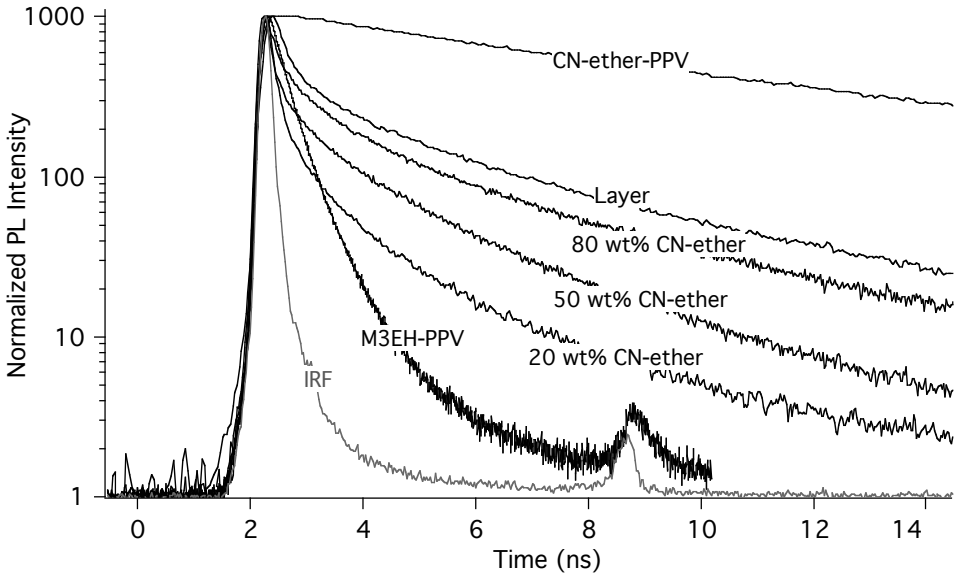

B. CN-ether-PPV vs PCBM heterojunctions

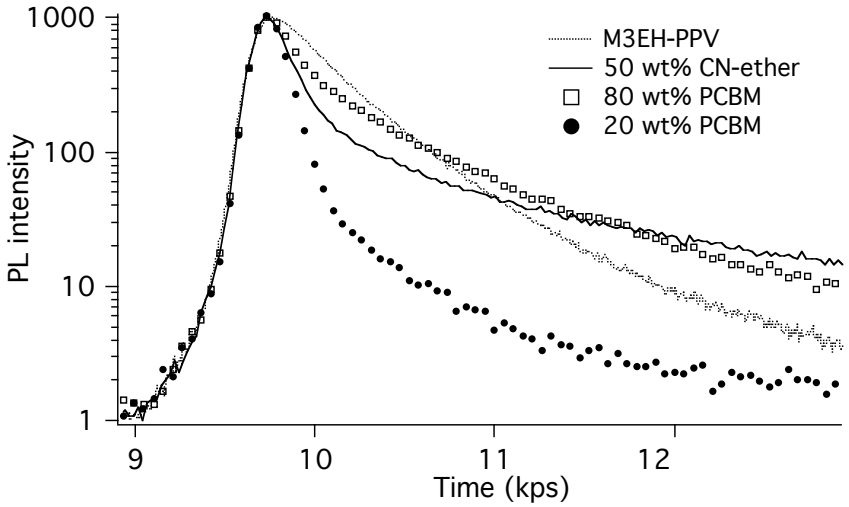

Figure 9.10. Decay curves for (A) M3EH-PPV, CN-ether-PPV, and heterojunctions at 650 nm emission and (B) M3EH-PPV, 50wt% CN-ether-PPV blend, and 20wt% and 80wt% PCBM blend at 600 nm emission. All films are 60 – 100 nm thick.

Decay times increase with additional wt% of CN-ether-PPV (see Figure 9.10A and Table 9.1), as would be expected by a simple linear combination of the decay components of the pristine polymers. The decay of the layered device is approximately equal to the measured decay of an 85 wt% (1:6) blend. The dominant component of M3EH-PPV is absent or shortened, and the dominant 12 ns component of CN-ether-PPV contributes negligibly to the excited state population (as measured by the normalized pre-exponential factor, not reported). This indicates that charge transfer in these heterojunctions out-competes recombination and that the excitons transfer between polymer states by hopping, exciton dissociation, or transfer to the acceptor polymer or to an excited state complex such as an exciplex.

I note that 1:1 blends decay substantially faster than layers, despite similar short-circuit currents in devices, suggesting that charge-transfer throughout the bulk is responsible for increased current in blends but not in layers. Layered film decay components were extremely variable, indicating differing morphologies within the film; the reported decay was chosen due to its similarity to that measured for a working layered photovoltaic device (J_{sc} = 2.2 mA/cm^2). Many layered films contained decay components characteristic of both M3EH-PPV and CN-ether-PPV suggesting lower rates of charge transfer in layers versus blends.

The rising edge for different heterojunctions varies, indicating a delayed luminescence in some samples as would be expected by interconversion between excited species within each polymer. Thus, as stated in Chapter 2, the decay times measured experimentally are no longer *lifetimes* but rather *decay times.* The lifetimes would need to be extracted from these decay times, which are now solutions to quadratic equation (Lakowicz

1999). This limits the physical meaning that may be assigned to the photoluminescence decay.

A new, fast 0.05 ns component is present for all heterojunctions, which I consider to be the 0.30 - 0.45 ns dominant M3EH-PPV component shortened due to a competing rate constant for charge transfer to CN-ether-PPV. This conclusion is supported by the increased yield and weight of the 0.05 ns component at higher emission energies, where the steady-state PL is dominated by M3EH-PPV, as well as the increased yield in blends with low wt% of CN-ether-PPV, similar to the behavior of the ultrafast component in M3EH-PPV:PCBM blends (Chapter 8). The substantially lower weight and longer decay time of this fast component compared to the best quenched M3EH-PPV:PCBM films (Figure 9.9B) would imply that either M3EH-PPV:CN-ether-PPV blends form larger domains than M3EH-PPV:PCBM (limiting exciton dissociation) or that CN-ether-PPV is not as good as an electron-acceptor as PCBM. In either case, the short circuit current would be lower for the polymer:polymer blend than for polymer:PCBM, as observed experimentally. The decay in PCBM blends is not as rapid compared to CN-ether-PPV blends as would be expected by the 10X improvement in short-circuit current, but it is important to remember that the majority of quenching in PCBM systems occurs on a timescale faster than our instrumentation can measure.

Because of the differing photoluminescence efficiencies of the pristine polymers, and the differing wt% in the blends, it is difficult to compare decay component yields across samples, and the normalized weights (pre-exponential factors) are a useful measure. Inspection of these weights reveals that the weights of the fast 0.05 ns component near the emission peak of M3EH-PPV are roughly similar (~0.90) for different samples, suggesting

that at 20 wt% CN-ether-PPV all singlet excitons are quenched, but 50 wt% offers more efficient charge transport. As in blends with PCBM, percolation pathways are just as important as efficient charge separation.

Of particular interest is the decay near 1.8 eV (690 nm) – the photoluminescence peak of the exciplex. Table 9.1B presents decay components at 700 nm (force fit to global values where possible), and Tables 9.2, 9.3, and 9.4 present spectral dependence of the decay parameters (float fits). The dominant decay component shifts from 0.05 ns at 600 nm to 1.9 – 3.1 ns at 700 nm for all heterojunctions, and the shift is less pronounced for samples with lower exciplex emission in the steady-state. This 1.9 – 3.1 ns decay component could be decay from the exciplex itself, although this lifetime would be expected to be much longer (~ 50 ns) as previously reported (Osaheni and Jenekhe 1994; Zhang, Kale et al. 2002; Morteani, Sreearunothai et al. 2004). Another possibility is that this decay is a shortened exciplex lifetime due to conversion to the triplet state: it is similar to the 1.6 ns decay time observed by Offermans et al. on blends of MDMO-PPV:CN-ether-PPV, who used PIA to determine that decay to the triplet state of the hole-transporting polymer comprised a significant loss channel for the exciplex, which at least partially accounts for its short lifetime (Offermans, van Hal et al. 2005). Loss to the triplet state is undesirable, as it will tend to compromise device performance.

Emission (nm)	τ_1 (ns)	τ_2 (ns)	τ_3 (ns)	τ_4 (ns)	Average τ
600	**0.05 (54%)**	0.44 (26%)	1.9 (18%)	9.1 (4%)	0.86
650	**0.06 (40%)**	0.47 (23%)	2.0 (30%)	8.4 (7%)	1.3
700	0.07 (24%)	0.67 (27%)	**2.4 (41%)**	10.4 (8%)	2.0
750	0.08 (15%)	0.75 (27%)	**2.5 (47%)**	11.9 (9%)	2.5

Table 9.2. Decay components in 4:1 M3EH-PPV:CN-ether-PPV (20 wt%); float fit.

Emission (nm)	τ_1 (ns)	τ_2 (ns)	τ_3 (ns)	τ_4 (ns)	Average τ
600	**0.04 (48%)**	0.38 (19%)	1.7 (24%)		1.0
650	0.05 (22%)	0.58 (20%)	**2.4 (47%)**	7.2 (11%)	2.0
700	0.08 (11%)	0.80 (22%)	**2.7 (57%)**	8.8 (10%)	2.5
750	0.10 (7%)	0.91 (23%)	**2.7 (59%)**	9.4 (10%)	2.8

Table 9.3. Decay components in 1:1 M3EH-PPV:CN-ether-PPV (50 wt%); float fit.

Emission (nm)	τ_1 (ns)	τ_2 (ns)	τ_3 (ns)	τ_4 (ns)	Average τ
600	**0.06 (57%)**	0.31 (25%)	1.4 (11%)	6.6 (6%)	0.70
650	**0.06 (31%)**	0.46 (25%)	2.2 (27%)	8.1 (18%)	2.1
700	0.07 (11%)	0.69 (20%)	**3.1 (45%)**	9.3 (23%)	3.8
750	0.09 (5%)	0.87 (18%)	**3.4 (55%)**	10.2 (21%)	4.2

Table 9.4. Decay components in 1:4 M3EH-PPV:CN-ether-PPV (80 wt%); float fit.

Emission (nm)	τ_1 (ns)	τ_2 (ns)	τ_3 (ns)	τ_4 (ns)	Average τ
600	**0.04 (37%)**	0.40 (18%)	2.1 (29%)	7.2 (16%)	1.8
650	0.06 (14%)	0.66 (18%)	**2.9 (51%)**	9.0 (16%)	3.1
700	0.06 (6%)	0.85 (18%)	**3.1 (59%)**	9.5 (16%)	3.6
750	0.07 (4%)	0.91 (17%)	**3.1 (62%)**	9.6 (16%)	3.6

Table 9.5. Decay components in M3EH-PPV/CN-ether-PPV, 100 nm thick; float fit.

An alternative explanation for the 2.4 – 3.4 ns decay is delayed luminescence from M3EH-PPV due to decay of singlet excitons formed from the thermally excited exciplex, as observed in other systems (Barker, Ramsdale et al. 2003). This new component does not appear to be due to CN-ether-PPV decay because (a) its yield does not increase with wt% of CN-ether-PPV in the blend, and (b) its yield is not correlated with that of the 9.4 – 11.9 ns

residual excimer decay from CN-ether-PPV. In devices, this would result in increased probability of charge separation since the exciplex would act as an exciton scavenger bound to the interface, and its subsequent release of that stored energy provides a second chance for charge dissociation.

The decay of the 30 nm / 30 nm M3EH-PPV/CN-ether-PPV layer is strikingly similar (as is the steady-state photoluminescence) to the 1:6 blend, and contains the decay components of pristine CN-ether-PPV. The planar layer is either similarly ineffective as a low M3EH-PPV ratio at quenching the excitons in CN-ether-PPV, or the layer is partially blended at the interface. CN-ether-PPV chains at this interface are unlikely to be quenched if the polymer chain does not lie flat along the interface. The decay components of M3EH-PPV, however, are efficiently quenched in this planar layer, probably by the same mechanism creating low luminescence in the pristine M3EH-PPV polymer; namely, efficient energy transfer that allows charges to visit quenching sites, either intrinsic or external.

In summary, layers achieve higher power efficiency than neat films by a substantially different mechanism than do blends. The excited state kinetics of layers and 1:1 blends varies dramatically despite similarities in J-V curves, and the decays of layers approximates that of a 1:6 blend despite the superior current of layered devices. However, because the PEDOT//Al device geometry results in the M3EH-PPV absorbing an appreciable amount of the photons before the CN-ether-PPV, a much larger fraction of excitons is expected to be generated in M3EH-PPV compared to CN-ether-PPV. Therefore, the layers could also achieve more efficient charge collection of excitons generated in the M3EH-PPV layers due to the ability to make much thinner layers (i.e. 25 nm) without shorting. The highest short circuit currents for layers consisted of very thin M3EH-PPV films (25 nm) and relatively

thick CN-ether-PPV films (50 nm) implying that both effects may contribute. To gain further insight into what mechanism is responsible for the increased power efficiency in layers versus neat films, we conducted numerical simulations as described below.

9.6 Modeling J-V characteristics of bilayer devices

We developed a model to simulate both exciton generation rate as a function of position and current-voltage curves for bilayer devices*. A one-dimensional numerical model was used to describe absorption of incident light, charge generation, and charge transport within the bilayer device. The model allowed us to calculate current-voltage characteristics for several device thicknesses and architectures where we assume a sharp interface between the donor and acceptor layers and between the electrodes and the organic material. The effect of blending as well as more detailed predictions of the model are considered elsewhere (Haerter, Chasteen et al. 2005) and I refer the interested reader to that publication for details of the simulations. The parameters and assumptions used in the simulation are reported in Appendix 4.

Results

The J-V curves from experiment are shown in Figure 9.11, and comparison of the short-circuit current for experiment and simulation are shown in Figure 9.12. Short-circuit current and fill factors are twice as high in simulation as in experiment, probably due to artificially high mobilities in simulations, but thickness dependence exhibits the same

* The simulations reported in this section were developed and run by colleague Jan Haerter, based upon a program created by J. C. Scott at IBM

behavior and is robust across a variety of simulations with different mobilities. In agreement with experiment, numerical simulations indicate that J_{sc} increases roughly linearly as the M3EH-PPV thickness decreases, as expected for transport-limited devices. CN-ether-PPV thickness was inversely proportional to J_{sc}; charge-transport is therefore not the crucial factor in the thickness of the CN-ether-PPV layer. Out of those layer thicknesses modeled, 25 nm / 50 nm M3EH-PPV/CN-ether-PPV gave the best J_{sc}, and 65 nm/25 nm gave the worst. This is roughly paralleled by experimental data that shows similar relative performance for comparable device thicknesses.

Open-circuit voltages of 1.2 V are comparable between experiment and simulations. The simulations further reveal that the clear tail near V_{oc} that gives rise to a relatively large V_{oc} of ~1.2 V is due to the build of space charge. For layers, when the applied voltage equals the difference in the work-functions of PEDOT and Al (~0.8 eV), the drift current is zero; however, the diffusion current still remains and is directed towards the contacts because electrons are less likely to jump to the LUMO level of the M3EH-PPV than to randomly diffuse to the Al electrode (and vice-versa for holes). At 0 V, space charge effects become more important, and a significant diffusion current resides in the device structure due to the charge carrier concentration gradient, even with no built-in potential across the device. Similar effects have been observed in simulations of layered films of F8BT/PFB (Barker, Ramsdale et al. 2003). The contribution of diffusion to V_{oc} in blended structures is less significant because a well-defined charge barrier does not exist in the blended device due to the interpenetration of the electron and hole-transporting species.

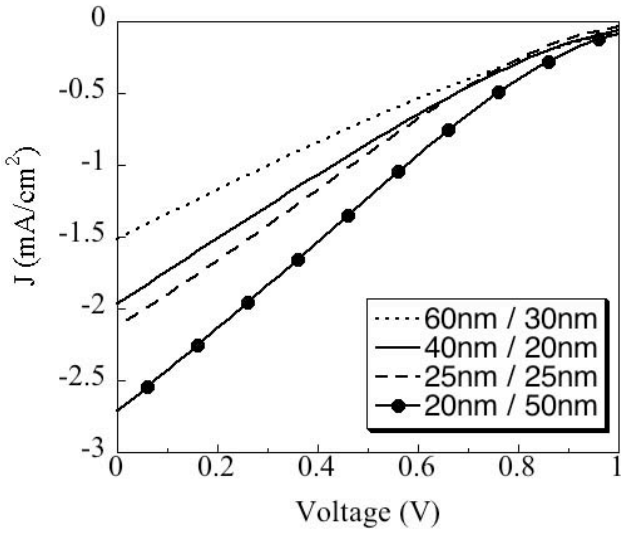

Figure 9.11. J-V Curves from experiment of M3EH-PPV/CN-ether-PPV layered devices as a function of layer thickness. The highest current is observed for 20 nm / 50 nm.

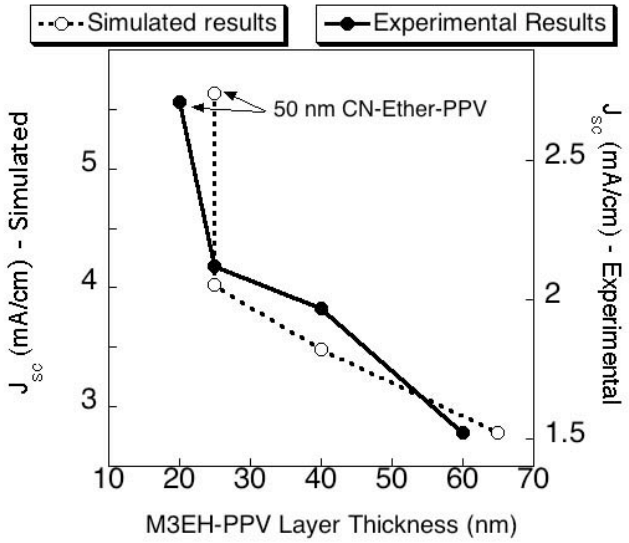

Figure 9.12. J_{sc} compared for experimental versus simulated M3EH-PPV/CN-ether-PPV layered devices as a function of M3EH-PPV thickness. Thickness trends are similar in experiment versus simulation, but simulated currents are ~2X as high as experimental due to artificially high mobilities used in simulation. CN-ether-PPV is 25 ± 5 nm, except for the points with the highest short-circuit current, in which the CN-ether-PPV thickness was 50 nm. Experimental thicknesses are ± 5 nm. A linear relationship between M3EH-PPV thickness and short-circuit current is observed, except for the 20 nm / 50 nm device, in which electric field maximization due to reflection at the interface results in enhanced current.

To understand why thicker CN-ether-PPV layers result in improved performance, the internal reflection within the device must be considered. With no reflection, exciton generation would attenuate exponentially. Instead, we observe a slight curvature (Figure 9.13), resulting from exponential light attenuation combined with absorbed light after reflection at the polymer/polymer and polymer/Al interfaces. We also see evidence for this reflection in experimental quantum efficiency measurements, where quantum efficiency is slightly antibatic with the absorption of CN-ether-PPV in some devices. Because of the large amount of light reflection at the CN-ether-PPV/Al interface, the electric field is minimized at that point, reducing exciton generation within the portions of the CN-ether-PPV layer closer to this interface. Thus, the further the polymer/polymer interface is from the CN-ether-PPV/Al electrode, the higher the exciton generation at that polymer/polymer interface and thus the higher the current density until the interference peak is reached (for devices around 100-200 nm thick).

Consequently, the superior performance of 20 nm / 50 nm layers can be explained by both more efficient charge collection in the very thin M3EH-PPV layer, and internal reflection effects, which increase the exciton creation flux density within a diffusion length of the polymer/polymer interface, as seen in Figure 9.13. The exciton generation is enhanced by ~2.5 times in the 20 nm / 50 nm layer over the 50 nm / 25 nm layer, and the short-circuit current is enhanced by 1.8 times, indicating that not all additional charge is transported out of the device. Clearly, an optimal set of film thicknesses exists to optimize device efficiency so that the layers are thick enough to maximize absorption and exciton generation (allowing for reflection effects) but thin enough to minimize recombination.

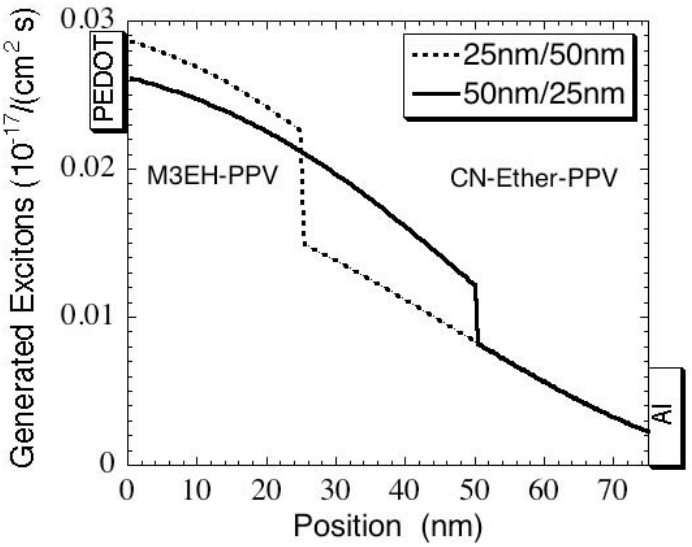

Figure 9.13: Exciton generation rate as a function of the two extreme layer thicknesses in layered heterostructured devices measured at 100 mW/cm^2 solar light. Exciton generation can be enhanced in the M3EH-PPV layer due to reflection from CN-ether-PPV/Aluminum interface.

9.7 Summary and conclusions

I have compared blends and layers of hole- and electron-transporting photoconductive polymers in photovoltaic devices. Blended devices tend to outperform layered devices although both show similar optimized photocurrents and efficiencies, and both are characterized by low fill-factors due to poor charge transport. Significantly longer exciton lifetimes exist for the electron-transporting CN-ether-PPV polymer than for the hole-transporting M3EH-PPV polymer, and correspondingly the decay time decreases with additional percent of M3EH-PPV in the blend. Residual CN-ether-PPV decay components contribute to the overall decay in disproportionately small amounts, suggesting that the long-lived excimer state is easily quenched even for small volume fractions of M3EH-PPV.

For blended structures, significant exciton quenching occurs in both the electron- and hole-transporting polymers due to the interpenetrating morphology; however, the lack of complete quenching limits the achievable short-circuit currents. In layered structures, decay times were longer than for blends; thus I conclude that exciton dissociation and charge transfer is more efficient in blended than in layered devices. The use of a better electron-acceptor would improve the performance of both blended and layered devices, as suggested by recent results (Alam and Jenekhe 2004).

Both steady-state and time-resolved data indicate that charge transfer occurs to an intermediate exciplex state. Formation of the exciplex aids device performance, as indicated by the predominance of the exciplex peak (and notable absence of M3EH-PPV emission) in steady-state spectroscopy on particularly efficient photovoltaic devices. The exciplex may thermally re-excite the M3EH-PPV exciton, providing an additional route for charge

separation, or dissociate directly under the influence of an electric field (Offermans, van Hal et al. 2005). In either case, exciplex formation results in efficient charge generation, accounting for the high performance of 1:1 blended devices in which both polymers are present in sufficient volume fraction for charge transfer to the exciplex.

Simulations of layered structures reveal that diffusion dominates the device properties when the applied voltage is near the built-in potential, creating space-charge buildup and leading to low fill factors but large V_{oc}'s. Moreover, internal reflection of photons at interfaces strongly affects the exciton generation rate throughout the device so that the best performance is achieved when the polymer/polymer interface is far from the reflective Al electrode. This effect accounts for much of the improved performance in layers, but places limits on the optimal thickness for polymer layers and poses technical challenges for optimization of this device architecture.

Overall, my results indicate that blended and layered structures achieve improved performance through substantially different mechanisms, which need to be considered in the device design. In fact, structures that consist of partially blended layers should result in the highest power efficiencies by combining the advantages of both systems. Finally, poor charge mobility, particularly for electrons, substantially reduces the achievable power efficiency in heterostructured polymer photovoltaics (Haerter, Chasteen et al. 2005) Substantial increases in mobility could result in power efficiencies closer to the 5% predicted (Echols and France 2004; Haerter, Chasteen et al. 2005) for 1:1 M3EH-PPV:CN-ether-PPV blends, with even higher efficiencies for materials with improved absorption across the solar spectrum.

9.8 References

Alam, M. M. and S. A. Jenekhe (2004). "Efficient solar cells from layered nanostructures of donor and acceptor conjugated polymers." Chem. Mater. **16**: 4647.

Arango, A. C., P. J. Brock, et al. (1999). "Charge transfer in photovoltaics consisting of interpenetrating networks of conjugated polymer and TiO_2 nanoparticles." Appl. Phys. Lett. **74**(12): 1698.

Arango, A. C., L. R. Johnson, et al. (2000). "Efficient titanium oxide / conjugated polymer photovoltaics for solar energy conversion." Adv. Mater. **12**(22): 1689.

Barker, J. A., C. M. Ramsdale, et al. (2003). "Modeling the current-voltage characteristics of bilayer polymer photovoltaic devices." Phys. Rev. B **67**: 075205-1.

Breeze, A. J., A. Salomon, et al. (2002). "Polymer-perylene diimide heterojunction solar cells." Appl. Phys. Lett. **81**(16): 3085.

Breeze, A. J., Z. Schlesinger, et al. (2001). "Charge transport in TiO_2/MEH-PPV polymer photovoltaics." Phys. Rev. B **64**(12): 125205.

Dittmer, J. J., K. Petritsch, et al. (1999). "Photovoltaic Properties of MEH-PPV/PPEI blend devices." Synth. Met. **102**: 879.

Echols, R. S. and C. E. France (2004). "Theoretical Investigations of Polymer Based Solar Cells." Mat. Res. Soc. Symp. Proc. **822**: S7.7.1.

Feldrapp, K., W. Brutting, et al. (1999). "Photovoltaic effect in blend systems and heterostructures of poly(p-phenylene vinylene) and C60." Synth. Met. **101**: 156.

Granstrom, M., K. Petritsch, et al. (1998). "Laminated fabrication of polymeric photovoltaic diodes." Nature **395**: 257.

Haerter, J. O., S. V. Chasteen, et al. (2005). "Numerical simulations of layered and blended organic photovoltaic cells." Appl. Phys. Lett. **86**: 164101.

Halls, J. J. M., K. Pichler, et al. (1996). "Exciton diffusion and dissociation in a poly(p-phenylenevinylene)/C_{60} heterojunction photovoltaic cell." Appl. Phys. Lett. **68**(22): 3120.

Halls, J. J. M., C. A. Walsh, et al. (1995). "Efficient photodiodes from interpenetrating polymer networks." Nature **376**: 498.

Jenekhe, S. A. and S. Yi (2000). "Efficient photovoltaic cells from semiconducting polymer heterojunctions." Appl. Phys. Lett. **77**(17): 2635.

Lakowicz, J. R. (1999). Principles of Fluorescence Spectroscopy. New York, Kluwer Academic/Plenum Publishers.

Loos, J., X. Yang, et al. (2005). "Morphology determination of functional poly[2-methoxy-5-(3,7-dimethyloctyloxy)-1,4-phenylenevinylene]/Poly[oxa-1,4-phenylene-1,2-(1-cyanovinylene)-2-methoxy,5-(3,7-dimethyloctyloxy)-1,4-phenylene-1,2-(2-cyanovinylene)-1,4-phenylene] blends as used for all-polymer solar cells." J. Appl. Polym. Sci. **97**: 1001.

Morteani, A. C., P. Sreearunothai, et al. (2004). "Exciton regeneration at polymeric semiconductor heterojunctions." Phys. Rev. Lett. **92**: 247402.

Offermans, T., P. A. van Hal, et al. (2005). "Exciplex dynamics in a blend of pi-conjugated polymers with electron donating and accepting properties: MDMO-PPV and PCNEPV." Phys. Rev. B **72**: 045213.

Osaheni, J. A. and S. A. Jenekhe (1994). "Efficient blue luminescence of a conjugated polymer exciplex." Macromolecules **27**: 739.

Osaheni, J. A., S. A. Jenekhe, et al. (1994). "Efficient photogeneration of charge carriers in a layered photoreceptor using a conjugated polymer." Appl. Phys. Lett. **64**(23): 3112.

Quist, P. A. C., T. J. Savenije, et al. (2005). "The effect of annealing on the charge-carrier dynamics in a polymer/polymer bulk heterojunction for photovoltaic applications." Adv. Func. Mater. **15**(3): 469.

Smilowitz, L., A. Hays, et al. (1993). "Time-resolved photoluminescence from poly[2-methoxy, 5-(2'-ethylhexyloxy)-p-phenylene-vinylene]: Solutions, gels, films, and blends." J. Chem. Phys. **98**(8): 6504.

Tada, K., M. Onoda, et al. (1999). "Photocell with heterojunctions of donor / acceptor polymers." Synth. Met. **102**: 982.

Veenstra, S. C., W. J. H. Verhees, et al. (2004). "Photovoltaic properties of a conjugated polymer blend of MDMO-PPV and PCNEPV." Chem Mater. **16**: 2503.

Yu, G., J. Gao, et al. (1995). "Polymer photovoltaic cells: enhanced efficiencies via a network of internal donor-acceptor heterojunctions." Science **270**: 1789.

Yu, G. and A. J. Heeger (1995). "Charge separation and photovoltaic conversion in polymer composites with internal donor/acceptor heterojunctions." J. Appl. Phys. **78**(7): 4510.

Zhang, F. L., M. Johansson, et al. (2003). "Polymer solar cells based on MEH-PPV and PCBM." Synth. Met. **137**(1-3): 1401.

Zhang, X., D. M. Kale, et al. (2002). "Electroluminescence of multicomponent conjugated polymers. 2. Photophysics and enhancement of electroluminescence from blends of polyquinolines." Macromolecules **35**: 382.

Chapter 10

Summary and Conclusions

In conclusion, I have fabricated photovoltaic devices with the hole-transporting polymers M3EH-PPV and P3HT combined with a variety of electron-transporting materials: CN-ether-PPV, PCBM, and TiO_2. Steady-state and time-resolved spectroscopy were used to understand the excited state dynamics in each system.

Comparison of the best devices of M3EH-PPV and P3HT heterojunction devices are shown in Figures 10.1 and 10.2, below. Pure M3EH-PPV and P3HT devices are dominated by hole-transport, as indicated by poor performance on a device structure (PEDOT//Al) which forces the electrons to cross the bulk of the polymer from the charge dissociation interface. P3HT devices are characterized by currents that are about half that of M3EH-PPV, indicative of poorer charge transport or separation.

TiO_2, the standard material in bilayered devices, is found to be an inefficient electron acceptor. No quenching is observed in the steady-state or time-resolved photoluminescence, despite attempts to reduce the signal from the bulk. Such quenching was observed in bilayered M3EH-PPV/CN-ether-PPV devices, on the other hand, even at relatively high film thicknesses, suggesting that TiO_2 is simply a poor quencher.

Combining M3EH-PPV and P3HT with the electron transporters CN-ether-PPV and PCBM resulted in improvements in device performance due to increased charge separation and reduced loss to recombination. A balance in the mobilities of electrons and holes is important in order to reach high currents as this results in bipolar transport and avoids space-charge limited current. This was not achieved for P3HT:CN-ether-PPV devices, whereas the mobilities of M3EH-PPV and CN-ether-PPV appear to be better matched.

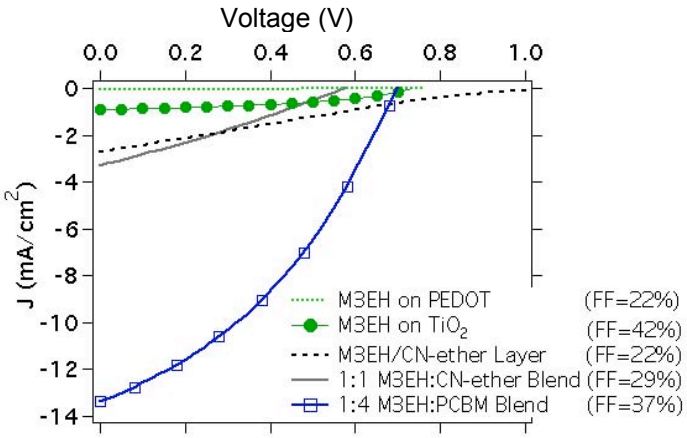

Figure 10.1. J-V curves for M3EH-PPV heterojunction devices.

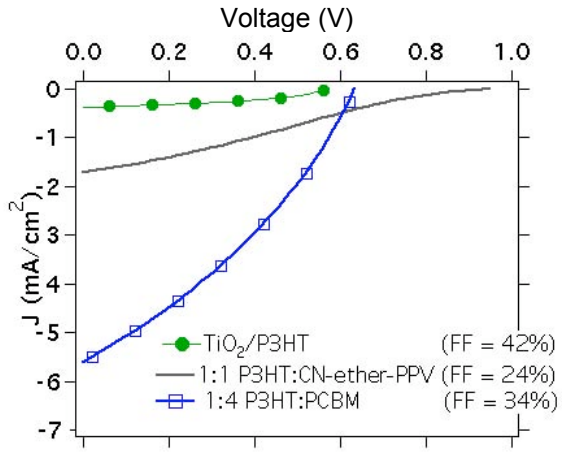

Figure 10.2. J-V curves for P3HT heterojunction devices.

Simulations reveal that performance of M3EH-PPV/CN-ether-PPV layers is similarly limited by space-charge buildup. Simulations also indicate that increased exciton generation (rather than charge separation) is the primary means of improved current in layered structures, due to reflected light from the Al electrode. This places restrictions on further optimization of this device structure.

CN-ether-PPV is characterized by a long 14 ns decay component, indicative of an excimer state. The broken conjugation imposed by the ether linkage results in a long lifetime for the excimer state due to a reduced ability to visit internal quenching sites. These excimers are particularly vulnerable to quenching via charge-transfer to other materials. CN-ether-PPV therefore serves as an efficient source of separable charge with a long radiative lifetime; these findings are important for design of materials for use in optoelectronic applications.

An exciplex state is present in blended and layered structures of CN-ether-PPV with M3EH-PPV (and probably P3HT). This may aid in device performance by acting as a scavenger for excitons. The exciplex state may thermally re-excite the M3EH-PPV exciton, providing a second chance for charge separation, thus enhancing exciton generation via indirect means. All blended and layered structures exhibit incomplete quenching of the excited state, suggesting that the use of a better electron acceptor would enhance device performance.

The use of PCBM, which efficiently separates excitons and transports electrons, has the expected effect of increasing device currents and efficiencies. Emission from PCBM aggregates is detected in all heterojunctions. These aggregates reduce the surface area available for exciton dissociation, but increase the available charge percolation pathways, enhancing performance. Past a critical size, PCBM aggregates appear to be detrimental to device performance, as observed in P3HT:PCBM blends. In M3EH-PPV:PCBM blends the ideal blend ratio for charge separation did not match the ideal ratio for efficient charge transport. Given the high efficiencies found for M3EH-PPV:PCBM blends, further optimization of the underlying morphology of the polymer phase and the PCBM domain size could result in competitive device performances. A pathway for such improvement is

suggested by the response of pristine M3EH-PPV film morphology and the size of PCBM domains to changes in the spin-speed, thickness of the film, and solution concentration. The ability to perform nanoscale SEM and/or TEM imaging would be necessary for continuation of these studies.

It is found that while the addition of PCBM enhanced device performance through an increase in the charge transport (indicated by a concomitant increase in FF) and exciton dissociation (indicated by TRPL quenching at short times), the same is not true for the addition of the electron-transporting polymer CN-ether-PPV. As seen in Figure 10.3 (A) and (B), below, the rise in device current is a mirror image of the rise in FF, indicating that the charge transport suffers for the same reason as the device current is enhanced – addition of CN-ether-PPV. The peak in FF does not mirror the peak in current for these devices. The destruction of efficient charge transport in polymer:polymer blends is a serious limitation, despite the enhanced exciton dissociation.

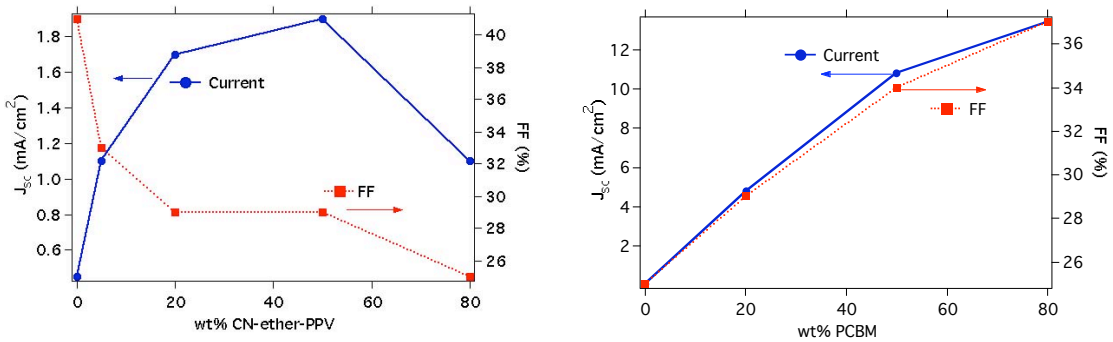

Figure 10.3. Current and FF versus (A) wt% of CN-ether-PPV, and (B) wt% of PCBM.

The quenching of the excited state in these two systems is poorer than expected. Table 10.1 below shows that, despite dramatically enhanced device performance in PCBM

blends, the quenching percentage ($Q = 1 - \frac{\tau_{composite}}{\tau_{neat\ film}}$) for the dominant decay time is around 75% for all heterojunctions with M3EH-PPV. Quenching of the CN-ether-PPV decay component is more predictive of device performance, as is quenching of the steady-state photoluminescence. Thus, it is easier to quench emissive species than non-emissive ones, presumably because rapid non-radiative recombination deactivates the excited state before charge transfer can occur.

	Film	η	τ_1 (ns)	τ_2 (ns)	τ_3 (ns)	τ_{ave} (ns)	Q1	Q 2
Pristine polymers	M3EH-PPV	0.36%	0.20 (43%)	**0.45 (53%)**	1.7 (3%)	0.38		
	P3HT	0.11%	**0.11 (68%)**	0.51 (27%)		0.41		
	CN-ether-PPV	N/A	0.30 (2%)	4.3 (26%)	**12.2 (73%)**	10.0		
CN-ether blends	50 wt% CN-ether w/ M3EH-PPV	0.86%	**0.05 (51%)**	0.46 (20%)	2.0 (22%)	1.0	75%	90%
	M3EH/CN-ether layer	0.89%	**0.05 (39%)**	0.46 (17%)	2.0 (27%)	1.8	75%	82%
	50 wt% CN-ether w/P3HT	0.56%	0.44 (18%)	**2.1 (42%)**	6.4 (24%)	2.5	0%	75%
PCBM blends	80 wt% PCBM w/ M3EH-PPV	4.3%	0.05 (36%)	**0.50 (49%)**	1.9 (16%)	0.6	75%	
	20 wt% PCBM w/ M3EH-PPV	1.3%	**0.02 (95%)**		1.0 (5%)	0.07	90%	
	80 wt% PCBM w/ P3HT	1.4%	**0.09 (73%)**	0.45 (15%)	1.2 (15%)	0.30	18%	

Table 10.1. Decay components for polymers in this study. Emission is at 600 nm (700 nm for P3HT) and films are ~100 nm thick. Q1 is the % quenching of the primary decay component of the hole-transporter (0.20 ns for M3EH-PPV and 0.11 ns for P3HT); see Chapter 2. Q2 is the % quenching of the average decay time of CN-ether-PPV. Power conversion efficiency (η) is based upon illumination at 80 mW/cm^2; actual illumination intensity may be up to twice as high, reducing efficiencies by half.

A comparison of % yield for these decay components across device architectures is illuminating, as in Figure 10.4, below.

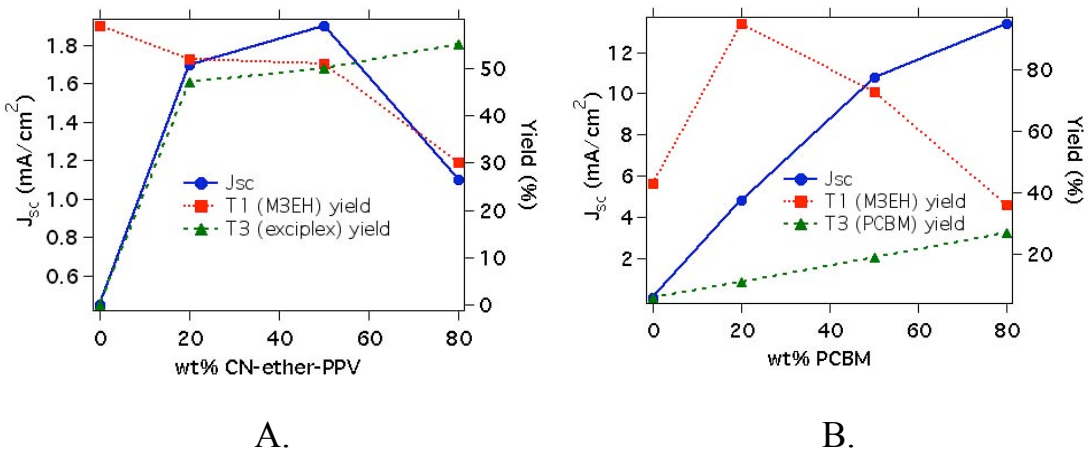

A. B.

Figure 10.4. Jsc and % yields of decay components in (A) M3EH-PPV:CN-ether-PPV blends, and (B) M3EH-PPV:PCBM blends. Emission is detected at the spectral peak for each component: 600 nm for T_1 and 700 nm for T_3 in each case.

In PCBM blends, the population of the M3EH-PPV exciton decreases monotonically as additional PCBM is added to the blend, up to the peak performance at 80 wt% PCBM, as expected for a decreased amount of M3EH-PPV. The same is not true for M3EH-PPV:CN-ether-PPV blends. The % yield for the M3EH-PPV component does not follow a linear decrease, as would be expected due to a simple linear combination of the polymer components as the wt% of CN-ether-PPV is added. Instead, the % yield remains essentially constant from 20 wt% to 50 wt% CN-ether-PPV, indicating that another mechanism is resulting in a boosted yield of exciton population at that blend ratio. Indeed, the % yield of the M3EH-PPV exciton almost mirrors the short-circuit current, suggesting that the same mechanism is responsible for the enhancement of each; namely, thermal re-excitation of

M3EH-PPV excitons via exiplex decay. Thus, as in layered structures, exciton generation is extremely important for device performance in polymer/polymer blends.

Implications of this research

These results suggest that excitations in polymers cannot be treated as a "plastic free electron gas." For all polymer films, decay kinetics are complex and not well described by a simple model, in which a single excited state carrier, X*, relaxes to inter- and intra- chain species which may relax radiatively or non-radiatively. It is well-known that device characteristics are affected by morphology as well as quenching of the PL. A complete understanding of the kinetics of polymer films requires that we broaden our description of excited state carriers to include the environment that those carriers find themselves in – such as a crystalline or non-crystalline film, in the middle or end of a chain, or trapped at a kink or defect in the polymer. These variables are all likely to affect the excited state kinetics, and are difficult to control.

The time-decay of thin and thick polymer films was found to vary drastically, due to underlying film morphology caused by spin-speed, evaporation rate, and/or interaction with the substrate. The effect of morphology thus affects the time-decay of the excited state can thus outweigh that of the effects of charge-transfer.

The morphological effects of blending electron-transporting materials may similarly change the decay parameters, or add new ones (such as exciplex decay). Therefore, improved device performance does not necessarily relate directly to quenching of the excited state. While important, charge-transfer between materials is insufficient for optimization of device performance. Morphology is critical for peak exciton generation and subsequent charge

transport, as well as reducing losses to recombination. This morphology is more easily controlled in layered device structures than in blended ones. Inherent obstacles to optimization of layered device structures require us to gain a better understanding and control of nanoscale morphology.

Overall, our results show that:

- Photoluminescence lifetime is only loosely correlated with device performance due to morphological variations and intermediate states;
- Exciton dissociation is insufficient for optimization of device performance. Exciton generation (through the presence of exciplexes or layer thickness control) and charge transport pose more important limitations to performance;
- Morphology is critical in all aspects of device performance, from deactivation of the excited state to charge transport;
- Emissive interchain excitations may serve as useful sources of separable charge, whereas poorly emissive single-chain excitations are difficult to quench due to competing non-radiative rate constants.

Thus, device performance may be enhanced by:

- Control of film thickness in layered devices;
- Exciplexes or other exciton scavengers;
- Use of materials with highly emissive interchain excitations;
- Control of nanoscale morphology (such as domain size, or chain-stacking) leading to better charge transport.

Suggestions for future research

Photoinduced absorption measurements would allow the analysis of charge-transfer processes occurring in the picosecond regime, which is important for investigating the rapid processes in M3EH-PPV:PCBM blends.

A useful direction for future research would be to analyze the temperature-dependence of the time-decay of photoluminescence. At lowered temperatures the decay time should increase due to a reduction in non-radiative mechanisms, allowing a more direct measurement of radiative decay. This is important for a more detailed characterization of the excited state species. Time-resolved emission spectra would also allow us to see rapid changes in the emission spectra over time, such as those expected by a rapid rise in an interchain excitation. Bias-dependent studies would allow us to test the binding energies of the different excited state species, which would be particularly useful for probing the exciplex state. The dissertation work of Ton Offermans in R.A.J. Janssens's group offers a useful model of such detailed study, including probing devices under operation (Offermans 2005).

Measurement of absolute quantum yield, via an integrating sphere, would be important for a more complete understanding of the photophysical processes in these materials in the future. Not only would this allow more accurate determination of the percent quenching achieved in heterojunctions, it would also provide the means to directly calculate the radiative and non-radiative rate constants in these films. Some understanding of the quantum efficiency of the creation of the emissive species would also be required.

Morphological effects in the pristine films and heterojunctions could be probed in some detail, either via imaging techniques as stated above, or by a systematic study of the effects of spin-speed, solution concentration, and dissolution in good/bad solvents upon the decay of film and/or solution. Anisotropy measurements, via polarization of the incident light, would also give insight into the degree of film ordering. The ability to distinguish between single-chain and interchain interactions would allow a more precise designation of aggregated versus non-aggregated pristine films. This would be useful in teasing out the effects of morphology versus charge-separation.

Bibliography

Offermans, T. (2005). "Charge carrier dynamics in polymer solar cells: An opto-electronic study." PhD Thesis(University of Eindhoven).

Appendices

Appendix 1: Solar Simulation

Introduction

The solar irradiance on the outer atmosphere of the earth, integrated over the entire spectrum, is about 1367 W/m^2. $Total\ irradiance = \int E(\lambda)\, d\lambda$, where E is the incident light spectrum. Thus, light intensity equal to 1367 W/m^2 is termed "one sun". This intensity is reduced to about 1050-1120 W/m^2 at ground level, due to absorption and scattering in the atmosphere (Watson 1993).

The light intensity reaching the earth varies due to such factor as clouds and altitude. This intensity also changes over the course of the day due to the zenith angle of the sun in the sky. When the sun is directly overhead, it passes through the earth's atmosphere to the ground in a shortest-path radial line. This radiation is termed "Air Mass 1" or "AM 1.0." On the other hand, solar radiation must pass through additional air mass when it is at an angle other than high noon. When the sun is at a zenith angle of 48.2 degrees, the incident radiation passes through 1.5 times as much air mass as at high noon: This radiation is termed AM 1.5. Similarly, radiation at a zenith angle of 60.1 degrees is termed AM 2.0. Radiation at the level of the outer atmosphere (1367 W/m^2, 1 sun), is termed AM 0. A distinction is also made between *direct* and *global* radiation. Direct radiation is that which is directly incident upon the object after passing through the atmosphere. Global radiation includes direct radiation, and also includes effects from reflected and scattered light. Solar simulated results are generally reported at AM1.5 Global.

Spectral mismatch (M)

Measuring device performance using a solar simulator is not as straightforward, however, as with a standard light bulb. One must take into account the Spectral Mismatch Factor (M) – a scaling factor that adjusts for the spectral difference between the solar simulator and the true AM 1.5 spectrum. The necessary correction depends upon the cell response – if the cell response is low in the area where the mismatch is highest, the effect of the mismatch may be negligible.

The standard procedure for adjusting for spectral mismatch is to:

1. Determine the Spectral Response (SR) for both the test cell and a reference cell
2. Determine M (see formula below)
3. Adjust lamp output for M
4. Measure test cell I-V curve

The following derivation is taken from Osterwald (Osterwald 1986). The formula for the spectral dependency of the short circuit current of a solar cell is:

$$I_{SC} = A \int E(\lambda) \cdot SR(\lambda)\, d\lambda$$

where A = the area of the cell, E = incident spectrum, and SR = spectral response of the cell.

What we want to do is match I_{sc} of the reference cell (a cell whose response is well-characterized and stable with respect to time and temperature) under AM 1.5 conditions to I_{sc} of that cell under illumination with the simulator. Thus, the response of the reference cell under solar simulation acts as a standard candle against which test device response may be measured.

$$I_{SC,R}\,(\text{AM1.5}) = I_{SC,R}\,(\text{sim})$$

where $I_{SC,R}$ is the short circuit current of the reference cell and "AM1.5" and "sim" designate the illumination conditions.

Thus,

$$1 = \frac{I_{SC,R}(\text{AM1.5})}{I_{SC,R}(\text{sim})} = \frac{\int E_{AM1.5}(\lambda)\cdot SR_R(\lambda)\,d\lambda}{\int E_{sim}(\lambda)\cdot SR_R(\lambda)\,d\lambda}$$

And multiplying the equation through by the right-hand side:

$$1 = \frac{I_{SC,R}(\text{AM1.5})}{I_{SC,R}(\text{sim})} * \frac{\int E_{sim}(\lambda)\cdot SR_R(\lambda)\,d\lambda}{\int E_{AM1.5}(\lambda)\cdot SR_R(\lambda)\,d\lambda}$$

We define the Fractional Error (F) as the mismatch between the test cell illuminated at AM1.5 and illuminated by the simulator:

$$F = \frac{I_{SC,test}(\text{AM1.5})}{I_{SC,test}(\text{sim})}$$

Then, using the normalization factor calculated above,

$$F * 1 = \frac{I_{SC,test}(\text{AM1.5})}{I_{SC,test}(\text{sim})} = \frac{\int E_{AM1.5}(\lambda)\cdot SR_{test}(\lambda)\,d\lambda}{\int E_{sim}(\lambda)\cdot SR_{test}(\lambda)\,d\lambda} * \frac{I_{SC,R}(\text{AM1.5})}{I_{SC,R}(\text{sim})} * \frac{\int E_{sim}(\lambda)\cdot SR_R(\lambda)\,d\lambda}{\int E_{AM1.5}(\lambda)\cdot SR_R(\lambda)\,d\lambda}$$

So, to correct for the short circuit current under AM 1.5 conditions:

$$I_{SC,test}(\text{AM1.5}) = \frac{I_{SC,test}(\text{sim})}{\text{M}} * \frac{I_{SC,R}(\text{AM1.5})}{I_{SC,R}(\text{sim})}$$

where M is the **Spectral Mismatch Factor**

$$M = \frac{\int E_{sim}(\lambda)\cdot SR_{test}(\lambda)\,d\lambda}{\int E_{AM1.5}(\lambda)\cdot SR_{test}(\lambda)\,d\lambda} * \frac{\int E_{AM1.5}(\lambda)\cdot SR_R(\lambda)\,d\lambda}{\int E_{sim}(\lambda)\cdot SR_R(\lambda)\,d\lambda}$$

Calculation of M is an often-neglected task of solar simulator calibration, resulting in power efficiencies that are difficult to cross compare. Note that if the short-circuit current of the reference cell under solar simulation is comparable to that under AM 1.5 illumination,

and if the Spectral Response (SR) of the reference cell is well-matched to the SR of the test cell, then M is approximately unity, and this calculation is no longer necessary.

In general, simulators should have M = 1 ± 0.01 in order to produce efficiency measurements within 2% (Emery and Osterwald 1989; Myers, Emery et al. 1989). Less expensive simulators sacrifice accuracy, giving only +- 5% (Myers, Emery et al. 1989). The reference and test cell should have roughly the same geometry, or else the measured current of the test device may be off by up to 20% (Myers, Emery et al. 1989) because of internal reflections in the reference cell package. A good check for this is to measure the same device on a second solar simulator using the same reference cell, then comparing the short-circuit currents.

Reference cell

We designed a reference cell apparatus suitable for our application, which was fabricated by the independent company PVMeas, and designed a reference cell and experimental apparatus that allowed us to calibrate the solar simulator and measure M with a reasonable degree of precision. The layers of the reference cell are described below.

1. Light from the Oriel 150W Solar Simulator passes through AM1.5D filters and enters a liquid light guide (Oriel 77566, 340-800 nm range, core diameter 3 mm). The core diameter roughly matches the 1mm x 3 mm size of our devices.
2. The light guide is fixed in position flush to the reference cell, to simulate the testing conditions of the devices, and thus match the proportion and part of the light beam that is intercepted.
3. Light passes through a 1 mm x 3 mm mask cut in a 1mm thick, black anodized aluminum disk. This ensures that the same amount of light hits the reference cell as

would be incident upon the test cell and reduces the problem of light non-uniformity. However, the extremely small size of our mask results in very low photocurrents, and thus a larger possible margin of error in photocurrent measurements.

4. Light passes through the Ealing BG40 colored glass filter. This filter cuts off transmittance below 300 nm and above 700 nm, giving a better spectral match between reference and test cell, as can be seen in Figure A.1 below. Without the cutoff filter, the EQE of silicon increases monotonically past 700 nm.
5. Light is incident upon a 1 cm x 1 cm solar cell

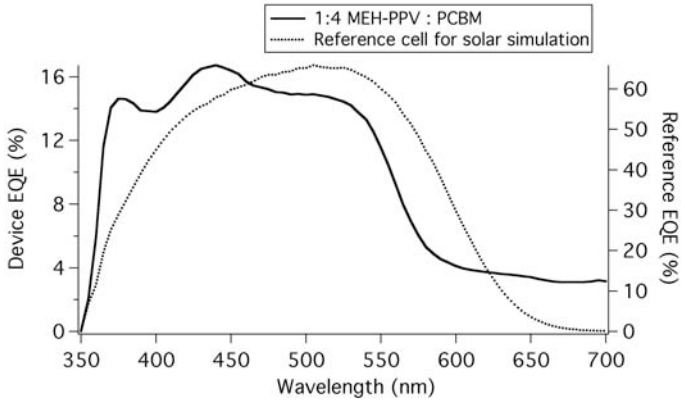

Figure A.1. Spectral match between reference and test devices.

The whole cell is assembled on a 1" aluminum disk and mounted in a standard 1" optics holder. This is mounted on 4" posts which are securely fastened in an adapter plate. This enables us to mount the light guide and reference cell in a variety of positions and orientations, allowing us to achieve optimal illumination conditions

The reference cell was sent to National Renewable Energy Labs for measurement of absolute EQE and I-V curves under AM1.5D and AM1.5G. With our solar simulator, the

intensity of the Oriel 150W solar simulator was adjusted until the I_{sc} of the reference cell matched that measured at NREL. The match of the entire I-V curve was excellent, as can be seen in Figure A.2 below. The I-V curves for the reference cell under AM1.5D and AM1.5G were indistinguishable.

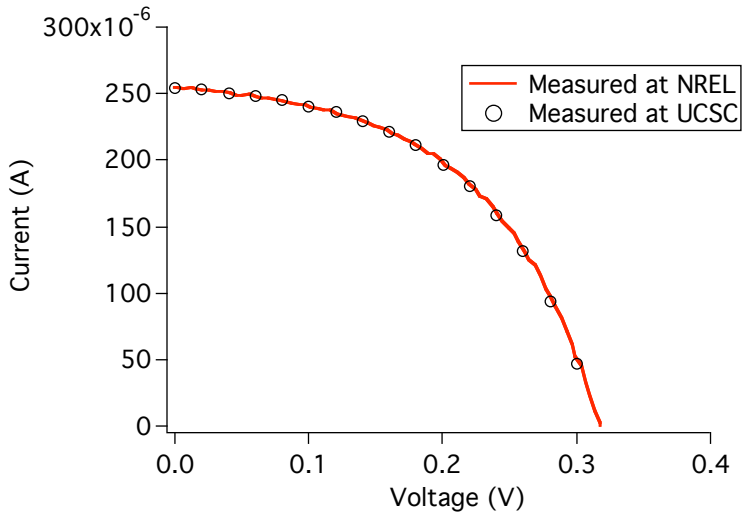

Figure A.2. I-V curve match for reference cell measured at AM1.5 at NREL and on our calibrated solar simulator.

Calculation of M

We calculated the mismatch factor as follows. Recall the formula for the mismatch factor, M:

$$M = \frac{\int E_{sim}(\lambda)\cdot SR_{test}(\lambda)\,d\lambda}{\int E_{AM1.5}(\lambda)\cdot SR_{test}(\lambda)\,d\lambda} * \frac{\int E_{AM1.5}(\lambda)\cdot SR_{R}(\lambda)\,d\lambda}{\int E_{sim}(\lambda)\cdot SR_{R}(\lambda)\,d\lambda}$$

For the various parameters used in the formula, we used the following:

1. E_{sim}: Using an integrating sphere, which diminished the intensity of light coming from the simulator without any spectral disturbance, light from the solar simulator was collected, via fiber optic, into an Ocean Optics CCD array spectrophotometer.

The spectral output was analyzed via a program in Labview in integrating sphere mode, resulting in a spectral radiance curve. *E* was converted to photon flux, as explained below.

2. $E_{AM1.5}$: Obtained from published data from NREL

3. SR_{test} and SR_R: The EQE of a 1:4 MEH-PPV:PCBM device and of the reference cell and was obtained with our EQE apparatus (see 2.__ EQE). Note that we also could have used the EQE provided by NREL for SR_R.

Note that the absolute magnitudes of the various parameters should not affect M – any scaling factor will appear in both the numerator and denominator of M.

The units of this calculation must be kept consistent. *E* can be used in units of irradiance (W/m2), along with the SR in units of A/W, giving a final unit of A/m2. Or, the time component of the units may be removed by using *E* in units of photon flux (photons/m2) and EQE (electrons/photon) in place of SR, giving the final unit of electrons/m2. We chose the former, and so converted EQE to SR as follows, for each wavelength:

$$EQE(electrons/photon)(\lambda) * \frac{1.6\times10^{-19}(C/e^{-})}{hc/\lambda\,(J/photon)} = \frac{EQE\cdot\lambda(C/s)}{1.23x10^{-3}(J/s)} = \frac{EQE\cdot\lambda}{1.23x10^{-3}}(A/W)$$

With that data, integrated over the same spectral range, the following values for M were obtained:

Under AM1.5D, M = 0.987

Under AM1.5G, M = 0.979

Thus, under AM1.5D, our power efficiencies are correct to within 2% error, whereas for AM1.5G the error is slightly larger. These are respectable levels of error.

Appendix 2. TCSPC technique

The generalized setup for the TCSPC technique is shown below, in Figure A.3. This figure, and the following description of this technique is borrowed heavily from the seminal work on the topic (O'Connor and Phillips 1984)and the interested reader is referred to that work for additional information. Another good discussion can be found in a useful reference by Lakowicz (Lakowicz 1999).

The TCSPC technique, as its name suggests, measures the probability that a single emitted photon will be detected at a time *t* after the excitation of the sample. This probability is calculated by sampling the emission resulting from a large number of excitation flashes. The probability *p(t)* for detection of a single photon is taken as the intensity distribution *I(t)* of all photons emitted as a result of excitation. In other words, the distribution of arrival times for single photons represents the time-decay of the photoluminescence intensity of the sample. The excitation flash is time-correlated with an electronic pulse by use of the trigger. The electronic pulse is routed through the *trigger channel,* while the excitation pulse is directed to the sample (the *fluorescence channel*).

Trigger Channel

The trigger pulse first passes through a discriminator, which essentially improves the signal-to-noise ratio of the pulse by weeding out dark noise pulses, single photon events, and multiple photon events so that the pulses arriving at the TAC are of constant amplitude. A leading edge discriminator is used in the trigger channel, indicating the time of arrival of the front of that (constant-amplitude) pulse. After the discriminator, the trigger pulse arrives at the time-to-amplitude converter (TAC), prompting the charging of a capacitor.

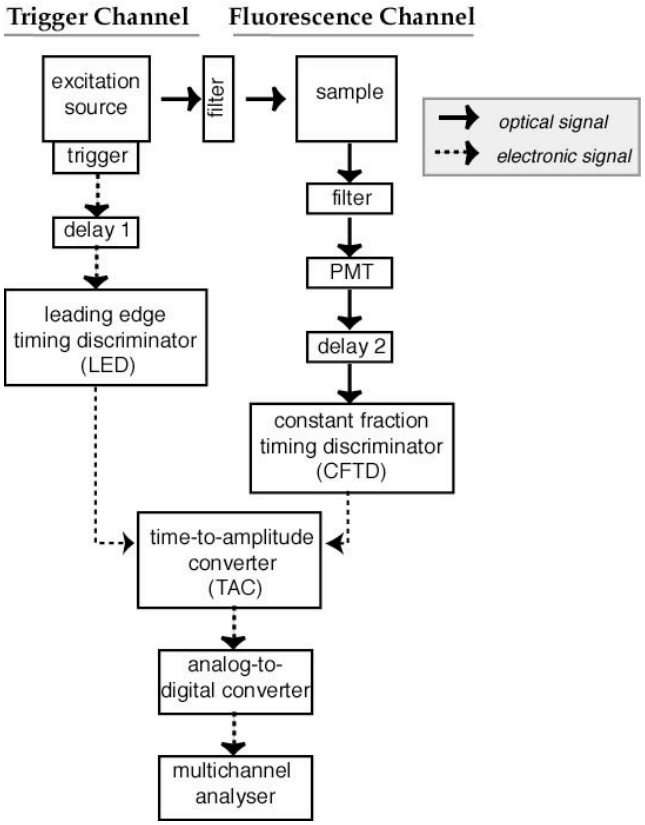

Figure A.3. Schematic of the TCSPC instrumentation.

Fluorescence Channel

The excitation pulse, on the other hand, hits the sample and a signal is detected at 90 degrees to excitation. For each signal flash, only the first arriving photon is detected. Thus, a large number of signal pulses are needed to gather adequate statistical data. The signal may need to be amplified before and after the discriminator to boost the signal for detection. A constant fraction timing discriminator (CFTD) is usually used in the fluorescence channel. In a CFTD the timing of the pulse begins at a point on the leading edge of the pulse that is a predetermined fraction of the pulse height. Since pulse height will vary in TCSPC experiments, the use of a CFTD removes variability due to pulse height. The timing of the

CFTD does depend on pulse shape, but this is constant in TCSPC. See O'Connor or Lakowicz for more information.

Time to Amplitude Converter (TAC)

The TAC acts like a very fast stopwatch. Once the fluorescence signal arrives at the TAC, the capacitor stops charging, and outputs a voltage pulse proportional to the time since the voltage ramp was started. (See Figure A.4 below)

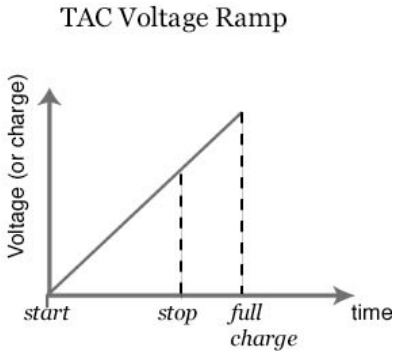

Figure A.4. Charging of the TAC.

The range of the TAC (i.e., the time delay corresponding to maximum capacitor charge) can be adjusted to fit the length of the decay curve being measured. Eventually, the time between the excitation flash and the detection of the signal is back-calculated from the charge on the capacitor and the magnitude of the input delays (which allow the experimenter to adjust the decay scale so that the decay curve is captured optimally in the multichannel analyzer channels).

Only one photon is counted per ~100 laser pulses because the dead time in the TAC after detection of a photon exceeds the laser repetition rate (generally 1 MHz). The count rate is kept low in order to avoid pulse pileup, in which more than one photon arrives per 50-100

laser pulses. Since emission is a random event, the probability *P(t)* for an arriving photon is directly related to *I(t)*. If, however, more than one photon is measured for each pulse of the laser, decay times will be skewed to earlier times since more photons are expected to arrive at earlier times than later times. Thus, it is important to keep the count rate low in order to prevent detection of more than one photon from each laser pulse. For our 1 MHz laser, the count was maintained at 5000-10,000 counts, well below the count rate threshold.

In practice, excitation signals reach the TAC at such a high rate that it does not have sufficient time to reset in between excitations. Since the repetition rate is much larger than the rate of photon emission, it makes sense to operate the TAC is operated in "reverse" mode, in which the TAC starts charging with the first detected photon, and stops with the subsequent excitation pulse, resulting in a reversed decay curve, as in Figure A.5 below. If, instead, the TAC began charging with the laser trigger, many counts would be lost while the instrumentation was reset – thus, reverse-mode ensures that every detected photon is counted. This technique was used in the current studies. Thus the ramp time is *(T-t)* instead of *t*, where *t* is the time between photons and *T* is the time between excitation flashes. The delays are thus arranged so that the TAC sweep is stopped by the arrival of the trigger signal that corresponds to the fluorescence signal starting the sweep.

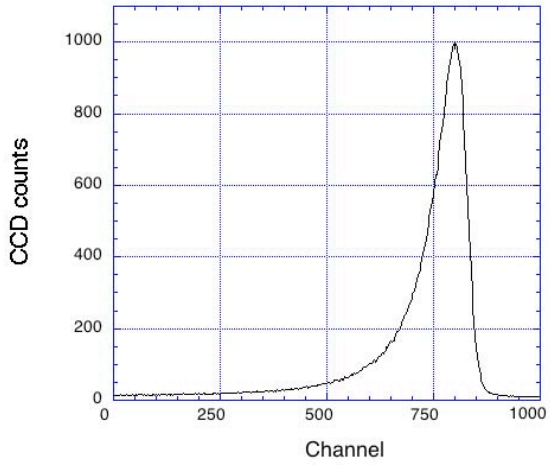

Figure A.5. Decay curve using TAC in reverse mode.

Multichannel analyzer

The analog-to-digital converter stores this time value as a number, which is sorted into one of 1024 channels (time bins) in the multi-channel analyzer. In this way, a histogram of photon counts versus channel number is obtained. Data gathering continues until a minimum number of total photon counts is obtained in the channel with the maximum counts, as determined by the researcher (typically around 10,000-20,000 for 5% precision with a single-exponent decay, and 30,000 for multiple-exponent decay. Increasing the number of channels used will give increased resolution, but also increase the time necessary to gather the data.

Appendix 3. Least-squares fitting

The least-squares technique (Lakowicz 1999) tries to minimize the difference between a calculated fitting function, Y(t), and the obtained sample decay curve, $I_0(t)$. In particular, the χ^2 (chi-square) function is minimized – the sum of the squares of the difference between the calculated and experimental values, as weighted by the photon counts for that particular data point:

$$\chi^2 = \sum_{i=1}^{n}\left[\frac{\left(I_0(t_i) - Y(t_i)\right)^2}{I(t_i)}\right] \qquad \textbf{(Equation 1)}$$

where *n* is the total number of data points, $Y(t_i)$ is the calculated fitting function, $I(t_i)$ is the corrected photon count, and $I(t_i)$ is the uncorrected photon count which serves as a weighting factor.

Recall that the convolution integral represents the measured decay as a convolution between the true decay *G(t)* and the instrument response function *P(t):*

$$I_0(t) = \int_0^t P_0(t')G(t-t')dt' = P_0(t) \otimes G(t)$$

The fitting function $Y(t_i)$ is obtained by expanding a particular solution (for t_i) of the convolution integral:

$$Y(t) = Y^0(t_i) + \sum_{j=1}^{l}\frac{\partial Y^0(t_i)}{\partial a_j}\delta a_j$$
$$\text{where } Y^0(t_i) = \int_0^{t_i} P_0(t')G(t-t')dt' = P_0(t_i) \otimes G(t_i) \qquad \textbf{(Equation 2)}$$

The a_j are the fitting parameters for the true decay function G(t) – both amplitude and decay:

$$G(t) = a_1 e^{-t/a_2} + a_3 e^{-t/a_4} \ldots \qquad \textbf{(Equation 3)}$$

Thus, the condition for a minimum in χ^2 becomes

$$\frac{\partial(\chi^2)}{\partial(\delta a_k)} = 0 = \frac{\partial}{\partial(\delta a_k)} \sum_{i=1}^{n} \left\{ \frac{\left[I_0(t_i) - Y^0(t_i) - \sum_{j=1}^{l} \frac{\partial Y^0(t_i)}{\partial a_j} \delta a_j \right]^2}{I(t_i)} \right\}$$

taking the derivative using the chain rule and rearranging yields

$$\sum_{i=1}^{n} \frac{\left(I_0(t_i) - Y^0(t_i)\right)}{I(t_i)} \cdot \left(\frac{\partial Y^0(t_i)}{\partial a_k} \right) = \sum_{i=1}^{n} \frac{1}{I(t_i)} \left(\sum_{j=1}^{l} \frac{\partial Y^0(t_i)}{\partial a_j} \delta a_j \right) \cdot \left(\frac{-\partial Y^0(t_i)}{\partial a_k} \right)$$

$$or \quad A_k = \sum_{j=1}^{n} \delta a_j B_{jk} \quad or\ in\ matrix\ form \quad \vec{A} = \overleftrightarrow{\delta a} \cdot \vec{B} \qquad \textbf{(Equations 4)}$$

$$so \quad \overleftrightarrow{\delta a} = \vec{A} \cdot \vec{B}^{-1}$$

where **A** and **B** are defined by the above equation.

Thus, the fitting function $Y(t_i)$ is found by choosing an educated guess for $G(t)$ as in Equation 3 and solving the convolution for $Y^0(t)$, as in Equation 2. The value of the initial guess should not affect the final answer. The above equations (Equations 4) are solved for **δa** and χ^2 is calculated (Equation 1). That **δa** is then fed into the equation for $Y(t_i)$, and the process is repeated until a convergent minimum value for χ^2 is found. Convergence can be achieved quicker through a modification of this method, as outlined by Marquardt (Marquardt 1963).

Appendix 4: Simulation methods and parameters

Simulation Methods

The absorption as a function of the position within the device can be modeled by solving Maxwell's equations at the layer interfaces with the appropriate boundary conditions. The donor-acceptor structure is sandwiched directly between the PEDOT anode and the aluminum cathode. The propagation and absorption of light is computed by using a transfer matrix method (Pettersson, Roman et al. 1999).

The absorption is taken to be related to the exciton creation flux J_{exc} (bound electron-hole pairs) by

$$J_{exc}(\nu, x) = P_{diss}(\nu, x)/h\nu$$

where P_{diss} is the dissipated power. Integration over all frequencies ν yields the total exciton creation flux as a function of position x.

Due to the large exciton binding energy in organic materials, exciton dissociation at small electric fields was found to take place predominantly at interfaces of materials with differing chemical potentials / molecular orbital energies (Ruhstaller, Carter et al. 2001). Therefore we only take excitons into account that are created within the exciton diffusion length of either the donor-acceptor interface or the interfaces with the electrodes.

The simulation of the transport is based on a numerical model proposed earlier for the behavior of space charges in organic light-emitting diodes (OLED) (Ruhstaller, Carter et al. 2001). In this model transport is governed by a system of partial linear differential equations relating current, charge generation, electric field, recombination, and mobility. For the charge injection from the electrodes a thermionic injection model (Scott and Malliaras 1999) is employed. The boundary condition is given by the difference of the externally

applied voltage and the built-in potential, taken to be the difference in work functions of the contacts. The steps in the chemical potential due to the internal layer interfaces are taken into account by a Miller-Abrahams form (Ruhstaller, Carter et al. 2001). The simulation performs a forward integration of Poisson's equation to obtain the electric field distribution. Integrating the continuity equation (advancing in time), the electron and hole charge densities are increased by the corresponding number of dissociated excitons. The effect of charge trapping is ignored in this simulation.

Parameters

The following quantities enter the simulation as parameters: The spectrum and intensity of the incident light, the complex refractive index $n(\lambda)$ of the anode, cathode, donor and acceptor, the work function of the electrodes, the LUMO and HOMO of the organic materials as well as their exciton binding energies and exciton diffusion lengths, the electron and hole mobilities and their field dependence, and the layer thicknesses.

For our simulations, we take the spectrum and intensity (100 mW/cm^2) for the lightbulb used for the experimental J-V measurements, the complex refractive index for Al (Weaver 1984) and ITO (Synowicki 1998), the absorption (*n*) and complex index (*k*) for M3EH-PPV and CN-ether-PPV estimated from our absorption data and ellipsometry data on CN-PPV (Greenham 1995) and MEH-PPV (Tammer and Monkman 2002) taken at IBM and work functions of 5.0 eV and 4.2 eV for PEDOT and Al, respectively. For M3EH-PPV, we use a HOMO and LUMO level of 5.3 eV and 3.0 eV, respectively, an exciton binding energy of 0.2 eV, an exciton diffusion length of 20 nm, and a zero-field electron and hole mobility of 10 x 10^{-6} cm^2/Vs and 100 x 10^{-6} cm^2/Vs respectively (Bozano, Carter et al. 1999). For CN-ether-PPV, we use HOMO and LUMO levels of 5.9 eV and 3.5 eV, respectively, an exciton

binding energy of 0.2 eV, an exciton diffusion length of 20 nm, and an electron and hole mobility of 100 x 10^{-6} cm^2/Vs and 10 x 10^{-6} cm^2/Vs, respectively. The field dependence of the electron mobility and hole mobility are taken as 5 x 10^{-4} $(m/V)^{1/2}$ for both materials. We did not have an independent measurement of the charge mobilities for CN-ether-PPV.

References

Bozano, L., S. A. Carter, et al. (1999). "Temperature- and field-dependent electron and hole mobilities in polymer light-emitting diodes." Appl. Phys. Lett. **74**(9): 1132-1134.

Emery, K. A. and C. R. Osterwald (1989). "Solar-cell calibration methods." Solar Cells **27**(1-4): 445.

Greenham, N. C. (1995). Electroluminescence in conjugated polymers. Ph.D. thesis, University of Cambridge.

Lakowicz, J. R. (1999). Principles of Fluorescence Spectroscopy. New York, Kluwer Academic/Plenum Publishers.

Marquardt, D. W. (1963). "An algorithm for least-squares estimation of nonlinear parameters." J. Soc. Ind. Appl. Math. **11**: 431.

Myers, D. R., K. A. Emery, et al. (1989). "Uncertainty estimates for global solar irradiance measurements used to evaluate PV device performance." Solar Cells **27**: 455.

O'Connor, D. V. and D. Phillips (1984). Time-Correlated Single Photon Counting. London, Academic Press.

Osterwald, C. R. (1986). "Translation of device performance-measurements to reference conditions." Solar Cells **18**(3-4): 269.

Pettersson, L. A. A., L. S. Roman, et al. (1999). "Modeling photocurrent action spectra of photovoltaic devices based on organic thin films." J. Appl. Phys. **86**(1): 487.

Ruhstaller, B., S. A. Carter, et al. (2001). "Transient and steady-state behavior of space charges in multilayer organic light-emitting diodes." J. Appl. Phys. **89**: 8.

Scott, J. C. and G. G. Malliaras (1999). "Charge injection and recombination at the metal-organic interface." Chem. Phys. Lett. **299**: 115.

Synowicki, R. A. (1998). "Spectroscopic ellipsometry characterization of indium tin oxide film microstructure and optical constants." Thin Solid Films **313**: 394.

Tammer, M. and A. P. Monkman (2002). "Measurement of the Anisotropic Refractive Indices of Spin Cast Thin Poly(2-methoxy-5-(2-ethyl-hexyloxy)-p-phenylenevinylene) (MEH-PPV) Films." Adv. Mater. **14**(3): 210.

Watson, J. M. (1993). Solar Simulation. Stratford, CT, Oriel Corporation.

Weaver, J. H. (1984). Optical Properties of Metals. CRC Handbook of Chemistry and Physics. R. C. Weast. Boca Raton, FL, CRC Press, Inc.**:** E-363.